ANSTO/E711

THE SCIENCE AND ENGINEERING OF HIFAR SAFETY

by

J. W. CONNOLLY AND B. E. CLANCY

with contributions from

D. R. H. BEATTIE, G. S. ROBINSON,

R. M. GODFREY AND B. V. HARRINGTON

December 1993

ISBN 0 642 59949 1

ISSN 1030-7745

REPORT E

AUSTRALIAN NUCLEAR SCIENCE
AND TECHNOLOGY ORGANISATION

LUCAS HEIGHTS RESEARCH LABORATORIES

THE SCIENCE AND ENGINEERING OF HIFAR SAFETY

by

J. W. Connolly and B. E. Clancy,

with contributions from

D. R. Beattie, G. S. Robinson,

R. M. Godfrey and B. V. Harrington.

ABSTRACT

Since the HIFAR Safety Document was first issued, major improvements have occurred in the quality of data and in the methods of calculation which are available for deterministic analysis of the behaviour of the reactor in normal or in accident conditions. Many such analyses have been carried out but the results have been reported in a wide range of internal memoranda and in external reports. In this report the most significant of the improved methods are described and the results of some of those analyses are reviewed. Principal areas covered are reactor physics of the core and reflector, the dynamics of the control systems, thermal hydraulic aspects important to safety margins, and the emergency core cooling system. Abnormal events discussed are inadvertent reactivity insertion sequences and the loss of coolant accident. Where possible, consistent sets of data are provided for use in future analyses.

ISBN 0 642 59949 1
ISSN 1030-7745

The following descriptors have been selected from the INIS Thesaurus to describe the subject matter of this report for information retrieval purposes. For further details please refer to IAEA-INIS-12 (INIS: Manual for Indexing) and IAEA-INIS-13 (INIS: Thesaurus) published in Vienna by the International Atomic Energy Agency.

HIFAR REACTOR: M1; REACTOR SAFETY: Q1,M2; COMPUTERIZED CALCULATIONS: Q2; COMPUTER CODES; EVALUATED DATA; EXPERIMENTAL DATA; HEAT TRANSFER; HYDRAULICS; MATHEMATICAL MODELS; NEUTRON REFLECTORS; REACTOR ACCIDENTS; REACTOR CONTROL SYSTEMS; REACTOR CORES; REACTOR COOLING SYSTEMS; REACTOR KINETICS; REACTIVITY COEFFICIENTS; RISK ANALYSIS; SAFETY ENGINEERING; SAFETY RODS; THEORETICAL DATA; TRANSIENTS

EDITORIAL NOTE

The Australian Nuclear Science and Technology Organisation (Ansto) replaced the Australian Atomic Energy Commission (AAEC) on 27 April 1987. Reports issued after April 1987 have the prefix ANSTO with no change of the symbol (E, M, S or C) or the numbering sequence.

ERRATA

Report: Ansto/E711

Section 2.

On page 2-1 the composition w/o of aluminium type 1050A should read

Al	Si	Cu	Fe	Mn	Mg
≥99.5	≤0.25	≤0.05	≤0.40	≤0.05	≤0.05

Section 3.

In the last 13 lines of page 3-19 two of the equations were in error as were some numerical values. The correct form of these lines is reproduced below with the changes shown in **bold** type.

about 0.250 s. At the time the braking cam engages the kinetic energy of the rod is **35.8** J and that of the drum is **7.5** J. However, the mechanical friction losses (mainly in the cam and lever) are quoted [1] as being rather high, 32 J, so that if we denote by E_s the energy stored in the springs and E_k the kinetic energy of rod and drum we have

$$E_k = E_s - Mg(z - z_0) + 32 \qquad \text{(correction)}$$

where $z - z_0$ is the distance fallen by the rod from the time the cam is engaged to the time the rod is brought to a halt. If we denote by x the spring compression (assumed equal for both pairs of springs, though this is not exactly true) then

$$E_s = 2\left[\tfrac{1}{2}k_1 + \tfrac{1}{2}k_2\right]x^2 = 7222\,x^2$$

and from the rod/cam geometry $z = 5.25\,x$, so that

$$7222\,x^2 - 233\,x - 11.3 = 0 \qquad \text{(correction)}$$

giving $x = \mathbf{0.059}$ m and $z = \mathbf{0.309}$ m. The latter value corresponds to an overshoot of the rod rest position of **0.10** m, **close to the observed overshoot of** 0.11 m.

CONTENTS

FIGURES

TABLES

SECTION 1

INTRODUCTION.

Consider yourself introduced, because I only remember one of your names, and that wouldn't be fair to the other.

Herbert Beerbohm Tree.

1. INTRODUCTION.

The DIDO reactor class, of which HIFAR is a member, was designed at the Harwell research laboratories of the United Kingdom Atomic Energy Authority; the design was loosely based on the CP5 reactor at Argonne National Laboratory in the United States. At that time, the primitive state of development of digital computers and nuclear data meant that design data had to be obtained from zero power integral experiments on core mockups. Although satisfactory for steady state operation, such data were inadequate for performance of detailed deterministic assessments; over the subsequent operational life of these reactors some data relating to safety were obtained but usually in response to particular safety concerns.

In the time between the first criticality of DIDO and the present day the design changes to these reactors have been

(i) the fuel element geometry has changed from parallel fuel plates contained in a box shroud to concentric tubes contained within a cylindrical shroud;

(ii) the fissile material content per element has been increased from 80 gm to 170 gm ^{235}U;

(iii) the operational power in some members of the class has been raised from 10 MW to 25 MW; and

(iv) the Emergency Core Cooling System has been altered because of the loss of the heat conduction path from fuel to the bulk moderator occasioned by switching to a concentric fuel tube design.

HIFAR commenced routine 10 MW operation in 1960 and the HIFAR Safety Document (HSD) was prepared in 1970. At about this latter time, development of the modular neutronics code system AUS began at Lucas Heights Research Laboratories; this was insufficiently advanced to make a contribution to the HSD which therefore continued to use rather coarse integral data from a limited range of experiments in the attempts to analyse system safety in a deterministic way.

The public controversy about nuclear safety in the 1970s and the complexity associated with attempting to provide deterministic answers to critics' concerns about safety of large power reactors saw the rapid growth of Probabilistic Risk Assessment (PRA) techniques which aimed at quantifying the overall risk to populations and the contribution of individual accident sequences to that risk. Though research and test reactors are simple compared with power reactors, and though both the paths to an accident situation and the consequences are far more limited, PRA methods have been applied to HIFAR; the emphasis on deterministic safety analysis has correspondingly decreased. Ironically, this shift in methodology has occurred over a time span during which the feasibility of meaningful calculation of reactor behaviour has increased markedly, mostly because of the huge increase in the power of digital computers and the high quality of information available in evaluated nuclear data files. These have allowed many earlier integral experiments to be used as benchmark data to test the soundness of calculational techniques.

To the authors of this report the time seemed appropriate to attempt a presentation of the current state of data and of the computational techniques of significance to deterministic safety analysis. We have given the report the title 'The Science and Engineering of HIFAR Safety', in part because no other suggested itself, and aware that such distinctions can arouse passions. As physicists, our classification is that Engineering has to do with anything that can break, rust, experience frictional losses, or can only be formulated in highly intractable equations whose variables are dimensionless. The bit left over is Science.

Our aims have been to present an insight into how well phenomena are understood by comparing calculation with experiment wherever possible and to provide a first source of data and references useful when examining postulated accident sequences.

There are many things which the resulting document is **not**. It is **not** a Safety Document in the accepted usage. It is **not** a complete compilation of data which describes the whole reactor; although we have attempted to provide a complete set of data for the core region, the original design manuals should be consulted for data about the parts of the reactor unchanged since commissioning. It is **not** a layman's guide to HIFAR safety.

A glance at the chapter headings may raise the legitimate criticism that the contents fall short of the promise implied by the title. Notably important topics, principally Instrumentation and Radiation Safety are not discussed. This is a result of deliberate choice, not carelessness, since it seems to us that both of these can only be compactly discussed within the framework of a particular postulated accident sequence of events. To do otherwise would require changing the emphasis to that of a text book, a temptation yielded to several times already in the text as it stands. We have justified this to ourselves on the grounds that a new generation of staff responsible for the reactor may benefit from restating this material in a HIFAR context.

In arranging the form of the report we have arbitrarily divided the reactor into component blocks to simplify and limit our discussion. At times this produces some awkwardness but should make it easier both to locate specific pieces of information and possible to identify areas where more information could be provided; this latter task we leave to others.

The seventh section introduces the problems and solutions associated with two classes of abnormal events, reactivity induced power transients and the loss of coolant accident (LOCA). Both these classes share a common basis, a mismatch between reactor power and heat removal which, if uncorrected, may lead to fuel melting. It will be noticed that the first class is given a much lengthier description than the second; this is not to be taken as indicating either that a reactivity accident is more likely than a LOCA or that its consequences are more significant but reflects the greater complexity attached to description of a transient overpower event. A LOCA, on the other hand, is almost completely described by arbitrary choices of leak location and size, and by an assumption as to whether falling film cooling is established or not.

We emphasise that, by restricting our discussion to just two classes of abnormal events, we do not imply that there are no other issues of potential significance to overall risk. However the PRA study on "frequency and consequences of fault sequences initiated by within-plant failures" identified the LOCA as the risk dominating event.

In the preparation of this report we have plundered material from a large number of sources and have received assistance from a large number of Ansto staff members; in particular we would thank John Matters, Ted Butcher and Ken Lloyd for patiently answering questions that must have demonstrated the depths of our ignorance. To those present and past Ansto officers whose assistance is not explicitly acknowledged we extend our thanks and apologies.

SECTION 2

THE REACTOR CORE.

Core.

The hard centre of a boil,
also
A central part of different character from that which surrounds it.

Oxford Universal Dictionary.

2. THE REACTOR CORE.

For the present purpose the core is defined as that cylindrical region within the Reactor Aluminium Tank (RAT) which has the length of the fuelled portion of the fuel elements and which has as its cross sectional area the sum of the cross sectional areas of the twenty five fuel element cells. We find it convenient to refer to that part of the core volume which is either inside the central thimble or external to the shroud tube as the moderator region, (with the additional definitions that the portion inside the thimble is occasionally called the inner moderator region and the portion external to the shroud tube is usually called the bulk moderator region); all of this contains heavy water. Also containing heavy water is that region between the fuel tubes which is referred to as the coolant region. The fuelled annulus of the fuel tubes is called the alloy-region while the usual term clad indicates the sheath surrounding the alloy-region, which consists of strips of uranium-aluminium alloy and aluminium. Data are presented for the (now) standard HIFAR fuel elements designated as Mark 4/23, and the fuel tubes are numbered 1 to 4, with number 1 being the inner tube.

2.1. Material Composition of the Core Components.

Fuel-alloy.

24.1 w/o uranium, 75.9 w/o aluminium type 1050A
^{235}U enrichment 60 w/o
Mass of ^{235}U per unit volume of alloy = 0.4827 g cm^{-3}
Uranium isotopic composition w/o

^{234}U	^{235}U	^{236}U	^{238}U
0.93	60.0	10.39	28.68

Aluminium type 1050A, composition w/o

Al	Si	Cu	Fe	Mn	Mg
99.5	0.25	0.05	0.40	0.05	0.05

Clad. Aluminium type 1050A (see above.)

Thimble. Aluminium to BS 1470 Grade 1B

Shroud. Aluminium to BS 1470 Grade 1B

Moderator/coolant D_2O 99.75, H_2O 0.25 (mole per cent)

Note that the uranium isotopic composition in a fresh element varies from order to order. The requirement currently placed on the fuel suppliers is that the ^{235}U content be 60 weight per cent and the numbers quoted refer to the fuel ordered in January 1988.

The moderator/coolant composition quoted refers to the heavy water purity following the 1991 upgrading prior to which the H_2O content was 1.4 mole per cent.

Whilst, in fact, the core region contains other materials in rigs and in the Coarse Control Arm blades we do not consider them here; the former are dependent on rig design while the latter are movable and more properly considered in the reactor control section.

2.2. Dimensional Data.

Fuel element lattice pitch = 0.1524 m
Area equivalent radius of unit cell = 0.0859 m
Length of fuelled section of element L = 60.325 cm
The radial dimensions of the unit cell are shown in Table 2-1 while Table 2-2 gives the volumes occupied by different materials in the cell.

Table 2-1
Unit Cell Region Data.

outer radius		region	volume		surface area
	(cm)			(litres)	(m^2)
r_1	2.536	inner D_2O	$\pi L r_1^2$	1.2188	.096
r_2	2.699	thimble	$\pi L(r_2^2 - r_1^2)$	0.1617	.102
r_3	3.039	coolant	$\pi L(r_3^2 - r_2^2)$	0.3697	.115
r_4	3.082	clad	$\pi L(r_4^2 - r_3^2)$	0.0499	.118
r_5	3.148	alloy-region	$\pi L(r_5^2 - r_4^2)$	0.0779	.119
r_6	3.191	clad	$\pi L(r_6^2 - r_5^2)$	0.0517	.121
r_7	3.529	coolant	$\pi L(r_7^2 - r_6^2)$	0.4305	.134
r_8	3.572	clad	$\pi L(r_8^2 - r_7^2)$	0.0579	.135
r_9	3.638	alloy-region	$\pi L(r_9^2 - r_8^2)$	0.0902	.138
r_{10}	3.681	clad	$\pi L(r_{10}^2 - r_9^2)$	0.0596	.140
r_{11}	4.019	coolant	$\pi L(r_{11}^2 - r_{10}^2)$	0.4932	.152
r_{12}	4.062	clad	$\pi L(r_{12}^2 - r_{11}^2)$	0.0659	.154
r_{13}	4.128	alloy-region	$\pi L(r_{13}^2 - r_{12}^2)$	0.1024	.157
r_{14}	4.171	clad	$\pi L(r_{14}^2 - r_{13}^2)$	0.0676	.158
r_{15}	4.509	coolant	$\pi L(r_{15}^2 - r_{14}^2)$	0.5560	.171
r_{16}	4.552	clad	$\pi L(r_{16}^2 - r_{15}^2)$	0.0738	.173
r_{17}	4.618	alloy-region	$\pi L(r_{17}^2 - r_{16}^2)$	0.1147	.175
r_{18}	4.661	clad	$\pi L(r_{18}^2 - r_{17}^2)$	0.0756	.177
r_{19}	4.990	coolant	$\pi L(r_{19}^2 - r_{18}^2)$	0.6017	.189
r_{20}	5.149	shroud	$\pi L(r_{20}^2 - r_{19}^2)$	0.3055	.195
r_{21}	8.590	bulk moderator	$\pi L(r_{21}^2 - r_{20}^2)$	8.9596	.326

2.3. Thermal Data.

Data for k, the material thermal conductivities and for C, the volumetric specific heats have been presented [1] as polynomials in the Celsius temperature T_C,

$$\begin{matrix} k \\ C \end{matrix}\Big] = A + BT_C + CT_C^2 + DT_C^3$$

where the coefficients are given in Table 2-3.

Table 2-2
Volumes in Unit Cell.

material/region	volume (litres)	volume fraction	
Coolant	2.451	0.1753	
Clad	0.502	0.0359	
Alloy-region	0.385	0.0275	
Thimble & shroud	0.467	0.0334	
Moderator	10.178	0.7279	Includes D_2O in central thimble.
Bulk Moderator	8.960		
Total cell	13.984	1.0000	

Table 2-3
Polynomial Forms for Material Properties.

Property	material	A	B $x10^4$	C $x10^7$	D $x10^{10}$	Temperature range T_K
Thermal	Alloy	174.0	-418.0	0.0	0.0	293 - 913 K
Conductivity		56.0	0.0	0.0	0.0	> 913 K
$W\ m^{-1}K^{-1}$	Clad	163.0	928.0	-1572.0	1011.0	293 - 922 K
		71.0	0.0	0.0	0.0	> 922 K
	D_2O	.566	13.4	-69.2	46.1	293 - 400 K
Volumetric	Alloy	2.232	14.1	-5.85	0	293 - 913 K
Specific		2.537	0.0	0.0	0.0	> 913 K
Heat	Clad	2.403	11.45	0.0	0.0	293 - 922 K
$MJ\ m^{-3}K^{-1}$		2.604	0.0	0.0	0.0	> 922 K
	D_2O	4.679	18.58	-739.4	2986.0	293 - 400 K

The listed coefficients for alloy and clad were obtained by least squares fitting to experimental data for 23.8 w/o U/Al alloy (close to the HIFAR alloy of 24.1 w/o) and for type 6061 aluminium respectively. This latter has the following composition

Al	Si	Cu	Fe	Mn	Mg
97.5	0.4 - 0.8	0.15	0.70	0.15	0.8 - 1.2

and although this differs somewhat from the HIFAR clad composition the data have been retained because they form a considered data set. The major differences between the two types is considered most likely to be in the thermal conductivity and this does not exert a crucial role in the discussion to follow. The data for D_2O were taken from Hill et.al. [2] and least squares fitted to give the listed coefficients.

With temperatures T measured in Kelvin, the coefficients (K^{-1}) of volumetric thermal expansion $\frac{1}{V}\frac{dV}{dT}$ are given as

Alloy $\quad 5.61\ 10^{-5} + 4.35\ 10^{-8}T - 3.87\ 10^{-11}T^2$

Cladding $\quad 7.02\ 10^{-5}$

Coolant $-7.874\ 10^{-3} + 4.2976\ 10^{-5}T - 5.3438\ 10^{-8}T^2$

These polynomial forms and those displayed in Table 2-3 are useful for the computer generation of numerical values. However they may be less convenient for simple hand calculations and the forms have been used to generate the tabulated numerical values given in Appendix A-5.

The phase composition as the alloy melts quoted in reference [1] is reproduced in Table 2-4.

Table 2-4
Phase Composition of the Fuel Alloy while melting.

T = 913 K	(a) Solid phase Al	0.654g
	(b) Solid phase UAl_4	U 0.238g
		Al 0.108g
T = 913 K	(a) Liquid phase U-Al	U 0.105g
		Al 0.702g
	(b) Solid phase UAl_4	U 0.133g
		Al 0.060g
T_- = 1003 K	(a) Liquid phase U-Al	U 0.160g
		Al 0.726g
	(b) Solid phase UAl_4	U 0.078g
		Al 0.036g
T_+ = 1003 K	(a) Liquid phase U-Al	U 0.162g
		Al 0.736g
	(b) Solid phase UAl_3	U 0.076g
		Al 0.026g
T = 1213 K	(a) Liquid phase U-Al	

The latent heat of fusion of the liquid phase at 913 K is given as 0.233 MJ/kg and this is based on experimental information. Data above this temperature are inferred and are represented in terms of energy absorption between temperature ranges. Thus between 913 and 1003 K, 0.0145 MJ/kg is absorbed and at 1003 K, 0.0022 MJ/kg. Between 1003 K and 1233 K a further 0.016 MJ/kg are absorbed. These figures do not include sensible heat taken in, and are expressed in terms of unit mass of alloy.

The latent heat of fusion for the cladding is assumed to be that of pure aluminium which is given [1] as 0.395 MJ/kg. The boiling point and latent heat of vaporisation of both alloy and clad are assumed to be those of pure aluminium given [3] as 2723 K and 11.7 MJ/kg.

2.4. Physical Properties of Materials.

The important properties of materials in a cell are given in Table 2-5.

Metal handbooks give 1050A aluminium strength data only at room temperature. The 1100 data are included in the table to give an indication of trends at higher temperatures; (1100 aluminium, at 99.0% Al, is nearly as pure as 1050A aluminium.) Discrepancies between data from different sources together with the number of significant figures of data, originally presented in psi, suggests an accuracy of perhaps ± 4 MPa. Interpolating and extrapolating higher temperature data as a function of impurity level suggests that 1050A aluminium tensile strengths at higher temperatures are described by the formula $\sigma = 8.29\ (T_{mu} - T)^{2.5}$, where $T_{mu} = 931$ is the upper melting temperature; σ is in Pascals and both T and T_{mu} are in degrees Kelvin. For U/Al alloys up to 17.3 % uranium the tensile strength is well fitted by the formula $\sigma = 8855\ (T_{ml} - T)^{1.5}$ and $T_{ml} = 919$ is the lower melting temperature, still in Kelvin.

Table 2-5
Cell Material Properties.

Young's Modulus E_γ	Aluminium	68.3 GPa
Bulk Modulus K	Coolant/moderator	2.2 GPa
Ultimate Tensile Strength	Aluminium	76 MPa at 024 C (Type 1050A)
		41 MPa at 200 C (Type 1100)
		14 MPa at 370 C (Type 1100)
Yield Strength	Aluminium	28 MPa at 024 C (Type 1050A)
		24 MPa at 200 C (Type 1100)
		11 MPa at 370 C (Type 1100)
Surface Tension	Aluminium	0.914 N m^{-1} at 650 C
	Coolant/moderator	0.071 N m^{-1} at 027 C
		0.063 N m^{-1} at 077 C
Kinematic Viscosity	Aluminium	0.545 μ m^2s^{-1} at 650 C
	Coolant/moderator	0.95 μ m^2s^{-1} at 27 C
		0.4 μ m^2s^{-1} at 77 C

The variation with absolute temperature T_K of the kinematic viscosity of molten aluminium is well fitted by the form $\eta = \eta_0 e^{(E/RT_K)}$ where R is the universal gas constant and the other terms have values $\eta_0 = 0.1492$, E=16500 J/mole.

It can be seen that the strength of aluminium decreases markedly at temperatures above 300C. This is not a structural problem since the strength of the elements is in the shroud tubes which support the weight of the shield plugs, the fuel tubes only being required to support their own weight. Provision is also made to allow thermal expansion of the fuel tubes to be accommodated by bending of the support combs.

2.5. Spatial Power Distribution.

For the steady state (constant fission rate) operation of HIFAR the power can be written as

$$P = \frac{\sigma_f N_0 E_f}{M} \int m(r)\phi(r)dV$$

where the integral is taken over that volume V of the reactor which contains ^{235}U and

P	= reactor power (MeV s^{-1})
N_0	= Avogadro's number
M	= atomic weight of ^{235}U
E_f	= energy release per fission (MeV)
σ_f	= microscopic fuel fission cross section
m(r)	= mass of fuel per unit volume at position r
ϕ(r)	= neutron flux at r

Because the neutron migration area is large in HIFAR it is possible to consider the flux ϕ(r) to be the superposition of a macroscopic (gross) flux distribution Φ(r), which defines the variation in flux between equivalent cell positions, and a fine flux distribution ψ(r), which defines the flux distribution throughout a cell. Thus $\phi(r) = \psi(r)\,\Phi(r)$ with the understanding that ϕ(r) is that for the critical reactor and m(r) is non-zero only at the fuelled regions of the cell. This simplified expression is introduced to allow discussion of the component terms and does not aim for analytic accuracy. If the reactor power is monitored by the flux Φ_0 at some reference position, then the assumption is made that P/Φ_0 is constant; this may not always be true.

2.5.1. Energy release per fission.

The total energy release per fission and the magnitude of the component terms (fission fragment kinetic energy, neutron energy, etc.) is discussed in many texts. In the environment of a long operating reactor this energy is augmented from capture reactions (which may exhibit a time dependence in the buildup and decay of species with appreciable half lives) and lessened by energy escape from the primary coolant circuit which then means that this energy cannot contribute to the heat balance across the primary heat exchangers. In HIFAR calculations the long standing value of E_f = 200 MeV is still adopted for the energy released into the primary circuit. This is in adequate agreement with more recent [4] assessments.

For analysis of steady state operation it is only necessary to know whether the energy from fission is deposited inside or outside the RAT; however this is no longer true for analysis of situations characterised by rapid changes in the reactor power. This is because the thermal diffusion time constants may be small when compared with power time constants so that the system is far from thermal equilibrium; further, reactivity feedback depends upon spatially dependent reactivity coefficients of energy, and the energy appearing within a region may be directly deposited there as well as diffusing in from adjacent regions. Fortunately for the analyst, the bulk of the energy release occurs unambiguously within the fuel element because of the short range of the fission fragments and β particles. In HIFAR transient studies the fractions of E_f deposited in the various regions are, for the sake of simplicity, taken to be just 0.95 to the alloy-region, 0.05 to the bulk moderator and zero to the other regions.

2.5.2. Thermal neutron flux distribution.

Because of the large neutron migration area, a characteristic of D_2O moderated reactors, the macroscopic flux at a fuel element lattice position is only weakly dependent upon the amount of fuel in that element. The predominant influence on the critical flux distribution comes from the position of the Coarse Control Arms (CCAs). At critical angles less than 10° the flux in the upper half of the core is greatly reduced and the peak flux is found near the bottom of the core. The ratio of this peak flux to the axial average flux is 2.0; no experience of operating the reactor at power has been obtained under these conditions - nor should it be. As the critical angle increases, the axial power distribution approaches that of a fully reflected cylindrical core and the peak/average axial flux ratio approaches the value [5] of 1.08 .

Not so much is known in general terms about the variation of the radial flux distribution from experimental measurements, although it is believed that, within their operational range, the influence of the CCAs is not so great and the distribution is more affected by the loading of the 2V and, to a lesser extent, the 6V facilities. In particular the 10H facility introduces a significant flux tilt across the core.

As a matter of routine, during the course of a HIFAR operating program the absolute thermal flux is measured at the centre of the C3 element by the activation induced in a gold wire placed there; relative fluxes in other fuel positions are obtained over the length of the element by irradiation of nickel wires.

Because of the large value of absorption cross section within the alloy section of the fuel tubes the flux within the fuel cell will exhibit a spatial variation $\psi(r)$ reflecting this. It is impossible to introduce flux measuring devices into the fuel elements and the determination of $\psi(r)$ must depend on calculation; for fresh elements, the results [6] are given in Table 2-6.

2.5.3. Fuel distribution.

The mass of ^{235}U in an element starts from 170g for fresh elements and reduces with burnup to about 70g at the end of life. The distribution of the fuel elements is entirely within the control of

Table 2-6
Flux and Power Distribution.

Fuel tube number	1	2	3	4	
Fractional power	0.193	0.225	0.265	0.317	
Normalised flux	0.865	0.857	0.877	0.929	1.0 at centre of element

the reactor management; since the lattice thermal flux values are sensibly constant, the power generated by an element at a given position will only be proportional to the mass of fuel in that element and quite gross values of the ratio of maximum element power to average element power could be produced by an ill advised fuel management strategy. The calculational basis of HIFAR fuel management is discussed in Section 2.7 below. The limits currently imposed on fuel element power are [7]:

> "The power output from any fuel element in any lattice position must not exceed 850 kW (11 MW power)", and
>
> "The power output from any fuel element in any peripheral lattice position must not exceed 700 kW (11 MW power)"

2.5.4. Total reactor power.

The total power output can be determined from the coolant flow rate and temperature rise across the core. The large thermal time constants of the fuel tubes mean that they rapidly reach an equilibrium value with the coolant and we have

$$\frac{dE}{dt} = P - f_C E$$

where E is the energy excess in the coolant above its value at zero time, up until which time we assume the power to be zero. At this time we assume an instantaneous jump in the the total reactor power to a value P, while f_C denotes the coolant flow time constant which is the volumetric coolant flow rate divided by the total coolant volume and has the numerical value $5.9\ s^{-1}$.
The solution of this equation gives

$$E = \frac{P}{f_C}\left[1 - e^{-f_C t}\right]$$

so that the coolant enthalpy rapidly reaches a steady value. From the heat capacity of the coolant given in Section 2.5 a reactor power of 10 MW corresponds to a temperature difference across the core of 5.97 K; this is in good agreement with observed values of 6.0 ± 0.1K.
Note: Here and throughout this report the symbol ± refers to one standard deviation or one standard error, depending on the context.

Alternatively, the integral power can be deduced from a measurement of the absolute thermal flux at some given position because these can be related, one to the other, by the insertion of fundamental nuclear data into the equation of Section 2.5. A value for the flux at this reference position can correspondingly be deduced if the power is known, and this value can be compared with the measured value. A detailed examination of the variation of measured to calculated flux ratios over many operating programs has been performed [8]; although the agreement is reasonable the analysis is hampered by the unexpectedly large scatter amongst the measured values.

2.6. Derived Quantities.

Some useful derived quantities can now be given.

The ratio D/ ^{235}U of the number of atoms in a reactor cell is 1562 for a new element and 2370 for an element at average burnup. The system is under moderated and, for this reason alone, core void and temperature coefficients can be expected to be negative.
In the complete core at 323 K, the heat capacities of various components are:
0.0224 MJ/ deg K for alloy-region
0.0313 MJ/ deg K for clad
0.2850 MJ/ deg K for coolant
1.1810 MJ/ deg K for moderator

Thermal time constants $\frac{k}{\rho c \delta^2}$ (all in units of s^{-1}) for fuel element regions of thickness δ are:

Alloy-region	Clad	Coolant
686	360	0.042

Table 2-7
Fuel Tube Power and Heat Transfer Data.

		tube 1	tube 2	tube 3	tube 4	all tubes
Clad/Coolant surface area	(m^2)	0.2361	0.2733	0.3104	0.3476	1.131
Surface area of alloy-region	(m^2)	0.2361	0.2733	0.3105	0.3475	1.131
Fuel content	(kg)	0.0336	0.0396	0.0456	0.0514	0.170
Fuel surface density	(kg m^{-2})	0.142	0.145	0.147	0.148	
Clad/Coolant heat flux at 1 W element power	(W m^{-2})	.817	.823	.854	.912	

For the whole core, the heats of fusion at 913 K are 7.50 MJ for the alloy-region and 9.99 MJ for the clad; these are to be compared with the heat of vaporisation for the coolant at 373 K which is 135 MJ. Some basic heat transfer data for the individual fuel tubes are collected in Table 2-7.

2.7. Neutronics.

HIFAR achieved initial criticality in 1958, and for the first years of operation fuel management and safety arguments were based on parameters measured during the commissioning period of the reactor augmented by additional measurements where these were thought necessary, chiefly as a consequence of changes in the type of reactor fuel element or disposition of irradiation rigs.

In the early seventies development of the modular neutronics code system AUS [9] began and in the intervening years a transition from use of experimental data to calculated parameters has occurred. This was partly the result of difficulty in gaining reactor time for experimental purposes but perhaps more importantly followed from a realisation of the difficulty of obtaining adequate accuracy in measurements of space and energy dependent data. Extensive benchmark testing and experience in using the codes has led to great confidence in the correctness of calculations to the point where the reactor could be almost entirely operated and managed with the use of calculated parameters. This section briefly describes the present status of the AUS code modules and the specific problems that have been addressed with them.

The AUS code system consists of linked modules for performing multigroup data preparation, collision probability, 1-dimensional S_N, 2- or 3-dimensional diffusion and burnup calculations. Several 2-dimensional S_N and Monte Carlo codes obtained from the Radiation Shielding Information Center (RSIC) in the United States are also loosely coupled within the AUS system. The AUS 200 group neutron/photon cross section library includes temperature dependent and

resonance data and was generated from ENDF/B-IV and the unrestricted portion of the ENDF/B-V data. The AUS scheme can be used for a wide range of problems including thermal and fast reactors, fusion blankets and many other neutron applications which may also include photons.

Some of the first extensive and significant calculations with AUS were detailed calculations of temperature and void coefficients of reactivity of the SPERT I and II cores [10] [11] [12]. These cores had been selected as a benchmark for the transient code ZAPP [13] being developed for calculations on the safety of a series of proposed fast neutron assemblies. These calculations demonstrated that difficulties in calculating SPERT transients arose from the lack of spatial resolution in measurements of reactivity coefficients. Attempts to highlight void formation as a shutdown mechanism by constructing cores of a range of fuel/moderator ratios were defeated with the calculations showing that as the void coefficient decreased, the temperature coefficient increased, resulting in the dynamic shutdown reactivity coefficient being only weakly dependent on the degree of core moderation.

The first detailed HIFAR model [14] developed was a five group 2-dimensional XY diffusion theory model capable of predicting reactivity coefficients, power distributions, and neutron fluxes near the core. To achieve satisfactory agreement in the end-of-program reactivity and the tilted flux shape across the core it was necessary to include all the reflector facilities in some detail. Temperature and void reactivity coefficients for HIFAR safety assessment were calculated by perturbation theory. Calculated fuel-plus-poison and 1/v absorber reactivity coefficients at each fuel element position are used in the HIFAR fuel management program HIFUEL [15] which predicts the end and start of program reactivities to within about 0.5% reactivity. The fuel management code HIFUME [16], developed as a replacement for HIFUEL, includes 2 group coarse mesh XY diffusion calculations and burnup of nuclides within AUS. Recently [17], three dimensional calculations of HIFAR neutronics behaviour have been performed; these included detailed estimates of the effects of the CCAs. The calculated changes in reactivity were higher by only about 6% than measured values over the whole angular range (56°) of CCA travel.

In anticipation of the restricted supply of 80 weight per cent ^{235}U fuel, neutronics models were used to assess the performance penalties and safety implications of using reduced enrichment fuel (with 45% and 20% ^{235}U) in HIFAR [18]. Calculations showed no significant changes in the reactivity coefficients and other safety related parameters. Confidence in the calculated HIFAR reactivity coefficients was given by the excellent agreement achieved between calculations and observations for the SPERT II D_2O moderated core BD22/24 [19] which is similar to the HIFAR core, and for the IAEA benchmark DIDO-like core [20].

2.7.1. Delayed neutron data and prompt neutron lifetime.

Although routine operation does not require more than a relative reactivity scale, establishment of an absolute scale is desirable for the following reasons:

- Safety assessments require a knowledge of absolute reactivity changes following systems failures or malfunctions.
- An absolute reactivity scale allows proper evaluation of the degree to which calculated and observed reactor behaviour conform.

The evaluation of the reactivity scale for HIFAR by use of the inhour equation remained unchanged for many years.

The latest revision [21] includes a recent evaluation of delayed neutron data, takes account of the differing energy spectra for emission of delayed neutrons compared with prompt neutrons and uses a calculated value of the photoneutron effectiveness factor α.

The data on delayed neutron fractions for ^{235}U were taken from ENDF/B V [22]. A small correction was made to account for the 0.75% contribution from ^{239}Pu. The resulting value of the total delayed neutron fraction β is 0.00682. Values for β_{eff} were calculated by taking the importance of each group of delayed neutrons relative to prompt neutrons according to an RZ diffusion calculation of HIFAR using a model based on that of Harrington [14]. This gave a β_{eff} value of 0.007045; the six delayed group data are given in Table 1 of reference [21], and are reproduced below.

Table 1 of TN-116
DELAYED NEUTRON AND PHOTONEUTRON DATA

Delayed neutrons, β_{eff} = 0.007045				
Group	Half-life		Decay constant (s^{-1})	$(\beta_i)_{eff}$
1	54.49	s	0.01272	0.000269
2	21.84	s	0.03174	0.001501
3	5.972	s	0.11605	0.001324
4	2.228	s	0.31105	0.002866
5	0.495	s	1.3997	0.000902
6	0.179	s	3.8675	0.000183
Photoneutrons, β_γ = 0.0010, α = 0.63				
Group	Half-life		Decay constant (s^{-1})	a_j
1	12.8	d	$6.26\ 10^{-7}$	0.00049
2	53.0	h	$3.63\ 10^{-6}$	0.00102
3	4.4	h	$4.37\ 10^{-5}$	0.00319
4	1.65	h	$1.17\ 10^{-4}$	0.02311
5	27.0	m	$4.28\ 10^{-4}$	0.02050
6	7.7	m	$1.50\ 10^{-3}$	0.03331
7	2.4	m	$4.81\ 10^{-3}$	0.06956
8	41.0	s	$1.69\ 10^{-2}$	0.20250
9	2.5	s	$2.77\ 10^{-1}$	0.64637

The total $\beta_{eff} = \beta_{eff}$ (delayed neutrons) + $\alpha\ \beta_\gamma$ (photoneutrons) = 0.0077

These data give the photoneutron yield for small samples in a large D_2O volume and they need to be multiplied by a factor α which accounts for photon energy degradation and absorption in the fuel elements and aluminium, as well as the reduced importance of photoneutrons produced in the reflector. The resulting α value of 0.63 has an uncertainty of ±0.02 and the reasons for this uncertainty are discussed in reference [21].

An appropriate value of the prompt neutron lifetime for general use in HIFAR calculations has been obtained from RZ diffusion calculations as 600 μs. Duerden's [23] value of 400 μs is not recommended.

2.7.1.1. Revised reactivity scale.

The relation between reactivity and doubling time T (seconds) is given by the equation

$$\frac{k_{eff}-1}{k_{eff}} = \frac{0.693\ l_a}{T} + \sum_i \frac{(\beta_i)_{eff}}{1+T/\tau_i} + \alpha\ \beta_\gamma \sum_j \frac{a_j}{1+T/\tau_j}$$

where

l_a is the prompt neutron lifetime,

τ_i, τ_j are the half lives of the delayed and photoneutron groups.

The unit of reactivity used in HIFAR operations is the percent, i.e. - $\rho\% = 100\,\frac{k_{eff}-1}{k_{eff}}$; however the dollar is a useful unit of reactivity and is defined so that $\rho(\$) = \rho_{absolute} / \beta_{eff}$

A revised tabulation giving values of reactivity from doubling time is given in reference [21]; however a useful approximation is obtained by use of the formula

$$\rho\% = \frac{a + bT + cT^2 + dT^3}{T + eT^2 + fT^3 + gT^4}$$

when the coefficients have the values

$a = 8.96399\ 10^{-2}$ $b = 6.40084\ 10^{-1}$ $c = 6.03402\ 10^{-2}$ $d = 8.90638\ 10^{-5}$
$e = 2.93609\ 10^{-1}$ $f = 8.39585\ 10^{-3}$ $g = 5.97489\ 10^{-6}$

For values of the doubling time T in the range $1.0<T<1000$ this produces values for $\rho\%$ for which the proportional error is less than 2 parts in 300.

Solution of the inverse problem is gained by using the approximation

$$T = \frac{a + b(\rho\%) + c(\rho\%)^2 + d(\rho\%)^3}{(\rho\%) + e(\rho\%)^2 + f(\rho\%)^3 + g(\rho\%)^4}$$

when the coefficients have the values

$a = 1.89918\ 10^{1}$ $b = 1.76433\ 10^{3}$ $c = -1.88999\ 10^{3}$ $d = -1.10998\ 10^{0}$
$e = 2.47366\ 10^{2}$ $f = 6.65011\ 10^{2}$ $g = 1.14395\ 10^{3}$

The accuracy in doubling time is then always better than one percent.

2.7.2. Critical mass.

It is of interest to establish the minimum core critical mass for elements loaded into the fixed lattice positions. During the initial loading of the reactor Mark 2 elements were used and criticality was determined with all vertical thimbles removed from the RAT. The minimum critical ^{235}U masses established for 115 g and 100 g Mark 2 elements were 1.12 kg and 1.08 kg respectively. The minimum critical mass for the current Mark 4/23 170 g elements has been determined by calculation as 1.02 kg. The aluminium content of this element is 0.8 kg greater than that of the Mark 2 elements, largely because of the presence of an internal thimble and the fuel enrichment is lower, 60% as compared with 80%. These differences would be expected to give a higher minimum critical mass with the Mark 4/23 element than with the Mark 2 element; however the compactness of the latter produces a more pronounced flux fine structure than in the former and this would appear to cancel out the advantage of lower aluminium and ^{238}U content.

2.7.3. Neutron source strength.

The photodisintegration of the deuteron by gamma photons of energy greater than 2.23 MeV produces additional delayed neutron groups in the kinetic equations. However, some of these groups have inordinately long half lives and are, in any calculation, more sensibly treated as contributing to a time dependent neutron source which varies slowly compared with any time dependent neutron power. Because the source of these neutrons comes almost entirely from the gamma spectrum of irradiated fuel it might be expected that the strength will depend on the irradiation history of the fuel elements making up the core.

The importance of the source term lies in the effect which it has on reactivity measurements on the reactor rather than in any direct link to safety questions. Both period and inverse kinetic measurements require knowledge of the source strength if good accuracy in reactivity estimates is to be obtained. Again, during an approach to critical by loading partly spent fuel, the source strength increases with the number of elements loaded and their irradiation history. This produces under-estimates of critical mass if the data are treated in a conventional manner.

At present the art is not sufficient to calculate source strength from the photodisintegration cross section and the gamma flux above 2.23 MeV. Simple sub critical estimates of the source strength have been made [24],[25] and for the experimental conditions employed these are probably accurate to ±20%. Estimates of the time dependent source strength have been made [24] from published photoneutron half lives, and by normalisation to the measured strength at three days from shutdown the data of Figure 2-1 is obtained. Further measurements are needed, particularly at long elapsed times after shutdown, if this situation is to be improved.

2.7.4. Reactivity coefficients.

The HIFAR Safety Document (HSD) quotes values for a number of reactivity coefficients; some of these were provided to allow approximate reactivity accounting estimates to be made while others were used in analysing postulated transients. Almost all of them had been established on cores using earlier fuel elements and enrichments by a variety of techniques and then scaled for a 3.75 kg ^{235}U core using the inverse mass rule, i.e. ρ proportional to (^{235}U mass)$^{-1}$.

The HSD gives measured values for reactivity coefficients associated with various rigs. Also quoted is a measurement of the whole-reactor coefficient of reactivity against temperature. The value –0.0434% δk/k per C^{o} , for a 3.2 kg ^{235}U core, is due mainly to variation of water density and to volume changes of structural material, principally aluminium.

We here present, as best estimates, results obtained by calculations with the AUS codes. These have been determined (G. S. Robinson - private communication) for 170 g Mark IV elements using 60% enriched fuel in a core uniformly burnt to a ^{235}U fuel loading of 2.75 kg.

The 1/v absorber and fuel+poison reactivity coefficients are presented for each fuel element with positions as follows:

	A1	A2	A3	A4	
B1	B2	B3	B4	B5	B6
C1	C2	C3	C4	C5	
D1	D2	D3	D4	D5	D6
	E1	E2	E3	E4	

Table 2-8
Absorber Reactivity Coefficient.
Scales as (^{235}U mass)$^{-0.88}$
100 times ρ% per cm^2. e.g. central value is ρ%=-0.02458

	-0.794	-1.094	-1.181	-1.090	
-0.922	-1.450	-1.889	-1.875	-1.563	-1.223
-1.580	-2.091	-2.458	-2.204	-1.750	
-1.274	-1.805	-2.197	-2.317	-1.873	-1.325
	-1.451	-1.789	-1.789	-1.342	

Table 2-9
Fuel plus Poison Reactivity Coefficient.
Scales as (^{235}U mass)$^{-1.83}$
100 times ρ% per g ^{235}U burnup.

	-0.532	-0.694	-0.760	-0.732	
-0.631	-0.880	-1.147	-1.217	-1.036	-0.837
-0.992	-1.351	-1.523	-1.405	-1.100	
-0.854	-1.115	-1.418	-1.400	-1.127	-0.884
	-0.953	-1.136	-1.118	-0.889	

Using the same core as that used for the absorber and fuel coefficients just given, temperature and void coefficients were also calculated; resulting δk/k values are given only for the central element and for an average element.

Table 2-10
Temperature and Void Coefficients per Fuel Element or Cell.

	average	centre
Fuel Temperature Coefficient. δk/k per ° C per fuel element Scales as (^{235}U mass)$^{-0.2}$	$-1.35\ 10^{-7}$	$-2.40\ 10^{-7}$
Fuel + Coolant Temperature Coefficient. δk/k per ° C per fuel element Scales as (^{235}U mass)$^{-1.1}$	$-3.37\ 10^{-6}$	$-4.70\ 10^{-6}$
Total Moderator Temperature Coefficient. δk/k per ° C per cell Scales as (^{235}U mass)$^{-1.1}$	$-7.00\ 10^{-6}$	(n.a.)
Coolant Void Coefficient. δk/k per 1% coolant void per fuel element Scales as (^{235}U mass)$^{-0.5}$	$-3.56\ 10^{-5}$	$-5.44\ 10^{-5}$
Total Moderator Void Coefficient. δk/k per 1% void per cell Scales as (^{235}U mass)$^{-0.5}$	$-1.32\ 10^{-4}$	(n.a.)

The temperature coefficients do not include the effects produced by the density changes which follow from temperature changes. No attempt is made to separate temperature coefficients into spectrum and Doppler contributions for the fuel; in any event the Doppler effect for 60% enriched fuel is very small.

In this tabulation, as elsewhere, the total moderator includes the D_2O in the central thimble as well as the bulk moderator.

From the data of Table 2-10 and the coefficients of thermal expansion given for D_2O in Section 2.3 the total coolant temperature coefficients arising from the changes in neutron spectrum and in coolant density with temperature can be calculated. These coefficients apply to the total volume of coolant in the core. The results are shown in Table 2-11 together with the corresponding coefficients for total moderator temperature and density changes.

Table 2-11
Total Temperature and Density Coefficients.

Coolant			
Material Temperature ° K	Neutron Spectrum Coefficient 1/k dk/dT	Material Density Coefficient 1/k dk/dT	Total Coefficient 1/k dk/dT
293	$-8.09\ 10^{-5}$	$-1.16\ 10^{-5}$	$-9.25\ 10^{-5}$
313	$-8.09\ 10^{-5}$	$-3.05\ 10^{-5}$	$-11.14\ 10^{-5}$
333	$-8.09\ 10^{-5}$	$-4.55\ 10^{-5}$	$-12.64\ 10^{-5}$
373	$-8.09\ 10^{-5}$	$-6.42\ 10^{-5}$	$-14.51\ 10^{-5}$
Total Moderator			
Material Temperature ° K	Neutron Spectrum Coefficient 1/k dk/dT	Material Density Coefficient 1/k dk/dT	Total Coefficient 1/k dk/dT
293	$-17.5\ 10^{-5}$	$-4.30\ 10^{-5}$	$-21.80\ 10^{-5}$
313	$-17.5\ 10^{-5}$	$-11.29\ 10^{-5}$	$-28.79\ 10^{-5}$
333	$-17.5\ 10^{-5}$	$-16.87\ 10^{-5}$	$-34.37\ 10^{-5}$
373	$-17.5\ 10^{-5}$	$-23.80\ 10^{-5}$	$-41.30\ 10^{-5}$

2.7.5. Techniques of reactivity measurement.

Safe operation of the reactor requires the ability to monitor and control the multiplication factor k_{eff}, and to accurately assess the effect on it of changes in the physical constitution of the reactor. This, in turn, requires the establishment of some fundamental standard of reactivity measurement which can conveniently and reasonably quickly determine the time dependent reactor power after some postulated change in the reactor and also ensure that safety margins are not exceeded.

In HIFAR this reactivity standard is the differential reactivity control $\frac{d\rho}{d\theta}$ of the CCA bank and all other reactivities and reactivity coefficients are referred to it. It is therefore pertinent to discuss briefly the methods used to establish a reactivity calibration of the CCA bank. These methods rely on measurement of the time dependent neutron flux which is analysed in terms of the point reactor kinetic equations

$$\dot{n} = [k(1-\beta)-1]\frac{n}{l_a} + \sum \lambda_i C_i + S$$

$$\dot{C}_i = \frac{k\beta_i}{l_a} n - \lambda_i C_i \qquad \text{and} \quad \beta = \sum \beta_i$$

where $k = k_{eff}$ is a function of time, the energy distribution in the reactor, and the distribution and concentration of nuclei important to the neutron balance equations.

The terms n, C_i, with $\dot{n}$, $\dot{C}_i$ denote the neutron and delayed precursor concentrations with their time derivatives, while λ_i, β_i are the decay constants and fractional yield in fission of the precursors, l_a is the prompt neutron lifetime and S is the neutron source strength.

Alternatively, steady state measurements of the neutron multiplication M can be employed to determine k from the relation

$$M = \frac{1}{1-k}$$

2.7.5.1. Positive asymptotic period measurements.

If a reactor has k made greater then unity and this value is held constant, then **ultimately** the power will rise with a fixed time constant α or period $1/\alpha$. Under these conditions the relationship between reactivity and the inverse period can be obtained from the kinetic equations in the form of the inhour equation

$$\rho = \frac{k-1}{k} = \left[\alpha l_a + \sum \frac{\alpha \beta_i}{\alpha + \lambda_i}\right] \frac{1}{1+\alpha l_a}$$

The major problem associated with this method is not in the accuracy achievable in measuring the time dependent flux but in determining whether or not the asymptotic value of the period has been reached. The problem has been examined by Toppel [26] who summarised his conclusions as follows.

> *A common method used to determine reactivity is to measure the reactor period and then refer to the inhour equation which relates asymptotic period to reactivity. The implicit assumption in such a method is that the neutron population is varying exponentially with time. The conditions necessary for this assumption to be valid have been obtained by a quantitative examination of the time behaviour of the neutron population. The results obtained show that under common experimental conditions, several minutes may be required following a positive step change in reactivity in order to achieve accuracy by means of period determination. In addition, in the case of a reactor with a constant extraneous source, a significant increase in this waiting time can result even if the reactor is initially only very slightly subcritical. Whereas in principle both positive and negative reactivities may be obtained from period observations, it is pointed out that in practice serious objections exist for the case of negative reactivities.*

This paper gives the results of calculating from the kinetic equations the instantaneous period n/ṅ as a function of time after a step increase in reactivity from some steady sub-critical level and determining the time taken for this period to approach the asymptotic value within a given precision. Figure 2-2 shows some typical results found by repeating Toppel's analysis.

These results cannot be directly applied to the HIFAR case because, with HIFAR, reactivity is added as a ramp and the source strength for measurements between programs is large. The behaviour in this situation can be approximately described as follows:

The source multiplied sub-critical power is $S / (1 - k)$ where S is the source strength in watts and k is constant. Provided that delayed critical is not approached too closely and provided that the ramp injection of reactivity is not too slow, then delayed neutrons can be ignored and the time dependent reactor power is given to a good approximation by $S / (1 - k(t))$. It follows that the instantaneous inverse period is $\frac{\dot{n}}{n} \approx \frac{k}{\rho} \frac{d\rho}{dt}$.

The maximum speed of CCA withdrawal is $0.0373°\ s^{-1}$ which gives, for typical starting angles, a reactivity ramp of $3.7\ 10^{-4}$ dk/k per second $\approx 5¢s^{-1}$ and the instantaneous doubling time as the reactor approaches delayed critical is shown in Figure 2-3, which figure also shows the source multiplied sub-critical power. It is clear that, at about \$1 subcritical during start up, the doubling time is approaching the trip level and the operator must slow the ramp by alternate use of the raise and stop buttons. At the same time the power has passed through the 1 kW range and is approaching the 10 kW range as the reactor approaches delayed critical. Since thermal effects produce feedback as 100 kW is approached, the time between reaching this power and the arms reaching their final super-critical position will be too short to allow reasonable expectation that the asymptotic doubling time will be observed. Calculation of the departure of the observed

doubling time from the asymptotic value would require the actual ramp rate as the arms approach their final position to be used; this has not been attempted.

Following the doubling time measurement the CCAs are reinserted to determine the critical angle at a steady power of 10 kW. However, because of the long lived delayed and photoneutron precursors taking appreciable time to come into equilibrium, the reactor must be maintained with $k \neq 1$ to obtain a constant power, as discussed by Cohn [27]. Whether $k < 1$ or $k > 1$ will depend on the precursor concentrations established at earlier times. Even when sufficient time is allowed to reach equilibrium, if the source term is large the steady power CCA position will correspond to $k < 1$; for a source strength of 5W the reactor will be subcritical by 7 ¢. This introduces significant errors in the determination of $\Delta\theta$ in calculations of the differential CCA bank worth.

It is important to consider the effect on the inferred reactivity of data errors and errors in measured period. The inhour equation for the periods of interest contains dominant terms of the form

$$Q_i = \frac{\alpha\beta_i}{\alpha + \lambda_i}$$

Partial differentiation with respect to β_i and λ_i gives the fractional error in Q_i as

$$\varepsilon_i = \left[\left(\frac{\delta\beta_i}{\beta_i}\right)^2 + \left(\frac{\delta\lambda_i}{\alpha + \lambda_i}\right)^2 \right]^{\frac{1}{2}}$$

and writing $X_i = \alpha/\lambda_i$

$$\varepsilon_i^2 = \left(\frac{\delta\beta_i}{\beta_i}\right)^2 + \left(\frac{\delta\lambda_i}{\lambda_i}\right)^2 \cdot \frac{1}{X_i^2 + 2X_i + 1}$$

Now for large X_i, corresponding to short periods and/or long lived precursors

$$\varepsilon_i = \frac{\delta\beta_i}{\beta_i}$$

while for small X_i, (long periods and/or short lived precursors)

$$\varepsilon_i = \left[\left(\frac{\delta\beta_i}{\beta_i}\right)^2 + \left(\frac{\delta\lambda_i}{\lambda_i}\right)^2 \right]^{\frac{1}{2}}$$

The fractional error ξ in the reactivity, neglecting the small term αl_a is thus

$$\xi = \frac{\left[\sum (Q_i \varepsilon_i)^2\right]^{\frac{1}{2}}}{\sum Q_i}$$

For purposes of illustration we have calculated ξ for a period of 33s; we use the values for, and the errors in λ_i and β_i given by Keepin [28]; the percentage error in ρ is 3.3% neglecting photoneutrons.

By the same method we find

$$\frac{\delta Q_i}{Q_i} = \frac{1}{1 + X_i} \frac{\delta\alpha}{\alpha}$$

so that for large X_i, $\frac{\delta Q_i}{Q_i} \rightarrow 0$; for small X_i, $\frac{\delta Q_i}{Q_i} \rightarrow \frac{\delta\alpha}{\alpha}$. Inserting numerical values of 10% for $\frac{\delta\alpha}{\alpha}$ and, as before, assuming a period of 33s gives a percentage error in ρ of 3.3%

Asymptotic period measurements under the conditions existing between program shutdown and start up can only yield coarse estimates of the CCA differential reactivity unless elaborate calculations are employed to determine appropriate corrections; if the source strength can be reduced to less than 0.5W the technique becomes feasible but still requires care and patience in establishing the correct conditions for the measurements to be valid.

This conclusion is not new; we emphasise it here because it there will always be a temptation for operators to place undue reliance upon this apparently simple technique.

2.7.5.2. Inverse kinetic measurements.

The restriction that the power be rising on a steady exponential period in order to determine the reactivity can be removed by recasting the kinetic equations in a more general way than the inhour equation. Thus, integration of the precursor equations and using the neutron generation time $l_g = \frac{l_a}{k_{eff}}$ gives

$$C_i(t) = C_i(0)\, e^{-\lambda_i t} + \int_{t'=0}^{t'=t} \frac{\beta_i}{l_g}\, n(t')\, \exp[-\lambda_i(t-t')]\, dt'$$

and substituting this into the first equation yields, after re-arranging

$$\rho(t) = \frac{l_g}{n(t)}\frac{dn}{dt} + \beta - \frac{Sl_g}{n(t)} - \frac{1}{n(t)}\sum\left[l_g\lambda_i C_i(0)e^{-\lambda_i t} + \int_{t'=0}^{t'=t} \beta_i n(t')\exp[\lambda_i(t'-t)]dt' \right]$$

In this form the transient terms are accounted for and the reactivity can be computed from the recorded time variation of power providing that the source strength and the initial precursor concentrations are known. This last condition can be met by maintaining a constant power prior to the measurements for long enough to bring all the precursors into equilibrium, for then

$$C_i(0) = \frac{\beta_i n(0)}{\lambda_i l_g}$$

However the time taken to saturate all delayed groups is prohibitively long and some degree of compromise is required unless the longer lived groups are treated as part of a time dependent source.

The influence of the source term and thus the accuracy required of its magnitude can be minimised by maintaining the power variation so that $l_g S/n$ is always small compared with ρ. This is generally no problem except in the cases where large negative reactivity additions are made and the power level becomes small.

In principle the inverse kinetics technique allows the inclusion of thermally induced feedback and xenon concentration variations during the reactivity measurement. However both these are subject to spatial effects, the first through the distribution of energy which is uncertain because of lack of information about the flow path of coolant in the RAT, and the second because of the link between xenon production and the neutron flux distribution; an additional complication may be establishing the initial condition for xenon concentration. If precision is required it is best that these terms be zero or at least represent only a second order correction.

2.7.5.3. Sub-critical measurements.

From the relationship between the multiplication M and the effective multiplication factor k

$$M = \frac{1}{1-k}$$

it is theoretically possible to determine k by measuring the steady state neutron density at some point; if the concentration of the source strength S at that point is known then

$$M = \frac{n_0}{Sl_a}$$

In practice the source strength and the relationship between the source distribution and the neutron density distribution are not at all well known; thus only apparent or relative multiplications can be measured and then only as long as the source/fission neutron ratio at the measurement point is constant. The effective source can be determined if it is possible to make the reactor a known and small amount subcritical for then, since

$$\rho = \frac{k-1}{k} = -\frac{Sl_a}{n_0 - Sl_a}$$

when ρ is very small M is very large and $Sl_a \ll n_0$ so that $Sl_a \approx -\rho n_0$. Experience shows that for detectors located either in the core or reflector the effective source strength determined in this fashion remains sensibly constant for negative reactivities up to 0.02 dk/k; beyond this the flux distribution is apparently changing in a different manner to the source distribution. Although this is a useful means of determining fairly large reactivities it is to be noted that the results are essentially normalised to supercritical measurements using either the inhour equation or a solution of the inverse kinetics equations.

2.8. Nuclear Heating of Non-Fissile Material.

The heating of structural, control, and experimental materials in HIFAR is occasioned predominantly by the absorption of gamma photons. There may be significant contributions from charged particles but this depends on the specific material. Such contributions are, however, fairly easily computed because of the known production mechanisms and the short range of such particles in matter. In this section, therefore, we limit the discussion to energy absorption from the gamma radiation fields.

The gamma heating in an introduced sample is normally considered to have two components. The first is that due to the gamma field existing in the RAT if the sample is absent and the second is that due to self-absorption of photons produced in the sample by neutron reactions, mainly neutron capture. This second component can be computed separately using either measured or calculated neutron fluxes. The remainder of this section is concerned with the first component.

Since routine high power operation of HIFAR commenced, calculations of heating of materials has been based on dose measurements made during the commissioning of the reactor [29]. These were obtained with small air ionisation chambers and converted to energy absorption rates by energy absorption coefficients evaluated at some mean gamma energy.

More recently, Robinson [30] has, by means of coupled neutron/photon transport calculations of a smeared representation of the reactor, obtained neutron and photon fluxes as a function of radial position and thus obtained dose and heating rates; these differed markedly from those measured, being about a factor of two smaller.

The reasons for this discrepancy have yet to be identified fully but the following remarks can be made:

The calculated photon spectra are in qualitative agreement with those in [29] and with measurements in the Bulk Shielding Reactor [31]. These show that the spectrum peaks in the keV region so that significant self shielding in samples can occur because of the large

photo-electric cross section there, particularly for high Z materials. This would lead to overestimates of energy absorption per unit mass in finite samples when dose based results are used.

Reference to the technical manual for the Baldwin instrument used to measure dose shows that the air ionisation chambers were intended for use in monitoring X-ray doses and not for operation in mixed radiation fields. Indeed, there appears a warning not to calibrate them using a radium source unless precautions are taken to screen out β induced ionisation which would certainly be present in the HIFAR environment. The plastic walls of the chambers may also give rise to ionisation from fast neutron (n,p) reactions. These effects would lead to an overestimate of dose rate but cannot be quantified.

The ionisation chambers were not sealed and may have been sensitive to humidity (E. Hetherington - private communication.) This would lead to more rapid discharge and to overestimate of dose.

The calculations used a rather crude model and did not represent local conditions where the measurements were made. Intuitively it may also be thought that the data file would underestimate the source of gamma photons because of the complexity of this source. This makes it relatively easy for a significant component to be neglected.

The data in this area is thus not in good shape. Because the calculated energy absorption is more exact and can include self shielding of samples it is desirable to use it with a substantial increment on the calculated gamma flux to allow for the possibility that the measured dose rates are correct.

Details of the local conditions can, in principle, be represented in the calculations which use standard neutron/photon transport codes. However, these are usually restricted to two dimensions and therefore require that some geometric simplifications to reality be made.

2.9. Fission Product Decay Heat.

Under normal shutdown conditions the decay heat is removed by the shut down pumps and presents no problem. However, under some Loss of Coolant Accident conditions the decay heat needs to be evaluated and the data necessary for this are given in Appendix A-4.

2.10. Comments - Conclusions.

Much of the data given in this section has been included in an attempt to provide a common source for calculations aimed at producing estimates of reactor behaviour under certain postulated situations; that is, calculations that do not warrant a full scale investigation. Although the data through to Section 2.4 can not be considered to form an evaluated data set they have been chosen with some care and the use of the same data by staff performing such calculations confers the advantage of consistency. This is not to prohibit the use of other data if the case can be made for so doing. The temperature dependent physical properties given are mostly only usable in computer analysis of abnormal events; however they do give an insight into physical behaviour at elevated temperatures. In particular we draw attention to the properties of molten aluminium with its low kinematic viscosity and its high surface tension.

The neutronics data come from an evaluated data file and thus, like Caesar's wife, are above suspicion. Calculational techniques are, of course, a different matter and the outcomes may depend upon the complexity of a problem and the simplifications made in addressing this. However the data given here come from well tested reactor models and computational techniques so that considerable confidence can be placed in them. An important part of this data are the scaling laws given for reactivity coefficients; to our knowledge this is the first time that these have systematised and their common use will avoid much of the confusion that has occurred in the past.

As a particular point there appears to be an unacceptably large scatter in the central neutron fluxes determined by gold wire irradiations. The purpose of these measurements is to permit calculation of reactor power independent of results given by the installed ion chambers but, to be useful in this way, the precision must be improved otherwise the procedure is not worth the effort.

An important part of the section is the brief description of reactivity measurement techniques and of the data required for them. It is desirable to maintain reactivity on an absolute scale; both to make comparison with calculation meaningful and to make accident studies realistic. As a general rule, it is apparent that inverse kinetics techniques are to be preferred to asymptotic period measurements but the important emphasis is that, whatever technique is employed, care is required both in the measurement and in the interpretation of the results.

The most unsatisfactory data are those for nuclear heating of core and experimental materials. Although many reasons for the discrepant assessments by experiment and calculation suggest themselves there is no immediate way of improving matters. A significant matter raised in the current work is the large amount of self shielding of samples from the low energy spectrum of gamma radiation in the reactor.

It is possible that some of the derived formulae presented in this section could form part of a computing package which could usefully be installed on a personal computer for routine use by operations staff. Prudence and awareness that small computers will always be inoperable at the most inconvenient times suggests that such a package should complement but not replace the tabulations currently provided in printed form for use by operators.

2.11. References.

(1) Houghtaling, J.E., Sala, A. & Spano, A.H. [1964] - Transient temperature distributions in the SPERT I D-12/25 fuel plates during short-period power excursions. Report IDO-16884.

(2) Hill, P.G., MacMillan, R.D. & Lee, V. [1981] - Tables of thermodynamic properties of heavy water in S.I. units. Report AECL 7531.

(3) Boyer, H.E. & Gall, T.L. [1984] - Metals Handbook, American Society for Metals.

(4) Taylor, N.D. [1982] - Energy release from fission in the Harwell material testing reactors. DIDO Operators Meeting, Sydney.

(5) Connolly, J.W. & McKenzie C.D. [1960] - Reactor physics studies on the HIFAR twenty-five element cores. Report AAEC/TM-064

(6) Robinson, G.S. [1987] - Unpublished minute to P Vekselstein, 6 October 1987. On Ansto files LH 84/209 and RD-606. Copy in Appendix A-1

(7) HIFAR Safety Document, Section 5.9

(8) Robinson, G.S. [1987] - An analysis of HIFAR fuel consumption and reactivity for the period 1980-1987. Ansto Internal Report NTD/TN-029

(9) Robinson, G.S. [1987] - A guide to the AUS modular neutronics code system. Report AAEC/E645

(10) Clancy, B.E., Connolly, J.W. & Harrington, B.V. [1975] - An analysis of power transients observed in SPERT I reactors, Part I. Report AAEC/E345.

(11) Clancy, B.E., Connolly, J.W. & Harrington, B.V. [1976] - An analysis of power transients observed in SPERT I reactors, Part II. Report AAEC/E383.

(12) Connolly, J.W. & Harrington, B.V. [1977] - An analysis of power transients observed in the SPERT II D2O moderated close packed core. Report AAEC/E418.

(13) Clancy, B.E. [1983] - ZAPP - A computer program for the simulation of reactor power transients. Report AAEC/E568.

(14) Harrington, B.V. [1983] - Neutronic models for the HIFAR reactor. Report AAEC/E571.

(15) Robinson, G.S. [1987] - A brief description of HIFUEL - a fuel management program for HIFAR. Ansto internal report NTD/TN-26.

(16) Storr, G.J. [1989] - HIFUME - A fuel management code for HIFAR. Ansto internal report NTP/TN-132.

(17) Robinson, G.S. [1991] - 3D Diffusion calculations of HIFAR including the coarse control arms and their burnup. Report Ansto/E703.

(18) Robinson, G.S. & Harrington, B.V. [1985] - Neutronic calculations for reduced enrichment fuel in HIFAR. At p.123 of Research reactor core conversion from the use of highly enriched uranium to the use of low enriched uranium fuels, Guidebook addendum: Heavy water moderated reactors. Report IAEA-TECDOC-324

(19) Connolly, J.W., Harrington, B.V. & McCulloch, D.B. [1993] - Self limiting transients in heavy water moderated reactors. Research reactor core conversion guidebook. IAEA Vienna.

(20) Robinson, G.S. [1985] - Australian benchmark calculations. At p.215 of Research reactor core conversion from the use of highly enriched uranium to the use of low enriched uranium fuels, Guidebook addendum: Heavy water moderated reactors. Report IAEA-TECDOC-324

(21) Connolly, J.W., Robinson, G.S. & Storr, G.J. [1988] - Re-evaluation of some HIFAR physics data. Ansto Internal report NT/TN-116

(22) Kinsey, R. [1979] - ENDF/B summary documentation. Report ENDF-201

(23) Duerden, P. [1973] - HIFAR physics data. AAEC internal report O/TN/12

(24) Wilson, D.J. [1972] - Reactor Physics measurements made to commission the Mark IV element core in HIFAR. AAEC internal report O/TN/4

(25) Connolly, J.W. [1983] Minute to G.Cybula on LH file

(26) Toppel, B.J. [1959] - Sources of Error in Reactivity Determinations by Means of Asymptotic Period Measurements. Nucl. Sci. & Engng. Vol. 5, page 88

(27) Cohn, C.E. [1959] - Errors in Reactivity Measurements Due to Photoneutron Effects. Nucl. Sci. & Engng. Vol. 6, page 284

(28) Keepin, G.R. [1965] - Physics of Nuclear Kinetics. Addison-Wesley.

(29) Connolly, J.W. & Nicholson, K.P. [1961] - Energy absorption by materials exposed to radiation from HIFAR. Report AAEC/TM109

(30) Robinson, G.S. [1991] - Gamma heating in HIFAR - particularly for 6H. On Ansto file LH 84/209. Copy in Appendix A-2

(31) Maienshein & Love, T. [1954] - Nucleonics. Vol. 12, page 5

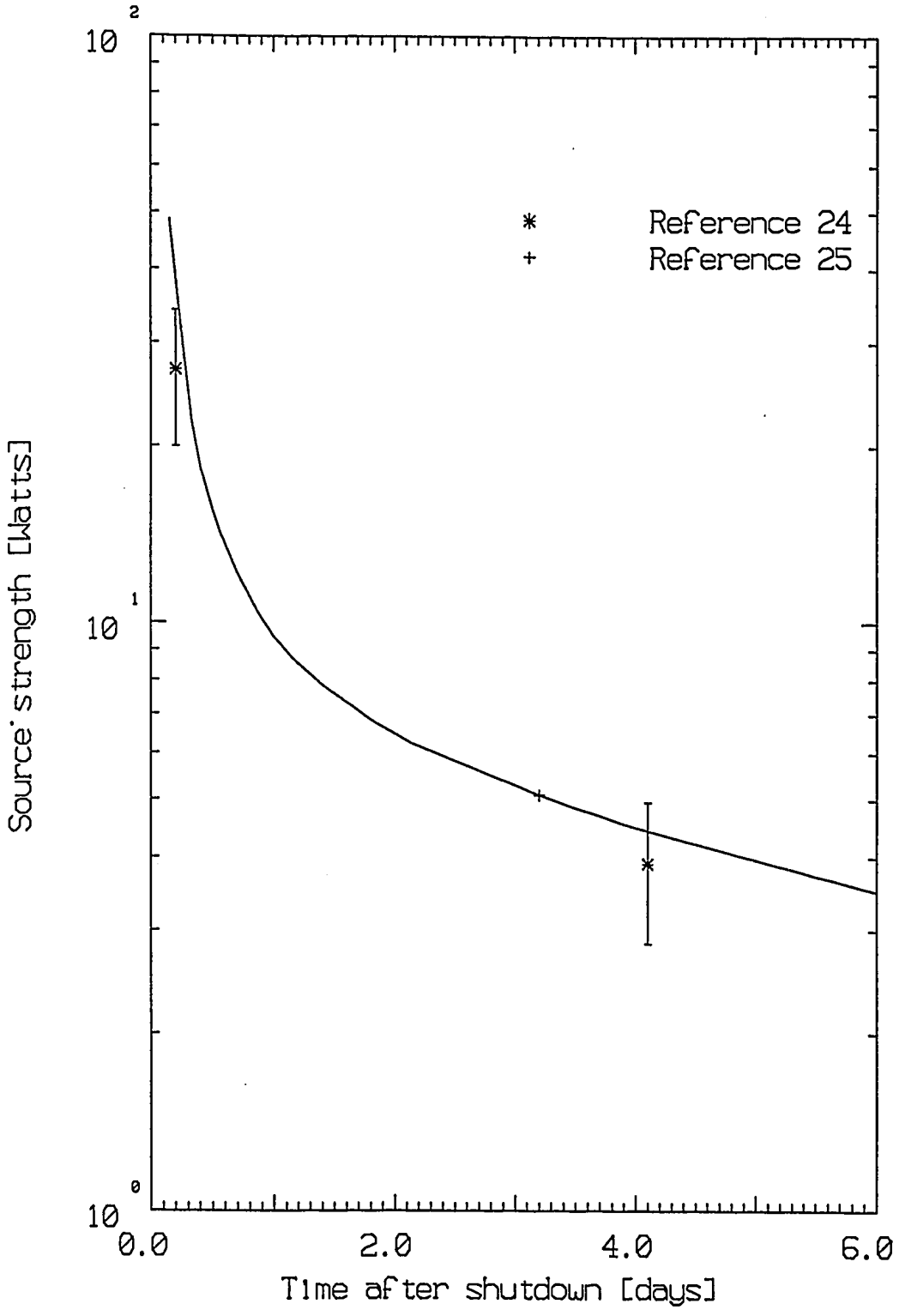

Figure 2-1 Time dependence of neutron source strength.

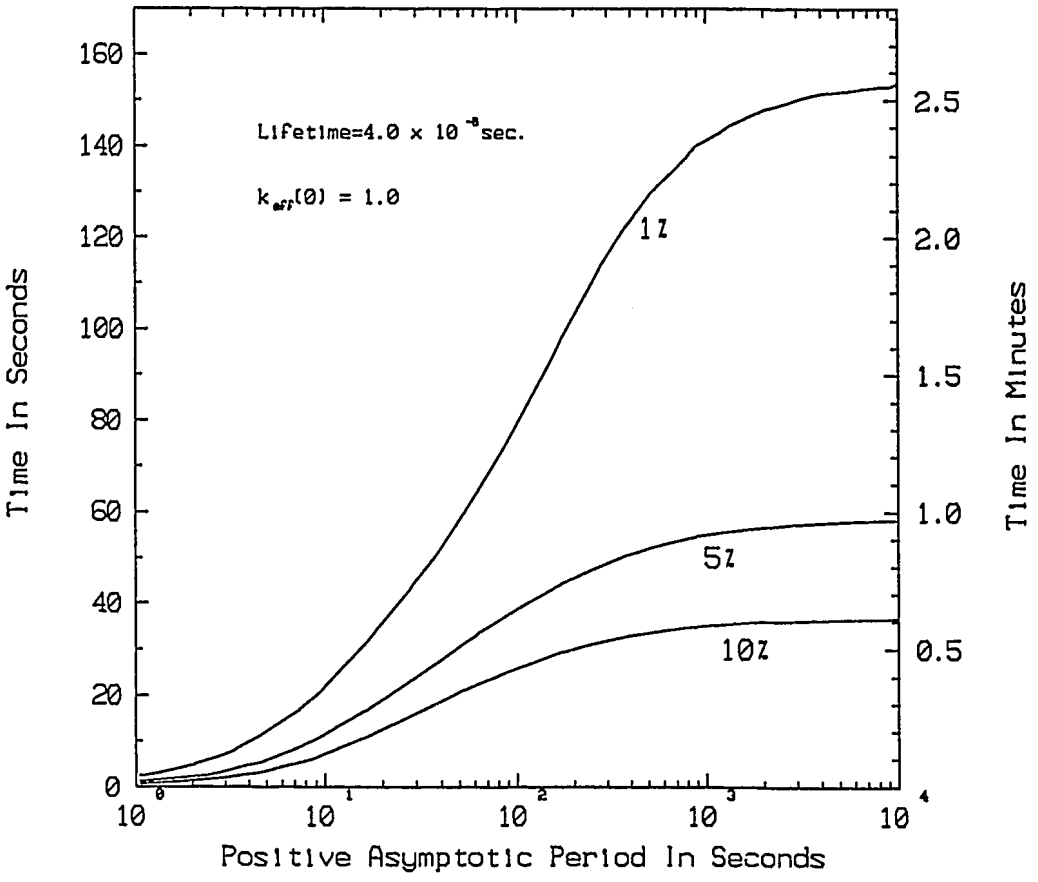

Fig 2. Time after a positive step change in reactivity to observe a period within 1, 5, and 10% of the asymptotic value as a function of positive asymptotic period.

Figure 2-2 Time after a positive step change in reactivity to observe a period within 1, 5, and 10% of the asymptotic value... (after Toppel [26])

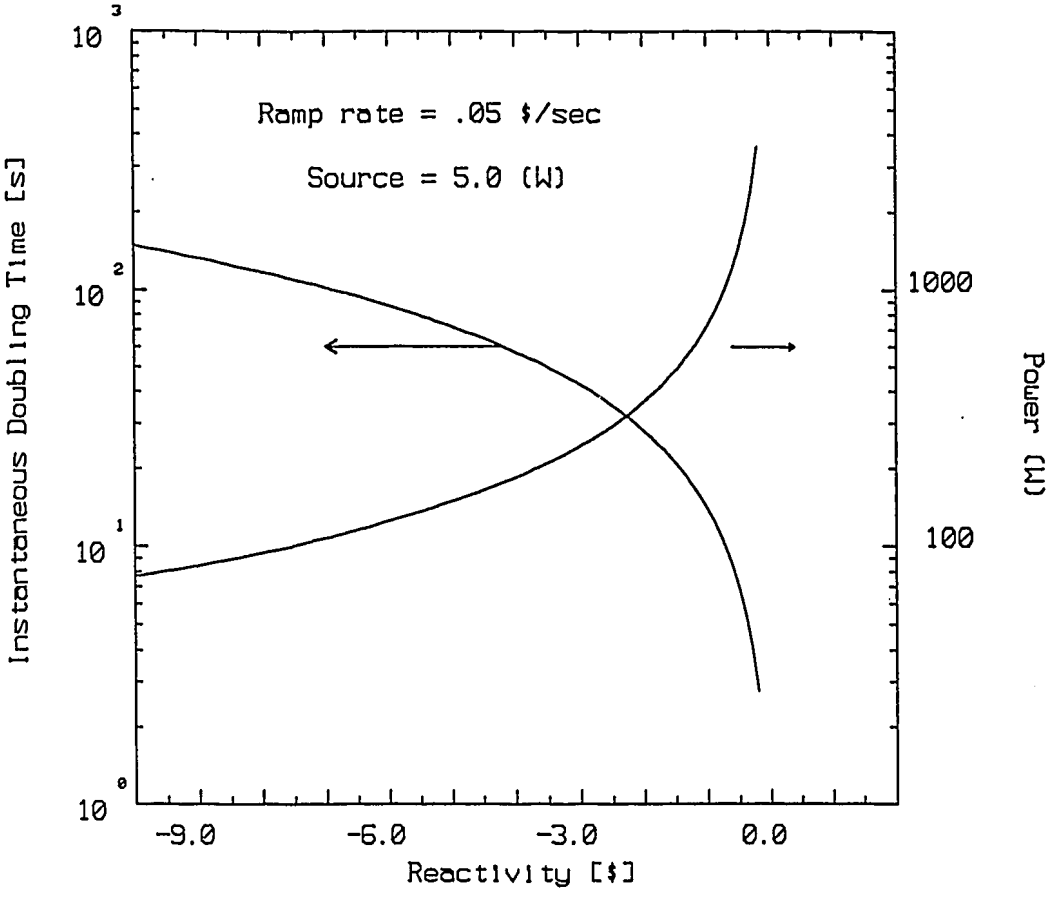

Figure 2-3 Doubling time and sub-critical power during a reactivity ramp approach to critical.

SECTION 3

REACTOR CONTROL.

And when they were up they were up,
And when they were down they were down,
And when they were only half way up
They were neither up nor down.

Anon.

3. REACTOR CONTROL.

The six neutron absorbing blades of the coarse control arm (CCA) bank serve a dual purpose. Under the control of the operator their position in the core may be altered to maintain criticality; under receipt of a signal from the guard lines they will fall into the core under gravity thus making the core subcritical.

The two safety rods are designed simply to provide a degree of independent reactivity control at shutdown. Unlike the CCAs they can not be used for a control function and must be in their fully raised position before the core can be taken critical. However they will, in the event of a complete trip, insert an additional negative reactivity which can be useful.

3.1. Coarse Control Arm Bank.

3.1.1. Functional description.

For the present purpose only those components of the CCA bank free to move after the breaking of the guard lines will be considered. Details of the drive mechanisms will be found elsewhere [1]. These components are:-

[a] the connecting rod and electromagnet armature,

[b] the datum stop lever,

[c] the plunger, datum and ring springs, and

[d] the coarse control arm blade.

A schematic drawing of the arrangement of these components, slightly modified from that given in design data [1] is shown in Figure 3-1.

3.1.1.1. Operation.

When the armature is engaged with the magnet face of the clutch the blades may be raised or lowered by the drive motors. The angular position of the blade is denoted by θ and the zero or fully in position $\theta = 0^\circ$ is at an angle of 34° to the vertical. In this section, θ is always measured in degrees unless the contrary is specifically stated. The absolute angular position is thus $(\theta + 34^\circ)$. The fully out position is when the arm is horizontal and θ is then equal to 56°.

Over the range $\theta = 0^\circ$ to $\theta = 56^\circ$ the linear displacement of the yoke bearing is 0.0711 m and the angular displacement of the connecting rod from the vertical is never more than 1.5°. The general relationships between the angular positions of the drive quadrant and blades are extremely cumbersome [1] and will not be discussed here. The design drive speeds of the arms are $2.24^\circ\ \text{min}^{-1}$ for raise or lower and $11.2^\circ\ \text{min}^{-1}$ for fast down.

Once the electromagnetic clutch is disengaged the connecting rod and blade are free to fall under gravity. The connecting rod passes through a hole in the datum stop lever until the armature contacts a bearing surface of the lever, which then rotates about a pivot. The free end of the lever depresses a plunger against the concentric datum and ring springs, the compression absorbing the kinetic energy of the connecting rod and blade. The maximum spring compression is 0.0203 m; after this the plunger strikes a mechanical stop. The datum spring is compressed by 0.0254 m when the control blade is at 0° whilst the ring springs are just free at this position. The datum spring thus ensures that the datum stop lever is returned against the mechanical reference stop.

3.1.1.2. Physical parameters of the control arm bank.

Connecting rod.

Length = 1.59 m
Mass = 3.86 kg
Smallest diameter = 0.01397 m
Material: Steel EN57

Datum stop lever.

Mass of lever = 1.17 kg
Distance of centre of mass from pivot = 0.069 m
Moment of inertia of lever about pivot = 0.0062 kg m^2
Material: Aluminium bronze DTD 164

Plunger, datum and ring springs.

Mass of plunger = 0.98 kg
Distance from bottom of plunger to mechanical stop = 0.020 m
Material: Steel EN 1A
Free length of datum spring = 0.184 m
Length with lever against mechanical reference stop = 0.158 m
Spring constant = 1.37×10^4N m^{-1} (= k_1)
Material: Steel DTD 215
Free length of ring springs = 0.114 m
Spring constant = 41.2×10^4N m^{-1} (= k_2)
Material: Steel EN 24 or S 95

Control arm blade.

Although the original design manual [1] gives 14.5 kg., the total mass of the blade as measured by HIFAR operations staff is 13 kg.
Length of arm from pivot to tip = 1.426 m (=2L)
Width of arm = 0.164 m (=2W)
Distance of centre of mass from pivot = 0.55 m (=s)
Distance between pivot and line of action of connecting rod = l cos(29°-θ) (=a)
Distance between pivot and yoke bearings = 0.0762 m (=l)
Angle between blade edge and line between yoke and pivot = 27°
Materials: Cadmium (2.0 mm thick nominal, original specification says 1.0 mm)
Steel EN58B or EN58E

3.1.2. Dynamics of falling arms.

Throughout this section all angles are measured in degrees and expressions like sin($\theta + \alpha$) should be interpreted accordingly.

Because the blade and the connecting rod are coupled by the yoke bearing it is necessary to calculate the inertial properties of the combination. We write the equation of motion of this system as

$$I'\ddot{\theta} + M'gs'\sin(\theta+\alpha) - m_w gL\sin(\theta+\alpha) - \int_0^{2L} R\, r\, dr = 0$$

where

I' = moment of inertia of rod and blade
M' = mass of rod and blade
s' = distance of combined centre of mass from pivot
$\alpha = 34^\circ$
m_w = mass of water displaced by blade
2L = length of blade
R = hydrodynamic resistance to blade motion per unit length
$= B v^2 = B r^2 \dot{\theta}^2$ where B is a constant (mass/unit area) and r is the distance of a point on the blade from the pivot bearing.

so that

$$\ddot{\theta} + \frac{M'gs'}{I'}\sin(\theta+\alpha) - \frac{m_w gL}{I'}\sin(\theta+\alpha) - \frac{4B\dot{\theta}^2L^4}{I'} = 0$$

where it is assumed that the blade is fully submerged at all times, that the connecting rod is always above the D_2O surface, and that the flow of D_2O over the blade is turbulent.

If we define the dimensionless constant

$$A = \frac{4BL^4}{I'}$$

then

$$\ddot{\theta} + \frac{gs'M'}{I'}\left[1 - \frac{m_w L}{M's'}\right]\sin(\theta+\alpha) - A\dot{\theta}^2 = 0$$

where

$$m_w = M\frac{\text{density of } D_2O}{\text{density of steel}} = 1.81 \text{ kg}$$

(Cadmium contributes only about 20% to the total arm mass.)

To utilise the equation of motion it is necessary that the constants appearing in it be evaluated. We first note that the centre of mass of the blade alone has been measured by operations staff as being 0.551 m from the pivot, essentially the same value as that given by Meister and Kalker [2] (0.554 m). For a uniform mass distribution this would be 0.718 m and the shift of the centre of mass towards the pivot is, no doubt, the consequence of the tapering of the blade stiffening sections and of the heavier construction of the bearing block. We cannot then make the assumption that the blade is a rectangle whose surface mass density is constant when calculating the moment of inertia. Instead we proceed as follows.

Assume that the blade is a thin rod whose line density σ is given by $\sigma(r) = a - br$ where a and b are determined by the constraints

$$M = \int_0^{2L} (a - br)\, dr = 13 \text{ kg}$$

$$s = \frac{\int_0^{2L} (a - br)\, r\, dr}{\int_0^{2L} (a - br)\, dr} = 0.55 \text{ m}$$

from which we determine

$$a = 15.39 \text{ kg m}^{-1}$$

$$b = 8.81 \text{ kg m}^{-2}$$

The radius of gyration about the pivot is then

$$k^2 = \frac{\int_0^{2L} (a - br)\, r^2\, dr}{\int_0^{2L} (a - br)\, dr} = 0.444 \text{ m}^2$$

and I, the moment of inertia of the blade alone, is equal to $Mk^2 = 5.77$ kg m^2.

For the blade alone making small oscillations in vacuum about its equilibrium position the angular frequency is

$$\sqrt{\frac{gsM}{I}} = 3.48 \text{ s}^{-1}$$

which can be compared with the value 3.32 s^{-1} measured on a mockup of a blade [2].

Now the moment of inertia of the blade/rod system is $I' = I + m_r s_r^2$ where it is assumed that the mass m_r of the rod is concentrated at the yoke bearing which is at a distance s_r from the pivot. Also the combined centre of mass is at a distance s' from the pivot, and

$$s' = \frac{M\hat{s} + m_r\hat{s}_r}{M + m_r}$$

The angle between the vectors $\hat{s}$ and $\hat{s}_r$ is 20.4° so that

$$s' = 0.44 \text{ m}$$

Thus, writing the equations of motion for free fall and submerged fall in the forms

$$\ddot{\theta} + \omega_0^2 \sin(\theta + \alpha) = 0 \text{ for free fall}$$

$$\ddot{\theta} + \omega^2 \sin(\theta + \alpha) - A\dot{\theta}^2 = 0 \text{ for submerged fall}$$

where

$$\omega_0^2 = \frac{M's'g}{I'} = 12.56 \text{ s}^{-2}$$

$$\omega^2 = \omega_0^2 [\, 1 - \frac{m_W L}{M's'}] = 10.38 \text{ s}^{-2}$$

an analytic solution for $\dot{\theta}^2$ can be deduced. If θ_0 denotes the initial angle of the blade, then for free fall we have

$$\dot{\theta}^2 = 2\,\omega_0^2\Big[\cos(\theta+\alpha)-\cos(\theta_0+\alpha)\Big]$$

while for submerged fall we have, writing $\gamma = \tan^{-1}(1/2A)$,

$$\dot{\theta}^2 = \frac{2\omega^2}{\sqrt{1+4A^2}}\Big\{\sin(\theta+\alpha+\gamma) - e^{2A(\theta-\theta_0)}\sin(\theta_0+\alpha+\gamma)\Big\}$$

In the submerged fall case, if $\theta \ll \theta_0$ and $A \gg 1$, then the exponential term is close to zero; also when A is large, the angular velocity at any angle θ varies approximately as $A^{-\frac{1}{2}}$ so that the dynamics are not heavily dependent upon the value of A for strongly resisted motion.

It is instructive, now, to discuss the physical basis for the constant A which characterises the resistance to arm motion during submerged fall.

Let ΔV be the volume of water set in motion in a time element Δt by an arm element Δr at r as the element moves through an angle $\Delta\theta$ and let Δm_w be the mass of this water. Then

$$\Delta V = \tau\, r\, \Delta r\, \Delta\theta$$

where τ is the thickness of the leading edge of the blade.

$$\frac{\Delta V}{\Delta t} = \tau\, r\, \dot{\theta}\, \Delta r$$

$$\frac{\Delta m_w}{\Delta t} = \rho_w\, \tau\, r\, \dot{\theta}\, \Delta r$$

$$\frac{\Delta(m_w v)}{\Delta t} = F(r) = \rho_w \tau\, r^2\, \dot{\theta}^2\, \Delta r$$

and this last is the rate at which momentum is transferred to the water. Also the moment about the pivot is

$$\Delta L^*(r) = \rho_w\, \tau\, r^3\, \dot{\theta}^2\, \Delta r$$

so that

$$L^* = \rho_w\, \tau\, \dot{\theta}^2 \int_0^{2L} r^3\, dr = 4\rho_w \tau\, L^4\, \dot{\theta}^2$$

Dividing by the moment of inertia I of the rod and blade assembly we write

$$\frac{4\rho_w \tau\, L^4}{I} = A$$

and putting in the numerical values

$\rho_w = 1.1 \times 10^3$ kg m^{-3}

$2L = 1.43$ m

$I' = 5.79$ kg m^2

$\tau = 0.024$ m = average thickness of blade leading edge,

gives A = 4.7; we see later that this value is in reasonable agreement with the value obtained from fitting to observed drop times. We thus conclude that the predominant braking effect in submerged fall of the blades comes from momentum transfer to the water and that viscous effects and other energy losses are small. The corresponding value of the constant B is 26.4 kg m^{-2}

3.1.2.1. Numerical solutions.

From a well established equation of motion for the falling arms it is a simple matter, for any starting angle θ_0, to obtain accurate numerical solutions which determine the variation of the arm angle as a function of time after release of the armature. However, it is convenient to establish a computationally simple formula which allows this variation to be calculated without further solution of the equation of motion. This we have done using the parameter values $\omega^2 = 10.38$ and A = 5.5 which, as we show later, are believed to model the CCA motion most accurately.

An analysis of the equation shows that for small angles θ or for small times t, the angle θ depends quadratically on t so that

$$\theta = \text{Coeff}_1\, t^2 + \text{Coeff}_2\, t + \text{Coeff}_3$$

but the coefficients have values different for small θ to those which they have for small t; for small t, Coeff_1 is actually zero. This makes it sensible to use, for all times, the general expression

$$\theta = \theta_0 \frac{1 + C_1\, t + C_2\, t^2}{1 + C_1\, t + C_3\, t^2}$$

where the coefficients C_i depend upon θ_0, and are well represented by the following forms:

$$C_1 = C_{11} + C_{12}\theta_0 + C_{13}\theta_0^2 + C_{14}\theta_0^3$$

$$C_2 = \frac{C_{21}}{(C_{22} + \theta_0)} + C_{23}$$

$$C_3 = C_{31} + C_{32}\theta_0 + C_{33}\theta_0^2$$

Finally, if the coefficients C_{ij} are given the constant values

$C_{11} =$	$1.24494\ 10^{-2}$	$C_{21} =$	$-1.48211\ 10^{+2}$	$C_{31} =$	$+4.40083\ 10^{+0}$
$C_{12} =$	$+9.55863\ 10^{-2}$	$C_{22} =$	$-2.70694\ 10^{-1}$	$C_{32} =$	$-5.68877\ 10^{-2}$
$C_{13} =$	$-9.76127\ 10^{-4}$	$C_{23} =$	$-2.68473\ 10^{+0}$	$C_{33} =$	$+1.62537\ 10^{-4}$
$C_{14} =$	$+6.28018\ 10^{-6}$				

then the resulting θ values will agree with the 'exact' values found from the differential equation to within some five minutes of arc.

3.1.2.2. Validation of the equation of motion by comparison with measured data.

Before this can be attempted it is necessary to consider the time delay between the breaking of the magnet coil voltage and the armature commencing to fall.

Provision is made within the CCA head unit to measure the time interval between the interruption of the magnet voltage and the operation of a microswitch sensing an armature/magnet separation between 0.381 and 0.508 mm. This time interval includes that for the decay of the magnetic field to a point where the armature is released, and the time taken for the magnet/armature separation to increase from zero to between the latter values. Clearly this last time interval forms part of the domain of the solution of the equation of motion and is not part of the delay in the arms beginning to move.

The linear limits to microswitch actuation correspond to angular CCA displacements of between 0.3° and 0.4°. Over this small range we can neglect the braking term in the equation to write

$$\ddot{\theta} = -\omega^2 \sin(\theta_0 + \alpha)$$

and for small times δt the changes $\delta\theta$ are given by

$$\delta\theta = -\tfrac{1}{2}\ddot{\theta}\,(\delta t)^2$$

where $\delta\theta$ lies between 0.3° and 0.4°. For the latter value these equations predict actuation times ranging from 48 ms to 35 ms for initial angles in the range from 4° to 56°. Unfortunately, at the higher angles these values, being greater than times observed, imply negative real delays in the system. It may be concluded that either the equation of motion is incorrect or a mechanism exists whereby the magnet separation time is greatly reduced. Since we find it difficult to believe such serious errors exist in the equation of motion we consider a representation of the mechanical arrangement as shown in the following sketch.

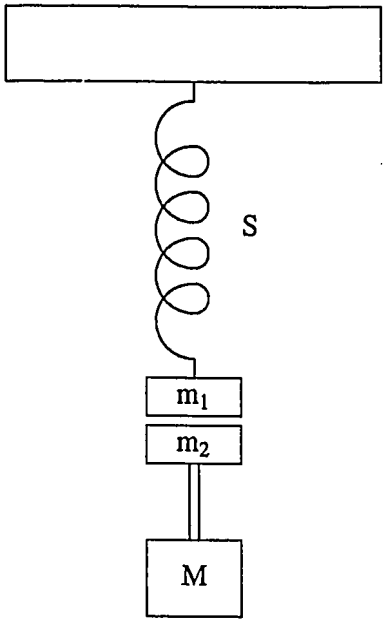

Here S is a spring representing the elasticity of the arm drive mechanism which has an equivalent spring constant k. We denote by m_1 and m_2 masses associated with the magnet and armature respectively, and by M a mass whose weight produces a downward force in the connecting rod equal to that produced by an arm. M is then $\approx$ 100kg. When the armature is coupled to the magnet face the spring extension is

$$z = (M + m_1 + m_2)\frac{g}{k}$$

If the magnetic field is instantaneously reduced to zero the initial upward acceleration of m_1 is

$$\ddot{z} = \frac{(M + m_1 + m_2)g}{m_1} - g = \frac{M + m_2}{m_1}\,g$$

while for M and m_2, the initial (and constant) downward acceleration is $\ddot{z} = g$.

Since $M + m_2$ is much greater than m_1 the initial acceleration upwards of the magnet will be much greater than the downward acceleration of the armature.

This effect has been observed [3] by comparison of the signal from a linear potentiometer sensing the spatial relationship between the end of the connecting rod and the connecting rod drive, and the signal from a potentiometer measuring CCA angle directly. It was found that the former signal led the latter by about 0.4°, which is close to the movement required for microswitch

actuation. The linear potentiometer arrangement could not distinguish between downward armature movement and upward magnet movement, but the evidence seems persuasive that the microswitch is activated by a very rapid movement of the lighter magnet while the heavier armature and arm components are still almost at rest; that is, the delay microswitch gives a true zero time from which to determine the drop time of a CCA and the indicated delay is the true delay in the magnetic forces decaying to a value equal to that of the downward force on the connecting rod.

The delay time data recorded in routine testing have been used in the past to calculate a mean delay time and its associated standard deviation under the assumptions that the raw data are observed values taken by a single normal variate and that all the errors are random. Historically the data have always shown a large scatter and the practice of augmenting the mean by three calculated standard deviations for a single arm has produced very large assessed delay times and consequent shrinking of calculated margins to trip.

We have re-examined the data and reached the conclusion that the observed scatter does not arise from random values taken by a single variate but rather from values selected from populations which differ because the electromagnet clutches have individual characteristics. If we take the magnet force to be equal to the force acting on the connecting rod at the time of magnet/armature separation and plot the force against the measured delay time for each CCA head unit, the curves of Figure 3-2 are obtained. It is clear that each head unit has its own characteristic signature. For the sake of clarity we have omitted units F and H, which closely resemble unit C, and have omitted unit A which resembles unit D. Unfortunately the disposition of head units is not always recorded but we have checked data back to 1989 and found these signatures to be essentially constant. The remaining units B and J, the former having been used in the measurements with a linear transducer discussed above have both been damaged, the latter beyond repair.

We have investigated the random error component of these data by performing four drop tests from angles reached with a CCA driving up and two reached by driving down; the scatter is found to be small, a few milliseconds at most. Treating the data as normally distributed is thus clearly wrong and adding three of the spurious standard deviations to the mean value simply compounds the error. The question remains: "How do we produce an appropriate single value of the delay time for calculations of margin to trip?" The only exact treatment is to perform calculations allowing each arm to have the delay characteristic of the head unit to which it is coupled but this, while possible, is not very practical. It would seem to us that a sensible approximation is to use the mean of units ECDG. This produces the results tabulated below.

Initial Angle (degrees)	ECDG ms
4	89
12	63
20	47
28	37
36	31

As noted, the random error associated with the this set of data items is small. A mean value could be found for the particular combination of head units in service at one time and this used in a series of assessments but it is still wrong to add three spurious standard deviations to any mean value selected.

We now turn to the question of the drop times for the arms. This is measured from the opening of the off-magnet microswitch to the operation of a microswitch set to actuate at a nominal CCA angle of 1.5°. The measured drop time will be influenced by the actual setting of this microswitch, particularly for drops from small initial angles. We have investigated this setting by

recording drop times from an angle of $1.6°$. For such a small range of travel the simple equation of arm motion previously discussed is valid so that the setting of the down microswitch θ_1 and the recorded drop time τ are connected by the expression $\theta_1 = \theta_0 - \frac{1}{2}\omega^2 \sin(\theta_0 + \alpha)\tau^2$

For the six CCAs we obtained a mean value of $1.45°$ and since these data can be considered to be normally distributed we quote the standard deviation as $0.13°$ and the error on the mean as $0.05°$. This is acceptable agreement with maintenance requirements that the setting should lie between $1.46°$ and $1.54°$.

The major influence on the drop times for operational angles is the value of the constant A in the equation of motion. We have shown that a simple theoretical evaluation of this constant gives 4.7, and this produces reasonable agreement with observations for drop times from angles less than about $28°$. However there will undoubtedly be other loss terms not considered in this evaluation and an 'experimental value' for A can be found by forcing agreement between observed and calculated drop times from a particular angle. This procedure has been followed [4] by considering the mean drop time of twenty three tests from an angle of $20°$ (378 ± 10 ms) and a value of 4.0 obtained. However this work erroneously assumed that the down limit microswitch was set at $0°$; re-evaluation with the correct setting of $1.5°$ yields $A = 4.91 \pm 0.6$. This is in good agreement with the value of 5.0 found [3] to give a good fit to measurements of the angular position versus time characteristics of a single arm.

Although the head units cannot influence the drop times it might be expected that some consistent effect could arise from the coolant flow pattern in the RAT producing hydrodynamic forces on the arms. Within the error bounds for a single arm there appears to be no difference in drop times recorded in the hot cell pond or in the reactor with main pumps running, except for a second order effect for drops from high angles [3]; since these are outside the range of normal operation they will not be discussed further. Table 3-1 shows three sets of drop times from various start angles; the first set obtained during the 1991 major shutdown with the core unloaded and without any pumps running, the second set the times computed from the equation of motion, and the third (rightmost) set are single arm data with two main pumps running [3].

Table 3-1
CCA Drop Times.

Initial	Drop Times (ms)		
Angle (degrees)	1991	calc.	Single arm
4	132 ± 4	126	135
12	267 ± 5	270	274
20	365 ± 5	378	392
28	449 ± 5	478	485
36	523 ± 7	576	587
56	659 ± 7	820	-

We note that for high angles the equation of motion becomes invalid as the arms cease to be submerged while at $56°$ the initial motion is through the helium atmosphere above the D_2O.

3.1.3. Stress on pivot bearing and connecting rod.

3.1.3.1. Static loading.

For blade angles at which no part of the blade is in the D_2O we have, using the nomenclature of Figure 3-1 and Section 3.1.1.2,

$$Q \sin(\theta + 34^c) + Mg - P = 0$$

$$P\,a - L\sin(\theta + 34^\circ)\,M\,g + W\cos(\theta + 34^\circ)\,M\,g = 0$$

so that with the blade in the horizontal position

$$P = 1340N$$

$$Q = 1213N$$

At the smallest connecting rod diameter the stress is then 10^7 Pa and the maximum tensile stress there [1] is 1.5×10^8 Pa. For static loading of the bearings a non-Brinell capacity of about 7000 N is given [1].

3.1.3.2. Dynamic loading.

Since the kinetic energy of a falling arm is given by

$$E_k = \tfrac{1}{2}\, I'\, \dot{\theta}^2$$

then, for free fall,

$$E_k = I'\,\omega_0{}^2\Big[\cos(\theta + \alpha) - \cos(\theta_0 + \alpha)\Big]$$

and, for submerged fall,

$$E_k = \frac{I'\omega^2}{\sqrt{1 + 4A^2}}\left\{\sin(\theta + \alpha + \gamma) - e^{2A(\theta - \theta_0)}\sin(\theta_0 + \alpha + \gamma)\right\}$$

From the numerical data already given we obtain, for the arms falling from $\theta = 56^\circ$ to $\theta = 0^\circ$,

$E_k = 3.8$ J for submerged fall, and
$E_k = 60.$ J for free fall.

Now let z denote the compression (change in length) of the springs when the arms are brought to rest. Then the energy deposited in the springs by the motion of the datum stop lever is

$$E_s = \tfrac{1}{2}k_2z^2 + \tfrac{1}{2}k_1(z + 0.025)^2 - \tfrac{1}{2}k_1(0.025)^2 = E_k$$

giving

$$z = 0.016 \text{ m} \quad \text{for free fall}$$

$$z = 0.0037 \text{ m for submerged fall.}$$

If we determine the lengths a,c, and d in Figure 3-1 when the arms are at the full-in position and consider small displacements of the angle of the datum stop lever and of the angle of the arms, then it can be shown that

$$z = \frac{ad}{c}\,\theta \quad (\theta \text{ here measured in radians}).$$

and appropriate values for θ are obtained for free or for submerged fall. The arms overshoot the fully in position by 6.1° in the case of free fall, and use up nearly all the free spring movement before the mechanical stop is encountered. This is good agreement with measured [1] data. In the case of submerged fall, the overshoot is only 1.3° .

Considering the forces acting on the system when the arms are brought to rest, the force P acting on the yoke bearing can be evaluated from the equations

$$S\,d = P\,c$$

$$zk_2 + (z + 0.025)k_1 = P\,c$$

where c and d are shown in Figure 3-1, to give the values

P = 3970 N (submerged fall)

P = 15860 N (free fall).

The measured values [5] range from 3560 to 5800 N for submerged fall and from 18200 to 19000 N for free fall; the agreement between calculation and measurement is reasonable.

The design requirement on the bearings [1] is that the ratio of $7100/Q_{max}$ should lie between 0.2 and 1.0, and this is just achieved under the assumption of Q acting normally to the blade length. (It is not understood why a maximum value of 1.0 is placed on this ratio.) However it must be noted that free fall through air is not an operational requirement for the arm bank and the manufacturers have submitted the mechanism to over two hundred air fall tests [1] without indication of damage to the bearings.

These drop tests in air showed that the arms bounced very heavily, recoiling to an angle of 36° on the first bounce after release from an angle of 56° ; subsequent oscillations indicate that the ring springs are absorbing in excess of 50 per cent of the kinetic energy as heat. This means that in the case of submerged fall the amplitude of the first bounce will be of the order of 4° peak to peak, and this has been observed experimentally. (See Figure 9 in reference [3].)

3.1.4. Reactivity controlled by the coarse control arm bank.

In the fully in position the tips of the blades are near the centre of the core and at an angle of 20° they are just leaving the core. Above this angle the arms control reactivity by poisoning the top reflector. To some extent the reactivity control is dependent on the disposition of fuel and experimental rigs which makes it important to ensure that the reactivity calibration is appropriate to the manner in which the reactor is used.

3.1.4.1. Reactivity calibration of the CCA bank.

The reactivity controlled by the complete bank is too large to permit a supercritical evaluation of the total reactivity. Instead, differential worths $\frac{d\rho}{d\theta}$ are determined either by period measurements when the arms are at some angle $d\theta$ above critical or by inverse kinetics techniques [6], [7] which do more than a simple determination of period. Both these methods require data for the yields and half lives of the delayed and photoneutron groups [8]. An additional technique is to employ sub-critical multiplication methods for integral measurements of fairly large reactivities, but these are essentially normalised to the results of critical experiments. Another parameter required is the magnitude of the prompt neutron lifetime. These matters are discussed further in section 2.7.5.

The current differential calibration for a core loading of 2.75 kg ^{235}U is shown in Figure 3-3 (from reference [7]) and that for integral reactivity controlled in Figure 3-4 (from reference [9]). The data for integral reactivity controlled as a function of CCA angle were obtained by a combination of sub critical and period measurements. A good least squares fit to this data is obtained with a shifted Gaussian expression and the derivative of this Gaussian with respect to θ produces values of the differential reactivity control. The differentiated Gaussian is

$$\frac{d\rho}{d\theta} = a\,(\theta + b)\,e^{-\frac{(\theta+b)^2}{c}}$$

with a = 0.00125, b = 7.609, c = 411.4, and $\frac{d\rho}{d\theta}$ is the rate of change of absolute reactivity with respect to change in θ (degrees). The integral curve is in good agreement with the calculations of Robinson [9] as shown on the same figure.

Although normal operation does not require information on the reactivity control of the bank outside the permitted operational range, safety studies do require this, and Figure 3-4 data ought to be extended down to 0° by analysis of the signal resulting when the bank has dropped from an angle of 11° to fully in. This has been done once but until further measurements are available it is preferable to use the calculated reactivity from 11° to 0° .

3.1.4.2. Reactivity dependence upon core mass.

A recent discussion of this dependence is given by Godfrey [10] from which the following is extracted.

The reactivity worth of the CCAs is known to vary with the mass of ^{235}U in the core. First order perturbation theory predicts that reactivity should vary inversely with core fissile mass, but experience shows that modification of the strict inverse relationship by a mass exponent provides more accurate predictions. The mass exponent of reactivity for HIFAR has been determined to be -0.75 by Harries [6]. This figure is in good agreement with the 1982 calculations of G S Robinson (unpublished) which showed that the exponent varies between -0.800 and -0.508 depending on the CCA angle. The reactivity worth in a core of mass m_1 is therefore calculated from the reactivity worth in a core of mass m_2 using the expression

$$\rho_1 = \rho_2 \left[\frac{m_2}{m_1} \right]^{0.75}$$

Whilst is is essential to use the most accurate value of the mass exponent for absolute calculations in safety assessment, routine HIFAR operation requires only a relative reactivity value to be known, normalised to a standard core mass. This provides operational ease without introduction of any significant error and is in keeping with reactivity predictions provided by HIFUEL (the reactivity accounting program used for HIFAR). Use of the mass exponent of reactivity has no safety implications in routine reactivity accounting, provided that a typical figure is used for the core mass to which reactivity is normalised.

3.1.4.3. Reactivity dependence upon heavy water purity.

The current CCA calibration discussed in the preceding pages was established before the 1991 upgrading of the D_2O prior to which the H_2O content was 1.4 mole per cent; it is now 0.3 mole per cent.

Robinson [12] has calculated, in a consistent fashion, the total reactivity controlled by the CCAs at various angles for D_2O purities appropriate to the states before and after the upgrade. The calculated difference at low angles is small but is substantially larger at high angles. If the current calibration is modified according to Robinson's calculations the difference made to the sensitivity $\frac{d\rho\%}{d\theta}$ is probably not large enough to have much operational significance, except near shutdown at the end of the period. Some typical values are

θ (deg)	$\frac{d\rho\%}{d\theta}$	
	D_2O fraction=0.986	D_2O fraction=0.997
10	1.037	1.014
16	0.762	0.762
22	0.440	0.463
28	0.204	0.233

3.1.5. Shutdown rates following scram of the CCA bank.

Numerical solution of the CCA dynamics equation provides values for the angular velocity and position of the control arms as a function of time after the bank begins to fall. In conjunction with the reactivity calibration as a function of position these solutions can be used to calculate shutdown ramp rates produced by the CCAs following scrams from various operating angles.

From the results of these calculations using the parameter values discussed in Section 3.1.2.1 Table 3-2 has been prepared. For a range of starting angles θ_0, two sets of values are provided. The first (left hand) set of values are calculated at the time when reactivity ρ = -0.014 (about \$2) has been inserted, with the second (right hand) set calculated at the time when the arms have reached the fully in position. Each set gives a time after the arms begin to fall, the angle θ of the CCAs at that time, the absolute reactivity ρ which the CCA bank will then have inserted, and the largest ramp rate $d\rho/dt$ which the CCA bank will have been inserting during this time.

Table 3-2
CCA Reactivity Insertion Rates.

θ_0 deg	time sec	θ deg	ρ inserted (absolute)	ramp at θ (absolute)	time sec	θ deg	ρ inserted (absolute)	max ramp (absolute)
40.0	0.269	26.58	-0.014	-0.180	0.654	0.0	-0.222	-0.727
36.0	0.223	25.98	-0.014	-0.186	0.604	0.0	-0.221	-0.725
32.0	0.182	24.91	-0.014	-0.198	0.554	0.0	-0.218	-0.723
28.0	0.148	23.17	-0.014	-0.220	0.503	0.0	-0.212	-0.718
24.0	0.122	20.72	-0.014	-0.248	0.452	0.0	-0.201	-0.709
20.0	0.103	17.69	-0.014	-0.283	0.400	0.0	-0.183	-0.690
16.0	0.091	14.28	-0.014	-0.312	0.347	0.0	-0.157	-0.655
12.0	0.084	10.60	-0.014	-0.330	0.291	0.0	-0.122	-0.593
8.0	0.083	6.74	-0.014	-0.327	0.231	0.0	-0.081	-0.497
4.0	0.089	2.63	-0.014	-0.293	0.159	0.0	-0.038	-0.366

3.1.6. Cadmium burn-up and blade lifetime.

The CCA bank controls the power level by capturing excess neutrons which would otherwise cause further fissions. As a consequence of the neutron capture the high cross section ^{113}Cd in the arms is converted to low cross section ^{114}Cd, mainly in the tips of the arms; as time goes on the neutron absorbing ability of the arms decreases - the blades burn up - and the blades must be replaced. The replacement of a burnt arm is done because its absolute shutdown capacity is less than that of a new arm. This results in a reduction of shutdown margin and affects the reactivity calibration of the CCAs. Since HIFAR reactivity accounting is ultimately measured by the angle of the CCA bank the arms are always replaced well before their shutdown capacity would be affected to any significant extent. An historical account of the way in which the current limits on blade lifetime originated has been given by Carlson [11]. These limits (adopted in 1967) are

CCA Position Number	Maximum Irradiation (MWh)
2 and 5	150000
3 and 6	180000
1 and 4	200000

Recently Robinson [9] has made detailed calculations of the absorption capacity of new and burnt CCA blades. His results agree with the reactivity calibration of Storr [7] and confirm that the historical lifetime limits are conservative ones.

At the time of writing CCA blades containing cadmium with europium tips in place of the arms with cadmium alone are being introduced into HIFAR. The reason is, that as it burns up, the europium - in the form of ^{151}Eu with its high cross section - is replaced by other europium and gadolinium isotopes which still have relatively high absorption cross sections. The reactivity worth of the arm is thus retained for a considerably longer time and the arms will not need such frequent replacement. In the work just cited, Robinson has examined the behaviour of the europium tipped arms and provided quantitative estimates of their worths both when new and after irradiation.

3.1.7. Heating of the coarse control arm blade.

The principal energy inputs to a blade come from the absorption of gamma energy from the radiation field in the core, and from the (n,γ) capture of neutrons by the cadmium.

For the former, it was early estimated [13] that for materials such as steel and cadmium, and for a reactor power of 10 MW, the in-core energy absorption from gammas is of the order of 1 kW/kg giving a power input of 13 kW to a complete blade. However, as noted in Section 2.8, this is possibly a high value because of the discrepancy between calculated and measured dose rates in the core. It is certainly a high value because of the neglect of self shielding of low energy photons in such large bodies as the CCA when calculating absorbed energy from dose rates. Until this uncertainty is resolved we retain the early energy input estimate on the basis of the usual excuse that it is probably a conservative value. Fortunately this value is well removed from those that might occasion concern in the situations being considered here. For the whole blade, because the effective absorption cross section is $0.08 m^2$ and the neutron binding energy is about 8 MeV, then for an average flux over the blade of $5\ 10^{13}$ n $cm^{-2}s^{-1}$ the energy input for a blade is 52 kW. However, because only a small fraction of this energy will remain in the blades, probably less than 1 per cent, this is unlikely to be of any significance. The heat transfer area of the blade is about $0.4\ m^2$ so that the heat flux from the blade to the heavy water is about $3\ 10^4 W\ m^{-2}$. The thermal resistance between the cadmium core of the blade and the stainless steel sheathing is not known but there is no evidence from many years of operation with arms of this type that thermal stressing or cadmium melting occurs.

3.1.8. Parameters affecting the CCA bank performance.

The ability of the CCA bank to terminate a power excursion is determined by several parameters. Although it is possible to determine the power history of a given excursion in some detail by use of the ZAPP code [14] such a procedure makes it difficult to observe the influence of these parameters on the outcome. We therefore consider a simple model in which delayed neutrons are neglected, that is, we consider a ramp reactivity insertion equation so that

$$\frac{1}{P}\frac{dP}{dt} = at$$

where P is the reactor power, feedback is neglected, and

$$a\ (s^{-2}) = \frac{1}{l_a\ k}\frac{dk}{dt}$$

This has the solution

$$\ln\frac{P}{P_0} = \tfrac{1}{2}at^2$$

and P_0 is the initial reactor power. If we use subscript 1 to denote the magnitude of variables when the trip power P_1 is reached and write $X^2 = \ln(\frac{P_1}{P_0})$ then

$$t_1 = X\,[2/a]^{\frac{1}{2}}$$

$$\alpha_1 = at_1 = X\,[2a]^{\frac{1}{2}}$$

$$E_1 = P_0 \int_0^{t_1} \exp(\tfrac{1}{2}\,at^2)\,dt$$

Now let τ denote the time delay between passing the trip power and the arms commencing to move, and let subscript 2 denote the magnitude of variables when the arms start to move; we have

$$t_2 = t_1 + \tau$$

$$\alpha_2 = a(t_1 + \tau)$$

$$E_{12} = E_2 - E_1 = P_0 \int_{t_1}^{t_2} \exp(\tfrac{1}{2}\,at^2)\,dt$$

If b denotes the initial shutdown ramp produced by the falling CCA bank then

$$\frac{1}{P}\frac{dP}{dt} = \alpha_2 - (b-a)(t-t_2) \quad (\text{for } t > t_2)$$

and $P = P_{max}$ when $t = t_3$ where

$$t_3 = \frac{\alpha_2}{b-a} + t_2$$

From the solution of the last differential equation we obtain, after some manipulation,

$$E_{23} = E_3 - E_2 = P_0 \int_{t_2}^{t_3} \exp[\,bt_2\,t - \tfrac{1}{2}\,(b-a)t^2 - \tfrac{1}{2}\,bt_2^2\,]\,dt$$

$$\ln\frac{P_{max}}{P_0} = \frac{b}{b-a}\left[X + \tau\sqrt{(a/2)}\right]^2$$

and the total energy release to the time of peak power is

$$E_{tot} = E_1 + E_{12} + E_{23}$$

We see that the parameters governing the power history are:-

the ramp rate a,
the shutdown ramp rate b,
the ratio of trip setting to initial power $\exp(X^2)$, and
the delay from the time when the trip setting is reached to the time the arms begin to fall.

Assessment of the degree of protection afforded by the arms can be based on the energy release in the transient or on a requirement that the peak power does not exceed the flow instability power. The latter is the criterion presently adopted for HIFAR; we briefly examine the implications.

For a given value of $\frac{P_{max}}{P_0}$ we have, according to the expression derived above for its logarithm,

$$X = \left[\frac{b-a}{b}\ln\frac{P_{max}}{P_0}\right]^{\frac{1}{2}} - \tau\left[\frac{a}{2}\right]^{\frac{1}{2}}$$

$$\frac{dX}{d\tau} = -\left[\frac{a}{2}\right]^{\frac{1}{2}}$$

When $X = 0$, $P_1 = P_0$ and the longest delay permitted under these circumstances is

$$\tau^* = \left[\frac{2(b-a)}{ab} \ln \frac{P_{max}}{P_0}\right]^{\frac{1}{2}}$$

We can form some estimate of the value of b from the data of Table 3-2 by using the time required for the falling bank to remove 0.014 δk/k. At an initial angle of 28° this table implies $b = 152 s^{-2}$ and at 12° $b = 268 s^{-2}$; an effective neutron lifetime of 600μs being assumed. The largest observed delay times for these two angles are 37 and 63 ms respectively; we note that there is a degree of compensation in these data since high angles reduce the initial shutdown ramp but decrease the delay time. For purposes of illustration we take the 28° data and assume the flow instability power to be 40 MW ($= P_{max}$). Ramp rates of concern are probably in the range from 0.01 to 0.05 δk/k per second so that the value of a is in the range from 17 to 83 s^{-2}. We adopt the latter (more severe) value and calculate the value of τ^* for a range of initial powers, obtaining

P_0(MW)	=	1	2	5	10
τ^* (ms)	=	201	181	151	123

These delay times are the maximum permitted for the assumed values of a and b if the flow instability power is not to be exceeded and the power trip point is maintained very close to the operating power; they are much greater than any observed delay times.

In practice, the margins to trip during a start up or at low power are not always small. We have therefore calculated values of X and P_1 for a range of initial powers, and for the three ramp rates with the same values of b and τ as used in the preceding calculation; the results are shown in Figure 3-5. When we recall that these results have no allowance for the reactivity feedback effects which will be significant, it is clear that only very fast ramps will defeat a power trip level set at 11 MW unless the initial power level is very small.

It is of interest to compare these calculations with the analogue computer studies in the HSD. Figure 11.1-5 in that document indicates that for an initial power of 15 MW a power trip set at 17.6 MW will just limit P_{max} to 40 MW for a ramp input of 0.011 δk/k per second, whereas the present calculations indicate that a power trip setting of 30 MW will limit the transient to 40 MW. However the HSD assumed a delay time of 240 ms, some six times that considered here; if we insert this value into our calculations the required trip setting falls to 15.5 MW. This value is in reasonable agreement with that quoted in the HSD particularly as the numerical value of the shutdown ramp used in the HSD calculations is not known, but only the initial angle of 30° .

Determination of the energy release in a transient terminated by the CCA bank requires numerical integration of the expressions given for E_1, E_{12}, and E_{23} so that it is not possible to generalise. Instead we calculate a rather severe transient characterised by $a = 83 s^{-2}$, $b = 152 s^{-2}$, $P_0 = 8$ MW, $P_1 = 11$ MW, and $\tau = 0.068$ s ; we obtain

E_1(MJ)	E_{12}(MJ)	E_{23}(MJ)	E_{tot}(MJ)	P_{max}(MW)
0.766	1.001	10.5	12.3	73.0

From the total heat capacities of clad and alloy given in Section 2 we find that the above energy release, if applied to adiabatically heating the fuel tubes, will result in a temperature rise of about 475K which is still short of the melting temperature. Thus although the flow instability power has been greatly exceeded the outcome of this transient would be acceptable.

Because it neglects the existence of delayed neutrons and reactivity feedback effects, and assumes an unbounded ramp reactivity input, the above discussion is not intended to provide realistic numerical results, but simply to illustrate the influence of the parameters on CCA bank performance. Serious consideration of transients should be treated with a code such as ZAPP.

3.2. Safety Rods.

3.2.1. Functional description.

For each safety rod system the components of interest here are:-

[a] The neutron absorbing rod.

[b] The rod cable.

[c] The winding drum.

[d] The braking system.

3.2.1.1. Operation.

When the electromagnetic clutch engages the drive motor to the winding drum the safety rod can be raised to the fully out position at which the bottom of the rod is level with the D_2O surface. The time taken to withdraw the rod is 8.2 min.

With the electromagnetic clutch disengaged the rod falls vertically within the thimble which contains it. The acceleration is determined by gravity, the mass of the rod, the mass and moment of inertia of the drum, and resistive (frictional) couples in the drum bearings. When the rod has fallen 1.17 m, a cam on the drum engages a lever which is both lifted and turns about a pivot; this lever compresses a pair of concentric springs and absorbs the kinetic energy of the falling rod and rotating drum. The spring compression is about 0.06 m. The rod is fitted with a deformable nose to prevent damage to the base of the thimble should the connecting cable break. A full description is given in reference (1).

3.2.1.2. Physical parameters of the system.

Safety rod.

The neutron absorbing section of the rod is formed from cadmium in the form of a hollow cylinder, wall thickness 2 mm, length 762 mm, and diameter 41.5 mm. The cylinder is enclosed on both sides by concentric stainless steel tubes and strengthening structures provide both rigidity and a point of attachment for the cable. The mass of a complete assembly is 4.54 kg.

Lifting cable.

This is a 3.2 mm diameter stainless steel cable made up of two lengths of 2.4 m and 3.5 m connected by a turnbuckle. The cable was prestretched before installation and is rated to a safe working load of 50 kg.

Winding drum.

This is made of cast iron in the form of a cylinder open at one end and with a maximum wall thickness of 0.0067 m and internal diameter 0.108 m. The moment of inertia is given [1] as 0.0025 kg m^2 implying a mass of about 0.7 kg. Apart from rotating, the drum moves axially, which both maintains the line of action of the cable and permits the engagement of the braking system when the rod has fallen a distance of 1.16 m. The drum performs 3.7 revolutions when the rod travels from fully out to fully in, a distance of 1.37 m.

The braking system.

When the drum has rotated through 3.1 revolutions a stop on the drum engages with a stop on the retardation cam which then rotates with the drum. The cam face bears against a roller attached to a lever, pivoted at one end and bearing against a pair of concentric springs at the other. These springs absorb the kinetic energy of the falling rod and the rotating drum. The spring constants are 1700 N m^{-1} and 5600 N m^{-1} respectively; the maximum spring compression is 0.07 m.

3.2.2. Dynamics of safety rod drop.

We consider the arrangement shown schematically in the sketch below where
M = mass of safety rod = 4.54 kg
I = moment of inertia of drum and other rotating components = 0.0033 kg m^2
r = radius of drum = 0.0589 m
θ = angular position of the drum
z = distance fallen by rod (m)
T = tension in wire cable
g = acceleration of gravity.

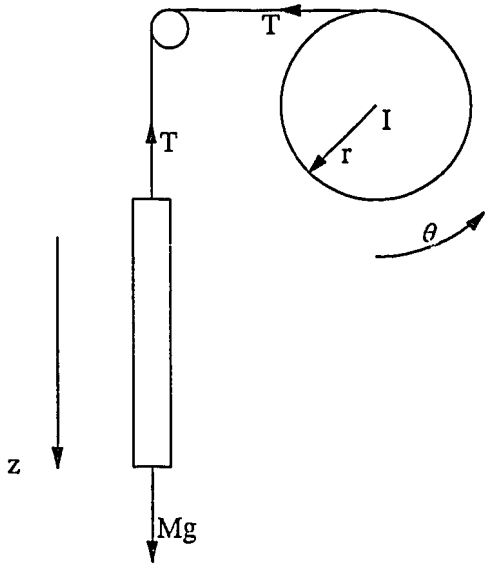

The force-acceleration relationships are,
for the drum, $rT = I\ \ddot{\theta}$ and,
for the rod, $\ddot{z} + T / M = g$
Since $z = r\theta$, $\dot{z} = r\dot{\theta}$, $\ddot{z} = r\ddot{\theta}$ we can eliminate the tension force T and get $\ddot{z} = \dfrac{g}{[1 + I/Mr^2]}$
which can be easily integrated twice to give

$$z = \frac{\frac{1}{2} gt^2}{[1 + I/Mr^2]}$$

Thus

$$\frac{T}{g} = \frac{I}{Mr^2 + I} M$$

Now friction losses in the system of the drum will increase the tension in the wire and increase the apparent moment of inertia of the drum; because

$$\frac{1}{g}\frac{dT}{dI} = \frac{Mr^2}{(Mr^2 + I)^2} M$$

it follows that $\frac{\Delta T}{g}$ = mass equivalent of friction = $\frac{M^2 r^2}{(Mr^2 + I)^2} \Delta I$

The mass equivalent of friction is given [1] as 0.726 kg so that $\Delta I = 0.00365$ kg m^2 and therefore the equation of motion including frictional losses becomes

$$z = \frac{\frac{1}{2} g t^2}{[1 + (I + \Delta I)/Mr^2]}$$

Inserting numerical values into this equation gives

$$z = 3.39\ t^2$$

The zero time in this equation is unspecified and it is easily modified to account for delays in the release of the the rod by the magnet. Thus if we denote this release time by t_0 then this theoretical solution can be written

$$z = 3.39\ (t - t_0)^2$$

Measurement of the rod position as a function of time has been made with time zero as the instant the magnet current was interrupted [15]. Least squares fitting of this data before the braking cam is engaged gave

$$z = 3.31\ t^2 - 0.3386\ t + 0.01105 = 3.31\ (t - 0.05115)^2 + 0.0024$$

This indicates a release time of 0.05115 seconds while the agreement between the coefficients of t^2 is excellent showing that the acceleration is well calculated. The residual value 0.0024 is interpreted as a consistent error of 2.4 mm. in determining the vertical position of the rods.

However, the analysis in the design report [1] predicts an acceleration of 8.4 m s^{-2}; this seems to have been produced by erroneously assigning frictional losses to an increase in the mass of the rod rather than to an increase in the moment of inertia of the drum.

The time taken from the interruption of the magnet current to the engagement of the braking cam is 0.645 s. Routine measurements of the time from magnet current interruption to operation of the down limit microswitches give about 0.900 s so that the time for which the rod is braked is about 0.250 s. At the time the braking cam is engaged the kinetic energy of the rod is 35 J and that of the drum is 18.5 J. However, the mechanical friction losses (mainly in the cam and lever) are quoted [1] as being rather high, 32 J, so that if we denote by E_s the energy stored in the springs and E_k the kinetic energy of rod and drum we have

$$E_k = E_s + Mg(z - z_0) + 32$$

where $z - z_0$ is the distance fallen by the rod from the time the cam is engaged to the time the rod is brought to a halt. If we denote by x the spring compression (assumed equal for both pairs of springs, though this is not exactly true) then

$$E_s = 2\left[\tfrac{1}{2} k_1 + \tfrac{1}{2} k_2\right] x^2 = 7222\ x^2$$

and from the rod/cam geometry $z = 5.25\ x$, so that

$$7222\ x^2 + 233\ x - 21 = 0$$

giving $x = 0.053$ m and $z = 0.44$ m. The latter value corresponds to an overshoot of the rod rest position of 0.075 m, somewhat less than the value measured on HIFAR [15] of 0.11 m.

Measurements show [15] that after reaching their lower limit the rods undergo several bounces. The mechanical arrangement is far too complicated to enable these to be simply treated as a damped harmonic oscillation; instead it will be considered that, after the springs are first engaged, the rod approaches its rest position at a linear rate of 0.15 m s^{-1}, so that $z = z_{(t=0.645)} + 0.15\,(t - 0.645)$. Combining this with the fitted quadratic for the falling rod motion gives the combined rules:

for $0.00000 < t < 0.05115$, $z = 0.0$
for $0.05115 < t < 0.64500$, $z = 3.31(t - 0.05115)^2$
for $0.64500 < t < 2.00000$, $z = 1.1673 + 0.15(t - 0.645)$

This approximation is shown in Figure 3-6.

3.2.3. Reactivity controlled by the safety rods.

Measurements [15] of the reactivity controlled by the safety rods in the cold clean reactor at a critical angle of 8° gave values of about 0.014 δk/k for each rod. This value decreased quite rapidly as the critical angle increased, being about 0.006 δk/k at 20° . This, however, is not a consequence of the position of the CCA bank. Rather, it reflects the manner in which the reactor was forced to higher critical angles by poisoning of the nine 2V facilities. These (and the safety rod positions) lie on the same lattice pitch as the fuel elements, and on the boundary of the core and radial reflector. It is clear from the measurements that the reactivity control of the rods is very sensitive to the manner in which these facilities are loaded. This dependence has been verified theoretically by Robinson [16]. Placing a black absorber in 2V6, adjacent to safety rod 2, halved the reactivity controlled by that rod. It is therefore necessary to determine rod worths under the loading conditions of the 2V facilities; for these reasons the experimental data for reactivity controlled as a function of vertical rod position have been normalised to that of the rod when fully inserted, ($\rho' = \rho/\rho_0$), to allow the user of this data to select an appropriate absolute reactivity control appropriate to the circumstances being considered. This data, shown in Figure 3-7, is well fitted by the expression

$$\frac{\rho}{\rho_0} = e^{-(bZ + cZ^2 + dZ^3)}$$

where Z (m) is the distance of the rod from the fully in position and the constants in this expression have the values b = 0.8814, c = 4.0859, d = 4.5996

3.2.3.1. Ramp rates following safety rod drop.

This last equation can be differentiated with respect to Z to get an expression for $\frac{d\rho}{dZ}$. This can be combined with the set of rules for z=1.37-Z as a function of time in the range $0 < t < 2.0$ to allow the normalised shutdown ramp rates $\frac{1}{\rho_0}\frac{d\rho}{dt}$ to be calculated.

3.2.4. Nuclear heating of safety rods.

There is no provision for heat removal in the design of the safety rods. Indeed, because the rod is hung from a cable in a closed thimble, both convection and conduction mechanisms are presumably very small and the only effective way of dissipating the heat energy is by thermal radiation. However the rods are normally removed from the radiation field of the reactor and are only exposed to the rapidly decreasing field that follows a reactor scram. We now examine this situation.

The equation describing the time dependence of the rod temperature, when only radiation losses are effective, is

$$H_r \frac{dT}{dt} + A\varepsilon\sigma[T^4 - T_0^4] = P(t)$$

where	H_r =	heat capacity of the rod	=	1700 J K^{-1}
	T =	temperature (K) of rod		
	T_0 =	temperature of environment	=	323 K
	A =	outer surface area of rod	=	0.1 m^2
	ε =	emissivity	=	2.5 $10^{-4} \times$ T (in K)
	σ =	Stefan-Boltzmann constant	=	5.67 10^{-8} W $m^{-2}K^{-4}$
	P(t) =	power (W) developed in the rod from nuclear heating		

Note that the heating power is assumed uniform over the rod length. From the same arguments presented when discussing CCA heating, we derive for P(t) a value of 5 kW when the reactor power is 10 MW and the safety rod is fully in.

Some useful information about the relationship between cadmium temperature and rod-heating power can be deduced from the above equation by assuming that the rod (and cadmium) temperature has reached and maintains a constant value, i.e. dT/dt = 0

The worst possibility for the safety rod is that its temperature could reach the cadmium boiling point (1038 K) leading to internal pressurisation and failure of the rod. If the reactor power was to be maintained at 3.4 MW then the heating power in the rod would be constant at about 1700 W. This level of heating power would be enough to bring the cadmium to the boiling point and to maintain it there in balance with the energy loss by radiation; however, the time to reach this temperature is in excess of ten minutes. It turns out that boiling of the cadmium can be dismissed from further consideration because if the safety rods control a total absolute reactivity of 0.007 (about $1) and they drop into the core then the reactor power will fall from 10 MW to 3 MW in a few (6.5) seconds and to less than 1 MW in about 45 seconds.

Of less concern would be melting of the cadmium and a similar calculation with T held constant at the cadmium melting point (594 K) shows that the corresponding rod-heating power would be about 88 W. This corresponds to a reactor power of 175 kW, but melting temperatures are not reached for several hours.

In an abnormal situation where the safety rods are alone responsible for maintaining the reactor in a relatively safe state, the reactor power may not have fallen to such a low value. We have, therefore, examined the time dependent behaviour of the rod temperature when the reactor power is maintained at a nominal value of 1 MW. Numerical solution of the heating equation shows that the melting temperature is not reached unless this reactor power is maintained for fifteen minutes. Because the reactivity controlled by the rods would force the power below 1 MW in less than 1 minute, melting of the cadmium will not occur.

3.3. Comments - Conclusions.

The central aim of this section has been to determine the rate of reactivity insertion following a SCRAM signal from the reactor guard lines. To do this requires an understanding of the dynamics of CCA and safety rod motion so that time dependent velocities can be calculated as well as the space dependent reactivity per unit displacement. This topic is fundamental to the analysis of system safety.

Other matters discussed are of lesser import and provide 'bookkeeping' data; however in combination and over time the importance of using consistent data is a sensible way should not be ignored.

3.3.1. The Coarse Control Arm Bank.

In formulating the equation of motion of the CCAs we have made two assumptions; that a CCA blade is fully submerged at all angular positions and that the flow of water past the blade is turbulent. The first assumption is clearly incorrect at high angles; 87% of the blade is submerged at 37° but this fraction decreases rapidly at higher angles. Since these angles are outside the operational range of the arms this is not of concern, however it should be borne in mind that some data such as drop times and component stresses have been measured from an initial angle of 56° and should not be analysed by our equation of motion.

The assumption of turbulent flow seems reasonable given the irregular cross section of a blade assembly and the aspect ratio of the leading edge. A theoretical justification has been given by Meister and Kalker [2] who claim that the Reynolds Number of the flow exceeds the critical value, but we have not examined this.

Most parameters appearing in the equation of motion can be determined simply and to high accuracy, probably better than manufacturing tolerances. However the determination of the moment of inertia of the blade and connecting rod requires some simplification. It can easily be shown that if the rectangular and uniform representation of the blade is used then the finite width of the arm contributes only a small amount to the total moment of inertia and it is more important to include the effect of the mass distribution along the blade length. We take the demonstration that such a model gives calculated values of the small angle oscillation frequency of a blade which agree with measurement as indicating that the calculated moment of inertia is not seriously in error.

Although the equation of motion for free fall does not require reference to measured arm velocities the submerged arm case is not so independent because of the braking term A which for its determination has required normalisation to measured data. A simple model has given independent verification of the value of A so obtained but its simplicity makes its application arguable. However we note that a direct determination of A could be made by determining the angle which a free arm would overshoot the vertical when released from rest. The equation of motion predicts that the tangent of the overshoot angle is simply 1/2A, provided that the initial angle is large.

The equation of motion is also important because it permits calculation of the stresses in components when the arm motion is arrested. Separation of an arm from the connecting rod following fracture produced by these stresses would result in the arm swinging from the core to a position of small reactivity control; a major power excursion would follow. These stresses may be considered proportional to the angular momentum of a falling arm when it reaches the normal full in position; for an arm falling through air from an initial angle of 56° this is about 3.5 times the momentum acquired in a fall through heavy water from an angle of 30° . Thus the two hundred air drops of a bank of six arms from 56° performed by the manufacturers were equivalent to some 700 operational scrams; because the blade lifetime in the reactor is only a few years the test schedule greatly exceeded the demands placed on the bearings. On the other hand the connecting rods are not replaced and must, after thirty four years, be considered to have exceeded the cumulative test load.

It must be noted that failure of a bearing or rod as the arms reach their down limit will not result in a power excursion if the remaining arms remain intact. Since the stresses in the system when the arm motion is arrested are some five times greater than the static stress during normal arm operation this is the most likely time for CCA failure to occur.

The second component in determining reactivity input rates following a scram is the reactivity controlled by the CCA bank as a function of its angular position. Because the integral bank worth is large it is necessary to determine differential worths as a function of position and to integrate these data if experimental methods are employed to obtain the integral reactivity control. This

necessitates poisoning the reactor to enable measurements over the operational range of angle and, to an extent, the data so obtained depend upon the spatial distribution of the poison. The availability of detailed computational methods giving good agreement with experiment has, to a large extent, removed these doubts and the absolute reactivity worth of the CCA bank can be regarded as well established.

From the data given in this section it is possible to comment on the design of the CCA bank and on the sometime expressed view that it is outmoded. It is true that because the design combines a control and scram function it breaches current design philosophy and the ability to operate at high angles with a consequent increase in the time needed for the falling arms to become effective is to be deplored. However, if administrative control is relied upon to limit the arm movement to less than 30° it can be seen from Table 3.2 that the time needed to remove \$2 of reactivity is less than ~160 ms and the maximum shutdown ramps are very large. In the past it has been the practice to assume very long delay times before the arms would commence to move, so long in fact that this delay time determined, to a large extent, the outcome of calculations. We consider it demonstrated here that these delay times are spurious. Thus, considering a \$2 reactivity injection which would give an asymptotic period of 100 ms, delay times given in Section 3.1.2.2 are less than one asymptotic period. It would probably be instructive if the above data were compared with those applying in a more modern research reactor.

3.3.2. The Safety Rods.

The equation of motion of the safety rods appears simpler than that of the CCA bank but, in reality, the fact that the rod is always coupled to the drum by the lifting cable introduces considerable complexity since the frictional losses in the system have been shown to be high. We have used the manufacturer's measurement of the 'mass equivalent of friction' to determine the effective moment of inertia of the rotating drum. Because it implies that mechanical energy is conserved this is subject to objection; but since we are interested only in the kinetics of the falling rod this will not influence the numerical outcome which has been shown to match observed accelerations very closely. In the same way, the reactivity controlled by the rods appears to be a simpler problem but the influence of local absorbers has been shown to have a major effect. If this is accounted for, either by measurement or calculation, there appears to be no difficulty in obtaining accurate rod worths or in ensuring that these are not unacceptably downgraded.

The inferred release time of 50 ms for the rod is insignificant compared with the 500 ms required for the rod to reach a position where the shutdown ramp begins. This is a consequence of the necessity to raise the uncooled rod to a position where nuclear heating is acceptable and cadmium burn up is low. It might thus be thought that the safety rods are only of use for terminating transients produced by relatively small reactivity injections (≈ \$1). However we consider that if inherent reactivity feedback is taken into account then the useful range of the safety rods will be greatly extended. We have not attempted this here.

Because of the complexity of the rod braking system we have not examined the cable tension as the rod motion is arrested. However failure of the cable would not produce any reactivity input of consequence and the rod itself has a deformable nose preventing a freely falling rod from damaging the thimble in which it is contained.

3.4. References.

(1) Hobson, H.M. Ltd. [1957] - Reports NED 121,122.

(2) Meister, G. & Kalker, K. [1964] - Analysis of possible coarse control arm accidents on the reactor FRJ-2. Report JUL-146-RE see AAEC Lib Trans 87

(3) Marshall, J. & Blevins, R.J. [1983] - Measurements of coarse control arm drop characteristics in the material testing reactor HIFAR. Report AAEC/E560

(4) Connolly, J.W. & Clark, N. [1986] - Analysis of hypothetical loss-of-control-arm accidents in HIFAR. Report AAEC/E631

(5) Vosper Ltd. Portsmouth UK [1958] - Stress measurements on coarse control arms for DIDO type research reactors. Also
Vosper Ltd. Portsmouth UK [1960] - Tests on DIDO Mark II coarse control arms.

(6) Harries, J.R. [1978] - Inverse kinetics reactivity measurements on the materials testing reactor HIFAR. Report AAEC/E456

(7) Storr, G.J. [1986] - Reactivity calibration of the HIFAR coarse control arms. AAEC internal report RD/TN-091

(8) Connolly, J.W., Robinson, G.S. & Storr, G.J. [1988] - Re-evaluation of some HIFAR physics data. Ansto internal report NT/TN-116

(9) Robinson, G.S. [1991] - 3D Diffusion calculations of HIFAR including the coarse control arms and their burnup. Report Ansto/E703

(10) Godfrey, R.M. [1989] - Adoption and implementation of new HIFAR physics data. Ansto internal Report NTP/TN-126

(11) Carlson, R.W.S. [1990] - The current limits for cadmium absorber lifetime (burnup) for the coarse control arms in HIFAR. Ansto internal report NTP/TN-154

(12) Robinson, G.S. [1992] - Effect of D2O Upgrade from 98.6% to 99.7% on integral CCA worth. Private communication to B.E.Clancy. Reproduced in Appendix A-6.

(13) Connolly, J.W. & Nicholson, K.P. [1961] - Energy absorption by materials exposed to radiation from HIFAR. Report AAEC/TM109

(14) Clancy, B.E. [1983] - ZAPP - A computer program for the simulation of reactor power transients. Report AAEC/E568

(15) Connolly, J.W. & McKenzie, C.D. [1960] - Reactor physics studies on the HIFAR twenty-five element cores. Report AAEC/TM-064

(16) Robinson, G.S. [1992] - Reactivity worth of HIFAR safety rods. - Minute to B. E. Clancy, 7 April 1992. On Ansto file LH 84/209. Copy in Appendix A-3

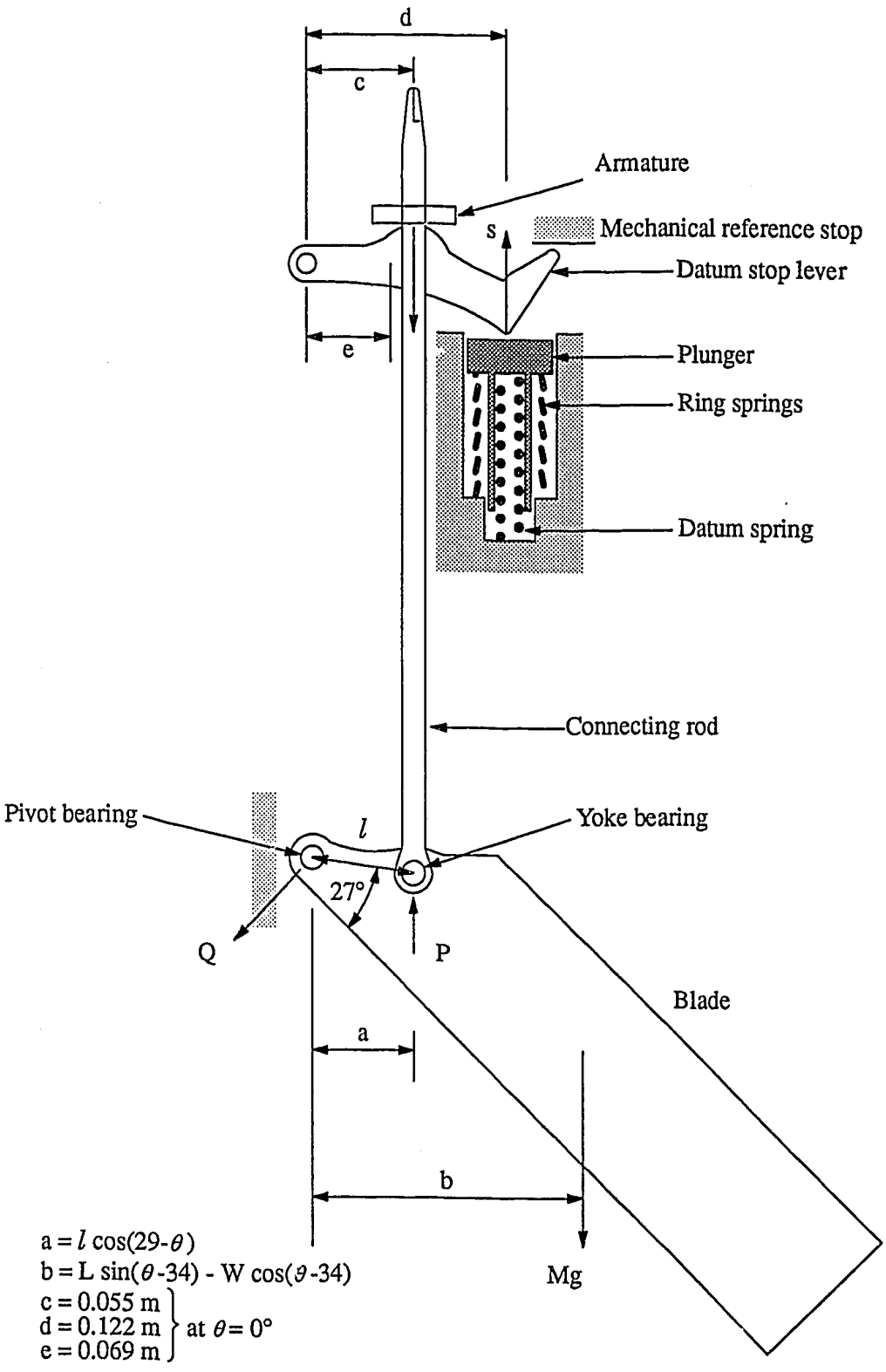

Figure 3-1 Schematic of CCA arrangements.

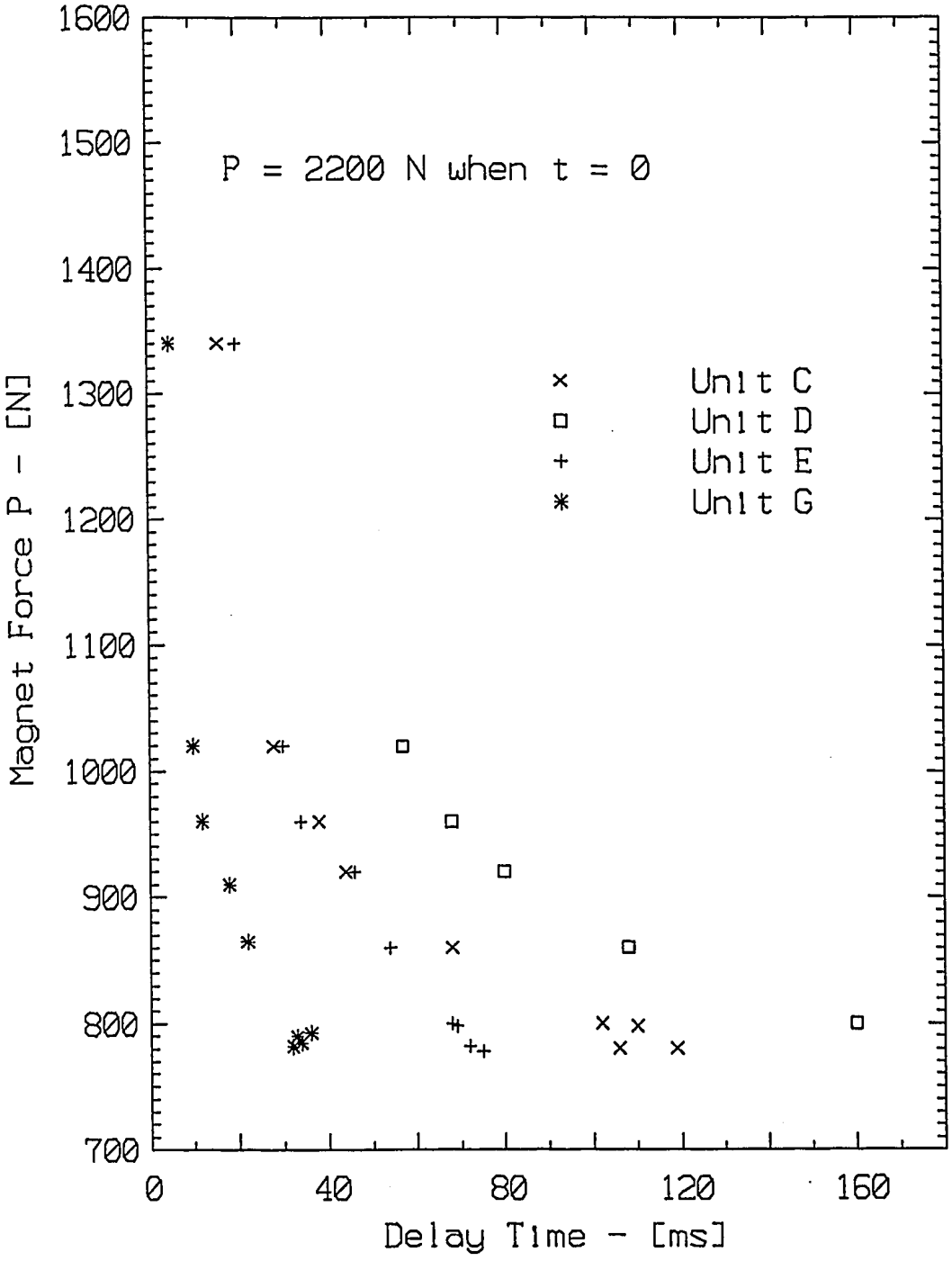

Figure 3-2 Delay time for CCA release v off magnet forces.

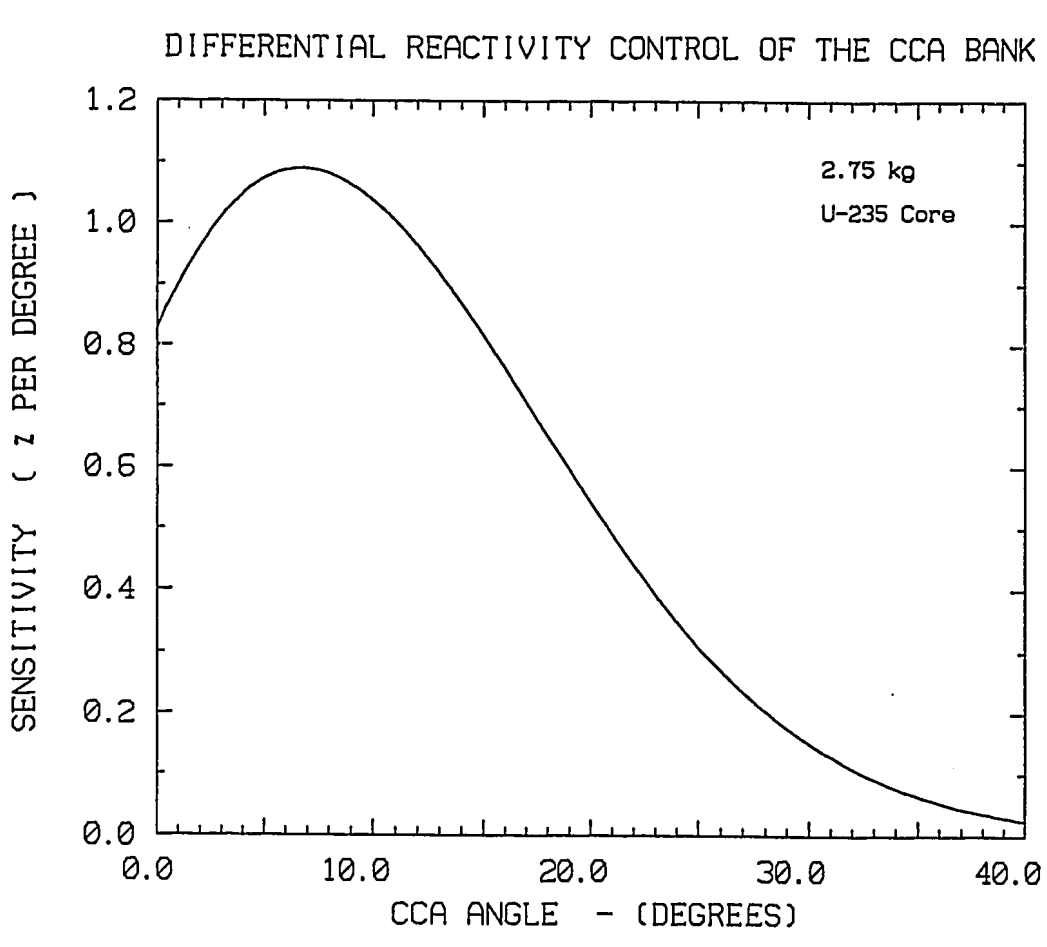

Figure 3-3 Differential calibration of CCA reactivity worth.

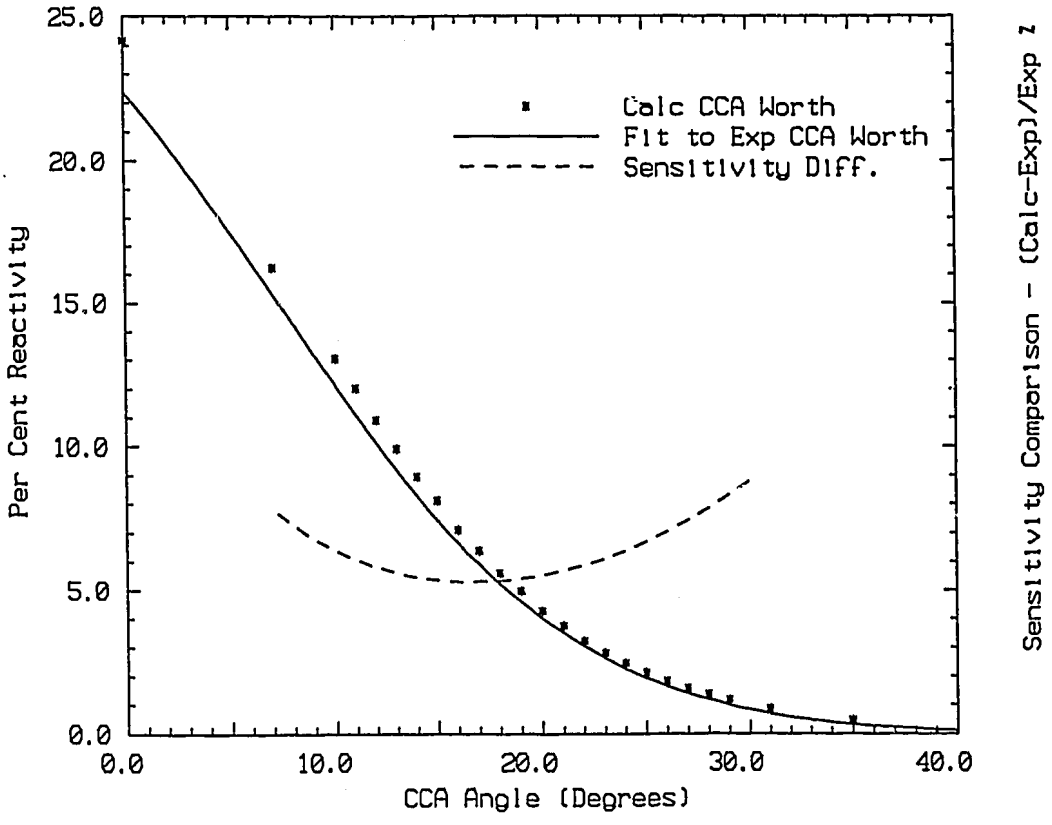

Figure 3-4 Integral calibration of CCA reactivity worth.

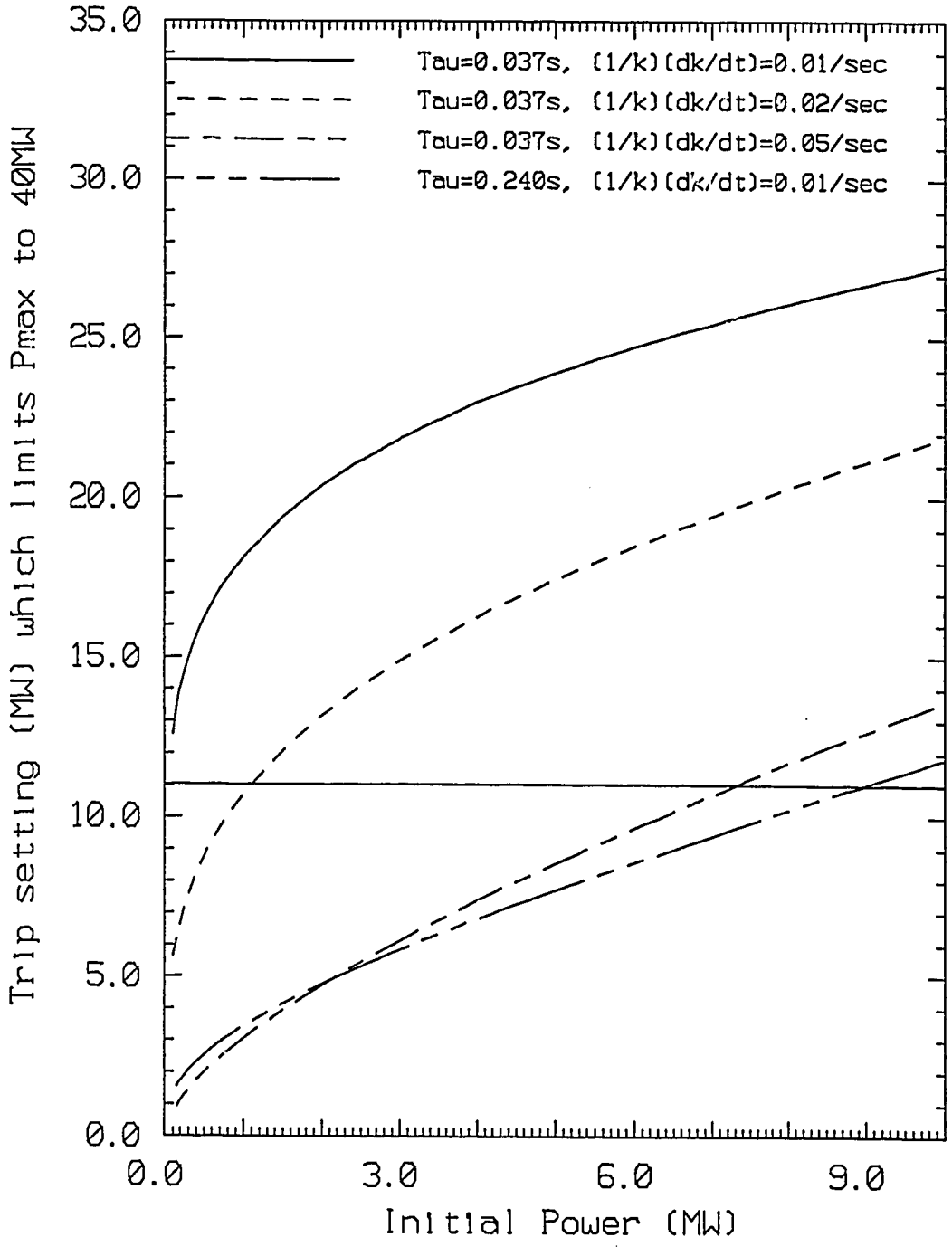

Figure 3-5 Trip settings to limit Pmax to less than 40 MW.

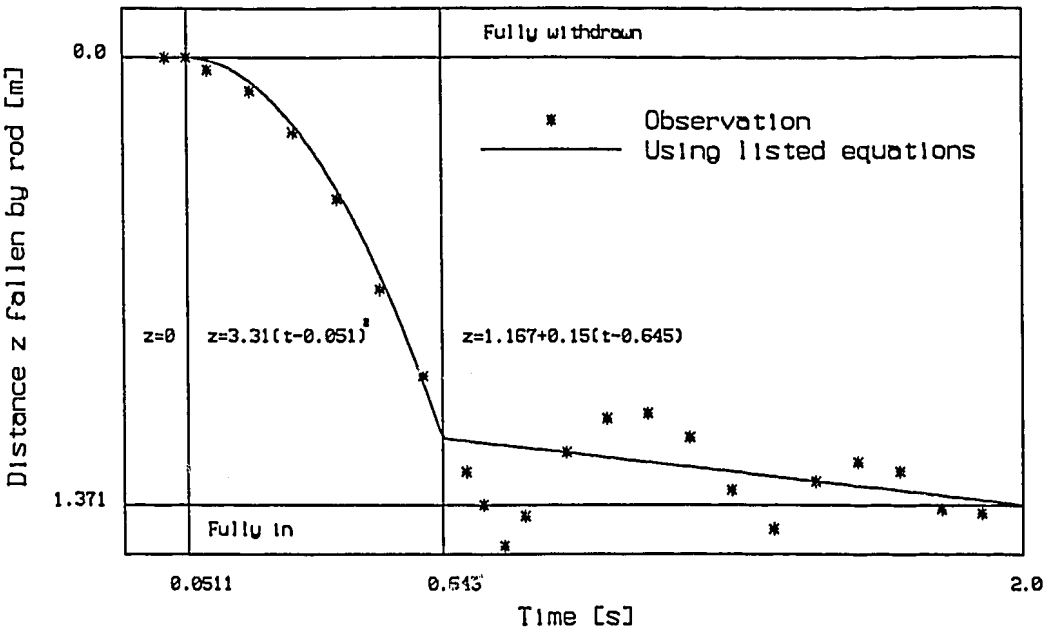

Figure 3-6 Drop characteristics of safety rod.

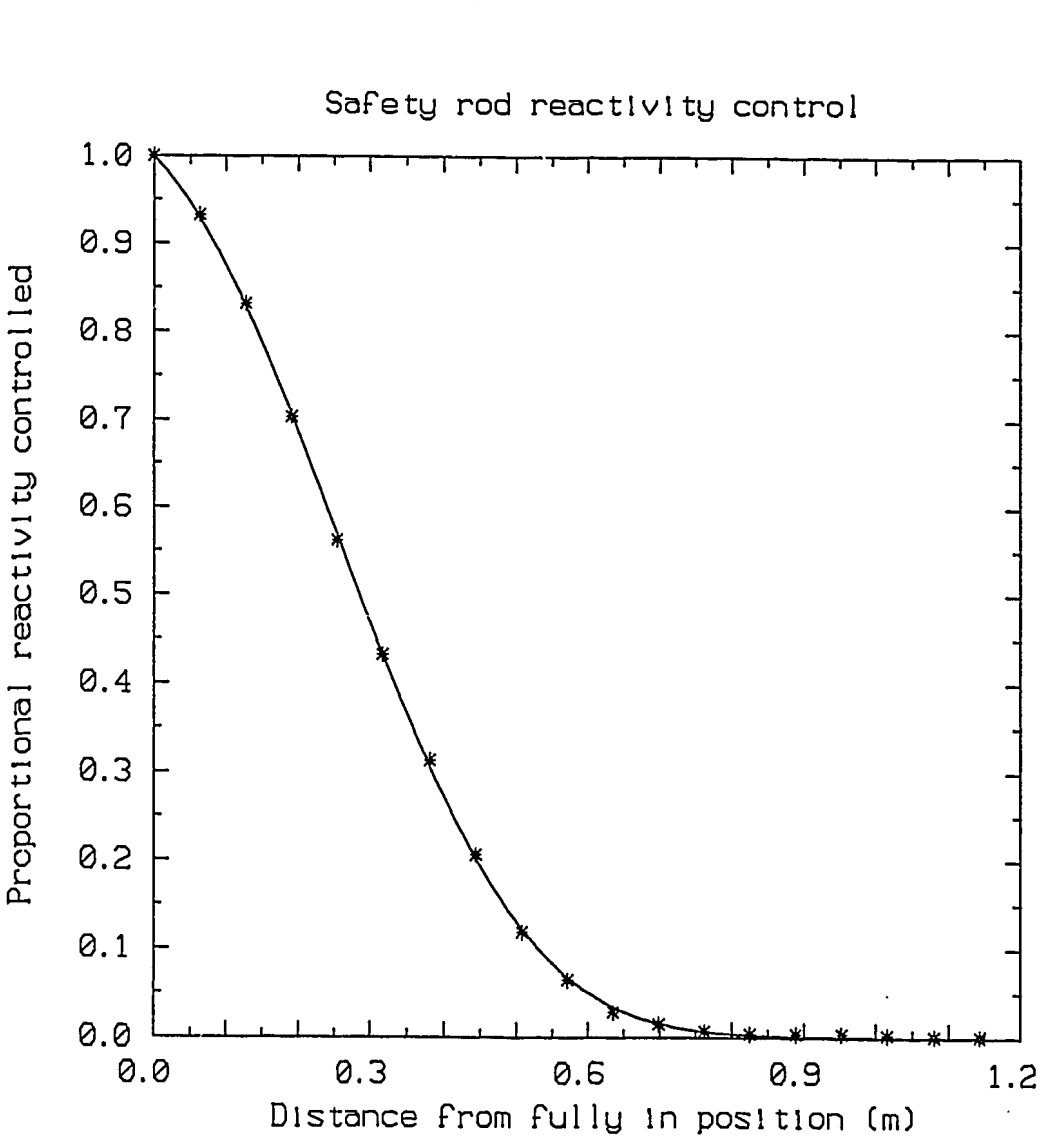

Figure 3-7 Reactivity control by safety-rod.

This page of Section 3 intentionally left blank

SECTION 4

THE REACTOR REFLECTOR.

He, to get the warm side inside,
Put the inside skin side outside;
He, to get the cold side outside,
Put the warm side fur side inside.

Anon. - The Modern Hiawatha.

4. THE REACTOR REFLECTOR.

The geometric buckling of the bare HIFAR core is 51 m^{-2} and a typical material buckling is about 20 m^{-2}, so that the reflector plays a large role in determining the flux distribution and reactivity of the system. The D_2O reflector is contained within the Reactor Aluminium Tank (RAT) which has the form of a cylinder with a spherical bottom. The side wall is 12.7 mm thick and has an outer diameter of 2.032 m. The bottom wall is 15.9 mm thick and the outside is a section of a sphere of radius 2.045 m centered 1.254 m above the centre of the core. All positions are given relative to the core centre. The core structure is supported on the 25.4 mm thick plenum header plate, the top surface of which is at -652.5 mm. The free D_2O surface is at 1056.5 mm. The 600 mm thick graphite surrounding the sides and bottom of the tank also serves as a reflector but its main purpose is to provide a large experimental volume.

4.1. Reflector Composition.

The D_2O reflector contains many irradiation facilities in the form of vertical thimbles and horizontal re-entrant tubes, as well as a pair of safety rod tubes and four downcomers. All these thimbles and tubes are of aluminium. The vertical irradiation thimbles are usually flooded with D_2O but the safety rod tubes and horizontal tubes are not. The CCAs, being movable, are not considered to be part of the reflector material inventory.

The location and dimension of each thimble or tube are given in tables 4-1 and 4-2.

Table 4-1
Specification of Horizontal Facilities.

Facility	End Coordinates (mm)				Dimensions (mm)	
	X	Y	Radius	Z	Inner Radius	Outer Radius
10H	-384.5	384.5	543.7	0.0	139.7	149.23
6H	341.2	-341.2	482.6	0.0	88.9	98.43
4H1	467.0	467.0	660.4	304.8	63.5	69.85
4H2	467.0	467.0	660.4	-304.8	63.5	69.85
4H3	0.0	419.1	419.1	304.8	63.5	69.85
4H4	0.0	420.69	420.69	-304.8	63.5	69.85
4H5	-467.0	-467.0	660.4	304.8	63.5	69.85
4H6	-467.0	-467.0	660.4	-304.8	63.5	69.85
2TAN		76.2		-406.4		

All locations are relative to the core centre, and the X axis is such that the C5 fuel position lies on the axis and has a positive X coordinate. The 'location' given for each of the vertical facilities is

Table 4-2
Specification of Vertical Facilities.

Facility	End Coordinates (mm)				Dimensions (mm)	
	X	Y	Radius	Z	Inner Radius	Outer Radius
Safety Rod Tubes						
SR1	-381.	-304.8	487.9	-620.	23.19	26.925
SR2	381.	304.8	487.9	-620.	23.19	26.925
Thimbles						
2V1	-533.4	-304.8	614.3	-620.	25.4	28.8
2V2	-533.4	-152.4	554.7	-620.	25.4	28.8
2V3	-457.2	0.0	457.2	-620.	25.4	28.8
2V4	-533.4	152.4	554.7	-620.	25.4	28.8
2V5	-381.	304.8	487.9	-620.	25.4	28.8
2V6	533.4	304.8	614.3	-620.	25.4	28.8
2V7	533.4	152.4	554.7	-620.	25.4	28.8
2V8	457.2	0.0	457.2	-620.	25.4	28.8
2V9	533.4	-152.4	554.7	-620.	25.4	28.8
4V1	-234.95	-838.2	870.5	-529.	50.8	54.95
4V2	-190.5	838.2	859.6	-529.	50.8	54.95
4V3	234.95	838.2	870.5	-529.	50.8	54.95
4V4	711.2	-457.2	845.5	-529.	50.8	54.95
4V5	234.95	-838.2	870.5	-529.	50.8	54.95
6V1	-190.5	-520.7	554.4	-634.	76.2	82.15
6V2	-190.5	520.7	554.4	-634.	76.2	82.15
6V3	190.5	520.7	554.4	-634.	76.2	82.15
6V4	190.5	-520.7	554.4	-634.	76.2	82.15
Downcomers						
	419.1	749.3	858.5	362.	88.9	95.25
	-368.3	749.3	834.9	362.	88.9	95.25
	419.1	-749.3	858.5	362.	88.9	95.25
	-419.1	-749.3	858.5	362.	88.9	95.25

the centre of the (inside) bottom of the thimble. The location given for most horizontal facilities is the centre of the endcap, i.e. the aluminium/D_2O interface closest to the core. The 10H and 6H endcaps are 12.7 mm thick and the 4H endcaps are 6.35 mm thick. All horizontal facilities except 2TAN are radially directed. The 2TAN facility is an obround tube of inner dimensions 104.8 × 38.1 mm and thickness 6.35 mm. It passes right across the tank and is centered on the line indicated in the table.

The additional materials included in the reflector are the nozzles on which the fuel elements sit and the unfueled ends of the fuel elements. The portion of each nozzle above the plenum plate has a mass of 0.97 kg and extends 145 mm above the plate. The fuel element ends have been represented by an aluminium mass per unit length of 2.18 kg m^{-1} in addition to the unfueled part of the fuel tubes.

4.2. Reactivity Coefficients.

The reactivity coefficients of the reflector regions are important in determining the dynamic response of the reactor to a reactivity injection. It is first necessary to consider the definition of appropriate reflector regions to use in calculating the coefficients. Consideration of the data of

Section 2 shows that the radius of the equivalent cylindrical core is 430 mm. It is thought that the inner section of the radial reflector responds more quickly to coolant temperature changes because of downflow in the vicinity of the fuel elements. This inner section has been arbitrarily defined to have a radius of 500 mm and all facilities within that radius smeared into that region in establishing an RZ model of the reactor. For neutronics calculations it may be necessary to divide the D_2O reflector into more than ten regions in order to position material in approximately the correct position. For the purpose of reporting reactivity coefficients, it is a computational simplification to replace the spherical lower cap by a plane base situated just above the plenum plate. It is then convenient to define the reflector as being made up of the five or six regions defined by Table 4-3 and Figure 4-1. The mass of aluminium in the top and bottom reflectors includes the unfueled ends of the fuel elements and the fuel element nozzles but not the plenum plate. The temperature and void coefficients calculated, just as in Section 2.7.4, for a 2.75 kg core are also included in the table.

Note that these reflector coefficients all scale as $(\,^{235}\text{Umass})^{-0.5}$

Note also that the calculated overall temperature coefficient for a change from 40° C to 50° C using this method is $-3.47\ 10^{-4}$ (the reflector contribution being $+0.22\ 10^{-4}$). This may be compared with the value deduced by fitting 7 years of data (1982-1989) obtained from balancing a temperature change with a CCA movement following the method of Harries [1]. Using the CCA calibration of Connolly et. al. [2] this deduced value is $-4.8\ 10^{-4}$ for a 2.75 kg core.

Table 4-3
Reflector Regions and their Reactivity Coefficients.

	Portion of D_2O Reflector				
	Top	Bottom	Inner Radial	Outer Radial	Top+Bottom Radial
Height (mm)	754.9	350.9	603.3	603.3	1105.8
Inner radius (mm)	0.0	0.0	430.0	500.0	430.0
Outer radius (mm)	430.0	430.0	500.0	1003.3	1003.3
Mass D_2O (kg)	458.	201.	128.	1468.	3040.
Mass aluminium (kg)	3.3	45.9	10.4	79.2	124.3
Mass steel (kg)	0.0	0.0	0.107	2.755	2.042
Heat Capacity (MJ K^{-1}) at 323 K	1.968	0.885	0.545	6.230	12.858
Reactivity Coefficients					
Temperature (δk/k) K^{-1}	$+1.44\ 10^{-5}$	$+1.43\ 10^{-5}$	$-1.30\ 10^{-7}$	$+4.19\ 10^{-5}$	$+2.27\ 10^{-5}$
Void (δk/k) per % void	$-3.40\ 10^{-4}$	$-3.22\ 10^{-4}$	$-3.59\ 10^{-4}$	$-5.96\ 10^{-4}$	$-3.76\ 10^{-4}$

4.3. Reactivity Control by Top Reflector.

The change in reactivity produced by decreasing the height of the top reflector has been determined for various critical angles [3]. These measurements showed that the CCAs exert a strong influence on the reactivity worth of the top reflector, largely because the fraction of the CCA absorption area within this region depends in a complicated way on the CCA angle. At twenty degrees the arms are just leaving the core and as the angle increases, an increasing layer of D_2O free of the arms is left above the core. At lower angles the fraction of the CCA in the core increases and that in the reflector decreases. Thus it might be expected that the reactivity worth of the top reflector would have a minimum at an angle of about 20° and this is found to be the

case as shown in Table 4-4

Table 4-4
Reactivity Control by Top Reflector.

CCA angle θ °	Reactivity loss on reducing reflector height to 0.17m
25	0.0154
16	0.0045
8	0.0123
6	0.0110

The change of reactivity with height $\frac{1}{k}\frac{dk}{dH}$ at the lowest height measured, 0.17m, was quite large at higher angles, ≈ -0.004 dk/k cm^{-1}, and clearly increasing in magnitude, indicating a loss > 0.03 dk/k at zero height. The calculated value (G. S. Robinson - private communication) is 0.09 dk/k. Provision was made in the original HIFAR design for reflector dump to be called on to reduce reactivity in certain circumstances, but the slowness of the dump and the small value of the corresponding reactivity coefficient at large heights led to this measure being removed.

However, more rapid rates of reflector height reduction could be achieved following large breaks in the primary coolant circuit; this is discussed in Section 7.

There is little interest in the reactivity worth of the remaining reflector regions since their loss can only be occasioned by complete draining of the RAT or by boiling off the D_2O. These are extreme events and the reactor would be so far sub-critical that knowledge of the exact amount of reactivity loss would not be helpful.

Calculated changes of reactivity with the isotopic ratio D_2O/H_2O have been discussed in Section 3.1.4.3. Changes in the ratio are essentially long term and result from the uptake of light water vapour.

4.4. Neutron Flux Distributions.

There is little of importance to the present study in the behaviour of the flux distributions in the reflector. As might be expected, the influence of the CCAs is not so marked as for the core and the axial distributions are fairly symmetric about a maximum value whose position moves towards the centre plane with increasing CCA angle. However, because the ion chambers used for reactor control are measuring neutrons leaking from the reflector, the loading of reflector thimbles or degradation of the D_2O might have an effect on the ratio of the ion chamber current to the reactor power. This possibility must always be considered in the operation of the reactor and is a major reason for the ΔT measurements undertaken routinely during each program.

Lastly, it has been shown that the 10H facility introduces a large flux perturbation resulting in a flux tilt across the core and an additional complication in reactor calculations.

4.5. Coolant Flow Pattern in the RAT.

Coolant leaving the core passes into the upper part of the fuel assembly from which it leaves through a diffuser outlet consisting of sixty circular apertures of diameter 0.019m. The mean velocity of this flow is 0.85 m s^{-1}.

The earliest attempts to quantify the flow pattern seem to have been performed on the Danish DR3 reactor by deriving, in the frequency domain, the transfer functions of non-boiling transients [4]. From temperature measurements in the top reflector, bulk moderator, and the bottom reflector it was concluded that a violent circulation existed in the RAT, with only a two

second time lag between coolant outlet temperatures from the core and the temperature of the top reflector; the bulk moderator temperature changed even faster. It may be inferred that a considerable portion of the flow from the diffusers is directed down into the bulk moderator, a not unreasonable event since the outlets from the diffusers are directed against the flow from neighbouring diffusers, or, for outer elements, partly against the 2V thimbles. (It may be noted that if the coolant flow were treated as flow into the mixing volume of the entire RAT contents the time lag would be of the order of fifteen seconds.)

This strong downward flow was confirmed visually [5] in a full scale mockup of the FRJ-2 reactor during measurements on their proposed ECCS. At LHRL, temperature transients have been produced by varying the secondary and primary coolant flows in HIFAR; analysis of the power/reactivity relationship in the time domain led to the conclusion that no long time lags occur in the coolant circulation through the RAT and that an appreciable part of the total flow must be downwards through the bulk moderator.

Thus there is a reasonable degree of independent evidence supporting the view that the bulk moderator region will play a role in determining the power behaviour of HIFAR for transients whose time constants are comparable with those of the coolant flows in the RAT. However, the partition of this flow is not known and transient calculations must rely on some estimate. Fortunately, analysis of a small reactivity transient performed on DR3 with the code HIDYN indicated that the power behaviour was sensibly independent of the fraction of the flow directed to the bulk moderator, provided that this fraction was greater than one half. The available evidence is that this proviso is satisfied.

4.6. Comments - Conclusions.

The subdivision of the whole reflector region discussed here is rather arbitrary but has been chosen partly to allow examination of the effect of coolant flow paths on the reactor kinetics to be explored, although this has not been explored here. At the present time the code HIDYN [6] is the only tool available for such an investigation and its usefulness has not been fully tested. It has been suggested that a detailed thermal hydraulic/reactor kinetics system model of the reactor may be developed using the RELAP5 code or versions of it developed to model research reactors. This may require different modelling of the reflector regions.

We note that the puzzling discrepancy between calculated and measured whole reactor temperature coefficients still exists and it would be comforting if this could be resolved.

4.7. References.

[1] Harries, J.R. [1978] - Inverse kinetics reactivity measurements on the materials testing reactor HIFAR. Report AAEC/E456

[2] Connolly, J.W., Robinson, G.S. & Storr, G.J. [1988] - Re-evaluation of some HIFAR physics data. Ansto Internal report NT/TN-116

[3] Connolly, J.W. & McKenzie C.D. [1960] - Reactor physics studies on the HIFAR twenty-five element cores. Report AAEC/TM-064

[4] Le Cour Christensen, P. [1963] - An experimental and theoretical investigation of the dynamic response of the nuclear reactor DR3. Report RISO/56

[5] Wolters, J. [1979 ?] - Spray film emergency cooling for the experimental reactors of the FRJ-2 type. Undated doctoral thesis, translated from the German by B. Pietroff and P. Holland.

[6] Harries, J.R. & Wilson, D.W. [1978] - Measurement of the dynamic response of the materials testing reactor HIFAR. Report AAEC/E428

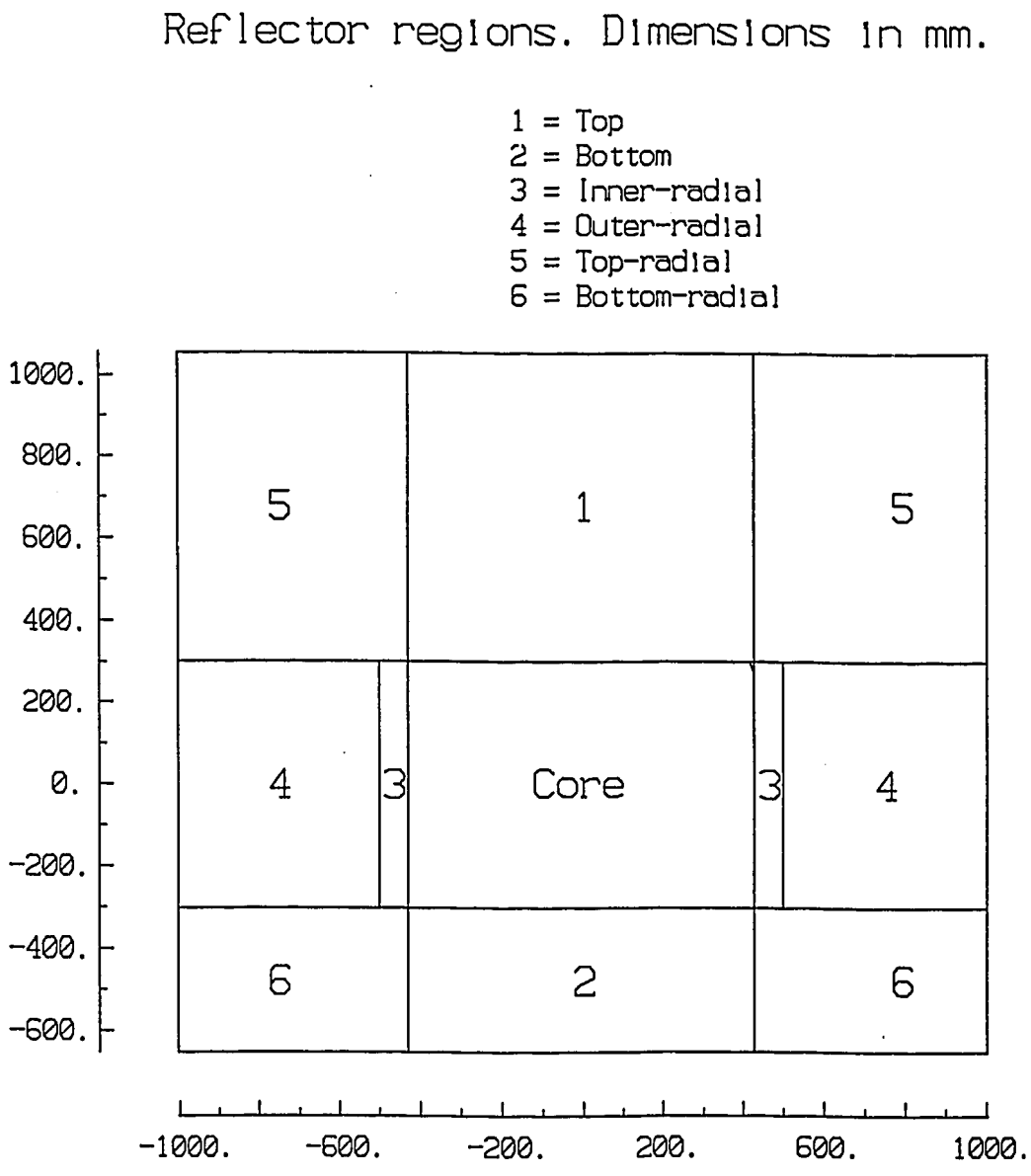

Figure 4-1 Calculational sub-division of reflector.

SECTION 5

THERMAL HYDRAULICS.

Big whirls make little whirls
Which feed on their velocity,
Little whirls make smaller whirls
And so on, to viscosity.

Anon.

5. THERMAL HYDRAULICS.

The D_2O forming the moderator of HIFAR also acts as a coolant to remove the heat generated in the fuel by the fission process. For this purpose, it is circulated through the fuel elements and thence through heat exchangers to remove the heat from the primary flow circuit.

Thermal hydraulic processes in the core under normal HIFAR operating conditions (10 MW thermal, coolant flow of 400 kg s^{-1}, and coolant exit temperature of 50 C) are considered here.

5.1. Coolant Temperature Rise Over Fuel Element.

In the steady state, conservation of energy requires that the heat generation rate in the fuel be equal to the rate of heat transfer to the coolant, ie

$$Q = MC_p(T_o - T_{in}), \tag{5.1.1}$$

where Q is the total power generated (10^7W), M is the total coolant mass flow (400 kg s^{-1}), C_p is the specific heat (approximately 4224 J $kg^{-1}K^{-1}$ at conditions of interest [1]) and subscripts "in" and "o" refer to inlet and exit conditions.

The temperature increase of the coolant for standard HIFAR conditions is calculated from the above to be 5.9 K. For an exit temperature of 50 C, the inlet temperature is then 44.1 C. Since little heat is lost from the coolant before leaving the RAT, the bulk moderator temperature is essentially the same as the temperature of the D_2O leaving the fuel elements.

The above temperature calculation applies to the overall coolant flow, and also to individual fuel elements having nominal power and coolant flow rates (i.e. 10 MW / 25 = 400 kW per channel and 400/25 =16 kg s^{-1} per channel). However, exit coolant temperatures for individual fuel channels differ from the above since fuel channel flow rates and powers differ significantly from the nominal values. Flow rates vary by up to 10%, depending on which pumps are operating (two of three available pumps are required for standard HIFAR conditions) and on the location of the fuel element [2]. Fuel element power varies with age of the element. A new fuel element may have a power of up to 850 kW (this is the maximum level permitted), and older elements may have powers as low as 250 kW. The above energy balance equation can be adapted to give the coolant temperature rise for any particular element with known power and coolant flow rate.

Moreover, since coolant flow rates are different for each annulus of a fuel element (see Section 5.3), and the power removed to each annulus is also different, coolant temperature rises are different for each annulus. The above calculation applies to the coolant after it has remixed downstream of the annuli. Temperature rises for individual annuli are considered further in Section 5.4.

5.2. Pressure Distribution Over Fuel Elements.

The pressure distribution over HIFAR fuel elements for a given coolant flow rate is required for three main reasons. Firstly, it is necessary that boiling be avoided in HIFAR since the operating range is limited by phenomena which would follow the onset of boiling. Boiling onset is determined in part by saturation temperature, and the local value of this is determined by the local pressure. Secondly, phenomena which set limits on HIFAR, such as critical heat flux (where overheating may occur at a local dry patch following boiling), or the various hydrodynamic instability mechanisms, depend in part on pressure-dependent fluid physical properties such as vapour density. Thirdly, a detailed examination of the coolant flow circuit requires knowledge of the total fuel element pressure loss dependence on coolant flow rate. As a special aspect of this, the pressure drop over fuel elements, and over the fuelled section of the elements, as set by the hydraulic circuit, are required to predict the onset of the different types of hydrodynamic instabilities.

From a fluid flow viewpoint, complete HIFAR fuel elements are too complicated to allow accurate estimates of pressure loss characteristics from simple engineering calculation methods. However, the geometry of the fuelled region of the fuel element is relatively simple, so standard pressure loss calculation methods can be expected to yield reliable predictions for this component of the element.

The frictional pressure gradient dp/dz in the fuelled section of the element is given by an adaptation of standard equations for axial flow in round tubes:-

$$\frac{dp}{dz} = \frac{2f}{D}\frac{G^2}{\rho} \qquad (5.2.1)$$

where f is the friction factor, ρ is the density, and G is the mass flux through the fuel. Nominally G lies between 3937 kg $m^{-2}s^{-1}$ (for zero flow through the central thimble) and 3701 kg $m^{-2}s^{-1}$ (for 6% bypass flow through the central thimble). D is the "equivalent hydraulic diameter" defined as (4× flow area/wetted perimeter). Using data from Table 2-1, D=4×0.004063 m^2/2.418 m =6.72 mm.

The friction factor f varies with Reynolds number Re=D G/μ, where μ is the dynamic viscosity (699.2 μPa s for the average D_2O temperature in the fuel, 47 C). For smooth round tubes, the friction factor f_t dependence on Reynolds number is given by

$$1/\sqrt{f_t} = 4\log_{10}(Re\sqrt{f_t}) - 0.4 \qquad (5.2.2)$$

Friction factors f for annuli [3] are larger than for tubes at the same Reynolds number by a factor $1 + 0.0925 r_i/r_o$ where r_i and r_o are the inner and outer radii of the annulus. Using radii from Table 2-1, an average value of this factor for the annuli of the fuel element is found to be 1.085.

For conditions of interest, the above may be approximated by

$$f = 0.085\,Re^{-0.25} \qquad (5.2.3)$$

Pressure loss characteristics for other components of the fuel element presented below are based on an examination of experimental pressure loss data for light water flow in simulated DIDO-type fuel elements [4] [5] [6] [7] [8] [9] together with an expectation that inlet and exit loss coefficients $\Delta p/\frac{1}{2}\rho u^2$ are constant.

The velocity u in the loss coefficient definition can be the velocity at any arbitrary section of the component considered. Although the coefficient value will depend on the velocity chosen, the predicted pressure loss is independent of this choice. The velocity chosen is often that in the section of pipe upstream of the component being considered. Coefficients given below are based on velocities in a hypothetical 101.6 mm tube, this being chosen as it corresponds to the nominal 4 inch shroud of the fuel element.

Examination of data in terms of loss coefficients has the advantage of simplifying the conversion of pressure loss data, as obtained from water flow, to pressure loss curves for D_2O flow:- the relation between loss coefficient and Reynolds number (again based on a suitably chosen region of pipe-work) applies to all fluids. (Although they are apparently different, the scaling methods of Gleed [4] [5], Gerrand [6], and Tarrant [7] are equivalent to that used here.)

In terms of loss coefficients as defined above, the exit loss coefficient, describing the loss from the end of the fuel section to outside the fuel element, of the Mk 2 and Mk 3 elements (Gerrand [6], Tarrant [7]) is empirically 3.0. This is assumed to also apply to Mk 4 and subsequent fuel elements. As exit losses are a small part (about one-seventh) of the total, errors involved in this assumption are not significant. The assumption does not affect flow rate calculations since, as discussed below, errors in the exit loss coefficient are balanced by corresponding errors in the inlet loss coefficient so that the total pressure loss is correctly simulated. The assumption does affect the estimated local saturation temperatures given below but only negligibly - a 25% error in the exit loss produces a change of only 0.3 K in the estimated saturation temperature at the exit of the fuel tubes.

The pressure loss over the cylindrical fuelled section of the element has been calculated by integrating equation (5.2.1) over the total 660.6 mm length of the tubes (rather than the 603.25 mm of Section 2.2, this being the length of the fuel within the tubes). The calculation assumes developed flow, so may slightly underestimate the pressure gradient in the first 10 cm or so of the tubes.

The loss coefficient for the inlet region was obtained by subtracting loss coefficients for the fuel and exit regions from coefficients determined from experimental total pressure loss data for simulated Mk 4/5a fuel elements. The experimental data cover a range of water flow rates at 40 C, 50 C and 60 C with 1% measured bypass flow through the central thimble [9], and a range of water flow rates at 50 C [5]. For the latter data, a "standard" bypass flow of 6% was assumed for the present data analysis.

These data collectively suggested an inlet loss coefficient, as defined above, of 9.3. This includes a small contribution from losses at the inlet of the fuel tubes not included in the analysis of the fuelled section pressure loss.

The above pressure loss prediction method agrees closely with water flow pressure loss data from simulated Mk IV/5a HIFAR fuel elements [5] [9]. Predictions for D_2O flow at 47 C - this being the average temperature in the fuel tubes - are shown in Figure 5-1. With regard to this figure it is to be noted that, for a given flow rate, the fuel region losses but not the inlet or exit losses will vary with temperature. Temperature effects are caused by the variation of viscosity with temperature. Since inlet and exit loss coefficients are independent of Reynolds number they are independent of viscosity and hence of temperature.

Calculated D_2O pressure losses for the nominal fuel element flow rate of 16 kg s^{-1} at 47 C are summarised in Table 5-1. For different flow rates, the inlet and exit losses vary as $(\text{flowrate})^2$, and the fuel section loss varies with $(\text{flowrate})^{1.75}$. (The exponent is actually 2-n where n is the Reynolds number exponent in the $C = aRe^{-n}$ relationship between loss coefficient C and Reynolds number Re.)

Allowing also for a 1.5 kPa gauge helium pressure at the D_2O surface in the RAT, and hydrostatic heads ρgh (the end of a fuel tube is 755 mm below the D_2O surface, and the inlet is 660.6 mm below this), inlet and exit pressures from fuel tubes for 16 kg s^{-1} and 6% bypass flow are 137.7 kPa and 116.3 kPa. Corresponding saturation temperatures [1] are 110.2 C and 105.2 C. Local fuel tube pressures and temperatures may be obtained by linearly interpolating between inlet and exit values.

Table 5-1
HIFAR Fuel Element Pressure Losses (kPa) at 16 kg s^{-1}.

Bypass	Inlet	Fuel	Exit	Total
0%	16.49	16.65	5.33	38.47
1%	16.49	16.36	5.33	38.18
6%	16.49	14.93	5.33	36.75

5.3. Flow Distribution Within Fuel Elements.

Local temperatures of a HIFAR fuel tube surface depend on the average coolant temperature in the annulus adjacent to the surface, and on the ability of the coolant to remove heat from the surface - the ability to remove heat increases with flow velocity. The average local coolant temperature at a given axial location in an annulus depends on the coolant inlet temperature, on the heat transferred to this coolant by the upstream region of adjacent fuel tubes, and on the coolant mass flow rate in the tube (cf equation 5.1.1).

Thus, there are two direct effects of flow rates in each annulus on fuel surface temperatures. It is therefore important to know how the total flow in fuel elements is distributed between the annuli of the fuelled section of fuel elements.

The flow in each annulus is set by the requirement that, for practical purposes, the pressures at the inlet and exit of the five fuel element annuli are equal, so pressure losses of the five annuli are also equal. Non-equal pressure losses could only be caused by unrealistically large cross-flows before and/or after the fuel tubes which would produce radial pressure gradients consistent with the different axial pressure losses.

The method of calculating the pressure losses for each annulus as a function of flow rate is described in Section 5.2 above. Using average values for viscosity for each annulus (but allowing for differences in average coolant temperatures for different annuli, as obtained in Section 5.4 below, in obtaining these viscosities), and allowing for different hydraulic diameters (obtained from dimensions in Table 2-1) of the annuli, the flow parameters summarised in Table 5-2 were obtained. Mass fluxes refer to a fuel element flow of 16 kg s^{-1} and 6% bypass flow; values for this condition may be simply scaled for other circumstances.

Table 5-2
Flow Distribution in Standard Fuel Element.

Annulus	Flow kg s^{-1}	% of total annuli flow	Mass flux kg $m^{-2}s^{-1}$
1 (inner)	2.273	15.1	3708
2	2.673	17.7	3737
3	3.054	20.3	3767
4	3.441	22.9	3734
5 (outer)	3.604	24.0	3614

A simpler but approximate approach to the flow distribution within fuel elements is obtained by noting that, to a first approximation, the friction factors and hydraulic diameters for the five annuli are the same. This arises from the closeness of the annulus gaps (see Table 2-1) and the small effect on friction factor of different tube radii and of the different coolant properties resulting from temperature differences. Thus, from equation 5.2.1 and the requirement of equal pressure

losses for the coolant annuli, equal mass fluxes (total flow in annuli)/(total flow area of annuli) = 3701 kg m^{-2} s^{-1} are predicted for all five annuli. Percent of total annuli flow is then simply the percent area of total annuli area. As can be seen, this simply-obtained approximate result is reasonably close to the more exact calculations of the table.

Unfortunately, the predictions of Table 5-2 are not confirmed by available experimental flow distribution data obtained from six different isothermal water flow simulations in DIDO-class fuel elements [4] [5]. Experimental flow rates for the different annuli differed by up to 25% from predictions given in Table 5-2. Moreover, experimental distributions from nominally identical, or very similar, flow geometries were incompatible with each other.

The above inconsistencies of data with each other and with the above predictions can be explained, at least in part, by noting that fuel elements are constructed with allowable tolerances on the annular gaps. Gap dimensions were apparently not measured for the experiments discussed by Gleed [4] [5], and may have differed from the nominal dimensions, for which the above predictions are given. If the prediction method is valid, gap sizes may be inferred by choosing them to produce consistency between prediction and experiment. Gap sizes so inferred are nearly all within permitted tolerances, particularly if stated experimental errors are allowed for.

Experimental flow distributions were also obtained by Green [10] with air flow in two different twice full size simulations of a HIFAR fuel element. Annulus gap dimensions were also measured in these experiments. Predicted annulus flow rates, using measured gap sizes in the calculations, agreed with measured values well within stated experimental errors. Of four different flow distributions (i.e. twenty flow rate values) the discrepancy between predicted and experimental flow rates was always less than 6%, and less than 3% in more than half the cases. This result validates the prediction method described above.

It may be concluded that the predicted annuli flow rates, mass fluxes, and flow fractions of Table 5-2 are valid for fuel elements with annulus gap dimensions coinciding with the nominal dimensions obtained from Table 5-2. Actual values of these parameters may vary because of the permitted tolerances in the annulus gap sizes; we discuss this in more detail later.

5.4. Temperature Distributions Within the Fuel Region.

As noted, limitations on HIFAR power are determined by phenomena that occur following the onset of boiling. As the onset of boiling on a heated fuel tube surface is determined in part by the extent to which the surface temperature is above the saturation temperature, it is important to be able to calculate fuel surface temperatures. This is not straight forward, and requires simultaneous calculation of coolant temperatures and the fraction of power of each fuel tube removed by the coolant flow on each surface. This complicating feature (i.e. the partitioning of power from each fuel tube) appears to have been ignored in previous thermal-hydraulic studies of HIFAR. These have instead assumed, incorrectly, that the power removed from the concave and convex surface of each fuel tube is equal.

The method of calculating temperatures is discussed below.

5.4.1. Coolant temperature distributions.

At each axial location, the bulk coolant temperature of each annulus flow channel depends on the total power added upstream from adjacent fuel surfaces; the coolant flow rate in that annulus (Section 5.3); and the inlet coolant temperature (nominally 44 C). The equation relating these is equation 5.1.1 but with parameters being replaced by local equivalents.

As noted, the power from a fuel tube surface to the coolant in an adjacent annulus is generally not 50% of the power from that tube.

5.4.2. Fuel surface temperature distributions.

The fuel tube surface temperature T_w at any location is related by a heat transfer coefficient h to the heat flux Φ (W m^{-2}) from the surface (i.e. local values of power from that surface per unit area, generally not the same on both tube surfaces) and the local bulk temperature T_c of the coolant adjacent to the surface:-

$$\Phi = h(T_w - T_c).$$

In the example discussed below, axial conduction along the fuel tube has been neglected. This leads to calculated peak temperatures which are conservative (i.e. pessimistically high) since axial conduction will tend to smooth out peaks and troughs in temperature profiles. However, axial heat fluxes in HIFAR are small compared to heat fluxes from the fuel tube surfaces, so the assumption is reasonable.

The heat transfer coefficient is given in dimensionless form by the Nusselt number Nu (defined as hD/k), where D is the equivalent hydraulic diameter (twice the gap for annuli) and k is the coolant thermal conductivity. The Nusselt number varies with Reynolds number Re, Prandtl number Pr, and, in the case of annuli, the ratio of radii of the inner and outer surfaces, the particular surface, and the heat flux on the other annulus surface [3]. (The simple extension of round tube equations to annuli via the hydraulic diameter concept, as used in Section 5.2, is not as valid for heat transfer calculations as for pressure loss calculations.)

Bhatti and Shah [3], present tabulated Nusselt number data for single-sided heated annuli and calculation methods to allow for heat flux on the opposite surface. These data were interpolated to provide Nusselt number data for a nominally dimensioned HIFAR fuel element (Table 2-2) with nominal flow rates (16 kg s^{-1}). The dependence on heat flux from the opposite surface is relatively small and, in the present calculations, Nusselt numbers pertaining to the central doubly-heated fuel channel annuli are those for equal heat fluxes on both surfaces. Nusselt number errors using this assumption are small. For nominal flows in the nominal annuli, this interpolation procedure led to the following dependencies of Nusselt number on local coolant bulk temperature T (C).

Table 5-3
Nusselt Numbers For Heated Fuel Surfaces at Nominal HIFAR Conditions.

Tube	Nu (Concave surface)	Nu (Convex surface)
1	206.5 + 1.13(T-50)	233.1 + 1.27(T-50)
2	225.3 + 1.22(T-50)	236.4 + 1.26(T-50)
3	226.5 + 1.21(T-50)	235.0 + 1.24(T-50)
4	224.4 + 1.19(T-50)	200.1 + 1.06(T-50)

It can be seen that, except for tube 4, Nusselt numbers (and hence heat transfer coefficients) are smaller on the concave surfaces, and also, because they apply to the heated surface of single-side heated annuli, on the two extreme surfaces of the four fuel tubes.

For flow conditions other than the nominal conditions, the tabulated Nu data given by Bhatti and Shah indicate that, in the vicinity of the nominal HIFAR conditions, $Nu \propto Re^{0.8} Pr^{0.4}$. This dependence is as for tube flow, and may be used to scale Nusselt number values obtained from Table 5-3 to give values for non-nominal gap size, flow rate, etc.

5.4.3. Partitioning of energy from fuel tubes.

As a result of the high thermal conductivity of aluminium, temperatures on the inner and outer surfaces of heated fuel tubes must be very similar. As a consequence, the calculated fraction of power from each surface at any axial location may be estimated by requiring that the surface temperatures, calculated as described above, are equal for the concave and convex surfaces of a fuel tube.

In the example given below, the energy partitioning is described in terms of a "power ratio parameter" β, defined such that $(1+\beta)/2$ of the power from a fuel tube is emitted from the concave surface of the tube (and hence $(1-\beta)/2$ is emitted from the convex surface).

5.4.4. Calculated temperature profiles for an 800 kW fuel element.

Temperature profiles have been calculated using the above method for an 800 kW fuel element with an axial power density distribution as shown in Figure 5-2 and with radial power distribution described in Table 2-7, and with an inlet coolant temperature of 45 C.

This particular case was considered as the fuel element power, 800 kW, is typically that of a new fuel element. The higher temperatures encountered for the higher than average power will be closer to temperatures which limit operation.

The coolant temperature increase in each channel, axial surface and coolant temperature profiles, and axial power ratio parameter profiles for each fuel tube are shown in Figures 5-3 to 5-5 respectively.

Examination of the behaviour of the power ratio parameter β (Figure 5-5) is instructive. It is negative for most of the fuel region. From its definition given in 5.4.3, this implies larger heat fluxes on the outer (convex) surfaces of the fuel tubes for most of the fuelled region. This follows from heat transfer coefficients mostly being larger on this surface, hence larger heat fluxes are required for this surface to produce a given surface-to-bulk liquid temperature difference. As a result, more power is given to the outer coolant annulus and less to the inner annulus than would be so for equipartition of energy from each fuel tube. (The total power to each of the central annuli is similar to that for equipartition of energy from each tube since a heat flux change, cf β=1, from one side of each of these annuli is compensated for by a corresponding opposite change on the other.)

The axial variations of β for each tube depends on bulk coolant temperatures on either side of each tube. Since the bulk coolant temperatures of the three central annuli are very similar at each axial location (Figure 5-3), the wall- coolant temperature difference on the two sides of each of the central two fuel tubes is the same at each axial position, leading to little axial variation of β for these tubes (Figure 5-5).

However, the coolant temperature difference on each side of the inner and outer fuel tubes increases with axial distance (Figure 5-3), as it must since the innermost and outermost coolant annuli are heated from one side only. The resulting divergence of wall-coolant temperature difference with axial distance on each side of the innermost and outermost fuel tubes requires an increasing fraction of power directed to the cooler annuli to maintain, within the constraints set by heat transfer coefficient values, equal temperatures on each side of the fuel tubes. This explains the axial variation of β for the innermost and outermost fuel tubes shown in Figure 5-5. The net effect is for coolant temperatures in the extreme annuli (1 & 5) to be closer to those in the other annuli (Figure 5-3) than would be the case with equipartition of energy from each fuel tube. The effect is enhanced with increasing power.

5.4.5. Effects of manufacturing tolerances.

The permitted manufacturing tolerances in annulus gap sizes lead to variations in flow parameters; these variations tend to be self compensating in their net effect on fuel surface temperatures

and hence on safety margins. Thus, for example, a fuel element with one fuel tube located at the extreme point allowed by its tolerance limit with the others placed at their nominal locations will produce a widened coolant annulus and a correspondingly narrowed one. For the widened annulus this would result in increases of about 22% and 9% in mass flow and mass flux, with corresponding reductions for the narrowed annulus. These changes then cause an increase of about 17% in heat transfer coefficient for the fuel tube surface facing the widened annulus and a corresponding decrease for the other surface of that fuel tube.

In order to ensure near-identical temperatures on each side of the fuel tube, as dictated by the high thermal conductivities of fuel alloy and cladding, the partitioning of heat transferred from the two sides of the tube must change from the nominal values in such a way that about 17% more must be directed to the widened annulus and about 17% less to the narrowed annulus. Compared with nominal conditions, the coolant temperature rise in the narrowed annulus would thus increase by 5% (= 22%-17%), i.e. about half a degree at the hottest part of the fuel tube. Again there would be a corresponding reduction in coolant temperature rise in the widened annulus.

Actual heat transfer partitioning would accommodate the lower-than-nominal and higher-than-nominal coolant temperature rises on each side of the fuel tube in such a fashion that the fuel surface temperatures would change by a considerably smaller amount.

Thus, within uncertainties in calculation methods, fuel temperatures as calculated above for nominally dimensioned fuel elements can also be regarded as applying to elements constructed within tolerance limits.

5.4.6. Adaptation of calculated temperatures to other conditions.

To a first approximation, the difference between bulk coolant temperatures and inlet coolant temperatures (Figure 5-3), and between wall temperatures and inlet coolant temperatures (Figure 5-4), will not change with different inlet coolant temperatures. As a result, the calculated coolant and wall temperatures for an inlet temperature of 45 C (Figure 5-4) can be simply adapted to other inlet coolant temperatures by shifting temperatures by the amount by which the inlet temperature differs from 45 C. This approach assumes coolant physical properties are those corresponding to an inlet temperature of 45 C.

To a less good (but still reasonable) approximation, temperature differences can be scaled according to power levels to modify the calculated temperatures in Figures 5-3 and 5-4 to yield temperatures for different power levels and/or axial power distributions. As well as assuming physical properties are those of the above example, this approach assumes that the β distributions of Figure 5-5 are unaltered. For reasons given above, this is not so.

In the case of different coolant flow rates, coolant temperature T_c rises vary inversely with coolant flow rate (equation 5.1.1 adapted to each annulus). As a result of the $Re^{0.8}$ dependence of heat transfer coefficients (Section 5.4.2), coolant-to-wall temperature differences vary approximately as $T_w - T_c \propto (\text{flowrate})^{-0.8}$ and may be scaled accordingly. Again, this assumes physical properties and β profiles are as for the example calculation.

5.5. Some Considerations on Safety Margins.

As indicated, thermal hydraulic phenomena which limit HIFAR power are those which occur in boiling flow: critical heat flux, Ledinegg or excursive flow instability, and hydraulic or dynamic flow instability. These phenomena have been examined previously as limiting conditions for HIFAR, and it has been shown that, of them, Ledinegg instability will appear first. This is because the vapour content required to alter hydraulic characteristics sufficiently to induce a Ledinegg-type flow excursion is smaller than those associated with dynamic instability or critical heat flux. Ledinegg instability thus sets the boundary conditions of HIFAR operation.

In connection with Ledinegg instability, it has been shown by Romberg [11] that, for normal HIFAR flow rates, the instability is initiated at the onset of net vapour generation during subcooled boiling. Thus, for practical purposes, a sufficient criterion for safety is the absence of boiling, subcooled or otherwise. (There are conditions, particularly at lower than normal flow rates, where the onset of net vapour generation does not trigger a boiling crisis or an instability. Thus, a blanket avoidance of net vapour generation is a conservative safety criterion.)

In view of the above, and the closeness of new fuel element surface temperatures to the saturation temperature (see Figure 5-4), it needs to be pointed out that boiling cannot occur on a heated surface purely as a result of the surface reaching saturation temperature. The boiling process requires some wall superheat for the bubble nucleation mechanism to be sustained. Moreover, the onset of subcooled boiling involves bubbles which do not depart from the wall. Higher power is required for net vapour generation, i.e. departure of bubbles from the wall. Atmospheric water data for flow in annuli obtained by McAdams et al [12] suggest that the superheat for this net vapour generation is about 35 K at the heat flux where subcooled boiling would occur in HIFAR for a coolant flow rate of 16 kg s^{-1}. Thus, conditions for the data of Figure 5-4 are considerably further from boiling, particularly in the form of net vapour generation, than the closeness of the fuel surface temperatures to saturation would suggest.

Conditions at which Ledinegg instability would occur in HIFAR have been examined extensively by Romberg [13]. However, Romberg's analysis [11] has several features which cause predicted instability powers to be conservative, i.e. the actual powers may be somewhat higher than predictions of the analysis. These features follow from an assumption that the heat flux is the same on both sides of a fuel tube. In terms of the power partition parameter β defined in Section 5.4.3, this amounts to an assumption β=1, instead of its actual values (see e.g. Figure 5-5), for all fuel tubes. The conservative consequences of this assumption are discussed below.

Firstly, Romberg's analysis considers instability onset in the most vulnerable channel. This was assumed to be the annulus with the highest power input, hence highest heat fluxes and largest coolant temperature rise. However, as discussed in Section 5.4.4, actual partitioning of energy release from each fuel tube leads to a reduction of power to the highest rated channel. Ledinegg instability will thus occur at higher overall channel powers than predicted for β=1.

Secondly, the assumption that a single channel can become unstable implies a Ledinegg-induced dry annulus adjacent to unaffected annuli. This further implies high temperatures on one side only of the fuel tubes bounding the unstable annulus. As discussed, this cannot occur because of the high conductivity of aluminium. (If a Ledinegg excursion of this type somehow did occur, the implied high temperature gradients in affected fuel tubes would ensure that the power input in these tubes would be released from the wetted surfaces only, allowing the Ledinegg-induced dried surfaces to rewet.)

Moreover, the onset of net vapour generation on a single fuel tube occurs at higher powers than would be the case if the fraction of fuel tube power released from each surface were fixed. In the latter case, onset of net vapour generation would first occur on one surface of the fuel tube, implying that the boiling surface would be hotter. In an actual fuel tube operating at the same power, this would be avoided by adjustments to the fractions of power released from each surface so that equal surface temperatures would result. Net vapour generation would be initiated on both surfaces simultaneously at a slightly higher power.

The above arguments can be extended to demonstrate that any tendency towards Ledinegg-induced single channel voiding of the type predicted by Romberg will be countered by redistribution of energy transport in the fuel element until a power level is reached at which the total fuel element undergoes Ledinegg instability. This of course will be at a higher power level than predicted power for single annulus instability with unaffected β values.

The result that Ledinegg instability will occur for the whole fuel element (rather than for a single annulus at a lower power) has a further stability-enhancing consequence. A boundary condition for single annulus instability is that the pressure drop over the annulus is approximately constant. On the other hand, the corresponding condition for total element instability is that the pressure drop over the total fuel element remains approximately constant. The total pressure drop is approximately the sum of the pressure drops over a single annulus plus, in single phase flow, a nearly equal pressure drop over the inlet region of the fuel element (see Table 5-1). The upstream region remains in single phase conditions throughout any instability. As discussed by Hsu and Graham [14], the addition of a single phase upstream pressure loss has a stabilising effect for both Ledinegg and dynamic flow instabilities.

It may be noted that, in a similar manner, the high thermal conductivity of the fuelled region of the fuel element will also cause critical heat flux (CHF) and dynamic flow instability predictions to be conservative if these are also based on the assumption that β=1 throughout the fuel element. In both cases, the maximum rated annulus will be less highly rated as a result of actual β values. Furthermore, any incipient approach to CHF will have a consequent redistribution of power such that CHF may only occur, at a higher power, simultaneously on both surfaces of a fuel tube. Moreover, the localised dry patches induced by low vapour content CHF (e.g. during subcooled boiling) cannot reach high temperatures normally associated with these boiling crises since the highly conducting aluminium permits heat flow along the aluminium away from the hot spot.

A full examination of boundary conditions for HIFAR safety, allowing for variations in the parameter β, would be complex. However, avoidance of boiling is a sufficient condition for safety since, as indicated, limiting phenomena are those occurring after the onset of boiling. Moreover, as discussed, the redistribution of β following the onset of boiling causes boiling onset to be further from any of the limiting phenomena than would be so with the assumption β=1 used for establishing the current thermal hydraulic limits for HIFAR operation.

5.6. Comments - Conclusions.

Although the fission process produces both neutrons and energy the energy component is often overlooked with research reactors which are, after all, designed to be sources of neutrons not energy. Nevertheless, the production of energy within the reactor is inevitable and the ability to remove it in the form of heat is of fundamental importance since, irrespective of the purposes to which the reactor is put, its safety depends on the application of sound thermal hydraulic principles.

This chapter has presented has presented an overview of HIFAR thermal hydraulics in the framework of reactor safety under normal operating conditions. As with similar research reactors this implies the avoidance of boiling in the form of net vapour generation since the onset of this could induce a Ledinegg instability and hence inadequate ability to remove heat from the affected fuel element. Safe heat removal by the emergency core cooling system and heat transfer aspects of abnormal reactor operation are discussed in the following two chapters.

Thus, aspects of HIFAR relevant to safe normal operation have been presented here. These are all ultimately connected with the margin to boiling onset, and include coolant temperature rises (overall; from individual fuel elements; and along individual coolant channels), pressure profiles along fuel elements, flow distributions between and within fuel elements, and temperature distributions within fuel elements. Wherever possible calculational procedures have been confirmed by comparison of predictions with experimental data.

The approach taken here includes some refinements not considered in previous assessments of HIFAR thermal hydraulics. These are the the use of heat transfer coefficient prediction methods appropriate to annular coolant channels (which methods allow for the effect of heat transferred

from an opposing surface), a means of predicting the partition of energy energy transfer from a fuel tube to its two surfaces (previously assumed to be a 50-50 split), and the evaluation of the effects of manufacturing tolerances on thermal hydraulic parameters.

These refinements do not invalidate previous assessments of HIFAR safety margins. Rather, they have demonstrated that the several effects of dimension variations within tolerance limits are almost totally self-compensating in their net effect on safety margins, and that effects neglected in previous analyses are safety-enhancing, implying that safety margins currently in use are more conservative than previously thought.

5.7. References.

(1) Hill, P.G., MacMillan, R.G. and Lee, V [1981] - Tables of thermodynamic properties of heavy water in S.I. units. Report AECL 7531.

(2) Carlson, R.W.S and Ido, A.A. [1969] - Measurements of heavy water flow rates throughout the core of HIFAR. AAEC Internal Report HIFAR/TN-036

(3) Bhatti, M.S. and Shah, R.K. [1987] - Turbulent and transition flow convective heat transfer in ducts. Chapter 4, Handbook of single-phase convective heat transfer, eds Kakac, S., Shah, R.K. and Aung, W. John Wiley.

(4) Gleed, D.B. [1971] - Head loss and flow distribution characteristics of MTR/Mk4 fuel elements fitted with Mk4, Mk3 and DBF4 guide noses. Report AAEC/TM 590

(5) Gleed, D.B. [1973] - Flow distribution, head loss and endurance characteristics of the MTR Mk4/5a fuel element. Report AAEC/TM 636

(6) Gerrand, R.P. [1959] - Flow and pressure drop characteristics of HIFAR mark II and mark III fuel elements. Report AAEC/X4

(7) Tarrant, E.A. [1963] - Hydraulic performance of DIDO D_2O circuit. Unpublished report DIDO/IS 30

(8) Griffin, J.R., Turk, W.R. and Powers, L.R. [1960] - Report on hydraulic tests carried out for Mk. III DIDO/PLUTO fuel element development. Report AEEW - R6

(9) Chapman, A.G. and Hargreaves, N.D. [1986] - Out-of-pile burnout experiments in a full-scale simulation of an irradiation rig in a HIFAR hollow fuel element facility. Report AAEC/E632

(10) Green, W.J. [1975] - Effect of flux scan assembly on coolant flow distributions in model HIFAR fuel elements. AAEC Internal Report ER/TN 387

(11) Romberg, T.M. [1972] - Analysis of excursive flow instabilities in multi-annular fuel elements. Ansto internal report ER/TN-243

(12) McAdams, W.H, Kennel, W.E., Minden, C.S., Carl, R., Picornell, P.M. and Dew, J.W. [1949] - Heat transfer at high rates to water with surface boiling. I&EC Vol. 41, No. 9, pp 1945-1953.

(13) Romberg, T.M. [1972] - Appendix 11.2, HIFAR Safety Document. AAEC

(14) Hsu, Y-Y. and Graham, R.W. [1968] - Transport processes in boiling and two-phase systems. American Nuclear Society

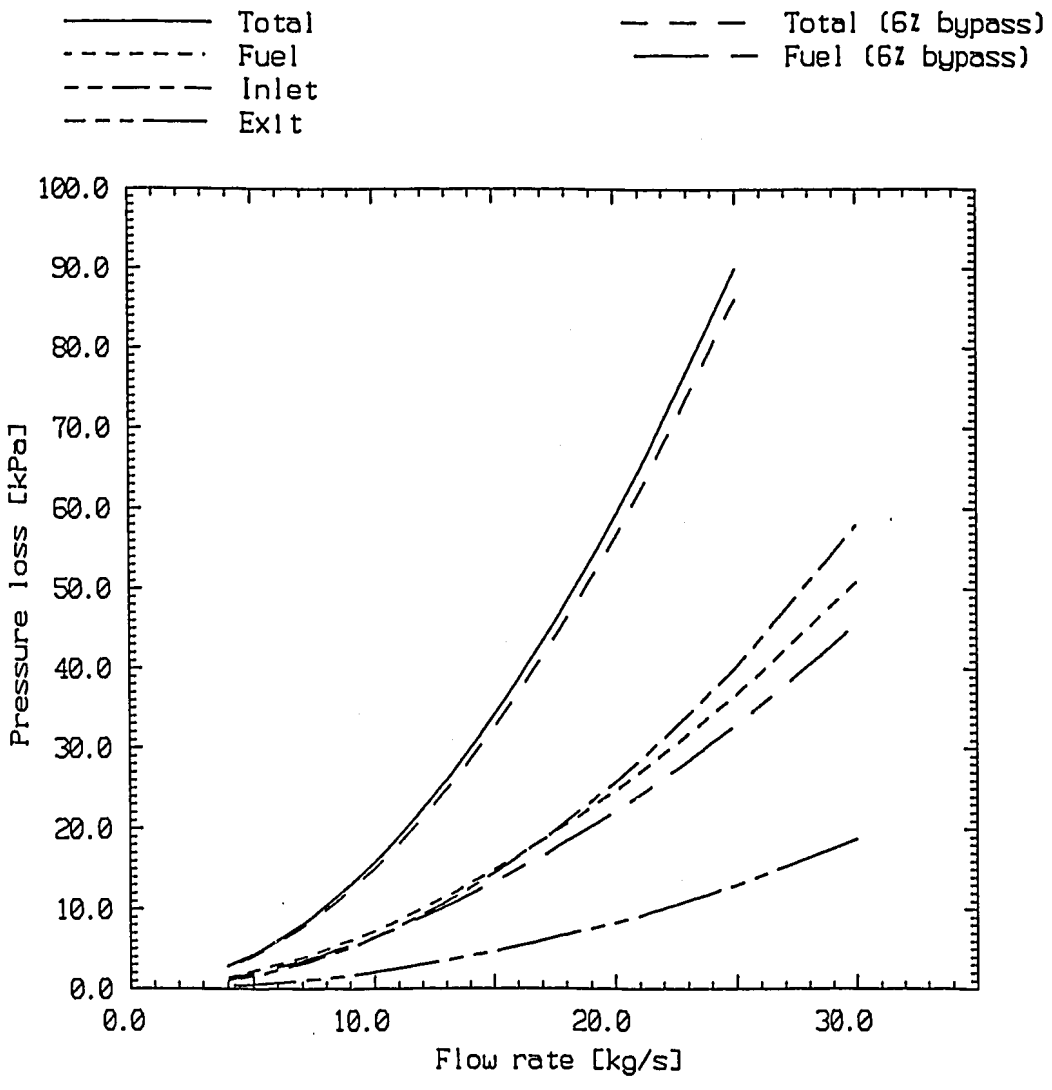

Figure 5-1 Pressure loss along HIFAR fuel elements.

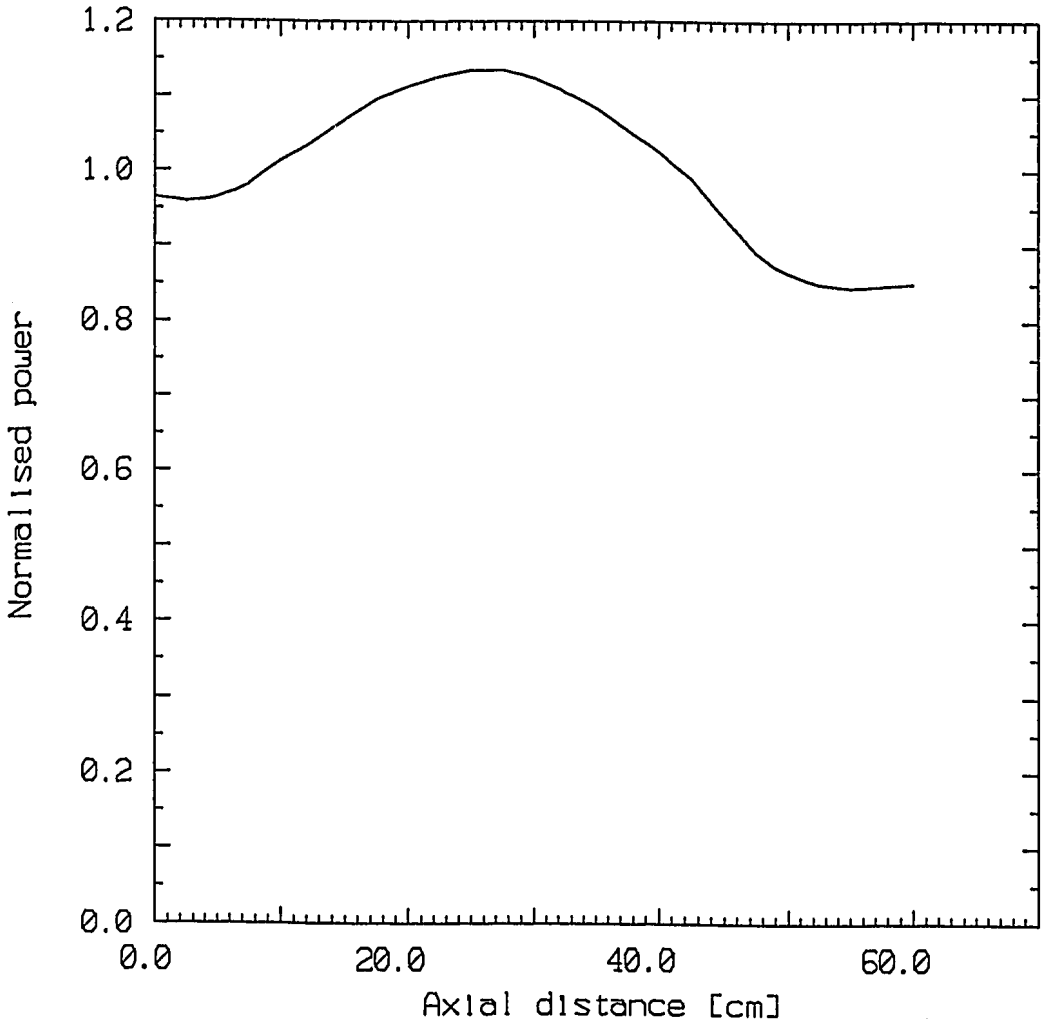

Figure 5-2 Assumed axial power distribution along HIFAR elements.

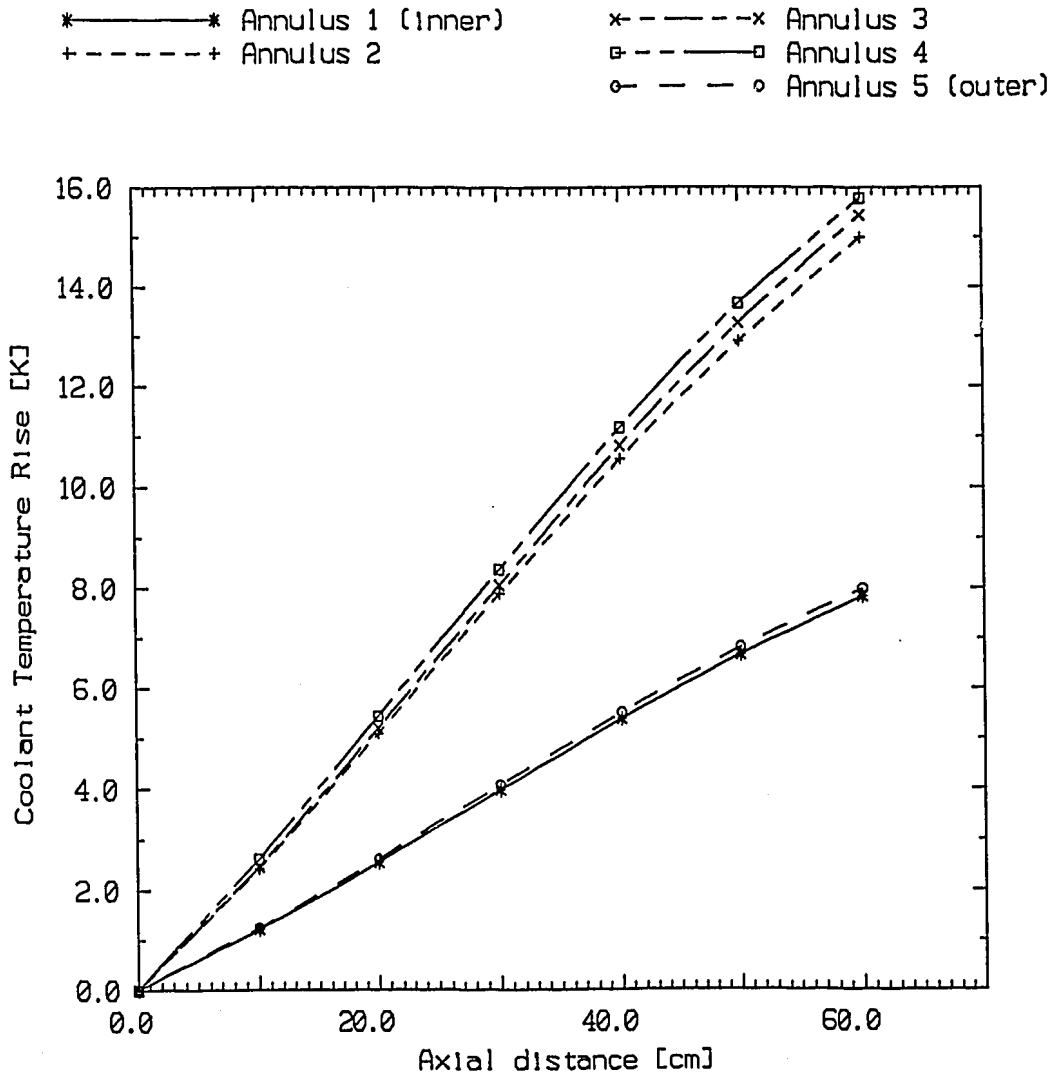

Figure 5-3 Coolant temperature increase along channels for an 800 kW element.

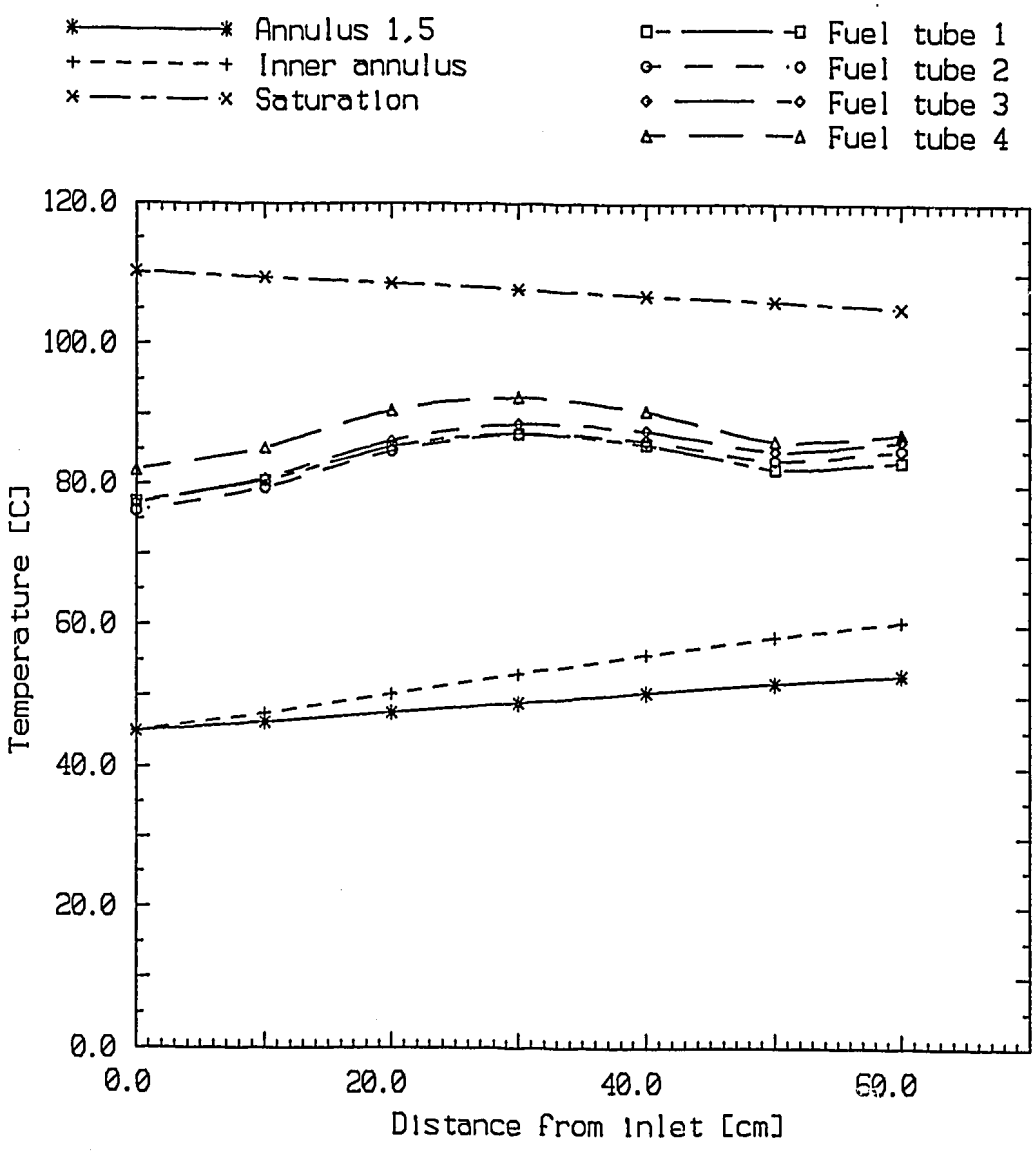

Figure 5-4 Axial surface and coolant temperature profiles for an 800 kW element.

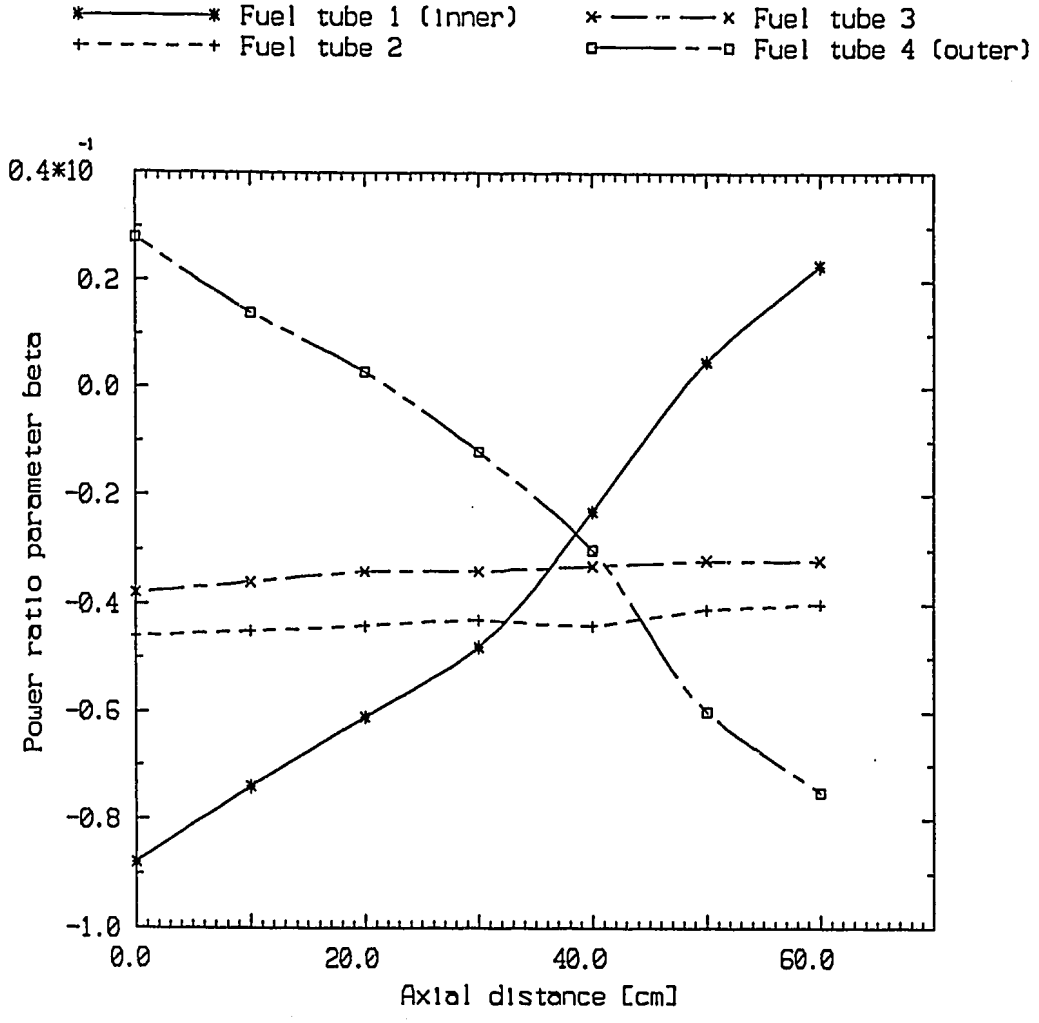

Figure 5-5 Axial power ratio parameter profiles for an 800 kW element.

SECTION 6

THE EMERGENCY CORE COOLING SYSTEM.

Graceful coolness in the heat,
Solace in the midst of woe,

Edward Caswell. - in Hymns Ancient and Modern.

6. THE EMERGENCY CORE COOLING SYSTEM.

The annular geometry of the HIFAR fuel elements results in almost complete loss of heat transport paths should the coolant drain from the flow annuli. Since this would produce a very large loss in reactivity, rendering the core highly sub-critical, the concern is with removal of fission product decay heat.

Loss of coolant from the fuel elements can only be occasioned by a leak developing in components of the primary coolant circuit that lie between the pump side of the non return valve and the inlet plenum; the ECCS is designed to provide heat removal capability under these and other circumstances.

The concept and development of the ECCS has been described in detail elsewhere [1] [2]. Briefly it relies on maintaining a sufficient head of water in the RAT to allow jets to pass through holes in the fuel element shrouds and, by being intercepted by the top edges of the fuel tubes, to form cooling films falling down the outer tube surfaces. The water head is maintained by the action of scavenge pumps which return water from the plant room sump to the RAT via two helium balance lines. The equilibrium water head is determined by the component flows in the system which are now discussed.

6.1. Total Flow into the Fuel Elements.

ECCS flow into the elements is provided through

(1) eight equally spaced 0.9 cm diameter holes whose centre is 0.15 cm above the tops of fuel tubes 2 and 3, and

(2) eight equally spaced 0.4 cm diameter holes whose centre is 2.2 cm below that of the 0.9 cm diameter holes.

If the water head is great enough, flow may also enter through the normal coolant flow diffuser outlet holes. The centre of the lowest of these sixty 1.9 cm diameter holes is 5.4 cm above the centre of the 0.9 cm holes; although these diffuser holes do not form part of the ECCS they may have some influence on its operation as will be discussed later. For convenience, all heights will be taken with the centre of the 0.9 cm holes as origin. The geometry is shown in Figure 6-1.

Flow rate is assumed to be determined by efflux through the 0.9 cm and 0.4 cm holes; thus

$$Q_9 = \mu_9 A_9 [2gh_9]^{\frac{1}{2}} \qquad Q_4 = \mu_4 A_4 [2g(h_9 + 2.2)]^{\frac{1}{2}}$$

where A denotes the cross sectional area of a hole, h_9 and h_4 denote water heights above the centres of the 0.9 cm and 0.4 cm diameter holes, and the flow coefficients μ_9 and μ_4 have been determined experimentally [1] as 0.7 and 0.9 respectively. For the complete core of twenty-five elements we have, evaluating the constants

$$Q_9 = 3918[h_9]^{\frac{1}{2}} \quad cm^3s^{-1} \qquad Q_4 = 864[h_9 + 2.2]^{\frac{1}{2}} \quad cm^3s^{-1}$$

6.2. Total Flow into the Downcomers.

Flow into the downcomers will be characterised by weir flow over the perimeter and efflux flow through weld imperfections in the downcomer extensions. The first of these presents a difficult problem at low water heads where surface tension forces are significant and the flow very dependent on the nature of the stream lines approaching the weir head. We initially adopt the standard weir flow equation

$$Q_w = C_w \frac{2}{3} U(2g)^{\frac{1}{2}} h^{1.5}$$

where U is the perimeter length of the down comer and h (= h_9 - 2.8) is the height of water above the downcomer lip. The value of C_w has been determined experimentally [1] as a function of h, being zero when h = 0.38 cm and constant for h > 1.0 cm. This data can be well fitted to the above equation if h is replaced by h+0.11 so that we obtain, for the total weir flow into the four downcomers,

$$Q_{dc} = 8900C_w[h_9 - 2.69]^{1.5} \quad cm^3s^{-1}$$

Flow through the weld imperfections will depend upon the location and sizes of these. Examination showed three downcomers with holes, one of which accounted for half of the total imperfection cross sectional area, which was estimated to be 5.25 cm^2 and approximately 5.7 cm below the downcomer extension lips. Assuming an efflux flow coefficient of 0.8 we then obtain for the weld defect flow

$$Q_{wd} = 186[h_9 + 2.9]^{\frac{1}{2}} \quad cm^3s^{-1}$$

6.3. Extraneous Flows.

The only other way of losing water from an intact RAT is by leakage past the fuel element seats. Measurements indicate that this is about 30 cm^3s^{-1} at a water head of 1.7 m and it would thus be about 15 cm^3s^{-1} for the head under LOCA conditions. It is to be noted that *one* measurement yielded a leak rate of 300 cm^3s^{-1}; it appears to us more sensible to treat this as an aberration which could be borne in mind when assigning uncertainties to the flow rate.

6.4. Water Head in Equilibrium.

If extraneous flow is neglected the total flow rate in the ECCS is thus

$$Q_{tot} = Q_9 + Q_4 + Q_{dc} + Q_{wd}$$

$$Q_{tot} = 3918[h_9]^{\frac{1}{2}} + 864[h_9 + 2.2]^{\frac{1}{2}} + 8900[h_9 - 2.69]^{1.5} + 186[h_9 + 2.9]^{\frac{1}{2}}$$

A plot of Q_{tot} against h_9 is shown in Figure 6-2. The intersection of this curve with the flow rate delivered by one or two ECCS scavenge pumps determines the equilibrium water heads in the RAT under these conditions; they are h_9 equal to 3.4 cm and 4.6 cm respectively. The latter value states that the lower rim of the diffuser holes will be reached and coolant will run down the inner shroud wall. Quantification of this flow is difficult because it is not a constant level weir flow. However the water level just reaches the lowest point of a diffuser hole at 4.45 cm and the value of Q_{tot} there is 22.84 litres per second. The two pumps are delivering 24 litres per second so that a total diffuser hole flow of 1.16 litres per second could be expected.

6.5. Partition of Jet Flow between Channels.

An important requirement of the system is that an adequate supply of coolant should reach all fuel tubes. The flow rate into the channels has been measured [1] as a function of water head but because of the importance of this aspect of ECCS operation we develop a simple theoretical description by considering the fuel tubes to have zero thickness and be located radially at their midpoint. We further assume that they may be represented as parallel plane plates. Then, referring to Figure 6-3 we define

x_i = horizontal position of centre of i-th tube measured from inner wall of shroud,
c_i = vertical distance from centre of jet inlet to top of i-th tube,
y_i = decrease in height of jet centre at x_i due to gravity = $x_i^2/2h_9$,
r = radius of inlet hole,
$a_i = c_i - y_i$,
θ_i = angle defining tube chord length across jet = $\cos^{-1}(a_i/r)$
A_i = area of jet intercepted by tube = $\theta_i r^2 - a_i r \sin(\theta_i)$,
Q_9 = total inlet flow from the eight 0.9 cm holes
$Q_9 = 8\mu_9\pi\, r^2\sqrt{2gh_9} = 158\sqrt{h_9}$.

From these definitions and counting tubes and channels radially outwards we can show that the flow of coolant to the i-th channel is

$$Q_i = \frac{158}{\pi} h_9^{\frac{1}{2}}[\theta_{i-1} - \tfrac{1}{2}\sin(2\theta_{i-1}) - \theta_i + \tfrac{1}{2}\sin(2\theta_i)]$$

if we further define $\theta_0 = \pi$ and $\theta_5 = 0$

For channel 5 this formulae has to be modified by adding in the flow component from the 0.4 cm diameter holes.

Inserting the numerical values and performing the calculations gave the results, which were compared with experimental values, shown in Figure 6-4. The agreement is quite good, except for channel five. About half the flow in this channel comes from the 0.4 cm diameter holes and this flow is well defined; the remainder relies on the calculation of the fraction of the jet intercepted by fuel tube four. Calculations support the view that a film is produced on only one side of a tube when the top of a tube intercepts a jet. Increasing the value of c_4 from 0.25 cm to 0.3 cm gave much better agreement with measurement, as shown. If all the c_i are augmented by 0.05 cm the data for channel one are in better agreement with experiment since this channel receives what remains of the flow after diversion into the outer channels. It is apparent that the performance is very sensitive to dimensional tolerances.

The calculations indicate that flow will cease to enter a channel for values of h_9 less than about 2.5, 1.7, 0.7, and 0.1 cm for channels one to four respectively; channel five is provided with the exclusive use of the flow from the 0.4 cm diameter holes. Channels one and two are therefore the first to suffer from any diminution of water head. However, the inner wall of channel two is the outer clad of fuel tube one so that, providing a cooling film is established on this wall, the flow into channel one will not be important. A head of 0.1 cm for channel four is, of course, meaningless since there is no longer efflux flow.

6.5.1. Perturbations to flow pattern.

There are three probable effects that can change the flow partition discussed above. The first is thermal expansion of the fuel tubes. If their temperature rises by 200 K then the tops of the tubes will rise by 0.15 cm. Recalculating the flow partition under these circumstances gave the following results compared with the standard case.

Flow (cm^3s^{-1})	Channel				
	1	2	3	4	5
Flow Q_9 (Standard)	72	43	62	77	60
Flow Q_9 (200 K)	22	34	57	78	123

As already noted, channel one flow is of little importance provided that an adequate supply is maintained into channel two; however the above results indicate that flow into this channel has decreased by 30 per cent so that fuel tube one is at greater risk of drying out.

The second effect is the generation of a strong enough steam flow to lift the incoming coolant jets. This is tantamount to altering the gravitational acceleration so that the path followed by the jet streamline becomes

$$y = \frac{\frac{1}{2} g^* x^2}{g\, h_9}$$

where $g^* = g$ - upward acceleration produced by momentum transfer from steam flow. Since the steam momentum flux is $\rho_s v^2$ where ρ_s is the steam density and v is its velocity, then for g^* to be zero

$$\rho_s v^2 A/m = g$$

where A/m = the surface area of jet per unit mass exposed to steam flow and, from simple geometric considerations, is probably of the order of 0.15 m^2kg^{-1}. The steam velocity required to cancel gravity completely is then about 10 m s^{-1} corresponding to a volumetric flow rate in a channel of ≈ 0.006 m^3s^{-1} which could be supplied by the evaporation of ≈ 0.004 kg of water per second; this in turn would require about 10 kW supplied as latent heat of vaporisation to a channel; if this is the highest rated channel then the total element power is about 30 kW and from the data of Appendix A-4 it can be seen that these powers are only achieved at times less than one minute after shutdown. In reality the critical steam flow rates will be somewhat less since channel flow will be impaired before the incoming jets reach the horizontal; we estimate that channel 2 will receive insufficient coolant for a steam velocity of 7 m s^{-1}.

Steam flow may interfere with the cooling of the tubes by interfering with the film flowing down the tube walls with the formation of waves and dry patches. An estimate † of the critical steam flow velocity for this interference gives 4.8 m s^{-1}. Experiments with an arrangement simulating channel three with a jet inlet temperature of 333 K and a film mass flow rate of 0.2 kg $m^{-1}s^{-1}$ showed that a power input of 11 kW was required to initiate upward steam flow [1] so that using the above crude estimate, 14 kW would be required to prevent the coolant from entering the channel. It has been shown [2] that these tube powers are only approached for massive leak rates ($\approx$ 300 litres per second) in the primary circuit.

The third effect arises from the method of returning water to the RAT. This involves releasing the flow above the free water surface with consequent formation of plumes and waves which, for large flows, have been shown to increase the weir flow into the downcomers with a consequent reduction of equilibrium water head [2]. The effect has not been quantified and in the case of the FRJ-2 reactor was avoided by introducing water below the free water surface in the RAT. HIFAR operates at a much lower power than FRJ-2 and an engineering judgement has been made that for credible leak rates the enhanced downcomer flow will not lead to unacceptable diminution of water head. Should this judgement be reversed an alternative solution might be the provision of a coffer dam about the tops of the downcomers.

† We are indebted to C. Don Fletcher of Idaho National Engineering Laboratory for providing this estimate, made using the Wallis countercurrent flow limiting correlation.

6.6. Nature of Film Flow.

Ideally the flow into each channel should rapidly reach the condition of a film of uniform thickness falling down the outer wall of each fuel tube. However, because the method of introducing the coolant onto the wall is by impact of a jet, it might be thought probable that the film would exhibit an azimuthal variation in thickness and that splashback of a jet might form a quasi-stable water bridge connecting the outer wall of one tube with the inner wall of its neighbour. Both these have been observed [1] in partial length mockups of a fuel assembly. The water bridges were found to maintain themselves over the length of the rig (165 mm) and thus might be expected to remain intact over the full length run in an actual element (600mm.) The tendency for water bridges to form was found to decrease with coolant temperature and above 60C occurred only rarely. The radial variation of fuel temperature was, however, slight; perhaps because of the high thermal conductivity of the aluminium tube but possibly indicating turbulent flow within the film.

We now examine the properties of an idealised film flow with no azimuthal variation in thickness. For the purposes of heat transfer calculations at the exit from the fuel tubes where the film flow is hottest, the flow is assumed to be hydrodynamically developed there. This assumption will be examined later. In this analysis we will require values of tube power and flow into the channels; we have assumed the former to be those for the fission power plus decay power ten seconds from scram when the fission power has been reduced by the reactivity effects of the CCAs falling into the core and of the loss of top reflector and coolant. The flow input is assumed to be that from a water head h_9 of 30 mm, corresponding to that maintained by a single scavenge pump.

Film flows are neglected in most thermal-hydraulic texts; however, thermal-hydraulic aspects of these flows are outlined in the review article of Seban [3].

The main thermal hydraulic parameters of this flow are summarised in Table 6-1.

Table 6-1
Film Flow Rate Parameters.

Channel	1	2	3	4	5
Tube cooled	Thimble	1	2	3	4
Film flow ($cm^3 s^{-1}$)	70	45	60	80	110
Flow per perimeter length gm s^{-1} m^{-1}	452	246	285	335	410
Power (kW)	0	5.2	6.1	7.2	8.6
Heat flux (kW m^{-2})	0	43.0	43.7	45.5	48.6
Inlet coolant temp (C)	50	50	50	50	50
Exit coolant temp (C)	50	75.1	72.0	69.5	67.0
Exit wall temp (C)	50	82.0	74.0	76.4	73.4
Re (inlet)	2734	1487	1721	2022	2491
Re (exit)	2734	2211	2450	2779	3284
Exit film thickness (μm)	496	341	370	403	451

Since mass flowrates per unit perimeter and flowrate Reynolds number are more relevant parameters for film flows than the supplied flowrates of Section 6.5.1, all three forms of flowrates are included in Table 6-1. (The exit Reynolds numbers are higher than inlet ones as a result of the higher exit coolant temperatures.) Similarly, axially-averaged heat fluxes are included as well as total power as both are necessary for temperature calculations.

Both fluidic and thermal behaviour depend on whether the flow is laminar or turbulent, so it is necessary to determine which of these two regimes applies to each film flow. As with normal pipe flow, film flows are usually assumed to be turbulent if the flow Reynolds number is larger than a

particular critical value. Unfortunately, although the critical Reynolds number is reasonably well defined for pipe flows (approximately 2000), different researchers suggest considerably different critical Reynolds numbers, ranging from 1600 to 3000, for film flows. Taken collectively, the different recommendations suggest (but only suggest) that all exit film flows are turbulent; as are the inlet flows for channels 1, 4 and 5; but there is uncertainty in the case of the inlet flows to channels 2 and 3.

An investigation of published hydraulic characteristics of film flows, undertaken as part of the present study to clarify the criterion for film flow turbulence, suggests that the apparent contradictory results of different researchers are a result of entrance effects. The data suggest that turbulence supplied by inlet conditions to film flows below the "critical Reynolds number" is suppressed, as with pipe flows, but with suppression occurring at a much slower rate, resulting in the natural laminar behaviour only after long distances. Thus, the relatively short length of HIFAR fuel elements imply turbulent flows at relatively low Reynolds numbers. With this in mind, it is highly likely that the ECCS flows of Table 6-1 would be turbulent for all Reynolds numbers quoted. The film thicknesses and wall temperatures of the table have hence been calculated with equations applying for turbulent rather than laminar conditions.

Bulk exit coolant temperatures have been calculated from a heat balance of the type discussed in Section 5.1. Heat transfer coefficients, relating the exit wall temperatures to the bulk ECCS temperatures, have been obtained from the empirical correlation of Gimbutis et.al. [4], whose experiments covered conditions similar to those of the HIFAR ECCS system.

It will be seen that the exit wall temperatures are below the saturation temperature, so boiling cannot occur. As discussed in Section 5.5, boiling requires some wall superheat. As with duct flow , discussed in Section 5.4.6, boiling is assumed to start when wall temperatures calculated for non-boiling and boiling flows are equal. The annulus data of McAdams et.al. [5] were used to predict the latter. Boiling film flow data of Gimbutis et.al. [4] confirm that this is valid for film flow. This indicates boiling will start, on the inner fuel tube, when the power is increased by a factor 2.1 of the maximum rated channel considered here. At this stage, the bulk exit temperature is still below saturation (but only just).

If the inlet ECCS temperature is raised, boiling would occur only after the film reaches saturation. Heat transfer processes then involve some evaporation, and the heat transfer coefficient must be calculated by a correlation appropriate to this rather than the correlation of Gimbutis et.al. [4]. Calculations show that, with evaporative cooling, boiling will not occur in the film for the maximum rated channel even if the ECCS flow is introduced at saturation temperature (101 C).

There is thus considerable margin to boiling onset with the ECCS cooling. However, unlike the case of normal HIFAR operation, where boiling must be avoided to avoid Ledinegg instability, there would be no adverse effect if boiling were to start in the ECCS flow; in fact, the improved heat transfer would result in lower wall temperatures. It has been suggested that nucleating bubbles would disrupt the film flow, causing a downstream dry patch. Film flow boiling crisis data of Gimbutis et. al. [4] are inconsistent with this assumption. It is more likely that boiling onset would lead to a more uniform film thickness and so reduce the margin to dry patch formation. (Prior to boiling, surface tension effects enhance any slight perturbation on the equilibrium film thickness. The surface of a thinner region of the film, being closer to the hot surface, has a lower surface tension than elsewhere, resulting in surface movement away from the thinner region, so tending to thin it further. Other effects prevent complete drying. With boiling onset, temperatures beyond the boiling layer are more uniform, so the above effect is reduced.)

An attempt was made to determine the margin to dryout for the ECCS flow. No appropriate correlation could be found. As a result, three different approaches were used to give at least some guide to the boiling crisis heat flux. Firstly, the power required to completely evaporate the film

was calculated. It is plausible that this is indeed the critical power since, with vapour-liquid flows in ducts, the boiling crisis at low flow rates - and the ECCS flows are indeed low rates - and high vapour content occurs when all the liquid is evaporated. Indeed, even at higher duct flowrates with high vapour contents, many crises occur as a result of the liquid film being evaporated, with remaining liquid flowing as droplets. Secondly, it was considered that boiling crisis in the low flowrate ECCS film may be similar to pool boiling critical heat flux. Thirdly, the subcooled film flow crisis correlation of Gimbutis et.al. [4], although not appropriate to the saturated boiling crisis that would occur with the HIFAR ECCS, was used to provide an indication of the critical heat flux.

All three approaches yielded similar heat fluxes, all greater than 1MW m^{-2}. Although these estimates cannot be regarded as accurate, they do give some guide to the boiling crisis heat flux. On the basis of actual heat fluxes (Table 6-1) it can be seen that the ECCS has considerable (the order of a factor of 10) margin to ECCS dryout.

The calculations of Table 6-1 have assumed developed ECCS flow at the exit. The extent to which flow development is achieved has been examined by considering gravitational and wall shear forces on the film. The ECCS flow on each surface falls as a cooling film of liquid accelerating until the gravitational and frictional forces balance. Initial conditions least favourable to development were chosen; the initial ECCS velocity was assumed to be sufficiently low that the film fully occupied the gaps between fuel tubes, even though initial velocities are likely to be much closer to final equilibrium velocities. Moreover, even though, as discussed, the ECCS flows are likely to be turbulent, flow development was calculated assuming laminar flows since this results in longer development lengths.

The results of the analysis are shown in Figure 6-5. Even with these adverse assumptions, it is seen that developed conditions are rapidly approached. (With regard to Figure 6-5, it needs to be remembered that the actual fuel starts about 25 mm from the inlet of the fuel tube).

6.7. Comments - Conclusions.

In summary, the HIFAR ECCS, if ever called into play, will achieve equilibrium conditions rapidly, and will adequately cool even the maximum rated channel. The emergency coolant will remain subcooled at the exit, have considerable margin to boiling onset, and have a considerably greater margin to formation of dry patches on the fuel surfaces.

The physical basis for operation of the ECCS is fairly simple up to a point where the jets impinge on the tube walls. The jet flow and the partition between channels can be well calculated with the only uncertainties being the effect of disturbances to the free surface of the D_2O in the RAT and the effect of manufacturing tolerances on the location of the fuel element tops with respect to the ECCS holes; this last effect could be investigated.

The development of film flow from the portion of the jet flow impinging on a tube wall is a rather difficult thermal hydraulic problem involving multi-dimensional effects so that it is difficult to provide an analyic description of the early stages of film development. However, it has been shown experimentally that film flow does develop, and although the film exhibits a circumferential variation in thickness the tube temperatures do not vary greatly in this direction. The most likely reason for this is the high thermal conductivity of aluminium and this conclusion could reasonably be extended to other phenomena producing heterogeneous film behaviour. This hypothesis could be examined theoretically by considering various hypothetical flow distributions such as a narrow 'river' flow from each jet where a film fails to develop.

6.8. References.

(1) Wolters, J. [1979 ?] - Spray film emergency cooling for the experimental reactors of the FRJ-2 type. Undated doctoral thesis, translated from the German by B. Pietroff and P. Holland.

(2) Connolly, J. W. [1982] - An assessment of the HIFAR emergency core cooling system. AAEC report NT/TN 424

(3) Seban, R. A. [1978] - Transport to falling films. Proc. Sixth International Heat Transfer Conference. Toronto. Volume 6, pp 417-428

(4) Gimbutis, G. J., Drobavicius, A. J. & Sinkunas, S. S. [1978] - Heat transfer of a turbulent water film at different initial flow conditions and high temperature gradients. Proc. Sixth International Heat Transfer Conference. Toronto. Volume 1, pp 321-326

(5) McAdams, W.H., Kennel, W.E., Minden, C.S., Carl, R., Picornell, P.M. & Dew, J.E. [1949] - Heat Transfer at High Rates to Water with Surface Boiling. Ind. Engng. Chem. Vol. 41, page 1945.

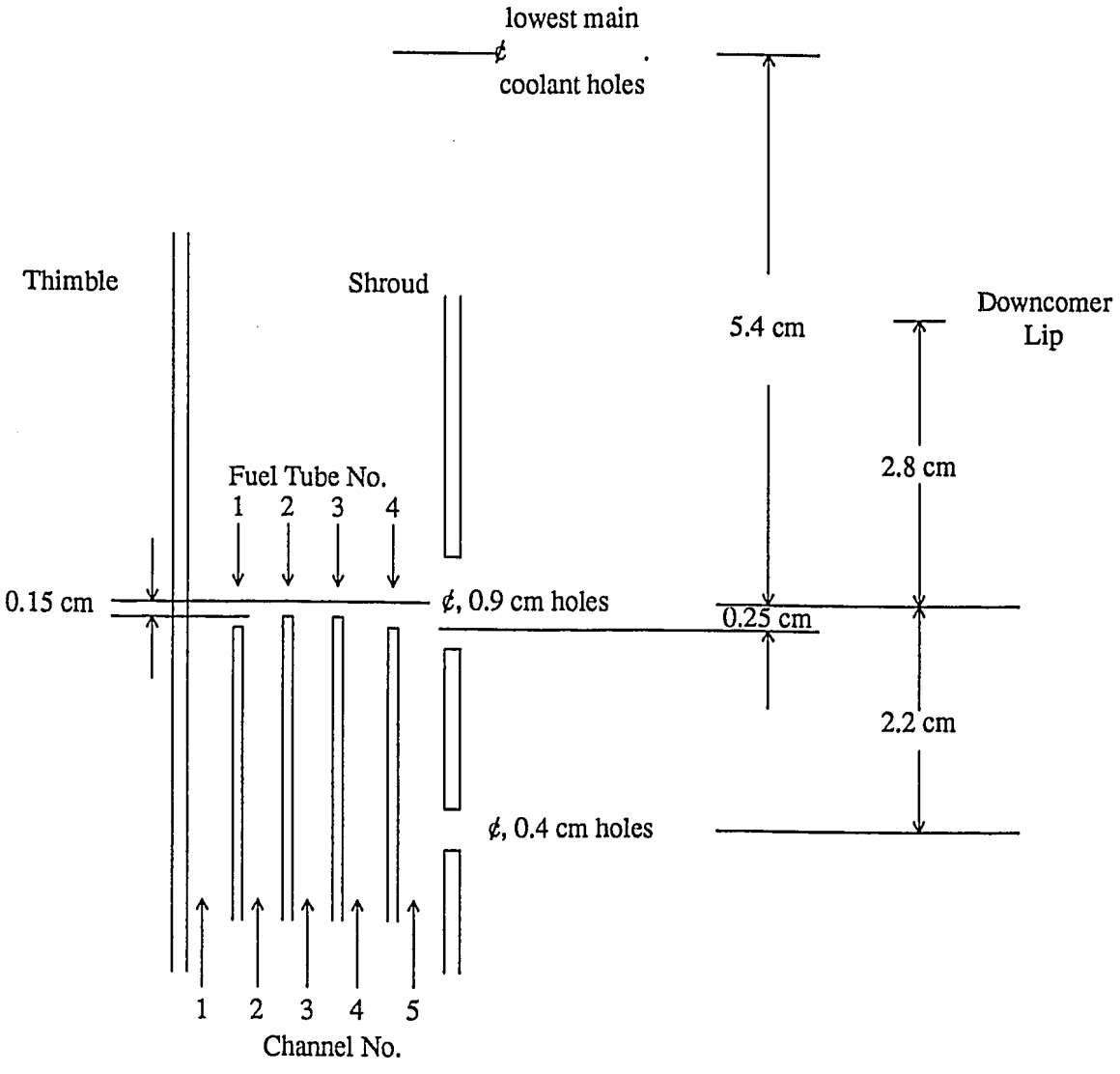

Figure 6-1 Geometric arrangement of ECCS.

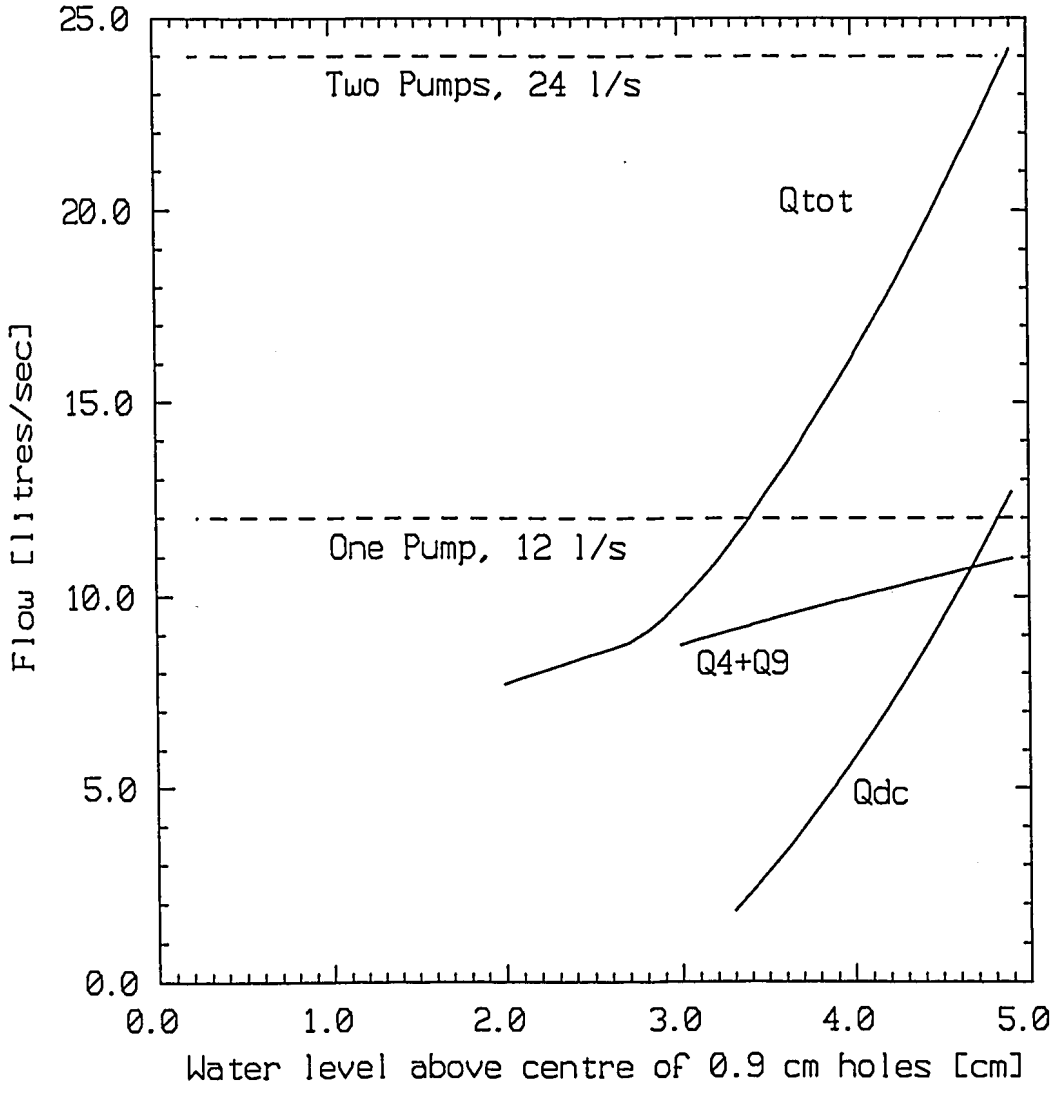

Figure 6-2 Components of equilibrium flow rates in ECCS as a function of water head.

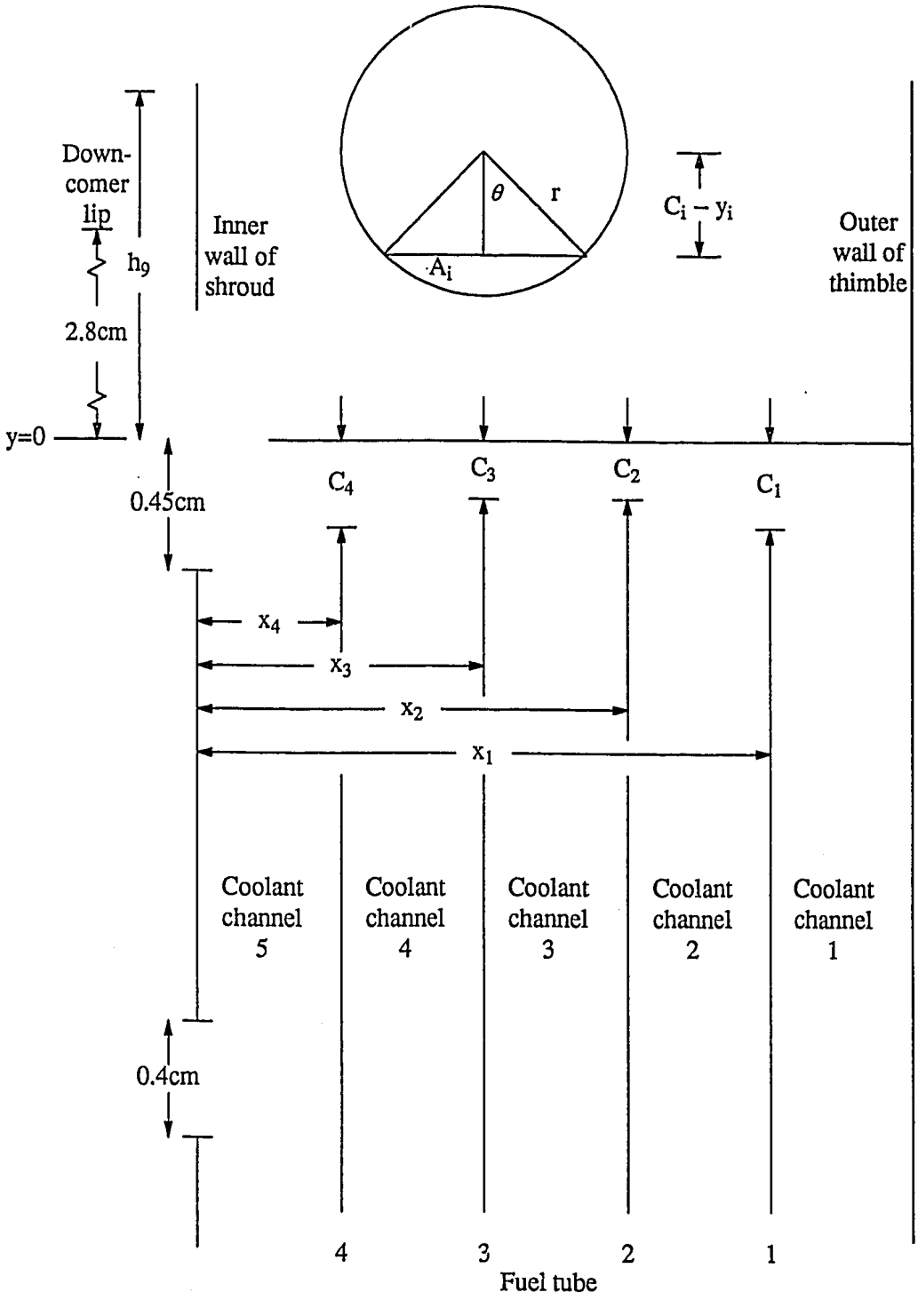

Figure 6-3 Geometry for flow partition calculation.

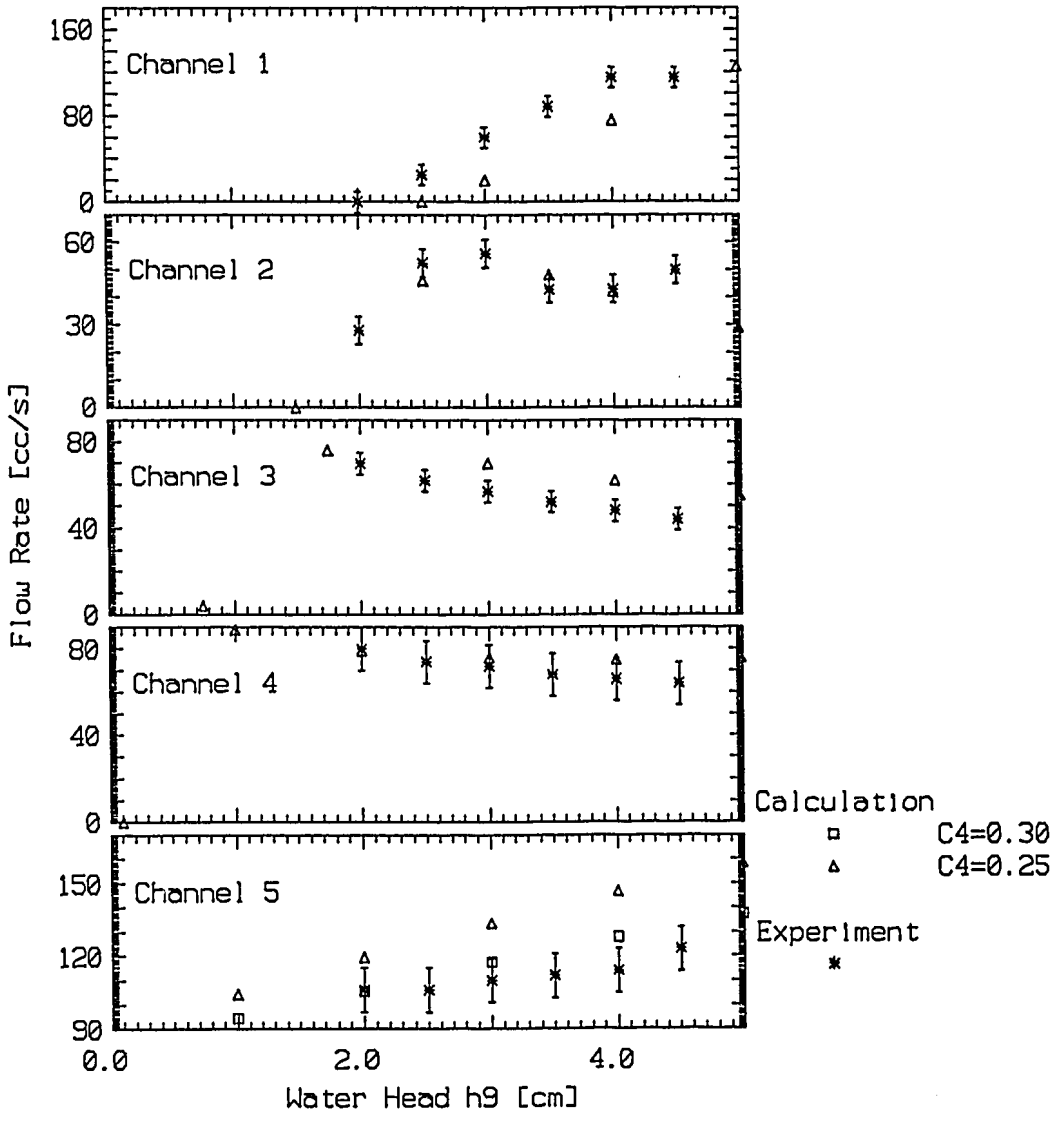

Figure 6-4 Partition of jet flow between channels.

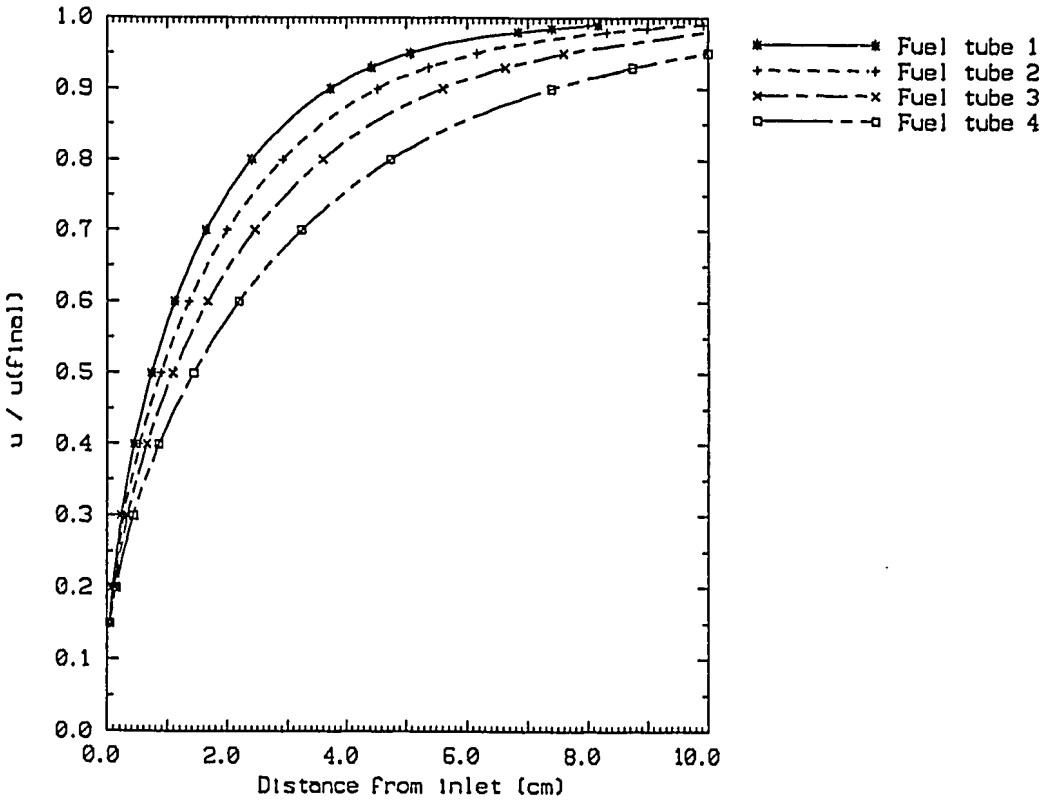

Figure 6-5 ECCS flow development for adverse initial conditions

This page of Section 6 intentionally left blank

SECTION 7

ANALYSIS OF ABNORMAL OPERATION.

The chapter of accidents is the longest chapter in the book.

John Wilkes. (1727? - 1797)

7. ANALYSIS OF ABNORMAL OPERATION.

In this section we consider the operation of the reactor outside the boundaries imposed by routine operational considerations. The boundaries are, of course, guarded by the reactor trip circuits; in what follows we assume these circuits to be inoperative or too slow to affect the course of events. It must be recognised that no device can store an infinite amount of energy and part of our consideration will be directed towards defining times at which the reactor must be made subcritical or cooling restored in order to keep the energy density in the fuel within acceptable bounds, that is, to keep the fuel below the melting temperature. From the data given in Section 2 we see that the specific power in the fuel tubes is very high, 450 kW/litre, and the heat capacity low, 0.054 MJ/K; the melting point is also low at 920K for fuel and even lower for the clad. These factors might be expected to severely limit the range of events which the reactor can safely accommodate and this matter will be discussed in what follows.

7.1. Reactivity Induced Power Transients.

Reactors such as HIFAR are used for research and irradiation purposes and are exposed to frequent reactivity manipulation such as rig removal and loading. They are therefore considered to be more likely to experience a reactivity induced power transient than is a power reactor, although the number of such events recorded is not great.

In the case of parallel plate fuel elements typical of light water moderated cores, we may, without loss of generality, consider a typical volume element of the reactor to consist of one half of the thickness of the fuel alloy, the clad thickness, and half the thickness of a coolant channel. The HIFAR tubular geometry must be represented in a more complex and complete way, with radial coordinates defining the regions called internal moderator, internal thimble, coolant channel, clad, alloy, clad, coolant channel, ... outer shroud tube, external moderator. It is the existence of this last outer moderator region that is one of the distinctions to be drawn between light water and heavy water moderated cores.

Experimental information on the physical response of research reactors to varying magnitudes of reactivity injection comes from the extensive tests performed at the National Reactor Testing Station (NRTS) at Idaho Falls in the USA and known as the SPERT programs; sometimes as SPERT I and SPERT II. Interpretation of the resulting experimental information requires a good understanding of the physical phenomena occurring during a power transient.

At this stage it is useful to describe the power transients in terms of the Nordheim-Fuchs equation. This is a point formulation in which delayed neutrons are neglected.

$$\frac{1}{P}\frac{dP}{dt} = \alpha(t) = \alpha_0 - E\frac{d\alpha}{dE} = \alpha_0 - bE$$

where P = reactor power

α_0 = initial inverse period (s^{-1})

b = reactivity feedback coefficient ($s^{-1}J^{-1}$)

$\alpha(t)$ = instantaneous value of inverse period = $\frac{1}{l_a}\frac{\delta k}{k}(t)$

l_a = prompt neutron lifetime.

We may modify this to account for the dimensionality of real reactors:

$$\frac{1}{P}\frac{dP}{dt} = \alpha_0 \pm b_1E_1 \pm b_2E_2 \pm \ldots.$$

where b_i , E_i refer to the i-th region of the reactor. We note that the E_i define pressures, temperatures, and densities by some equations of state and that there will be b_i appropriate to these parameters. Also the E_i will be connected by some energy transport mechanisms between the regions.

This equation can be further modified in a number of ways.

(i) Incorporation of a 'non-linear with energy' feedback,

$$\frac{1}{P}\frac{dP}{dt} = \alpha_0 - b' E^n \qquad , E \equiv E(t)$$

which gives the energy to the time of peak power as $E_{tm} = (\alpha_0/b')^{1/n}$ This decreased dependence on α_0 can be clearly seen in the SPERT results where the slope of a log-log plot of E_{tm} against α_0 changes from 1 to .5 after boiling heat transfer dominates the reactivity feedback.

(ii) Incorporation of a delay between energy generation and appearance of feedback,

$$\frac{1}{P}\frac{dP}{dt} = \alpha_0 - b\,E(t - t_0)$$

This can have important consequences for the stability of the reactor under transient conditions. Typically the delays are due to heat transport processes.

(iii) Incorporation of an energy threshold before the manifestation of feedback,

$$\frac{1}{P}\frac{dP}{dt} = \alpha_0 - b(E - E_0), \quad b = 0 \text{ for } E < E_0$$

The most common such threshold is a change of phase in the material of a region. If the threshold is large then the energy release is determined by the threshold energy.

An overview of the problem for plate type, water moderated cores can be gained from the temperature-time characteristics of a thin platinum ribbon immersed in a water pool and subjected to an exponentially rising heating current [1]. This is sketched in Figure 7-1 . At first the ribbon temperature increases with the same time constant as the heater current. The water saturation temperature is overshot and the ribbon temperature then suffers a sharp and well defined setback which becomes smaller with decreased water subcooling. This is attributed to the onset of nucleate boiling (ONB) and the nature of the setback indicates that a discrete volume of water at a lower temperature has become closely thermally coupled to the ribbon, whose small heat capacity results in the drop in temperature. The ribbon temperature then rises at a quasi linear rate, perhaps attributable to the increasing volume of water coupled thermally to the ribbon by boiling. At some point the ribbon temperature exhibits a sharp increase which is attributed to the departure from nucleate boiling (DNB) and the development of stable film boiling over the ribbon surface. If the current is not interrupted the ribbon melts. These experiments also attempted to measure the growth of voids in the water by photography of bubbles forming at the ribbon surface.

If we translate this behaviour to the reactor situation it is apparent that there will be a space-wise distribution of ONB determined by the power distribution. Only a small temperature setback will occur because of the much greater heat capacity of the fuel plates compared with the ribbon. However, with the occurrence of ONB, the temperatures of some plates will be increasing at a linear rate while others are still increasing exponentially; this means that the temperature distribution through the core will no longer be proportional to the power distribution and will become much flatter.

From the foregoing discussion it is clear that the successful calculation of transients in water cooled and moderated cores requires identification of:

(i) the regions generating feedback,

(ii) the energy flows between these regions,

(iii) the time delays relative to the instantaneous reactor power for the appearance of reactivity feedback,

(iv) the magnitude and sign of the coefficients relating reactivity to energy,

(v) the thresholds at which changes to heat transport mechanisms occur, and

(vi) equations of state for the materials in the regions. It is to be noted that, in general, the problem involves thermal non-equilibrium; for example, for water the system is not necessarily moving along the saturation line.

7.1.1. SPERT data.

The majority of plate type cores investigated in the SPERT program were light water cooled and moderated and they are thus not directly relevant to HIFAR studies. The major difference between them and HIFAR is the much greater prompt neutron lifetime in the latter; there is also a bulk moderator region in HIFAR which is not characteristic of the former. However, the SPERT results are an excellent test of computer code capability and, since most changes between code input for different cores are parametric, a demonstration of the ability to reproduce experimental data for one core can inspire confidence in calculations of a different core if the nature of the parameter changes are well understood.

Fortunately, of the two SPERT D_2O cores [2], one - BD22/24 - was almost a replica of HIFAR excepting that

(i) the fuel element consisted of parallel plates rather than concentric tubes and

(ii) both the D_2O/Al volume ratio and the temperature coefficient of reactivity were smaller than those of HIFAR.

The feedback coefficient (b) with respect to energy is similar for HIFAR and BD22/24. If the total heat capacity of fuel alloy, clad, and coolant is denoted by H, then in the Nordheim-Fuchs formalism this feedback coefficient is given as

$$b = \frac{d\alpha}{dE} = \frac{1}{l_a}\,\frac{1}{k}\,\frac{dk}{dT}\,\frac{1}{H} \quad (s^{-1}J^{-1})$$

At 293K the coefficient (b) thus has a value of $-5.1\ 10^{-7}\ s^{-1}J^{-1}$ in HIFAR and $-4.0\ 10^{-7}\ s^{-1}J^{-1}$ in BD22/24. For transients which do not reach ONB the behaviour of the two reactors should be similar.

The coefficient values are derived from consideration of the following tabulated quantities.

Property	BD22/24	HIFAR	Units
Coolant feedback coefficients (whole reactor)	$-6.5\ 10^{-5}$	$-10.3\ 10^{-5}$	$\delta k/k\ K^{-1}$
Total coolant volumes	36	63	litres
Feedback coefficients per volume of coolant	$-1.8\ 10^{-9}$	$-1.6\ 10^{-9}$	$\delta k/k\ cm^{-3}K^{-1}$
Alloy heat capacity	$2.2\ 10^{-2}$	$2.2\ 10^{-2}$	$MJ\ K^{-1}$
Clad heat capacity	$5.5\ 10^{-2}$	$3.1\ 10^{-2}$	$MJ\ K^{-1}$
Coolant heat capacity	$1.7\ 10^{-1}$	$2.9\ 10^{-1}$	$MJ\ K^{-1}$
Total heat capacity	$2.5\ 10^{-1}$	$3.4\ 10^{-1}$	$MJ\ K^{-1}$

If the heat capacities of alloy and clad are small compared with that of the coolant then the Nordheim-Fuchs coefficient will be the same for BD22/24 and HIFAR. However for the two reactors the actual heat capacities are sufficiently different to produce the values quoted. For near isothermal heating (slow transients without coolant flow) we expect similar behaviour.

It may be noted that the ratio of the BD/HIFAR heat transfer areas is 1.5 and the ratio of the total heat capacities is 0.72; apart from power and energy release we would expect similar temperatures.

For a no flow transient with inverse period α the approximate form of the temperature distribution in an infinitely wide channel is $T(x) = T_W\ e^{-x/X}$ where the relaxation length $X = \sqrt{k/\alpha c}$, and for finite width channels this is an adequate approximation if X is smaller than half the channel width, We can then retain the isothermal model by replacing the actual channel width by a water layer X which is at the same temperature as the clad coolant interface. As α is made larger, X decreases and the different clad heat capacities for the two reactors will start to have a greater influence on the Nordheim-Fuchs coefficients. The calculations show, however, that nucleate boiling just occurs at the time of peak power for relatively slow transients in both reactors ($\alpha \approx 1s^{-1}$.) On our model this results in a rapid increase in the volume of water thermally coupled to the fuel plates and the reactors should continue to behave in the same way for transients in which the dominant shut down mechanism is nucleate boiling. For transients under conditions of forced convection the coolant channel geometry is presumably important but we feel that the dominant effect will be the time constant defined in Section 2.5.4 .

The view that BD22/24 and HIFAR will behave in a similar ways is also supported in part by the facts that:
(a) calculations of the behaviour of BD22/24 agree well with experiment, and
(b) calculations of the behaviour of HIFAR and BD22/24 produce similar results.

7.1.2. Transient codes.

Four codes that have been successfully tested against SPERT are known to us. They are:

1. PARET, a one dimensional (along the coolant channel), point neutron kinetics code originating at NRTS [3] and subsequently modified at Argonne National Laboratory [4],
2. NAIADQ, a similar code developed at LHRL [5],
3. TANK, which has a heat transport treatment similar to the above but has a two dimensional space representation. This code originated at the Whiteshell Nuclear Research Laboratory in Canada [6] ; we are only conversant with the broad outlines of its construction.
4. ZAPP, a code developed at LHRL [7]. This code uses an approach to the modelling of transient heat transport which is completely different to that in the first three, which basically use the same treatment.

All four of these codes were designed to analyse fast power transients whose time scale is such as to make the modelling of heat transport unimportant for regions outside the core. For slower

transients it is necessary to include treatment of plant items such as pumps and heat exchangers. Such a code, HIDYN [8], which treats the primary and secondary coolant circuits of HIFAR as lumped parameters connected by delay lines has been developed at LHRL. Because it considers the energy from fission to be released directly into the coolant it cannot be used for fast transient studies except in an approximate way.

7.1.3. Determination of feedback coefficients of reactivity.

Analysis of the SPERT I and II cores by means of the LHRL AUS codes has indicated that the only two physical processes producing significant feedback come from the change in water density with temperature or steam formation, and the change in neutron spectrum with water temperature. There is a second order effect arising from the change in metal/water volume ratios with fuel plate expansion but the Doppler effect is negligible. The magnitudes of these coefficients were calculated by perturbation theory; the techniques of calculation and some revised values have been given in Section 2.7 but the revisions are sufficiently minor as not to invalidate the original results of the transient calculations. The original coefficients for SPERT I and II have been used as input data for the codes PARET, ZAPP, and NAIADQ; differences in the output produced by these codes should thus be a consequence of the differences in modelling of heat transport. Coefficients used in TANK were established with a version [9] of the WIMS code but we are not familiar with the details of the calculations. Confidence in the correctness of these calculations is given by their adequacy in reproducing measured values of whole reactor temperature coefficients, and by their similar performance in the estimates of space-wise coefficients as shown in blind benchmark comparisons [10].

7.1.4. Methods of modelling heat transport.

Calculation of heat flow from a solid surface to a liquid is surrounded by many difficulties because of the complexity of the physical processes within the liquid. The 'classical' method of proceeding is to treat the liquid as a lumped material whose average properties are known, and to develop correlations for the heat transfer coefficient from solid to liquid in terms of parameters appropriate to the system under consideration. These (steady state) correlations usually have the form

$$h_{sl} = K\, k\, Re^n\, Pr^m$$

where h_{sl} is the heat transfer coefficient, K is a constant to be determined, k is the thermal conductivity, Re and Pr are the Reynolds and Prandtl numbers respectively, while m and n are indices to be established. The codes PARET, NAIADQ, and TANK use basically this approach except that for small Re and non boiling of the coolant, correlations of this form were found to be unsatisfactory (W. L. Woodruff - private communication.) Since the methodology of the three codes is similar, we will briefly discuss the PARET formulation, which has a modification of the original code so as to allow the SPERT fuel plate geometry to be modelled.

For zero coolant flow or low values of Re the Rosenthal-Miller relationship [11] obtained from the one dimensional heat conduction equation with an exponentially rising heat source

$$h = \sqrt{k\, c\, \alpha_0}$$

where h = heat transfer coefficient
k = thermal conductivity of water
c = volumetric specific heat
α_0 = inverse period of power rise

was found [4] to give best agreement with experimental data, even though the formulation does

not allow the varying period during a reactor excursion to be accounted for. The McAdams [12] correlation was used to obtain the heat transfer coefficient for fully developed subcooled nucleate boiling and the Bergles-Rohsenow [13] method applied to detect ONB and the transition to fully developed nucleate boiling. The original PARET correlation for DNB was retained and a voiding model containing four adjustable parameters was incorporated into the code.

There has long been concern about the application of steady state correlations to highly transient events [4]. However, the above prescription gave good agreement with a range of SPERT data, although the results were found to be very sensitive to the choice of correlations. For many correlations it was found that two phase heat transfer, flow instability, and DNB were overly conservative and prematurely predicted film boiling. A two channel model was chosen to represent the reactor, one being based on the highest rated channel and the other on an average channel. The axial dimension for each channel was divided into 21 equally spaced nodes and the appropriate conservation equations applied along the channels.

In the code ZAPP spatial representation is obtained by the specification of zones; each zone contains a number of identical cells each subdivided into material regions whose physical properties are given in the code input. For the type of reactor of interest here these regions comprise fuel alloy, cladding, and coolant; the energy flows between them are calculated from the one dimensional heat conduction equation. In most of the calculations to be described the reactor was represented by a single zone containing N cells each one cm high and the fission power developed in the alloy of a cell was taken to be the mean power P_{tot}/N where P_{tot} was the total reactor power.

Each region of a cell has an appropriate feedback coefficient with respect to energy in that region; for simplicity we consider, for the moment, that these are only non-zero in the coolant. If the rate of energy appearance is proportional to the fission power in the alloy P_i, and b_i denotes the feedback coefficient with the subscript i denoting a cell at a particular spatial position in the real reactor, then the rate of generation of reactivity feedback is

$$\sum_{i=1}^{N} A\, P_i\, b_i$$

and therefore, if we represent the whole reactor by a single average cell, the correct rate of reactivity feedback will be obtained if we specify the effective feedback b′ by the identity

$$b'A\,\frac{P_{tot}}{N} \equiv \sum_{i=1}^{N} A\, P_i\, b_i$$

so that

$$b' = \frac{N \sum_{i=1}^{N} P_i\, b_i}{P_{tot}}$$

That is, the correct feedback coefficient is given by the term $N\,\bar{b}$ where $\bar{b}$ is the power weighted reactivity coefficient. It is to be noted that this prescription only holds if all the P_i have the same time dependence but this is the ordinary assumption of point reactor kinetics analysis.

In order to enable a description of nucleate boiling heat transfer the coolant region of a cell is divided into a number of very fine sub-regions and temperature dependent thermal data provided for each in the code input. The temperature coefficient of reactivity per unit volume is assumed constant so that the temperature coefficient for these fine regions is the total coolant coefficient of reactivity multiplied by the ratio of the sub-region volume to the total channel volume.

To model the enhanced heat transfer under nucleate boiling conditions the thermal conductivity of the coolant regions is made large when the average temperature of a region reaches some 'trigger'

value. This results in an expanding boundary whose temperature is slightly less than the clad, and an increase in the rate of feedback, since the energy in boundary layer of thickness x(t) and temperature $\theta(t)$ per unit heat transfer area is c.x(t).θ(t) and the rate of feedback is then

$$b\,c\left[\frac{\partial x}{\partial t}\theta + x\frac{\partial \theta}{\partial t}\right]$$

Although this appears simple, in actuality the coupling of the power behaviour to the feedback through the neutron kinetics equations makes it difficult (impossible) to proceed further analytically. However some insight can be gained by considering a numerical approach and writing the rate of reactivity feedback as

$$\sum_{1}^{n(t)} b_i P_i' + \sum_{n(t)+1}^{N} b_i P_i$$

Here P′, P denote heat fluxes into the coolant under conditions of nucleate boiling and conductive (strictly speaking, non-boiling) heat transfer respectively, while n(t) is the number of cells at time t that have exceeded some threshold heat flux P_{th} for the initiation of nucleate boiling; consequently n(t) = 0 if all $P_i \leq P_{th}$. If the reactor is represented by a single cell and the contribution to the feedback rate from conductive heat transfer is small compared with that from boiling heat transfer then we can write

$$N\,\bar{b}\,\bar{P}' = \sum_{i=1}^{n(t)} b_i P_i'$$

where P′ is some scaled heat flux chosen to satisfy the identity

$$\bar{P}' \equiv \frac{1}{N\,\bar{b}} \sum_{i=1}^{n(t)} b_i P_i'$$

Since the volume of the core required to enter nucleate boiling and terminate the transient is a function of the reactivity insertion, it is clear that a single scaling factor does not exist. An approximation has been used with ZAPP by defining the single cell threshold for nucleate boiling as being the heat flux into the coolant when the cladding temperature reaches a temperature given by

$$\frac{(\theta_{sat} + 20K - \theta_0)}{F} + \theta_0$$

where θ_0 is the initial temperature and F is the core power form factor. It can be seen that for large core power form factors the single cell is required to enter nucleate boiling at temperatures less than saturation; however it is clear from the above discussion that the original reality associated with the trigger temperature has now been modified drastically. The temperature of 20K was derived from wall superheats observed in experiments [1] where thin ribbons were heated with an exponentially rising heat source.

The above representation of heat transport after ONB has presumed that the coolant remains in the liquid phase with no net generation of steam. This assumption, while proving satisfactory for most SPERT core experiments analysed, was found unsatisfactory for two of them. Accordingly a model for reduction of coolant density with vapour formation was derived by finding a trigger temperature for the onset of vapour formation and a linear rate of density decrease with temperature in the expanding boundary layer which would satisfy the observed power shape in the most severe transient launched in SPERT BD22/24 [2]. These were 423K and -8 kg m^{-3} K^{-1}. Thus the model allows considerable coolant superheat if local pressures are assumed to remain at atmospheric. This may not be unrealistic since severe SPERT transients show sharp pressure pulses

produced some time after peak power.

A very simplified flow model has also been incorporated into ZAPP by allowing axial flow of coolant from one zone to another. Heat conduction is still in the radial direction across a boundary layer and into the bulk coolant whose conductivity is made large enough to flatten the radial temperature distribution. It is not possible to use the previously described voiding model in this model/description. Fortunately however, voiding is only important for fast transients in which the power time constant is greater than that for coolant flow. In such cases it has been shown experimentally [15] and theoretically [14] that the parameters of the initial burst are independent of flow rate, although the quasi constant post burst power is proportional to it.

Although HIDYN requires heat transfer coefficients for the heat exchangers (but not in the core) knowledge of the flow distribution in the RAT is required because the HIDYN model is cast in terms of mixing and delay volumes. Information about the governing parameters is largely circumstantial and could only be improved by measurement of the reactor transfer functions. Some indication of the time delays in the system has been obtained by the analysis in the frequency domain on the Danish PLUTO type reactor DR3 [16] and from best fitting HIDYN parameters to actual reactivity variations observed in HIFAR [8].

7.1.5. Code verification.

As already indicated the prime source of experimental power transient data for research reactors with water coolant/moderator and highly enriched uranium, uranium alloy fuel plates is that obtained from the SPERT program. The principal parameters measured were as follows.

(i) P_{max}, the initial peak power in the burst which is usually the maximum power. The measurement time was usually long enough to record the post power peak secondary power oscillations before the reactor was shut down. Apart from the intrinsic interest of these power histories the use of inverse kinetics techniques allows the time dependent reactivity to be determined.

(ii) E_{tm}, the energy release to the time of peak power. This was obtained by numerical integration of the power traces and by modern standards of data processing the evaluation may have been somewhat primitive. In some cases the total energy in the initial power burst was determined where this was a well defined quantity (small post peak power oscillations.)

(iii) θ_{tm}, the clad temperature at the time of peak power. This was usually, but not always, quoted as the maximum of values taken by many in-core thermocouples at the time of P_{max}.

(iv) θ_{max}, the maximum recorded clad temperature during the burst. This usually occurred shortly after the time of peak power.

(v) In some cases the pressure/time characteristics of sensors external to the core.

Table 7-1 lists some of the SPERT reactors whose transient behaviour has been calculated by means of ZAPP together with some of their properties which are important in determining the reactor response to various amounts of reactivity insertion.

In this table H_{fp}/H_c is the ratio of the heat capacity of the fuel plates to that of the coolant, F is the core power form factor (maximum to average power ratio), the temperature coefficient of reactivity is that of coolant alone and includes the effect of thermal expansion of the water as well as the change in neutron spectrum. The ratio of temperature and void coefficients of reactivity is listed to indicate the relative importance of void formation as a shutdown mechanism. The P18/19 core differed somewhat from the others in that it had fuel plates with stainless steel alloy and stainless steel cladding rather than the aluminium alloy and aluminium clad more representative of most research reactors.

Table 7-1
SPERT Reactor Properties.

Reactor	Moderator	Prompt Lifetime (μs)	H_{fp}/H_c	F	Void Coeff / Temp Coeff ($\%^{-1}$ K)	Temperature Coeff dk/k (K^{-1})
P18/19	H_2O	14	0.19	2.2	19.7	$-8.3\ 10^{-5}$
B24/32	"	50	0.52	2.5	10.7	$-23.3\ 10^{-5}$
D12/24	"	60	0.19	2.4	11.2	$-26.2\ 10^{-5}$
B16/40	"	70	0.27	2.1	5.3	$-28.1\ 10^{-5}$
B12/64	"	77	0.18	2.2	1.9	$-30.4\ 10^{-5}$
BD18/68	D_2O	480	0.31	2.4	30.2	$-6.9\ 10^{-5}$
BD22/24	"	660	0.38	1.5	8.0	$-6.5\ 10^{-5}$
HIFAR	"	600	0.19	1.5	8.5	$-10.4\ 10^{-5}$

7.1.5.1. Transients reaching peak power at or before ONB.

These transients are chiefly of interest because, as has been shown, an exact feedback coefficient of reactivity can be derived for a single cell and therefore the calculation of calculated to experimental burst parameters is a direct check on the calculated feedback coefficients, their temperature dependence and the thermal data input to the code which performs the calculations. In the case of transients under no coolant flow conditions the conductive heat transfer model is tested.

Before examining the degree of correlation between experimental and theoretical data it is necessary to note the major sources of systematic error. Although firm data is not available it is probable that the absolute power determined for the experimental cores differs from that calculated by ±10% and the feedback coefficients by a like amount. Since these are consistent errors and for non-boiling transients the burst parameters are inversely proportional to the shutdown coefficient we might look for levels of agreement between ±20% if other sources of error are small. This is generally observed but E_{tm} is generally better calculated than P_{max}. Since the former is just the time integral of the power trace up to the time of peak power this suggests that the numerical techniques employed to obtain the energy may produce some bias - the power trace in SPERT was recorded as an oscillograph trace and not as direct digital readings.

A quantity of direct interest is the ratio $\alpha_0 E_{tm}/P_{max}$ since this indicates the pulse shape. For very rapid shutdown in the prompt critical regime it takes a value of one, for shutdown proportional to energy release in the prompt critical regime a value of two, and for delayed critical shutdown a maximum value of about three. The calculations are generally in good agreement with experimental values of this quantity except for cores B24/32 and P18/19 where the experiments seem to suggest shutdown which is non-linear with energy; since such a mechanism has not been found in this range of transients which are all terminated well before boiling it would seem that a consistent error is present between the power and energy data.

Transients launched with initial coolant temperatures from ambient up to a few degrees below saturation were well calculated except for the latter. Again, energy release was consistently estimated better than peak power and well correlated with the calculated variation of the shutdown coefficient with temperature. When the initial temperatures were close to saturation the trend was reversed with energy releases poorly calculated but it is clear that for these (θ_0 = 369K) large scale boiling is rapidly established over the whole core.

7.1.5.2. The ONB boundary.

It might be expected that the threshold inverse initial period (α_0^*) at which ONB occurs at the time of peak power for the highest rated region in a core would depend on specific core parameters. Simple considerations [17] show that if ONB occurs exactly at peak power, then $\left(\frac{dk}{k}\right)_{tm}$, the compensated reactivity at that time, is given by

$$\left(\frac{dk}{k}\right)_{tm} \approx \frac{H_{fp}}{H_c} \cdot \frac{(\theta_{ONB} - \theta_0)}{F} \cdot \frac{1}{k}\frac{dk}{d\theta} \cdot \frac{1-\zeta}{\zeta}$$

$$\left(\frac{dk}{k}\right)_{tm} = \alpha_0^* l_a \quad \text{for super prompt critical transients}$$

where ζ is the fraction of the energy remaining in the fuel plates at the time of P_{max}. From the data of Table 7-1 it can be seen that the heavy water moderated cores with their long prompt neutron lifetimes and smaller temperature coefficients will produce ONB for much smaller α_0^* than the light water cores.

It may also be noted that since

$$\frac{\delta\alpha_0^*}{\alpha_0^*} = \frac{\delta\theta_{ONB}}{(\theta_{ONB} - \theta_0)}$$

the fractional change in α_0^* for a change in the nucleate boiling threshold temperature will be small for initial coolant temperatures well below the threshold temperature.

7.1.5.3. Transients with parameters determined predominantly by boiling heat transfer.

The immediate consequence of the occurrence of nucleate boiling is the greatly enhanced heat flux into the coolant and the loss of the equilibrium between fuel plate and average coolant temperatures existing under conductive heat transfer conditions. As can be seen from the time constant data of Section 2.6 the time constants for alloy and clad are very large so that fuel plate temperatures will rapidly respond to the new conditions; the time constants of the fine coolant subregions will also be large in the ZAPP boiling heat transfer model since their volumes are small and the conductivity has been made high. This enhanced energy flow into the coolant is derived from energy stored in the fuel plate prior to boiling and results in reactivity feedback appearing at a rate which is no longer proportional to the rate of energy input from fission. This results in P_{max}, E_{tm}, and θ_{tm} increasing more slowly with α_0 than would be the case with the linear mode and the value of $\alpha_0 E_{tm}/P_{max}$ becomes smaller, indicating a faster turn around of the power pulse. The pulse shape becomes asymmetric, that is, there is less energy released after peak power than is released before. All these effects are well calculated with ZAPP and, in particular, where a plot of $\alpha_0 E_{tm}/P_{max}$ against α_0 falls below the value two, indicating that the value of α_0 for onset of ONB is quite well matched by experiment except [18] for core P18/19. This gives support for the method used to derive the threshold for ONB, particularly since the agreement holds for a range of initial temperatures θ_0 which do not approach saturation temperatures too closely as well as core pressurisation in BD22/24 increasing θ_{sat}.

7.1.5.4. Transients producing vapour void before peak power.

As noted, severe discrepancies between calculated and experimental data were found to exist for the greatest reactivity insertions in two SPERT cores, the H_2O moderated D12/25 and the D_2O moderated core BD22/24. This discrepancy indicated the appearance of another, more marked non-linear shutdown mechanism than that provided by nucleate boiling heat transfer. As

discussed in Section 7.1.4 a vapour generation model was obtained by fitting a threshold and rate of void growth into the calculations so as to reproduce the experimental power trace for the fastest transient in BD22/24. This model satisfactorily resolved the observed discrepancies in D12/25 and the data away from the normalisation point in BD22/24 used to develop the model.

A qualitative comparison can be made with the void growth predicted by the model and experiments measuring void growth rates and water expulsion velocities for a tubular heating element surrounded by a coolant annulus [20], geometry quite similar to that of the fuel elements in HIFAR. Heating was supplied in the form of a short duration electrical current in circuitry designed to produce a square wave power of height P_{max}. If it is assumed that the void growth scales as the adiabatic temperature rise rate of the heater then ZAPP calculations of void growth may be compared with those observed in the experiment. Such a comparison is shown in Figure 7-2 for a calculated HIFAR transient of initial period 50 ms where the adiabatic rate of temperature rise at peak power is 2700 K s^{-1}. If this growth in void fraction is scaled to that of the tubular heater rig of 12900 K s^{-1} quite good estimates of the measured void development are obtained.

7.1.5.5. Transients under conditions of forced convection and nucleate boiling.

SPERT data analysed is limited to the core B18/68. This core was something of a curiosity for the fuel elements were disposed on a light water pitch but heavy water was used as the moderator [15]. This resulted in a flat flux distribution across most of the core with a pronounced flux maximum at the core/reflector boundary so that severe flux gradients existed across the width of outer fuel plates. The system pressure was 1.33 MPa corresponding to a saturation temperature of 466K which was attained for initial reactor periods less than 100 ms. Coolant flow rates ranged from zero to 4.3 ms^{-1}.

The most notable feature of these measurements was the demonstration that power burst parameters were sensibly independent of coolant flow rate for the initial rise to peak power if the coolant flow constant f_c (cf. Section 2.5.4) was less than the power time constant α_0. Subsequent to the initial power peak, the reactor power exhibited oscillatory behaviour which became less pronounced as f_c approached α_0. The ZAPP calculations for this core were with two zones so that the region of high flux at the outer core would be explicitly represented and allowed to boil before the inner core. The flow model was used which did not allow inclusion of void formation in the analysis. It might be thought, because of the large ratio of void coefficient to temperature coefficient shown in Table 7-1 that this would produce large errors; however the calculations showed that the volume of the core actually above saturation was small compared with the remainder. The calculations gave very good agreement with observed values and showed the same independence on flow rate for the initial burst. The average ratio of experiment to calculated temperature at peak power for seven transients was 0.88 .

The post primary power peak power behaviour was quite well represented in the calculations and it proved possible to obtain good estimates of the quasi equilibrium run out power by coupling the flow equation

$$\frac{dE}{dt} = P - f_c E$$

to the Nordheim-Fuchs equation, giving

$$P_\infty = \alpha_0 \frac{f_c}{b}$$

The frequency and amplitude of the power oscillations and their dependence on flow rate obtained from the numerical solution of the first of these equations are in reasonable agreement with

observation and with ZAPP calculations, so that, although the power behaviour appears complex it is really only a result of the interplay between the rate of energy removal from the core (coolant flow out) and the rate of energy input (fission power). It may also be inferred that the time delay between the release of fission energy in the core and its transfer to the coolant is small.

7.1.5.6. Departure from nucleate boiling (DNB).

As discussed in Section 5 the limiting condition for reactor operation is the establishment of film boiling or a redistribution of coolant flow rate in the coolant channels leading to channel dry out. The code ZAPP has no built in criterion from which to establish whether or not the conditions for these phenomena have been attained although, in principle, the output from the code could be examined to check this. As noted in Section 7.1.4 codes such as PARET rely on steady state correlations to detect DNB and to establish heat transfer coefficients under these conditions, and thus to allow the calculations to proceed in a more meaningful way than ZAPP if the correlations are correct. Given the above comments it appears worthwhile to discuss briefly a transient in SPERT BD18/68 that resulted in a rather severe DNB condition and the partial melting of some twenty fuel plates in the high flux portion of the core [15]. This transient was one of a group sharing the common experimental parameters:

- initial period 100 ms (reactivity injection \$1. 6),
- system pressure 1.33 MPa (saturation temperature 473K), and
- coolant inlet temperature 300K.

With these values set, transients were launched with coolant flow velocities of 0.1, 0.122, 0.427, 1.07, 2.1 and 4.3 m s^{-1}. With the exception of the last of these nucleate boiling was established in the high flux region of the core at about the time of the first power peak and maintained for several seconds thereafter until the reactor was shut down by control rods. However, in the case of the transient with a flow velocity of 2.1 m s^{-1} a rapid temperature transient occurred about two seconds after the initial power peak. At this time the power oscillations had almost damped out and the reactor power was approaching an equilibrium value of 140 MW. The temperature transient began near the channel exit and, as indicated by the melt pattern of affected plates, spread down the channel towards the core centre plane. The recorded rate of temperature rise was about 700 K s^{-1} which is about half the adiabatic rate that would be produced by the power at that time. The change in heat transfer conditions was sufficiently fast and localised to prevent heat conduction in the plate in a lateral or vertical direction to play a role, since the unfuelled edges of the plate and the region of plate away from the high flux zone remained unmelted.

Measured cladding temperatures remained approximately constant, slightly above saturation temperature, from the time of the first power peak to the occurrence of the first temperature transient indicated two seconds later by a thermocouple 228 mm above the core centre. The temperature transient 76 mm above the core centre commenced about 0.75 seconds later, presumably from the rate at which film boiling spread down the channel. Some thermocouples indicated temperature spikes suggesting dry out and rewetting in their vicinity; these did not attain melting temperatures. Of a total of 396 fuel plates in the high flux region of the core only 20 were subsequently found to have partially melted which suggests that rewetting is a significant factor in the thermal behaviour.

These general features are illustrated in Figure 7-3. Here we have converted measured reactor power to the corresponding surface power density in the high flux region; in the region of constant cladding temperature this is identical to the heat flux into the coolant. From the parameters given for the core we have determined the critical heat flux using tables [21] and find the value 5.5 MW m^{-2}. This is reached briefly on the trailing edge of the first power peak and for even less time at the maximum of the second power oscillation. At the time of the first temperature transient, however, the heat flux was only 4 MW m^{-2}, and it seems probable that nucleate boiling in

the high flux channels caused flow redistribution to the remaining channels which did not reach saturation temperatures during the test. From the same method as used to determine the critical heat flux we estimate the flow in the affected channels would need to be halved to have led to film boiling. However we note that the coolant flow velocity is not very well defined in reference (15) and the core construction allows for considerable core bypass flow so that the actual channel flows may have been considerably less than the nominal ones given.

From the point of view of HIFAR safety the above data are important because they indicate that, under oscillatory power behaviour, nucleate boiling can be maintained for times which are long in units of control system response time, and, as shown in Figure 7-3, a plate undergoing a temperature transient will rapidly rewet and cool when the reactor transient is terminated by scram action.

7.1.5.7. Comparison with PARET.

It is of interest to compare ZAPP calculations over a range of transient behaviour with the predictions of other codes. Generally, where comparison is possible the results of TANK, NAIADQ, and PARET are in good agreement with ZAPP; we briefly discuss the ZAPP-PARET comparison because the PARET code and results are more familiar to us, and the calculations used the reactivity feedback coefficients developed for use in ZAPP. Thus the results obtained from the two codes should highlight the different approaches used to describe heat transfer and to a lesser extent the difference in spatial representation of the reactors analysed.

As previously discussed, ZAPP incorporates somewhat novel descriptions of the sub-cooled nucleate boiling heat transfer regime and only allows radial heat transfer form fuel plate to coolant. Although it is quite possible to represent the reactor in greater spatial detail by appropriate specification of zones, in the calculations discussed here only a single average zone was used to represent the reactor and maximum plate temperatures were obtained by assuming the power form factor to be unaltered from the static measured value during the course of the transient. PARET, on the other hand, uses a set of correlations which are chosen to give the 'best' agreement with measured data; the reactor is represented spatially by two axial channels, a 'hot' and an average channel. Each channel was divided into 21 equally spaced nodes and the fuel and clad regions assigned 5 and 2 nodes respectively for the radial heat transfer solution.

A comparison between burst parameters obtained with the two codes and those measured on the SPERT core D12/25 is shown in Figure 7-4. For small values of α_0 both are in good agreement with the measured data, indicating that the feedback coefficients for non-boiling of the coolant and the spatial reactor representation are correct. For α_0 in the range between 5 and 10 both codes overestimate P_{max} and E_{tm} and it may be that both are predicting ONB too late, although ZAPP is, in our judgement, somewhat better than PARET in this regard. For faster periods the ZAPP data (calculated with the voiding model which is necessary for α_0 greater than $40s^{-1}$) are in good agreement with measured data, even that recorded for the excursion which destroyed the core. PARET shows a greater non-linearity in the feedback reactivity in the range above ONB as can be seen from the flatter shape of the E_{tm} versus α_0 curve. Both codes give rather similar estimates of temperatures at peak power and are higher than those recorded; however, it is difficult to know what level of agreement should be looked for in such an intensive parameter.

The most astonishing thing in this data is not that the two codes exhibit differences in their results but that in the region above ONB their results are so similar. This, given the differences in the heat transport modelling, must be due to the highly non-linear rate at which feedback is generated which lessens the importance of the actual magnitude of feedback rate in determining burst parameters. In other words, if a model makes a reasonable estimate of ONB and the heat transfer coefficient under these conditions is large, then any question as to the physical reality of the model becomes difficult to answer.

Both PARET and ZAPP [22] predict melting for α_0 greater than 150 s^{-1} and ZAPP estimates that for the destructive burst about 35% of the core was molten. Both these are in reasonable agreement with observation.

7.1.5.8. Calculation of SPERT BD22/24 data with ZAPP.

As has already been mentioned, the SPERT core BD22/24 is very similar to the HIFAR core. Unfortunately no transient tests under conditions of forced coolant flow were made although the consequences of core pressurisation were explored. ZAPP calculations [19] of these transients are shown compared with experimental data in Figure 7-5. Agreement between them is good and the threshold for nucleate boiling under a pressure of 2.6MPa is well modelled.

7.1.5.9. HIDYN.

As already discussed, this code was developed to allow analysis of transient reactor behaviour influenced by the characteristics of the primary and secondary coolant loops. As the fission energy is considered to be released directly into the coolant, the code is essentially based on the Nordheim-Fuchs linear with energy release model and non-linear feedback from nucleate boiling and void formation cannot be represented. As given in Section 2.6 the thermal time constant of the coolant channels is 0.042 s^{-1} so that the rule of thumb for the applicability of HIDYN is that the period of the reactor power rise should not be much less than 24 s or the reactivity input greater than 200 10^{-5} dk/k. As discussed in Section 4.5 the largest uncertainty is in the description of the coolant flow path in the RAT which must be a rather stochastic process. However analysis, by means of HIDYN, of a slow ramp addition of reactivity to an amplitude of 140 10^{-5} dk/k in the Danish PLUTO type reactor DR3 [16] showed that the computed power history was in good agreement with that observed, provided that the fraction of coolant assumed to flow to the bulk moderator was greater than one half. This transient occupied one minute or about two primary coolant cycle times. The reactivity coefficients used in this calculation were those for coolant and bulk moderator only, and were obtained by use of the AUS codes.

Subsequent to the construction of HIDYN the code was used to analyse transients produced by valving off secondary coolant flow and by switching on a third main circulating pump, with the aim of determining constants such as temperature coefficients of reactivity that gave best fits to observed data, and models of flow partition in the RAT consistent with observed power variations [8]. The temperature coefficient derived from the secondary coolant flow perturbation was less than the static whole reactor coefficient which may be interpreted as a consequence of only a part of the coolant flow being directed to the bulk moderator; however, the data obtained from an increase in primary coolant flow indicated a temperature coefficient in much better agreement with the static value which implies a change in the flow distribution at the higher flow rate. Both experiments indicated that there were no long delays in the circulation. Now that better knowledge of the spatial distribution of reactivity coefficients in the RAT is available it might prove profitable to re-analyse this data with a more detailed representation of the RAT regions and their associated reactivity contributions.

Note. In Section 3.4 of reference [5] it is stated that calculations indicate that 75% of the whole reactor temperature coefficient arises from heating the coolant. This is an error that arose when specifying data for the original AUS perturbation calculations and should be 25%; this error is also present in the calculations described in reference [24].

7.1.6. Application of ZAPP and HIDYN to HIFAR transient calculations.

ZAPP is the only verified code available that can explicitly represent the HIFAR fuel element geometry. It has already been noted that the basic version of the code operated with a fixed inlet

temperature so that its early use was restricted to modelling fast transients. On the other hand, HIDYN treats the energy as being released directly into the coolant which is a satisfactory approximation for slow power changes. A natural subdivision of this section is thus into fast and slow changes in reactivity and power. The subdivision is very loosely defined by choosing fast transients as those which will be terminated before flow of coolant can have any perceptible effect; this ignores the grey area of transients of intermediate speed.

7.1.6.1. Fast transients.

Since it is not possible for the reactor to tolerate an unbounded power excursion it is necessary to determine what combination of intrinsic reactivity feedback and control absorber intervention is adequate to safely terminate a given transient. The constraints on this problem are often assumed to be that neither the flow instability power nor the critical heat flux will be exceeded for times long enough for fuel melting to occur. As noted in Section 5.4.6 both these parameters have been determined for the steady state under rather conservative assumptions; calculations have shown that under transient conditions both may be exceeded before ONB and therefore the occurrence of Ledinegg instabilities or film boiling will be predicted to occur too early.

Notwithstanding this reservation, a survey was conducted [23] using the ZAPP flow model to establish the reactor response to a range of reactivity ramp rates and amplitudes with the assumption that the fuel tube temperatures at the core centre increased adiabatically as soon as the flow instability power was exceeded. The safe termination criterion was taken as that confining the whole core energy release to that which would just bring the highest rated fuel element to the melting point (25 MJ). Accordingly, a response time T_r was defined as the maximum time which could elapse (after the trip setting was passed and before the CCA bank would be inserting its maximum negative reactivity ramp) for the CCA action to limit the energy release to this value. This may then be compared with the delay time T_d which is the sum of three components; the time after passing the trip point for the guard line relays to open, the time after this that the arm electromagnet clutches take to disengage, and finally, the subsequent time for the CCA bank to reach its maximum rate of reactivity insertion. The requirement for safe termination of a transient is therefore that $T_d < T_r$.

A series of trial and error calculations with ZAPP made it possible to plot loci of T_r on the ramp rate/amplitude plane thus making it possible to identify areas containing transients for which $T_d > T_r$, that is transients which, given the assumptions, would lead to fuel melting. The calculations were limited to those where it was believed that steam void did not contribute to shutdown, a limitation imposed by use of the flow model in ZAPP. The consequences of only part fall of the CCA bank, of degraded fall, and of transients launched from low power were also explored.

In general this survey showed that the reactor would safely self limit transients produced by the injection of 90 ¢ of reactivity at any rate and rather more for slow ramps launched at full power. For normal operation of the CCA bank ramp rates in excess of \$4 per second and amplitudes greater than \$2 were required to seriously challenge the performance of the bank.

With hindsight it would have been more exact to have defined the response time T_r as the interval between the time at which the power level is such that the heat generation first exceeds the rate of conduction to the coolant, and the time at which the power level drops to a value where this is no longer true; an corresponding redefinition in the allowable delay time T_d would also have had to be made.

However the calculated fuel element temperature rises were checked against that temperature rise which would lead to melting. Even on the bounding loci this condition was never reached and the conclusions of the study provide conservative limits.

In the light of the present work the above analysis could be refined since ZAPP now contains an explicit reactivity insertion function for the scram action of the CCAs, and a better understanding of the 'off magnet' time delay exists; both these features will significantly reduce the calculated values of T_d. However, to repeat these calculations would be tedious and probably not worth while since it has already been shown that only a severe reactivity accident is likely to be of concern. Such an accident is the postulated fracture of a CCA connecting arm whilst the reactor is critical at a low CCA angle, thus allowing an arm to swing from a position of considerable reactivity control to the vertical where the reactivity controlled is exceedingly small. This presupposes that the rod fractures under static loading conditions whereas, as shown in Sections 3.1.3.1 and 3.1.3.2 the rod stress is some five times greater when an arm is brought to rest following a scram and it might reasonably be assumed that fracture would occur at this time; since the remaining arms would also have fallen into the core such an eventually is of little consequence. However, because this postulated accident is severe and illustrates very well the complexity of transient over power calculations we will discuss the significant features that examination [25] of it has revealed.

The starting point in any transient analysis is to determine the form of the postulated reactivity insertion. In the case being considered, fracture of a connecting rod produces the curious feature of initially driving the reactor sub critical in the early part of the arm motion, thus allowing high angular velocities to be attained before positive reactivity begins to be inserted. This leads to the reactor response approximating a step change of reactivity. Mechanical motion of the arm in the case of a single arm dropping 'off magnet' - the remaining arms failing to drop under a misalignment signal - and the connecting rod failing at the time the rod armature engaged the datum stop lever would be difficult to analyse because of the unknown boundary condition on the subsequent motion; and simultaneous failure of both pivot and yoke bearings would produce arm motion which could only be guessed at.

By combining the equation of motion given in Section 3.1.2 for restricted fall with the data for the reactivity control of a single arm as a function of angular position, the required reactivity input function can be obtained; the exact form during the sub critical regime is not overly important except in determining whether the halving time trip will function.

> [As a particular side issue, it is of interest to determine whether the maximum angular swing of the arm allows it to strike the wall of the RAT. Reference to the solution of the equation of motion given in Section 3.1.2 for $\dot{\theta}^2$ shows that the arm swings through the vertical to an angle γ (radians) = arctan (1/2A) ≈ 1/2A. From the geometric relations between the RAT wall and the pivot bearing, and assuming A=5, it can be shown that only the outer arm can reach the wall and does so 0. 8° before the arm velocity would become zero.]

The absolute gain in reactivity following a central arm swinging through the core to the vertical position has been determined by a synthesis of experimental data [26] [27] and from AUS 3D calculations [28]. A comparison between these data is shown in Table 7-2.

Table 7-2
Reactivity Gain on Loss of Central CCA.

Critical Angle (degrees)	Experiment (dk/k)	Calculation (dk/k)
10.0	0.0219	0.0211
12.0	0.0191	0.0172
14.0	0.0151	0.0136

Agreement is good and, since the experimental data were obtained from sub critical multiplication techniques which may be questionable when applied to determining large reactivities,

perhaps better than might reasonably be expected. When the arm is removed the reactor is thus well super prompt critical; taking the prompt lifetime as 600 μs, the loss of an arm from 10° would result in an inverse period of 24 s^{-1} if the reactivity were added as a step. This is close to the maximum value of inverse period calculated using the actual reactivity input function.

Analysis of the power history following loss of an arm has been made with the no coolant flow version of ZAPP because of the necessity of including a voiding model in the shutdown process. Immediate justification of this rests with the experimental evidence from SPERT BD18/68 which showed that the parameters of the initial burst were independent of flow rate when the coolant time constant for flow was less than the power rise time constant. The reason for this can be seen in a simplistic way by solving the flow equation of Section 2.5.4 with an exponentially increasing power of time constant α. It can then be shown that

$$\frac{\text{Rate of energy flow out}}{\text{Rate of energy flow in}} = \frac{f_c}{f_c + \alpha}\left[1 - e^{-(f_c+\alpha)t}\right]$$

This ratio is small for $f_c < \alpha$ and $t < (f_c + \alpha)^{-1}$. The last inequality is satisfied because nearly all the reactivity feedback occurs in a small time interval about the time of peak power. We have seen that the maximum power time constant in the burst is 24 s^{-1} and for normal 10 MW operation f_c is 5.9 s^{-1}; under operation of the shutdown pumps it is 0.65 s^{-1}. However the evidence supports the case that an appreciable fraction of the coolant flow from the fuel passes to the bulk moderator region; if we express the temperature coefficient as an energy coefficient we obtain $-31\ 10^{-5}$ dk/k per MJ, which is close to the coolant value of $-37\ 10^{-5}$ dk/k per MK and the rate of energy removal is decreased because of the longer residence time of coolant in the bulk moderator.

There are two threshold reactivity effects of importance in determining the parameters of the initial burst; the onset of nucleate boiling and the development of a significant void fraction in the coolant. The threshold for the former is only a few MJ and the reactivity feedback generated before threshold small so that the dominant effect is the rate of heat transfer under nucleate boiling conditions and the calculated behaviour is not unduly sensitive to the threshold value assumed for ONB. The threshold temperature for void development is set in the calculations not far above that for ONB; however nucleate boiling will slow the rise of cladding temperature as the rate of heat transfer to the coolant becomes faster than the rate of power rise. This will result in a considerable energy release between the ONB and void thresholds; since the voiding model indicates the power rise is arrested some 70 ms after void growth commences, the total energy release is then more sensitive to the choice of this threshold.

The ZAPP calculations are performed on an average cell and the threshold value for this cell is related to the core centre threshold by means of the core power maximum to mean ratio; this is assumed to be the same as the same ratio of temperature rises. However, with the onset of nucleate boiling (first in the core centre) the temperature rise distribution over the core will become flatter than the power distribution and the average cell threshold temperature will be underestimated; by way of example, changing the temperature ratio from 1.5 to 1.2 increases the threshold temperature for the average cell from 390K to 406K. The possibility also exists that the removal of a central arm from the core will produce a significant change in the power form factor from that obtaining with a normal CCA configuration, but 3D diffusion calculations indicate that the effect is slight, -3% at a CCA angle of 10° .

It is now of interest to compare the ZAPP results obtained for the two cases of a loss of CCA at low power and a comparable transient in SPERT BD22/24. These are as follows.

	BD		HIFAR	
Reactivity injection	\$2.94	(step)	\$2.92	(near step)
Inverse period	20 s^{-1}	(initial value)	29 s^{-1}	(max value but increasing l_a from 500 to 600 μs gives 24 s^{-1})
Maximum power	306 MW		455 MW	(increasing l_a would reduce this)
Energy release at peak power	19.7 MJ		22.8 MJ	(increasing l_a would increase this slightly)
Max clad temperature	610 K		641 K	
Void volume	6 to 8 l	at unspecified time	4.9 l	at peak power

The general level of agreement between these data gives confidence that the ZAPP calculations will give a good description of the power history to the time of peak power following loss of a CCA. The power history data for loss of an arm from 10 ° has been used to construct an input signal to actual HIFAR power amplifiers and period meters, and the time to trip determined. (The period meters have since been replaced with units of different design.) A useful measure of the effectiveness of these units is to compare the time interval between trip relays opening and the attainment of peak power - without scram action - to the off magnet time interval discussed in Section 3.1.2.2. These are

Power (MW)	Trip	Time from trip to P_{max} (ms)
0.01	Period	338
0.01	Power	248
10.0	Period	80
10.0	Power	180

The off magnet time determined from the mean value of head units ECD is 84 ms so that it is only the period trip at 10 MW that cannot prevent the self limited power from being reached. Referring to Table 3-2 we see that the time required for the complete bank to remove \$2 of reactivity once they start to move from an angle of 10° is 87 ms; although this will be somewhat longer for a five arm scram nevertheless, because the prompt reactivity in this accident is \$1.93 , it can be seen that the shutdown system can make the consequences less than for the self limited transient except in the case of the period scram for high power operation. Note that the order of tripping reverses between the low power and high power cases; this is a consequence of the greater margin to trip for the power amplifiers in low power mode.

It is of interest to determine whether or not the safety rods can influence the outcome of this accident. From data given in Section 3.2 it can be shown that the rods do not enter the core until 527 ms after the trip relays open and for the data tabulated above this is at times 189 ms, 279 ms, 447 ms, and 347 ms after peak power for the low power period, low power power, high power period, and high power power trips respectively. Thus if the CCAs fail to drop the safety rods can terminate the excursion if their combined worth is kept above the worth of the lost arm but not before the peak power has been passed and the uncontrolled power has started to oscillate about some run out power value. As previously discussed, this run out power can reasonably be estimated from $\alpha f_c/b$ for the B18/68 value. Note, however, that for this core there was no bulk moderator region and the coolant flow passed unequivocally into the top reflector. For HIFAR the run out power, neglecting reactivity feedback effects arising from the reflector is given by

$$P = \frac{\alpha_0}{b_1/f_1 + \zeta b_2/f_2}$$

where subscript 1 denotes values of the feedback coefficient and flow constant for the fuel elements while subscript 2 denotes those for the bulk moderator; ζ denotes the fraction of coolant flow directed into the bulk moderator. Where this fraction takes values 0.0, 0.5, and 1.0 then P takes the corresponding values 200 MW, 75 MW, and 46 MW if the reactor is operating in the high power mode; when operation is in the low power mode the power values are 16 MW, 6 MW, and 4 MW. It is thus very unlikely that the safety rods will prevent melting in the high power mode. In the low power mode case the flow instability power level is 5 MW: the energy release after the power first passes this level is just 0.2 MJ so that it is physically impossible for boiling to occur. Instead, if we assume that adiabatic heating of the fuel commences at the time of peak power then it can be calculated that a further 16 MJ of reactor energy are needed for the highest rated element to reach melting temperatures and an additional 12 MJ of latent heat to melt the element completely; this makes a total of 28 MJ. For a run out power of 6 MW, corresponding to half the coolant flow being directed to bulk moderator, this means that 4.7 seconds are required to melt the highest rated element entirely and 2.0 seconds required for this element to reach its melting point. It would seem that the safety rods are effective in this situation although it must be remembered that the mixing time constant of the bulk moderator is small at these low flow rates; if it is assumed that no flow passes to this region the time required to reach melting temperatures shrinks to one second but this is still greater than that required after trip for the rods to enter the core.

7.1.6.2. Slow transients.

Paradoxically, a slow power transient may pose a greater risk of causing fuel element melting than a fast transient. This is because safety depends on the power level trips if the rate of power rise is less than that required to activate the period trips. If these power level trips are wrongly set, or if the ion chambers are operated in a non-saturated condition, then the power may reach the flow instability level should the operator continually override the effect of feedback by raising the CCA. Under these conditions the calculated flow instability power level is a valid criterion for defining the onset of inadequate cooling of portion of the core.

The code HIDYN was developed to allow calculation of transients involving all the primary and secondary cooling loop components. As discussed in Section 4.5 the major uncertainties lie with the description of the coolant flow path in the RAT. It has been shown [17] that inserting a delay between the coolant leaving the core and the fraction entering the bulk moderator will cause oscillations in reactor power about the power level predicted when there is no such delay. It was found that the calculated power history was relatively insensitive to the fraction of coolant passing straight to the bulk moderator provided that this fraction was greater than one half.

Only a very limited range of events has been examined by use of the code and these were rather artificial, requiring almost deliberately perverse actions by the operators to bring them about [23]. The first assumes that the reactor is shut down without any primary coolant pumps operating but pumps and fans in the secondary circuit are left on. The temperature of the D_2O in the RAT is taken as 50C and that in the secondary circuit 20C. After all of the D_2O in the three heat exchangers has been cooled to this latter temperature the reactor is, somehow, taken critical at low power still without any primary circuit pumps, until a single main pump is switched on; this deliberately induces a 'cold slug' transient. The temperature coefficient of reactivity produces a reactivity ramp of about $4.0\ 10^{-3}$ dk/k per second and a ramp amplitude of about 0.011 dk/k. This transient is rather fast to allow full confidence in the applicability of HIDYN but the results are compatible with those for similar transients examined by means of ZAPP. The peak power is about 90 MW but temperatures do not exceed saturation; the run out power is about 15 MW which is in good agreement with that obtained (14 MW) by use of the equation in Section 7.1.6.1 with half of the flow passing to the bulk moderator.

The second case considered is equally implausible but less severe, involving the switching on of three H_2O pumps with a pond temperature of 15C and the reactor already critical at a temperature of 50C with two main pumps operating. The ramp rate and total reactivity inserted are sufficiently low to enable the reactor to self limit the power to a value below the flow instability level.

7.2. The Loss of Coolant Accident (LOCA).

If a leak develops in the primary coolant circuit (PCC) external to the RAT, coolant will be lost from the circuit and collected in the plant room sump and floor. If no remedial measures are employed the core will ultimately be left without means of sufficient heat removal and partial or complete fuel tube melting will follow. The course of such an accident will be determined by intrinsic properties of the core such as the time dependent power and flow rate of coolant. The overall time scale of a LOCA, which we define as the time from the occurrence of the leak to the attainment of equilibrium flow distributions in the circuit, will largely be set by the size and location of the postulated break in the circuit. Within this time interval the following events are considered to occur.

(i) The pressure drop caused by the leak and flow through it will reduce the flow through the core towards a quasi equilibrium level. For very large breaks the flow may reverse. Increase in coolant temperature will produce a slow fall in power from the negative temperature coefficient of reactivity. The central concern in this phase is whether the coolant flow/power mismatch is sufficient to damage fuel tubes.

(ii) The reactor will trip when the water level in the RAT falls by 15 cm. or the central fuel element outlet temperature exceeds 62 C. Concurrently the main pumps are switched off and they run down in about three seconds; the shutdown and ECCS scavenge pumps are switched on. Flow through the core will largely be determined by the leak size for large leaks and may reverse for certain leak locations.

(iii) decrease in the height of the top reflector and any draining of the coolant channels will occasion large losses of reactivity, and will accelerate the decline in fission power.

(iv) Ten seconds from scram the scavenge pumps commence returning water to the RAT.

(v) If the water level falls by 56 cm. the shutdown pumps are turned off.

(vi) Ultimately the coolant flow rate and distribution in the coolant channels of the core will reach some equilibrium values determined by the leak location and size. The aim of the analysis is to determine whether these values are sufficient to prevent damage to the fuel elements from excessive temperatures.

In this section we do not attempt a detailed examination of the above phenomena but, by suitable assumptions and definitions, provide an outline of the expected behaviour under LOCA conditions. The justification for this approach is that while it might not provide an exact description of a particular LOCA, it provides a range of data within which any plausible LOCA behaviour would be found.

7.2.1. Overall behaviour of the PCC.

We find it convenient to examine the PCC and ECCS in terms of the simple current analogue circuit shown in Figure 7-6. Here the capacitor C_1 and resistor R_1 represent the initial water level and the rate at which the level reaches the leak after the pumps are turned off. R_2 represents a small bore (1.8 cm) bypass line and R_1 and R_2 are much greater than the other resistances in the circuit which represent flow impedances in heat exchangers, pumps etc. The diode represents the non-return valve and may permit reverse flow simulating partial sealing of the non-return valve. The ECCS is represented as a constant current source with a switch closed at a suitable time after closure of a leak select switch. The flow impedances in this circuit will depend on the cross

sectional area and length of components, and on the flow rate through them. For the sake of simplicity we will assume the total impedance in each leg to be equal under flow conditions with main pumps off. Some justification for this can be seen from the following cross sectional area data.

- Water area in RAT. (≈ cross sectional area of RAT less cross sectional area of 2V and 6V thimbles) = 3.1×10^4 cm^2.
- Four downcomers = 993 cm^2.
- Three risers = 1236 cm^2.
- Core coolant channels = 1015 cm^2.
- Heat exchanger tubes = 3 exchangers, each with effective area 727 cm^2.
- Element coolant outlet holes = 4273 cm^2.

In contrast, the ECCS holes have a total cross sectional area of 152 cm^2 and the bypass line 2.5 cm^2, so these are of little importance when the total flow in the system is large.

It can be seen that for a break between A and B, the water flow through the core will reverse direction but not that in the heat exchangers; whereas for a break between C and D, flow will reverse in the complete leg. For a break at E the flow in the leg will be set by the leak size but the pumps, heat exchangers, upcomers, and core will drain at a rate set by R_2 and reverse flow through the diode. It is clear that a dominant parameter setting the time behaviour of the system will be the size of the leak. In the following we have arbitrarily chosen a maximum leak cross sectional area of 250 cm^2 which is half that of the pump discharge header. A crude visualisation of such a leak is that it corresponds to a complete circumferential break in a pipe of radius r and a separation of the break ends by a distance d = 40/r (cm). In what follows we will calculate the time dependence of water level from the equation

$$t = \frac{2A^*[h_0^{\frac{1}{2}} - h^{\frac{1}{2}}]}{CA[2g]^{\frac{1}{2}}}$$

where

A^* = free water surface in leak path

A = cross sectional area of leak

C = discharge coefficient of leak = 0.6

h_0 = height of upper boundary of free water surface area A^* above leak

h = height of water surface above leak at time t (seconds).

and all dimensional data are expressed in centimetres.

7.2.2. Core water flow from time of break to reactor trip (h = 0 to h = 15 cm.)

The greatest change in core flow will come from a large leak in the pump discharge header where the pressure is greatest. For obvious reasons experimental data for this situation does not exist and reliance must be placed on calculation. For a leak area of 250 cm^2 RELAP-3 calculations [29] showed that, with three main pumps running, the core flow reached 50% of the normal value in about one second if the flow delivered at the pump outlet was held constant; in actuality the flow should increase because of the pressure drop caused by the leak and it has been estimated [29] that this causes the core flow rates to be underestimated by about 20%. The calculated time dependent flow rate is not dissimilar to that observed [30] in PLUTO in the first second after tripping three main pumps with the reactor at an initial power of 15 MW. Temperature increases

measured in this experiment were modest and the reactivity feedback reduced the power by 12% in this first second; we conclude that the time interval for the core flow to approach an equilibrium value does not hold any hazard to the well being of the fuel tubes.

The equilibrium flow rate in the core, including the effect of enhanced pump output, has been determined in a separate calculation [29]. If we denote by F_{ce} the equilibrium core flow rate, by F_{co} the initial value, and by F_L the leak flow rate then these calculations have the approximate forms

$$\frac{F_{ce}}{F_{co}} = 1 - 1.2 \times 10^{-3} F_L$$

$$F_L = 1.2 A$$

and since, from the data of Section 2.7.1, there are 468 litres of water between normal level and the trip level, the time to trip T_t is

$$T_t = \frac{468}{F_L}$$

where all flow rates are expressed in litres per second. From the first and third of these equations we can prepare a plot of the parameter F_{ce} / F_{co} against the parameter T_t and this is shown in Figure 7-7. It can be seen that as the flow perturbation becomes large (small F_{ce}/F_{co}) the time to trip decreases rapidly. Thus if we assume the reactor power to remain constant from the time of break to the time of trip (a poor assumption because of feedback), the energy release is 10 T_t MJ. From the data of Section 2.6 we calculate that to raise the contents of the highest rated fuel element from 50C to 100C would require a whole core energy release of 11.3 MJ and this can only occur for values of F_{ce}/F_{co} greater than 0.5, roughly equivalent to the failure of one pump in normal HIFAR operational terms. Since this analysis assumes equilibrium conditions to be established instantaneously and neglects the power coast down, it is over conservative and again we conclude that this phase does not threaten fuel element integrity.

No information is available as to the flow characteristics following a break on the suction side of the pumps. The pressure there is close to atmospheric and for modest leaks it is probable that the core flow will diminish by the flow rate from the leak. However, for greater leak rates it would seem certain that a large amount of air would become entrained in the flow to the core; we have not investigated this situation.

7.2.3. Time interval from trip to equilibrium ECCS conditions.

The fission power falls rapidly with insertion of the CCAs. The prompt drop is given by

$$P_p = \frac{\beta_{eff} P_0}{\beta_{eff} + \Delta k}$$

where P_0 is the power at scram, β_{eff} the effective delayed neutron fraction, and Δk the sub-critical reactivity with the CCAs inserted. Subsequent decrease in power will be governed by decay of delayed neutron precursors and loss of reactivity with falling water level in the RAT. These effects can be calculated by ZAPP. Some typical results for a scram from an angle of 25° and constant water level are shown below.

Time (s)	CCA no safety rods Power (kW)	CCA with safety rods Power (kW)	Safety rods alone Power (kW)
Prompt drop	363	244	2733
10	120	110	1541
20	75	68	1037
30	55	50	784
40	42	38	620
50	33	30	501
60	26	24	411

The fission product decay heat will reflect the previous power history of the fuel. Calculations show that it is greater at the end of a single cycle than is the case for four cycles with diminishing power output. Thus from the data of Section 2.9 we obtain the decay power in the maximum rated element that has operated for one complete cycle at 830 kW

Time after scram (s)	Decay Power (kW)	Fission Power (kW)
10	23.8	9.1
20	20.7	5.7
30	19.0	4.1
40	17.8	3.1
60	16.3	2.0

Here the decay power is calculated on the basis of 26% of the gamma decay energy being absorbed in the fuel element.

It can be seen that the fission power, although less than the decay power, remains a significant contributor to the total element power; thus calculations of the time dependent power in this phase of the LOCA must include the effect on the fission power of the loss of reactivity as D_2O is lost from the RAT. However, for leak rates greater than the capacity of the scavenge pumps, the end of this phase of the LOCA will be marked by either loss of the top reflector or by loss of the top reflector with draining of the coolant channels in the core. The reactivity loss occasioned by these circumstances is so great that the fission power is of little importance.

The leak rates in this phase are determined by efflux flow from the leak

$$F'_L = \mu A[2gH]^{\frac{1}{2}}$$

where μ is the efflux flow coefficient and H the water head above the leak. The value of μ will depend on the geometry of the leak; for lack of better information a circular hole is assumed. Although the water head decreases continuously at this stage it is sufficient to consider a fixed value since the change in H is small. When the water level in the RAT has fallen by 56 cm. the shutdown pumps are switched off. There are 1156 litres of D_2O between the trip level and this point which is therefore reached at the time

$$T_1 = 1156/F'_L$$

after the reactor has tripped and the ECCS pumps have been switched on. Since it requires ten seconds for these pumps to commence water flow into the RAT, leak rates greater than 115.6 litres per second are needed if the shutdown pumps are to be turned off prior to the commencement of water return to the RAT.

The change in water level in this time interval is $10\ F'_L/A^*$ where A^* is the free surface area of the RAT so that for a leak rate equal to the capacity of the scavenge pumps (24 litres per second) the level will drop 7.7 cm below the trip level leaving 52.8 cm of D_2O above the core. There will

be no significant reactivity loss at this level so that the system behaves in the same manner as a normal shutdown since the level at which the shutdown pumps would be switched off has not been reached. For lesser leak rates the RAT will refill to the point where the output from the scavenge pumps falls by entraining air because of lack of water in the plant room sump. It is therefore evident that leak rates less than or equal to 24 litres per second are of no concern.

Consideration of larger leak rates requires specification of the location of the break in the pipework. As shown in Figure 7-5 a break between the non-return valve and the RAT will lead to flow through the core and heat exchanger determined by the bypass and any leakage past the non-return valve; the bulk of the flow will be through the downcomers until the level nears the downcomer tops and, presumably, vortex flow into the downcomers develops to be followed by weir flow over the downcomer perimeter. If no water is returned to the RAT by this time, weir flow will cease and the downcomer flow will be determined by the weld imperfections in the downcomer extensions located 5.7 cm below the tops of the downcomers. This is estimated to be less than 0.5 litres per second. It is therefore of interest to determine the level in the RAT when the scavenge pumps begin returning water to the RAT. This can be obtained from the equation given in Section 7.2.1. For $h_0 = 400$ cm, $A = 250$ cm^2, and $C = 0.6$ this equation predicts a time of 3.6 seconds to reach the trip setting, and a water level fall of 56 cm when the time is 13.6 seconds (when water begins to be returned to the RAT.) This height is 16.7 cm above the tops of the downcomers so that the level will fall until the combination of weir flow into the downcomers with flow through the bypass and non-return valve becomes equal to the capacity of the scavenge pumps. We use the standard formula for weir flow

$$F = 0.667 \mu_0 \, U[2g]^{\frac{1}{2}} h^{1.5}$$

where μ_0 is the overflow coefficient (0.57 [29]), U is the perimeter length of the four downcomers and h the height above the downcomer lips of the free D_2O surface. Assuming two litres per second for extraneous flow we recover an equilibrium level of 2.8 cm above the tops of the downcomers. Thus the core remains covered at all times during this LOCA.

For leaks developing between the outlet of the heat exchangers and the RAT the flow through the former will not reverse whereas it will for a leak between the pump outlet and heat exchanger inlet. Apart from this difference, which is not important, the predominant parameter determining the time to drain the core coolant channels is the water head above the leak for a given leak size.

A quantity of importance to be determined is the leak size that will result in the coolant channels just emptying at the time ECCS flow into the RAT commences and the leak occurs at a low point in the primary circuit. To do this we use the equation in Section 7.2.1 modified to account for the difference in free surface area between reflector and core coolant channels. Thus we write

$$t = \frac{2A^*[h_0^{\frac{1}{2}} - h_1^{\frac{1}{2}}] + 2A_c[h_1^{\frac{1}{2}} - h_2^{\frac{1}{2}}]}{0.6 \, A \, [2g]^{\frac{1}{2}}}$$

for the time t (after the trip) at which the coolant reaches the bottom of the core. Here A^*, A_c, and A are the cross sectional areas of the free water surface in the RAT, the coolant channels, and the cross sectional area of the leak. h_0 is the height of the trip level above the leak, h_1 is the height of the downcomer lips above the leak, and h_2 is the height of the bottom of the coolant channels above the leak. If we assume a leak 750 cm below the normal operating level of the D_2O in the RAT then for t = 10 seconds we find $A = 265$ cm^2. This does not mean that for such a leak size and position the fuel tubes are deprived of coolant. Although the bulk coolant in the channels drains very quickly coolant will be introduced through the ECCS holes in the shrouds. The time taken for the D_2O level in the RAT to fall from 2.8 cm to 2.0 cm above the centre line of 0.9 cm diameter holes (at which latter level flow to some channels ceases) is 3.9 seconds if flow

through the 0.4 cm diameter holes is neglected. Thus the ECCS pumps are required to commence delivery of water to the RAT within 13.9 seconds of the trip if dry out of the fuel tubes is to be prevented. Whilst dry out may not present a problem, this is contingent on fuel tube surfaces re-wetting upon establishment of film cooling; although this is likely the problem has not received detailed examination. However, from the data given above, the decay heat from a maximum rated element would be 24 kW after ten seconds into the LOCA and in the circumstances being considered the loss of top reflector and coolant in the channels will make the fission power small. From the data of Section 2.6 we deduce the adiabatic rate of temperature rise for the dried out fuel tubes to be 11 $C^{o}\ s^{-1}$. Thus taking an initial tube temperature of 80°C and guessing about 200^{0}C as the rewetting limit, we see that there is a further eleven seconds leeway for the pumps to begin returning water to the RAT.

7.2.4. Equilibrium conditions for heat removal.

We here consider a leak between the pump inlet and the RAT. As shown, this produces an equilibrium level of D_2O in the RAT of 2.8 cm above the tops of the downcomers, that is about 0.2 cm above the centre of the lowest coolant discharge holes in the fuel element shrouds. For A = 250 cm^2 and h_0 = 400 cm, the shutdown pumps will be turned off at about the same time as the scavenge pumps begin to return water to the RAT and the water level above the downcomers is 17 cm. The water flows in the system are then a downwards flow through the core and heat exchangers to the leak via the bypass line and non-return valve, which we assume to have the nominal value of 2 litres per second, and decreasing flow to the equilibrium level into the downcomers. Because this flow is considered to be complex (vortex formation) we do not attempt to calculate the time to reach equilibrium.

Now the flow into the downcomers is from the bulk moderator and reflector alone; the heat sources in them come from the fraction of the decay gamma source not absorbed in the fuel tubes and from heat conduction across the fuel element shrouds. The former may be quantified as 0.375 of the total decay heat; we have not attempted to evaluate the latter. This downcomer flow has no access to a heat sink other than the plant room floor.

If we choose time zero as being when the shutdown pumps are turned off (10 seconds from scram for the case being considered) then from the data of Section 2.7.3 we have

Decay power in maximum rated element	=	24 kW
Fission power corrected for top reflector loss	=	5 kW
Total core power	=	348 kW
Total power in D_2O	=	130 kW

From these we can derive

Rate of temperature rise in bulk D_2O	=	0.007	$C^{o}s^{-1}$
Rate of average temperature rise in core	=	1.0	$C^{o}s^{-1}$
Rate of temperature rise in maximum element	=	2.0	$C^{o}s^{-1}$

We have taken the flow rate through the bypass and leakage past the non-return valve to be 2 litres per second; if we further assume a temperature difference of 40 C^{o} across the core we finally deduce

Total rate of core heat removal	=	340 kW
Rate of heat removal in maximum rated element	=	13 kW

It is apparent that boiling will occur in the highest rated elements and will continue until the decay power has halved; this will require about five minutes from the time of the scram. Coolant expelled from boiling elements will return by flow in from the lower coolant outlet holes and the

ECCS holes; because the outer channel has a smaller power input than inner channels it is likely that a stable circulatory flow may establish within the element but this has not been investigated. However, the heat flux is not large, 26 kW m^{-2}, so that adverse effects on the fuel tubes are not to be expected. The major effect is to enable part of the coolant inventory to flow into the heat sink represented by the D_2O in the RAT.

The heat transfer properties of the heat exchangers at the low, reverse flow conditions encountered in this LOCA are not known to us but because the tube cross sectional area is large the flow velocity will be small and it might be expected that the outlet temperature would approach that of the secondary coolant. For an inlet temperature of 90 C and an outlet temperature of 30 C, the rate of heat removal would be 500 kW compared to the total input of 483 kW. Temperatures would then change only slowly with time.

For a leak elsewhere in the PCC boiling of the film is relied on and this is discussed in Section 6.6.

With regard to heat removal from the PCC we refer to Figure 7-6 which shows that, for a break between C and D, the flow through the heat exchanger will be the core aggregate film flow. For a break between A and C, it will be the aggregate flow through the downcomers; this is the flow returned by the scavenge system less the aggregate core film flow. That is, for a single scavenge pump operating, the flow through the heat exchangers will be either 9 litres per second or 3 litres per second; for operation of both scavenge pumps these flows become 10 litres per second or 14 litres per second. As before, assuming a temperature drop across the heat exchangers of 60C, the smallest flow (3 litres per second) can remove 750 kW. Since this is greater than the maximum decay power to be removed it is clear that boiling of D_2O in the RAT cannot occur.

7.3. Fuel Melting.

It is apparent from the foregoing discussion of major accident sequences that failure of parts or the whole of the protective system may result in melting of fuel tubes. While it is not possible to provide a quantitative assessment of the time scale and magnitude of a core melt nevertheless a qualitative description is of some value since available data suggest that in many instances melting would not lead to more than economic loss and public outcry. These consequences, while to be deplored, are a long way from the catastrophe usually associated with the words core melt.

The broad categories within which fuel melting may arise are

(i) Fuel melting in the presence of water/steam. The most likely path to this is through a sufficiently severe reactivity accident and the dominant heat source is that from fission.

(ii) Fuel melting in the presence of steam/helium. This can only be occasioned by a LOCA that drains the coolant channels with failure to return scavenge flow to the RAT. (The helium is supplied from the gas holder which is assumed to contain sufficient helium to prevent ingress of air to the RAT.)

It will be noticed that we have not included, as pathways to melting, loss of coolant flow or a LOCA which leaves the fuel channels flooded. This is because the former would require failure to scram of both the CCAs and safety rods, and, even then, the reduction in power produced by reactivity feedback would probably be sufficient to prevent excessive fuel temperatures. In the latter case the loss of top reflector would make the core so far sub-critical that fission power would be of small importance, so that the expulsion and return of water to the channels should cope with the fission produce decay heat until the temperature of the D_2O in the RAT approaches saturation.

Historically, fuel melt accidents that have occurred in research or test reactors have been caused

(a) by reactivity accidents producing high transient over powers,

(b) by reduction of coolant flow in some channels coupled with an operator attempt to maintain power or rate of desired rise of power, or

(c) by poor thermal contact between clad and fuel alloy;

the major and immediate concern in such accidents is the breaching of the fission product release barrier represented by the solid alloy and clad. However, there are two phenomena which may worsen the foregoing events. The first is the possibility of exothermic chemical reaction between fuel element material and coolant, resulting in increased melting; the second is the production of damaging pressures by rapid coolant nucleation, the so called steam explosion. Such an event has the potential to fail the RAT and pipe-work, and, by the generation of missiles, possibly to fail the containment. The analysis of the radiological consequences of fuel melting is beyond the scope of this report. Here we briefly discuss chemical reactions and steam explosions.

The most significant difference between most experimental data and the HIFAR case is the existence of large amounts of noble gas fission products in the HIFAR fuel alloy. Using the AUS codes, the volume of these at 600 C and atmospheric pressure is found to have the approximate form

$$V = 17.71 - 0.0806\ M$$

where V is the volume in litres and M is the mass (g) of fuel remaining in the Mark 4/23 fuel element. Thus melting of a whole fuel element depleted to 50 g ^{235}U would release 9.7 litres of these gases at 600 C and if, the release is fast enough, foaming with increase of heat transfer area may eventuate. However, the large surface tension of the melt and the fact that the clad will melt after the alloy is believed to reduce the possibility of this occurring; nevertheless the topic should be subject to further enquiry.

A very large body of experimental and theoretical work on these topics is to be found in the literature. Here we select data relevant to HIFAR culled from reports [31], [32] which contain the references to the source material.

7.3.1. Chemical reaction.

The reaction of importance is

$$2\ Al + 3\ D_2O \rightarrow Al_2O_3 + 3\ D_2$$

which, per kg of aluminium reacted, gives an energy release of 18 MJ accompanied by the formation of 1240 litres of deuterium at standard temperature and pressure. From the data of Section 2.3 the latent heat of fusion of aluminium is 0.395 MJ/kg so that the chemical reaction of one kg of aluminium has the potential to melt 45 kg of core material at a temperature just below the melting point; this is 75% of the HIFAR core inventory. We do not consider detonation of the D_2 to be a hazard because of the helium atmosphere in the RAT and the purging of radiolytic oxygen from the system by means of the recombiner unit.

Studies of the Al/H_2O reaction have been made at small (tens of gm) and large (kg) scales. Some of the earliest of this work involved dropping large quantities of molten aluminium into water in the search for the origin of severe explosions encountered in aluminium smelters. The absence of any visible light flash when some of these tests were performed at night indicated that the explosions did not involve significant chemical reaction. Smaller scale experiments investigated the effect of melt geometry (fine sprays, jets, drops) and indicated that the reaction does not occur at significant rates at temperatures below 1000C. These experiments were marked by rapid cooling of the melt since the samples were not continuously heated.

The melt may be continuously heated by induction in the case of pure aluminium and additionally by fission heating for a sample of fuel alloy placed in a test reactor such as TREAT. Results obtained for pure aluminium heated in the presence of flowing steam gave a reaction of 0.1 mg cm^{-2} in thirty minutes at a melt temperature of 800C. This is equivalent to 1.13 grams of metal reacting in a single HIFAR fuel element. (Note that the time of thirty minutes does not imply a linear time dependence; the reaction could have started very rapidly and then stopped as a surface layer of Al_2O_3 became established.) Pulsing of 23 w/o U samples in TREAT showed that energy inputs needed to be greater than 1250J per gram of plate (alloy + clad) before any indication of the reaction was noted. Since the HIFAR fuel tubes have a total mass of 2.4 kg this corresponds to a single element energy release of 3 MJ, or, assuming a ratio of maximum to mean energy release of two, 37 MJ for the whole core. As already shown in Section 7.1, this can only be achieved by a severe reactivity accident; a LOCA event without intervention by the ECCS and the coolant channels drained would have the reaction limited by the small mass of steam in contact with the melt.

Lastly we consider the extent of the reaction in the destructive power transients in the SL1 [33] and SPERT D12/25 [34] cores. Examination of the debris in the former suggested that 1.3 ± 0.6 kg of fuel plate material had undergone the reaction and estimated the mass of molten material as 61 kg - a recent theoretical estimate by Storr [35] puts this as 43 kg. Thus about 2.5% of the melt interacted; however the temperatures were very high and have been estimated to exceed the vaporisation temperature (2700C) at the core centre. In the case of D12/25 both post accident analysis and calculations by Storr give about 18 kg as the maximum amount of the melt, the former estimating about 200 g or 1.1% of the melt as having reacted chemically. Temperatures of the alloy in this test were about 1400 C. Both these transients involved power rate of rise time constants of about 300 s^{-1}, comparable with the thermal time constant of the clad given in Section 2.6. Such values are simply unattainable in HIFAR.

7.3.2. Steam explosions.

A well documented phenomenon is the generation of large amplitude, energetic pressure pulses (explosions) when a hot liquid at a temperature above the saturation temperature of a colder liquid is introduced into the colder liquid. A necessary condition appears to be that both components are in the liquid phase, indicating that heat transfer from a fixed solid/liquid interface cannot be high enough for the explosive generation of vapour; the heat transfer area itself must undergo a rapid increase which implies a rapid intermixing on a fine scale of the hot and cold liquids. A description of such a process is the Board/Hall detonation model. In this, the hot liquid is assumed to be coarsely mixed (cm scales) within the cold liquid and film boiling to be occurring at the boundary of the liquids providing a limiting rate of vapour generation. The occurrence of a pressure pulse, the 'trigger', collapses the vapour film allowing very rapid hot/cold liquid contact and rapid nucleation of the cold liquid. Shock pressurisation occurs and velocity differences between the two liquids behind the shock front may lead to further fragmentation of the hot liquid, and propagation of the interaction through the remainder of the coarsely mixed materials. Such a mechanism relies upon the provision of a suitable trigger; certainly it has been shown that explosions can be reliably produced by detonating a small chemical explosive or dropping an object into the cold liquid after the hot liquid has been introduced into it. Such a model cannot explain the occurrence of explosions when a large amount of hot material is poured into a vessel containing the cold liquid and the heavier hot liquid settles to the base of the vessel. Although explosions in this case are less predictable than triggered events the fact that they occur without an apparent trigger has led to the surmise that entrapment of a body of cold liquid within the hot liquid allows spontaneous nucleation of the cold liquid and inertial restraint to allow the development of high pressures. Such events are usually referred to as base triggered explosions.

The disposition of the fuel elements in a research reactor is considered to provide pre-mixing of the aluminium and water components; thus rapid in situ melting such as could be produced by a large reactivity injection would be favourable to a Board/Hall type event if a suitable trigger is provided. It is widely believed that the pressures which destroyed SL1 and D12/25 were generated in this way; the trigger for the latter may have been the scram of shut down rods but no trigger has been identified for the former.

These two destructive events have been examined by Storr with the aim of quantifying the intrinsic conversion efficiencies (mechanical work performed in deforming reactor components per energy available in melt.) The mechanical work was derived from measured deformation of core and containment structures and from the kinetic energy of water expelled from the reactor vessels and movable components. The available energy was derived from estimates of the mass of melt obtained with ZAPP. Although the agreement between calculated and observed quantities was generally good, considering the complexity of the calculations, a significant discrepancy was in the calculated mass of melt in D12/25. The maximum fraction of core molten was in good agreement with that derived from post transient analysis but the calculations showed that the melt was rapidly cooling after peak power and at the time of the explosion (an accurately known quantity) was one-sixth of the maximum value. This produced a calculated value of the intrinsic efficiency which was too large to be believable (0.895). It seems reasonable to believe, since the heat transfer geometry must have been entirely lost at this stage, that ZAPP is grossly overestimating the melt cooling rate. Keeping the fraction of melt closer to the maximum calculated and observed produces efficiencies closer to that calculated for SL1 (0.26). In this analysis, where the time of the explosion was not known, the quantity of melt interacting was taken to be that calculated when the energy release was the same as that determined by post accident analysis.

The significant point to be found in this analysis is the indication of very high conversion efficiencies which are in the upper range of those measured in shock tube experiments and much greater than those estimated to occur in base triggered explosions - such as might be predicted to occur in HIFAR following failure of the scavenge pumps and melt dropping into risers partly filled with D_2O. However it must not be assumed that these efficiencies can be applied to all circumstances for these transients produced large volumes of melt at very high temperatures. Lesser accidents have produced no indication of damaging pressure pulses and it is worth noting the remarks [34]

> *These transient pressures measured during these (* SPERT 1D) *tests gave no indication of any increase with the occurrence of melting and thus substantiate the conclusion that the simple fact of fuel plate melting does not of itself constitute a sufficient condition for the generation of destructive pressures.*

With HIFAR well guarded against fuel melting produced by transient over power events there seems to be no way in which the preconditions for a Board/Hall event can occur. Only a single base triggered sequence has been identified which seems even possible and this latter requires the occurrence of a LOCA accompanied by complete failure of the ECCS; to say the least, an accident scenario with probability bordering on zero.

7.4. Comments - Conclusions.

The available experimental data suggest very strongly that production of significant chemical reaction or pressures requires temperature and melt volumes sufficiently high as to make them impossible to attain in HIFAR accidents of believable severity.

The two classes of abnormal reactor operation events discussed at most length in this section have been the transient overpower (TOP) and loss of coolant accident (LOCA). This emphasis is not meant to assert that these two classes present the only operational hazard but they have the potential for leading to the most damaging consequences.

In the case of TOP accidents it will be apparent from the preceding text that analysis of thes requires a considerable amount of data; much of this, such as material properties, has no assigned errors but it must be expected that these errors will be consistent rather than random and the calculation of core energy releases, powers, and temperatures will always be biased accordingly. A particularly significant bias when comparing calculations with SPERT results is the experimental determination of SPERT power which probably has a consistent error in the range ± 10%.

Of great significance is the good level of agreement obtained with ZAPP in calculation of SPERT transients terminated without nucleate boiling of the coolant. Since the point kinetics model can be made exact by suitable weighting of the feedback coefficients this means that the coefficients themselves are correct and that no significant contribution to reactivity feedback has been neglected. This, of course, states that the neutronic codes and data used to obtain the feedback coefficients are correct, and since these data and methods are essentially the same for a variety of research reactor cores the coefficients calculated for HIFAR can be applied with confidence.

Of greater difficulty is the representation of the threshold effects of nucleate boiling and net vapour generation. As discussed in the text, it appears impossible to reduce the feedback from these to a form which will fit into a point kinetics model and, at the same time, to retain exactness. However, approximate representation in ZAPP and PARET have given quite good agreement with observed reactor transient powers in situations dominated by these effects. This is somewhat puzzling; the answer probably lies with the rapid flattening of the core temperature distrubution once nucleate boiling starts but, before it can be justified, this conjecture requires detailed examination of the effects of varying threshold energy levels and spatial core representation. However, the present methods do give results of sufficient accuracy to satisfy the requirements of safety analyses.

An important fact to flow from existing analyses is the very large negative reactivity ramps generated by nucleate boiling heat transfer and by void formation. These are of the same order as those produced by engineered shutdown devices and, like the latter, have a non-linear variation with energy release; the result is that transients involving these inherent mechanisms will have energy releases which depend only weakly on the initial excess reactivity producing the transients. Insofar as film boiling does not occur this means that fuel temperatures will also vary slowly; however, it must be remembered that should film boiling occur the temperatures could increase rapidly even though the reactor power is falling. All indications are that film boiling will not be significant in HIFAR transients of believable severity.

Another important feature of the calculations reported here is the demonstration that the steady state Ledinegg instability power level can be greatly exceeded without the onset of boiling in a coolant channel; thus the use of this instability power level as a criterion for assessing safety margins in a transient will be a highly conservative procedure.

Most of the above comments refer to fast transients; considered as transients whose time scale is less than or of the order of the transit time of coolant across the core. For slower transients the feedback from coolant mixing in the RAT will become important since this will have a major influence on the run out power following an initial power pulse.

The HIDYN code has been rather neglected, which is a pity since it can handle a range of postulated TOP events perhaps more likely to occur than the severe cases considered with ZAPP. However the code needs more exercise to determine the influence of coolant mixing in the RAT and the nature of the calculated power instability produced by long delay times.

Unlike the TOP events without intervention of the engineered shutdown system, where the response of the reactor is determined by inherent phenomena, the ECCS performance in a LOCA is dependent upon a mixture of active and passive systems. As concluded in Section 6, if a falling coolant film is established on one surface of each fuel tube then the ECCS will remove the

maximum power expected in a worst case LOCA and fuel melting will not occur. Discussion of the effectiveness of the ECCS is thus an examination of the circumstances that may prevent the formation of this falling film. Most of these circumstances, such as failure of start of the scavenge pumps can only be assessed on a probabilistic basis; we make the following final comments on components of the system for which behaviour can be analysed by deterministic methods.

Downcomer flow.

Experimental data for this flow as a function of water head can be well fitted to the standard weir flow equation with a slight zero offset to the measured water head under conditions of a free water surface without significant perturbations. The effect of perturbations produced by water being returned to the RAT remains unquantified but is believed to be acceptable.

Flow into the fuel elements.

The standard efflux flow equation has been shown to give good agreement with measured total flows into a fuel element as a function of water head.

Partition of flow between channels.

A simple geometric evaluation of the flow partition gives good agreement with measurement and supports the case that the film is established on one wall only of each fuel tube. This partition is sensitive to the relative heights of the tops of the fuel tubes and there will be a statistical fluctuation in the partition of flow depending on manufacturing tolerances. Quality control has to be relied upon here and the variation should be examined by use of the geometric model.

Power to be removed by the film.

The methods and data used to evaluate the residual fission power and decay power are well established to an accuracy better than required to evaluate ECCS performance.

Leak flow rates.

Any real break in the primary system would appear to be certain to possess a complicated geometry so that any attempt to relate leak rate to break geometry must be artificial and only of use in providing a basis for scoping calculations.

7.5. References.

(1) Johnson, H.A., Schrock, V.E., Selph, E.B., Lienhard, J.H. & Rosztoczy, Z.R. [1961] - Temperature variation heat transfer and void volume development in the transient atmospheric boiling of water. University of California, Berkeley. Report SAN 1001

(2) Grund, J.E. [1963] - Self limiting excursion tests of a highly enriched plate type D2O moderated reactor. Part 1, Initial test series. Report IDO-16891

(3) Obenchain, C. [1969] - PARET - A program for the analysis of reactor transients. Report IDO-17282

(4) Woodruff, W.L. [1984] - A kinetics and thermal-hydraulics capability for the analysis of research reactors. Nuclear Technology. Vol. 64, page 196.

(5) Dalton, A.W. [1983] - NAIADQ, A computer program for calculating reactivity transients in low power experimental reactors. Report AAEC/E566

(6) Ellis, R.J. [1988] - TANK - A computer code for the two-dimensional modelling of transient behaviour in research reactors. Report AECL-9888

(7) Clancy, B.E. [1983] - ZAPP - A computer program for the simulation of reactor power transients. Report AAEC/E568

[8] Harries, J.R. & Wilson, D.W. [1978] - Measurement of the dynamic response of the materials testing reactor HIFAR. Report AAEC/E428

[9] Donnelly, J.V. [1986] - WIMS-CRNL A user's manual for the Chalk River version of WIMS. Report AECL-8955

[10] International Atomic Energy Agency [1985] - Research reactor core conversion from the use of highly enriched uranium to the use of low enriched uranium fuels, Guidebook addendum: Heavy water moderated reactors. Report IAEA-TECDOC-324

[11] Rosenthal, N.W. & Miller. R.L. [1957] - An experimental study of transient heating. Report ORNL 2294

[12] McAdams, W.H., Kennel, W.E., Minden, C.S., Carl, R., Picornell, P.M. & Dew, J.E. [1949] - Heat Transfer at High Rates to Water with Surface Boiling. Ind. Engng. Chem. Vol. 41, page 1945.

[13] Bergles, A.E. & Rohsenow, W.M. [1964] - The determination of forced-convection surface-boiling heat transfers. Trans ASME, J. Heat Transfer, Vol. 86, page 365.

[14] Connolly, J.W. & Harrington, B.V. [1977] - An analysis of power transients in the SPERT D_2O moderated close packed core. Report AAEC/E418

[15] Johnson, R.L., Larson, H.A., McClure, J.A. & Norburg, J.A. [1965] - An analysis of the excursion behaviour of a highly enriched plate type D_2O moderated core in SPERT II. Report IDO-17109

[16] Le Cour Christensen, P. [1963] - An experimental and theoretical investigation of the dynamic response of the nuclear reactor DR3. Report RISO/56

[17] Clancy, B.E., Connolly, J.W. & Harrington, B.V. [1975] - An analysis of power transients observed in SPERT I reactors. Part 1. Transients in aluminium plate type reactors initiated at ambient temperature. Report AAEC/E345

[18] Clancy, B.E., Connolly, J.W. & Harrington, B.V. [1976] - An analysis of power transients observed in SPERT I reactors. Part 2. Dependence of burst parameters on initial temperature and core moderation. Report AAEC/E383

[19] Connolly, J.W., Harrington, B.V. & McCulloch, D.B. [1993] - Self limiting transients in heavy water moderated reactors. Research reactor core conversion guidebook. IAEA Vienna.

[20] Singer, R.M. [1963] - Expulsion of water from a rapidly heated channel. Report ANL-7337

[21] Groeneveld, D.C., Cheng, S.C. &Dean, T. [11986] - 1986 AECL Critical Heat Flux Lookup Table. Heat Transfer Engineering 7, page 46

[22] Storr, G.J. [1989] - Molten fuel-coolant interactions resulting from power transients in aluminium plate / water moderated reactors. Report ANSTO/E685

[23] Connolly, J.W. [undated] - HIFAR transient-over-power calculations. AAEC internal report NT/TN-454

[24] Connolly, J.W. & Ferguson, H. [1978] - An analysis of self-terminating power transients in the reactor HIFAR. Report AAEC/E435

[25] Connolly, J.W. & Clark, N. [1986] - Analysis of hypothetical loss-of-control-arm accidents in HIFAR. Report AAEC/E631

[26] Connolly, J.W. & McKenzie C.D. [1960] - Reactor physics studies on the HIFAR twenty-five element cores. Report AAEC/TM-064

(27) Meister, G. & Kalker, K. [1964] - Analysis of possible coarse control arm accidents on the reactor FRJ-2. Report JUL-146-RE see AAEC Lib Trans 87

(28) Robinson, G.S. [1991] - 3D Diffusion calculations of HIFAR including the coarse control arms and their burnup. Report Ansto/E703

(29) Wolters, J. [1979 ?] - Spray film emergency cooling for the experimental reactors of the FRJ-2 type. Undated doctoral thesis, translated from the German by B. Pietroff and P. Holland.

(30) Byfield, J.B.H. [1963] - Experiments in DIDO and PLUTO on simulated loss of coolant flow. Report AERE-R4127

(31) Connolly, J.W. [1982] - On the possibility of fuel coolant interactions and steam explosions if HIFAR. Report AAEC NT/TN425

(32) Clancy, B.E. & Connolly, J.W. [1985] - An assessment of possible events following a LOCA in HIFAR. Report AAEC NT/TN453

(33) SL1 Report Task Force. [1962] - Nuclear Incident at the SL1 Reactor. Report IDO 16883.

(34) Miller, R.W., Sola, A. & McCardell, R.K. [1969] - Report on the SPERT 1 Destructive Test Program. Report IDO 16883.

(35) Storr, G.J. [1989] Molten Fuel-Coolant Interactions resulting from Transients in Aluminium Plate / Water Moderated Reactors. Report Ansto/E685.

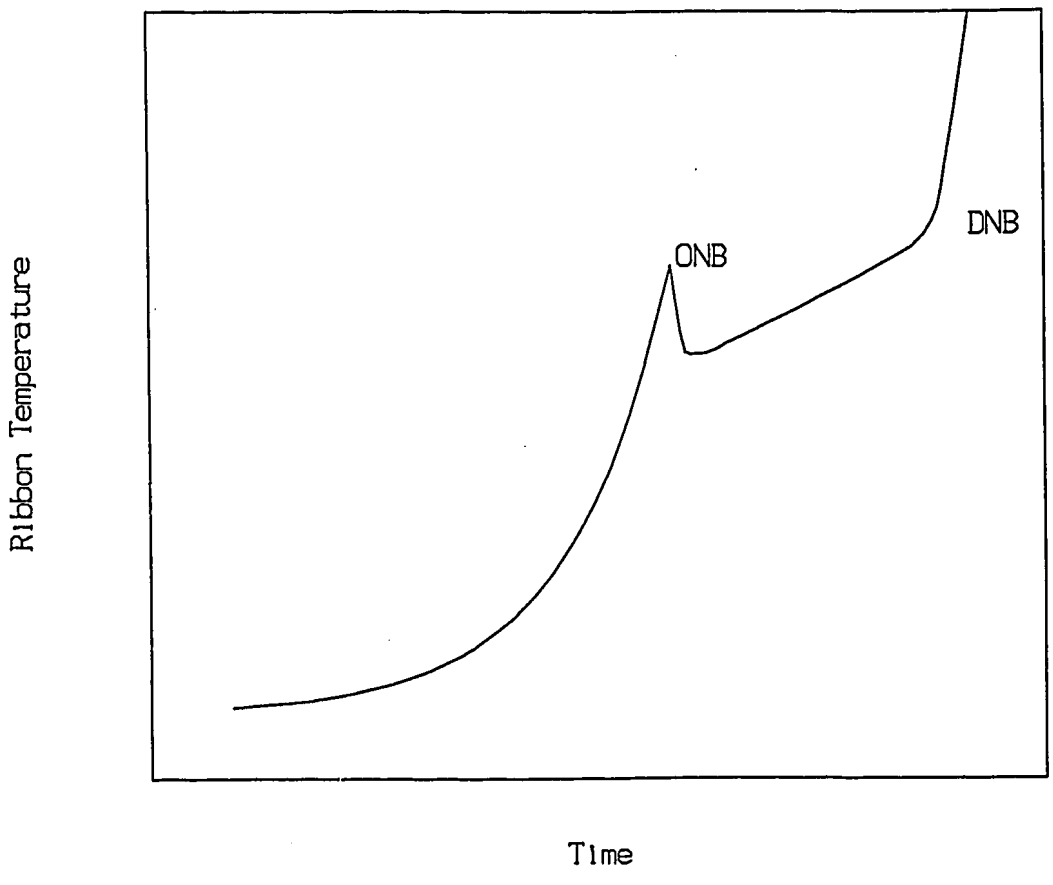

Figure 7-1 Temperature/time behaviour for exponentially heated platinum ribbon immersed in water.

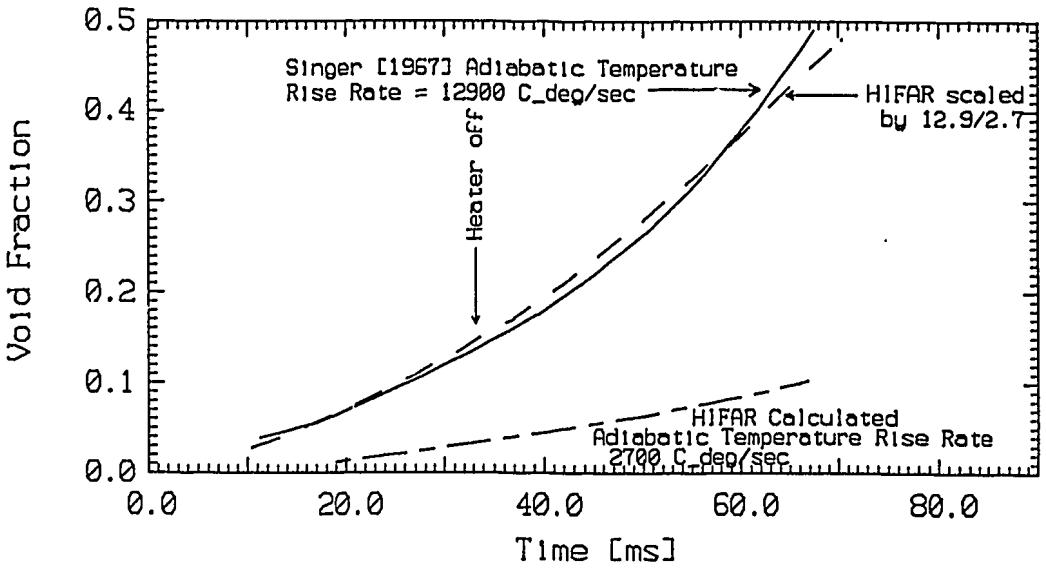

Figure 7-2 Comparison of void development data.

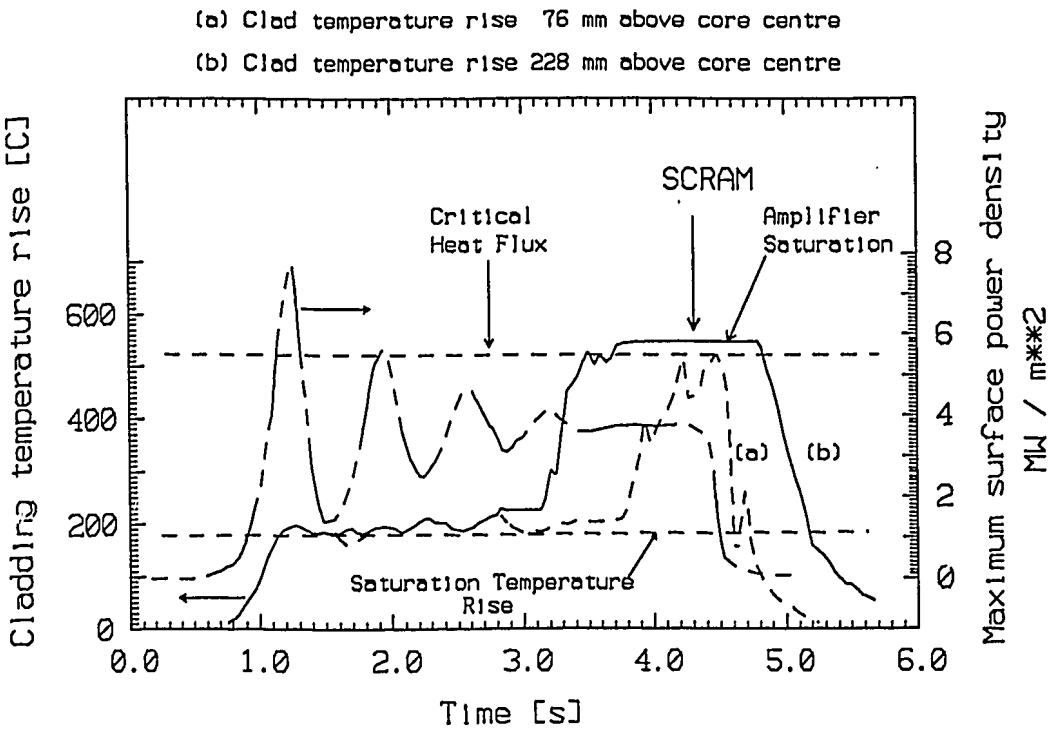

Figure 7-3 Transient maximum surface power density and typical high rated fuel clad temperature rise following a reactivity rise of $1.6 in SPERT II core B18/68 with a coolant flow velocity of 2.1 m/s

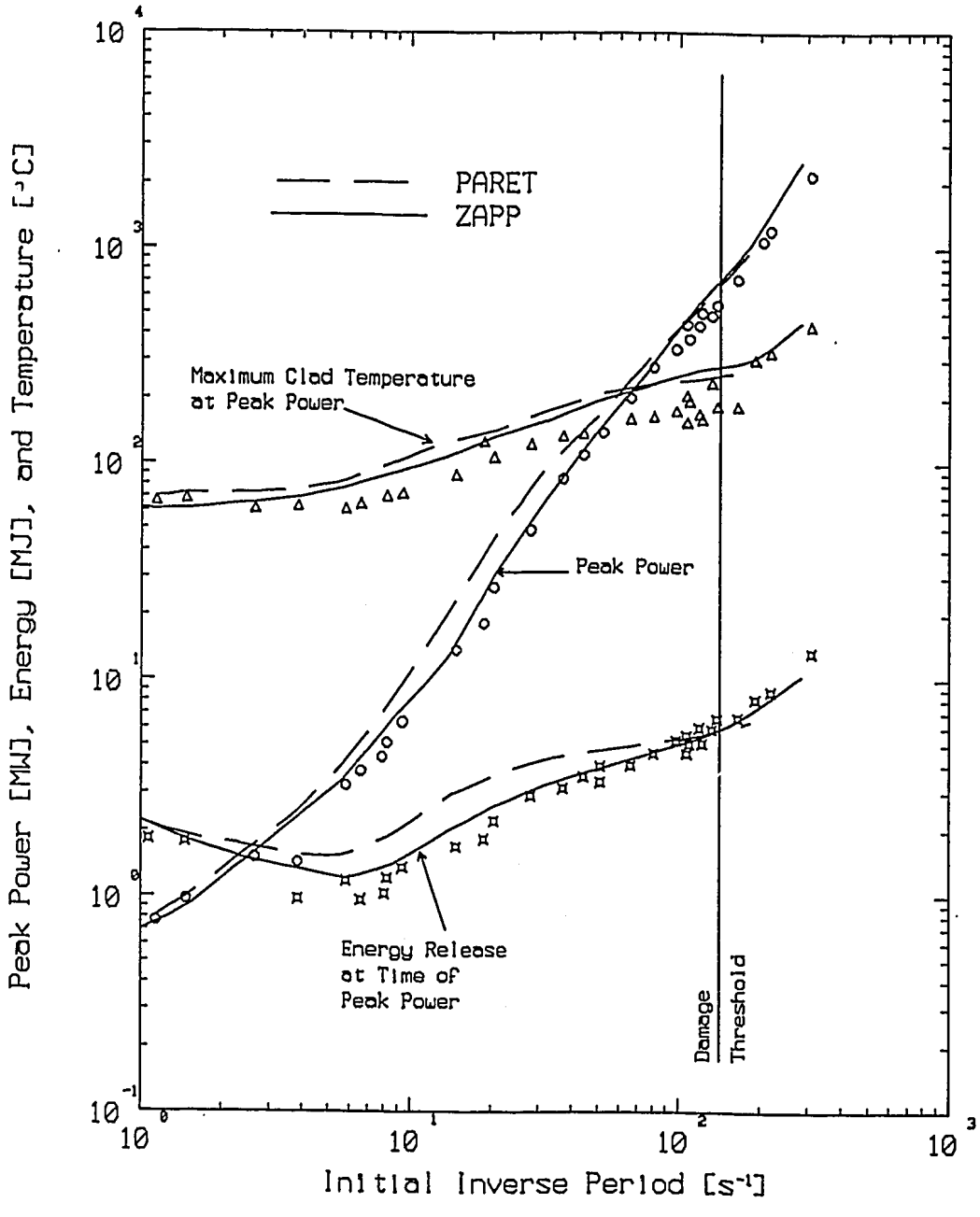

Figure 7-4 Comparison between experimental burst parameters and those calculated with the codes PARET and ZAPP for no-flow conditions in SPERT I core D12/25.

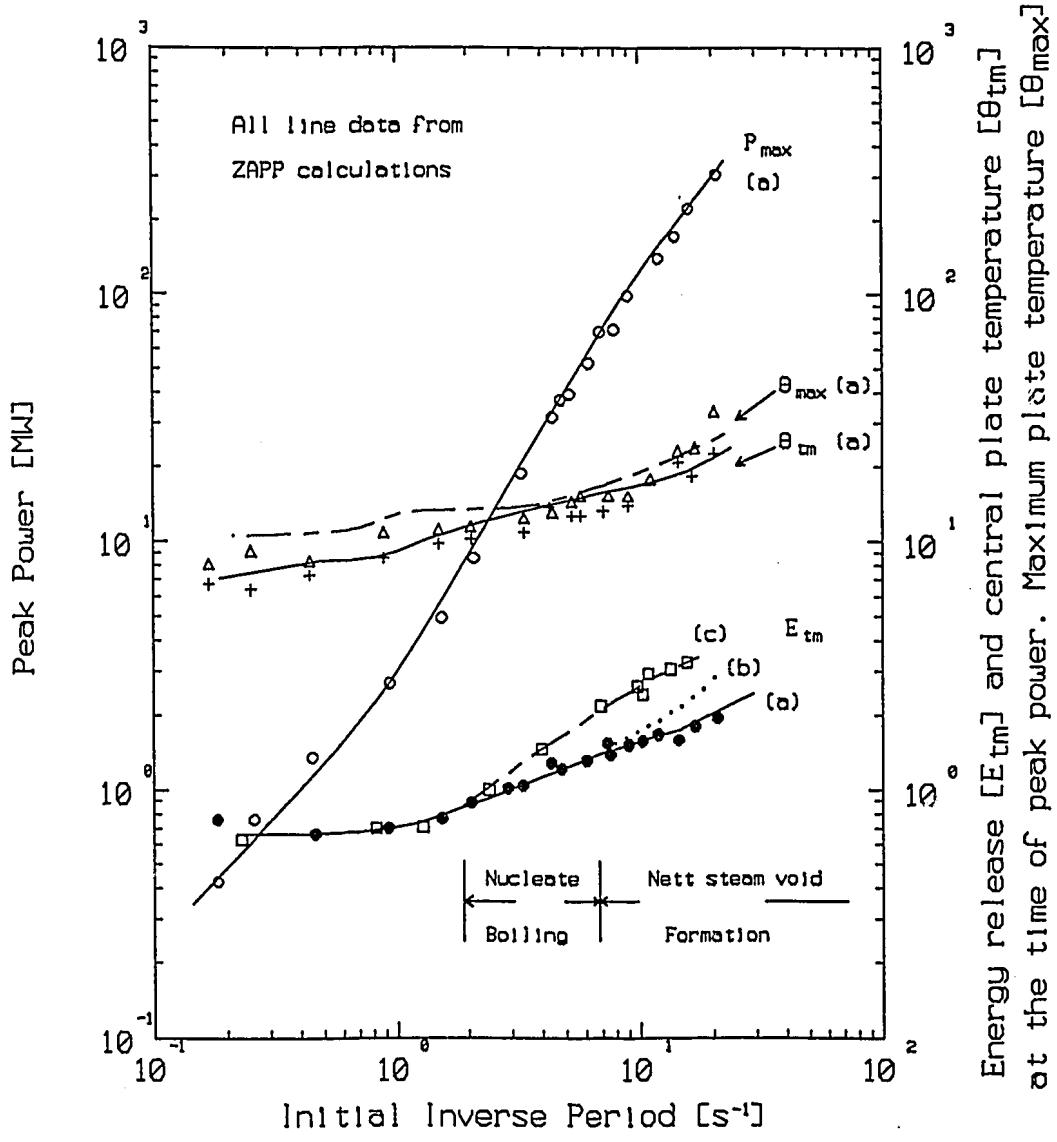

(a) Atmospheric Pressure
(b) Atmospheric Pressure, calculation without void model
(c) Pressure 2.6 MPa

Figure 7-5 Comparison between burst parameters for no-flow conditions in SPERT II core BD22/24 and those calculated by ZAPP.

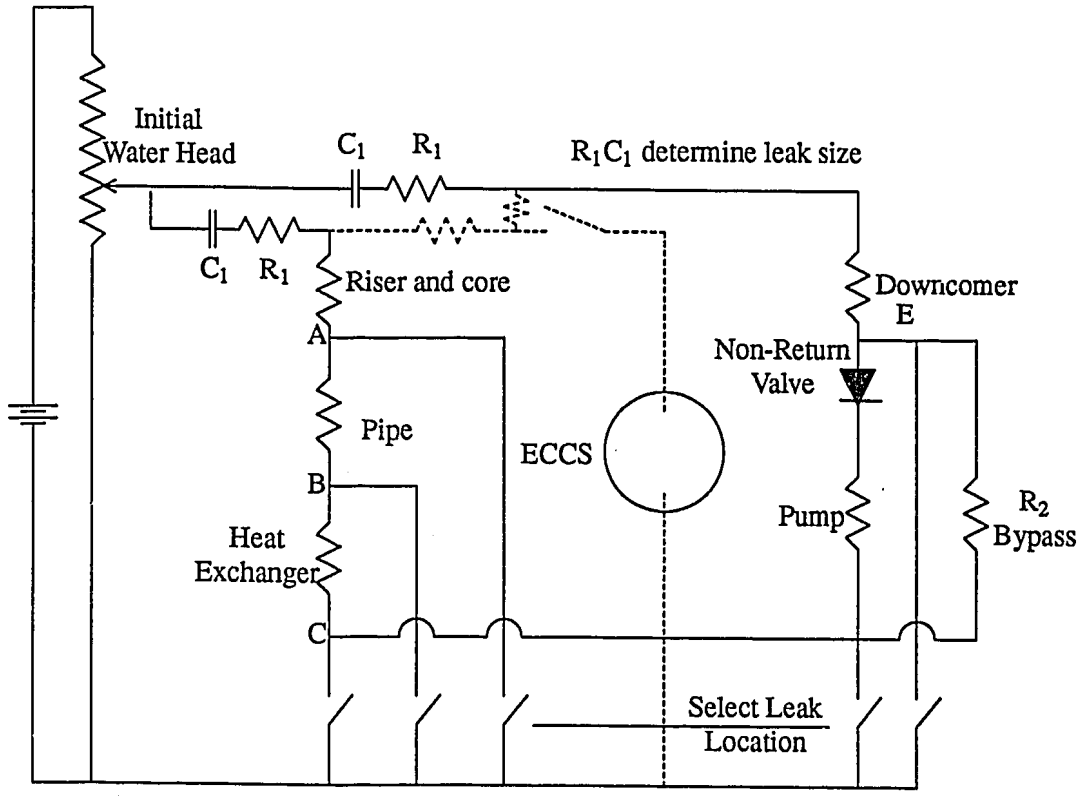

Figure 7-6 Current analogue circuit for primary coolant circuit

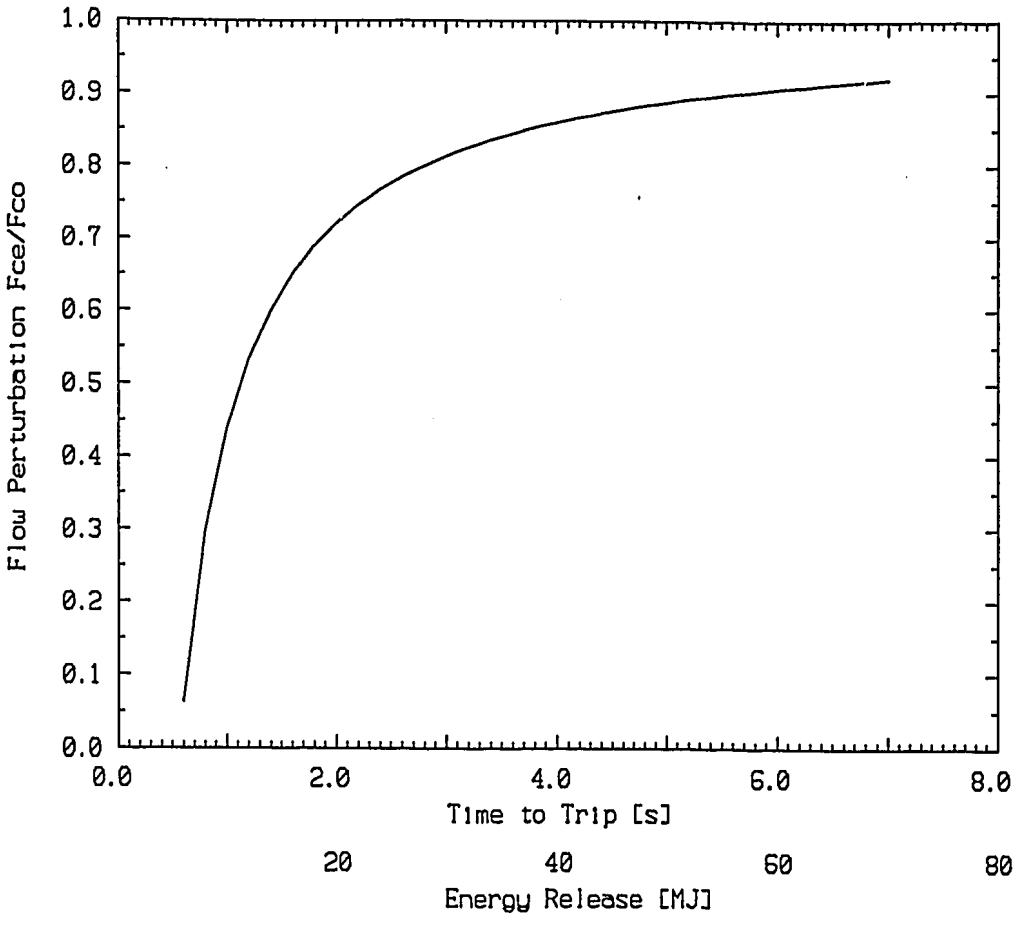

Figure 7-7 Core flow perturbation and time to trip.

SECTION 8

APPENDICES.

History is better written from letters...

Lord Acton. (1834-1902)

8. APPENDICES.

In earlier sections reference has been made to various documents which only exist in files held at LHRL. Such placing of these documents does not make it easy for the reader to locate and read them; to simplify the access problem this section contains copies of the documents.

Certain other material which has been referred to in the body of the report is also included.

8.1. Appendix A-1

AUSTRALIAN NUCLEAR SCIENCE & TECHNOLOGY ORGANISATION

MINUTE PAPER

6 October 1987

NTD ASSISTANCE - HIFAR CORE CONVERSION TO 170g FUEL ELEMENTS

File: LH84/209
Your ref: RD606

MR P. VEKSELSTEIN,
HIFAR Operations Section

The following information is supplied in response to your request for assistance in the conversion of HIFAR to the use of Mark 4/23 fuel elements containing 170g of U235.

New versions of the HIFUEL program and associated nuclear data library have been prepared which are suitable for use with fuel elements of either 150g or 170g of U235. It is recommended that the Reactor Analysis Group begin using the new versions at the next convenient time. A paper 'Modifications to HIFUEL for use with 170g Fuel Elements' which documents the changes is attached.

As an indication of expected results, the effects of replacing a new 150g element in C3 by a new 170g element calculated by HIFUEL are:-

* an increase in reactivity of 0.24%,
* an increase in the power of the central element by 7%,
* a decrease in the central fuel flux of 6%,
* a decrease in the C3 centre line flux of 5%.

Reactivity coefficients and absorber coefficients for a core of 170g elements with a uniform burn-up of 52.4 MWd per element have been compared with those in a core of 150g elements at 40.5 MWd. In all calculations, the 150g fuel had an initial composition of 80% U235 and 20% U238 while the 170g fuel had an initial composition of 60% U235, 1% U234, 9% U236, and 30% U238. The composition of 170g fuel has been assumed to be the same as the last batch of 60% enriched fuel of UK origin. The calculated results for the void and temperature coefficients (in dk/k per fuel element for 1 degree change in temperature or 1% change in void fraction) were : -

	Average fuel element		Central fuel element	
	150g	170g	150g	170g
Fuel Temperature	-0.44E-7	-1.31E-7	-0.61E-7	-2.15E-7
Fuel & Coolant Temperature	-3.69E-6	-3.53E-6	-5.48E-6	-5.18E-6
Coolant Void (Const. Temp.)	-3.59E-5	-3.52E-5	-5.48E-5	-5.38E-5

All differences are small except for the insignificant fuel temperature coefficient which has increased as the U235 enrichment decreased.

The calculated absorber coefficients for a core of 170g elements for fuel element positions A1 to E4 are given below. The values are 100 times % reactivity per cm**2 in a core with 3.2 kg of U235.

	-0.853	-1.133	-1.135	-0.974	
-0.881	-1.441	-1.877	-1.830	-1.476	-1.088
-1.462	-1.993	-2.352	-2.101	-1.617	
-1.056	-1.579	-1.985	-2.131	-1.723	-1.172
	-1.075	-1.416	-1.521	-1.174	

These results are 2.2% less at the centre and 1.4% less on average than for the corresponding core of 150g elements. The comparison between types of fuel element was made for cores which are intended to be typical loadings at shut-down for the same assumed rig burden. The two cores had loadings of 2.49 kg of U235 for the 150g fuel and 2.63 kg for the 170g fuel. In terms of actual reactivity (or dk/k), the core with 170g fuel has 5.2% lower absorber coefficient on average than the core with 150g core. Thus all absorbers, including rigs, coarse control arms and shut down rods should be reduced in worth by about 5%. This small variation due to the change to 170g fuel is less than occurs during an operating program or for a change in core U235 loading due to a changed rig burden.

The calculated power fraction in each tube of a new 170 g fuel element was (inner to outer) 0.193, 0.225, 0.265, 0.317. The corresponding values for 150g fuel were 0.194, 0.225, 0.266, 0.315.

G. S. Robinson,
Nuclear Technology Division

8.2. Appendix A-2

AUSTRALIAN NUCLEAR SCIENCE & TECHNOLOGY ORGANISATION

MINUTE PAPER

11 December 1991

GAMMA HEATING IN HIFAR - PARTICULARLY FOR 6H

File:LH84/209

Dr B. E. Clancy
Leader, Nuclear Analysis Section

1. Introduction

Nuclear heating of non-fissile materials at any location in HIFAR is due chiefly to the photon flux at that location plus the absorption of some of the photons produced in the material by thermal neutron capture. Previous estimates of HIFAR gamma heating have all been based on the approach of Connolly & Nicholson [1961] which is outlined in the following. The heating due to incident photons is based on the measurements of gamma dose distributions performed during the HIFAR startup experiments on a clean core of 100g Mark II fuel elements [Connolly & McKenzie 1960]. To use these dose measurements, an average photon energy is required to relate dose to heating of a particular material. Typical energies used are 1 to 2 MeV. This approach also assumes that there is no self-shielding of the sample material for incident photons. The neutron capture component is calculated from measurements of the thermal neutron flux, the thermal cross section, the photon production data and photon absorption factors which depend on the size and shape of the sample. Burnett [1965] provides prescriptions for calculating the two components from measured gamma dose and thermal flux. Wilson [1970] provides tables giving the nuclear heating in several materials in a number of facilities. These are misleading because the data given are for 100g spheres which absorb many of the neutron induced photons. This report, which was used in the recent analysis of the 6H facility [Melville 1991], is also very error prone. (Correcting one of these reduces the estimate of the peak steel heating rate in the 6H facility from 1.5 to 1.1 W g^{-1})

The results for nuclear heating presented here are derived from direct calculations of the neutron and gamma fluxes in HIFAR and the resulting energy release. As this is the first significant attempt to calculate HIFAR nuclear heating in this manner, the models used are outlined and comparisons with the available measurements are presented before the final results for 6H are considered.

2. Simple models and comparison with measurements

In order to gain an understanding of the processes important to nuclear heating in HIFAR, a simple radial model of the reactor was adopted. This model used a coupled neutron/photon S_N calculation of a smeared representation of the HIFAR core and radial reflector. This provided multigroup neutron and photon fluxes as a function of radial position. These fluxes were used directly with the appropriate cross sections to give results for gamma dose rates and heating of infinitely small samples due to incident photons. To obtain the heating due to incident photons on real samples, the gamma flux at the required radius in the radial calculation was used as a boundary source

in a subsidiary S_N calculation in which the sample was explicitly represented. It was discovered that using gamma fluxes typical of the inner reflector, there was significant self-shielding even for a 1.22 mm thick slab of stainless steel. This gave almost 40% reduction in the heating due to incident photons. This effect is a consequence of the low (<0.5 MeV) energy peak of the calculated spectra. Photons of these energies have very high cross sections for interaction with nuclides of high charge number.

The heating due to the induced photons was also calculated in subsidiary S_N calculations using the photon production rate in the sample at the required radius in the radial calculation as a volume source. These calculations also demonstrated that very high SN orders were required for accurate calculations of photon sources in thin steel slabs.

The only available HIFAR measurements with which the calculations may be compared are the gamma dose measurements of Connolly & McKenzie [1960] which were increased by 20% by Connolly & Nicholson [1961], and the gamma spectrum measurement of Connolly & Nicholson. As well as the standard radial model of HIFAR which represents current operation, another model representing the startup measurements was developed. This had a clean core of 100g Mark II elements and steel worth 8% in reactivity smeared into the inner radial reflector. Both radial models included 3% by volume of aluminium in the reflector, 1% of aluminium in the core and 0.5% of steel in the core. This served to make the calculations critical and give some representation of additional absorbers. These variations affected the results by only a few per cent. There was qualitative agreement with the spectrum measurement but the measurement had a limited range and a large correction was required below 0.5 MeV. The comparison was sufficient to rule out a major error. A comparison with the dose measured on the core centre plane is given in the following table.

Comparison of Gamma Dose Distributions

Position	Radius (mm)	Gamma Dose (R/hr) at 10 MW Meas.	Calculation Mark II	Calculation Standard	Ratio MkII C/M
C3	0.	1.5e+9	8.0e+8	6.9e+8	0.53
E1	38.1	1.0e+9	4.2e+8	4.2e+8	0.42
2V3	45.7	4.8e+8	2.28e+8	2.06e+8	0.47
2V6	61.4	2.23e+8	0.75e+8	0.64e+8	0.34
2V7	55.5	3.1e+8	1.26e+8	0.99e+8	0.41
4V1	87.	7.2e+7	1.5e+7	1.5e+7	0.21
4V5	87.	4.5e+7	1.5e+7	1.5e+7	0.34
6H	(48.5)	1.96e+8	1.84e+8	1.58e+8	0.94

The agreement is very poor. The calculated values are actually axial averages over the core height multiplied by the axial form factor (for power) of 1.05. The photon form factor is about 1.17, so the difference is minor compared with the discrepancy. Considerations of the overall energy balance eliminate the possibility of the calculations being in error by a factor of two to three. The total photon energy released per fission in the calculation is 18.6 MeV. An upper bound may be obtained by assuming 8 MeV of photon energy per neutron capture to give a total of 24 MeV per fission. The discrepancy remains unexplained. The fact that the facility in which the measurements were performed is not represented in the model may make a significant contribution. The 6H result is considered later.

Connolly & Nicholson include values for gamma heating in 2V8 calculated from the dose measurements and compare these with the heating measurements of Anderson [1959]. The size of the Anderson samples is not known, and the results are simply compared with calculations of infinitely small samples in the following table.

Comparison of Gamma Heating in 2V8			
	Gamma Heating (W g^{-1}) at 10 MW		
Material	Anderson	Connolly & Nicholson	Calculated
H	1.90	2.67	1.12
Al	0.92	1.30	0.62
H2O	1.01	1.49	0.66
Zr	0.91	1.25	2.03
Pb	1.37	1.91	6.61

The very poor agreement for zirconium and lead is probably due to sample size effects. For aluminium and water for which there should be little such effect, the agreement with Anderson is a little better than with the result based on measured dose. Both the HIFAR dose measurements and the DIDO heating measurements were performed during low power startup experiments. Renormalization to full power may contribute to the discrepancies.

Measurements of the gamma heating in small iron samples of 2.7 mm diameter in DIDO have been reported by Crick & Nicholson [1966]. The axial average result in C3 at 10 MW of 2.40 W g^{-1} from the measurement is in good agreement with the value of 2.20 W g^{-1} calculated for a sample of this size at the centre of the standard HIFAR radial model. The induced gamma heating subtracted from the measurement was only 0.14 W g^{-1}.

The good agreement with the DIDO measurement is sufficient to provide support for the calculations of HIFAR gamma heating. The reason for the discrepancy between calculated and measured HIFAR gamma doses is not known. Sufficient calculations of gamma heating of reasonable size samples have been performed to demonstrate that sample size effects are important, particularly for nuclides with high charge number. Estimates of gamma heating should no longer be made using the methods traditionally used for HIFAR.

3. Detailed Calculation of 6H

The calculation of gamma heating in 6H has been based on a coupled neutron/photon RZ S_N calculation in which the 6H facility is explicitly represented on the Z axis. The aluminium endcap was positioned 47 mm from a smeared cylindrical core. The calculation was performed as a source calculation with an assumed distribution for the neutrons emitted from fission. The calculation gave a fission emission rate of 0.946 of the total source, which shows the model to have reasonable neutron balance. As the angular quadrature set was designed to calculate neutron streaming down the facility rather than photons escaping from a thin slab, the induced gamma heating in the steel was corrected. This correction was obtained from the calculated neutron capture rate and subsidiary slab calculations. The resulting nuclear heating in the steel liner and aluminium re-entrant tube are given in Figure 1. The values for the endcaps are 5800 kW m^{-3} and 1800 kW m^{-3} for the steel and aluminium. The gamma dose rate at the end of the steel liner is 1.63e+8 R/hr which is in good agreement with the simple radial calculation. This also implies quite good agreement with the HIFAR dose measurements, which is surprising considering the comparison at other positions. The introduction of the steel liner since the dose measurements could make a significant contribution.

The core is poorly modelled in the above RZ model and it is not possible to obtain heating rates for different core loadings. The poor modelling of the core also increases the uncertainty in the result. Therefore, supplementary calculations were performed using a superposition model developed for aluminium damage studies [Robinson 1991]. The photon fluxes about a single fuel element were calculated in an S_N RZ model and then combined using a given power distribution to obtain values for photon reaction rates at a point corresponding to the centre of the 6H aluminium

endcap. This approach works well for fast neutrons and photons because the nearest fuel elements have a large contribution and aluminium is not too dissimilar in nuclear cross sections to moderator. The superposition model can not include 6H but the reactions may be compared with the core RZ model without 6H. When the standard calculated power distribution was used, the superposition model gave gamma doses at the location of the centre of the aluminium endcap only 2% higher than the RZ model. This helps to confirm both models. The power distributions [R. M. Godfrey, private communication] calculated using HIFUEL [Robinson 1987] for Programs 409 and 412 which are the first and fourth after the major shutdown have also been used in the superposition model. This gave gamma doses of 8% lower and 12% higher than the standard calculation for programs 409 and 412 respectively. As the induced gamma heating in the steel is only about 1000 kW m^{-3}, this may also be taken as a reasonable estimate of the variation of the total nuclear heating in the 6H between these two programs. The superposition model may also be used to give a fairly reasonable approximation to nuclear heating in 10H by scaling the heating in 6H by the ratio of the gamma dose rates at the aluminium endcaps. The value obtained for the ratio was 0.65.

It is difficult to estimate the possible accuracy of the above calculations. The discrepancy with the HIFAR gamma dose measurements remains a problem. The necessity to model the geometry of the 6H facility and core by a combination of two dimensional models suggests that a plausible accuracy may be ±20%.

4. References

Anderson, A.R. [1957] - Energy absorption from reactor radiation in DIDO. AERE C/M 315.

Burnett, I.B. [1965] - Heating of materials in HIFAR. HIFAR/TN 31.

Connolly J.P. & McKenzie C.D. [1960] - Reactor physics studies on the HIFAR twenty-five element cores. AAEC/TM 64.

Connolly J.W. & Nicholson K.P. [1961] - Energy absorption by materials exposed to radiation from HIFAR. AAEC/TM 109.

Crick N.W. & Nicholson K.P. [1966] - Physics parameters and principles for the operation of DIDO at 15MW with Mk. 3E fuel elements. AERE - R 5196.

Melville M.D. [1991] - HIFAR 6H facility finite element heat equilibrium analysis - Minute to F. Nicholson (15 Nov 1991).

Robinson G.S. [1987] -A brief description of HIFUEL - a fuel management program for HIFAR. NTD/TN 26.

Robinson G.S. [1991] - Calculation of neutron damage fluences for the HIFAR reactor aluminium tank. NTP/TN 172.

Wilson D.J. [1970] - Neutron and gamma fluxes and their heating effects in HIFAR with special reference to 15 MW operation. HIFAR/TN 65.

G. S. Robinson,
Nuclear Analysis Section,
Nuclear Technology Program

Figure 1. NUCLEAR HEATING RATES IN 6H FACILITY

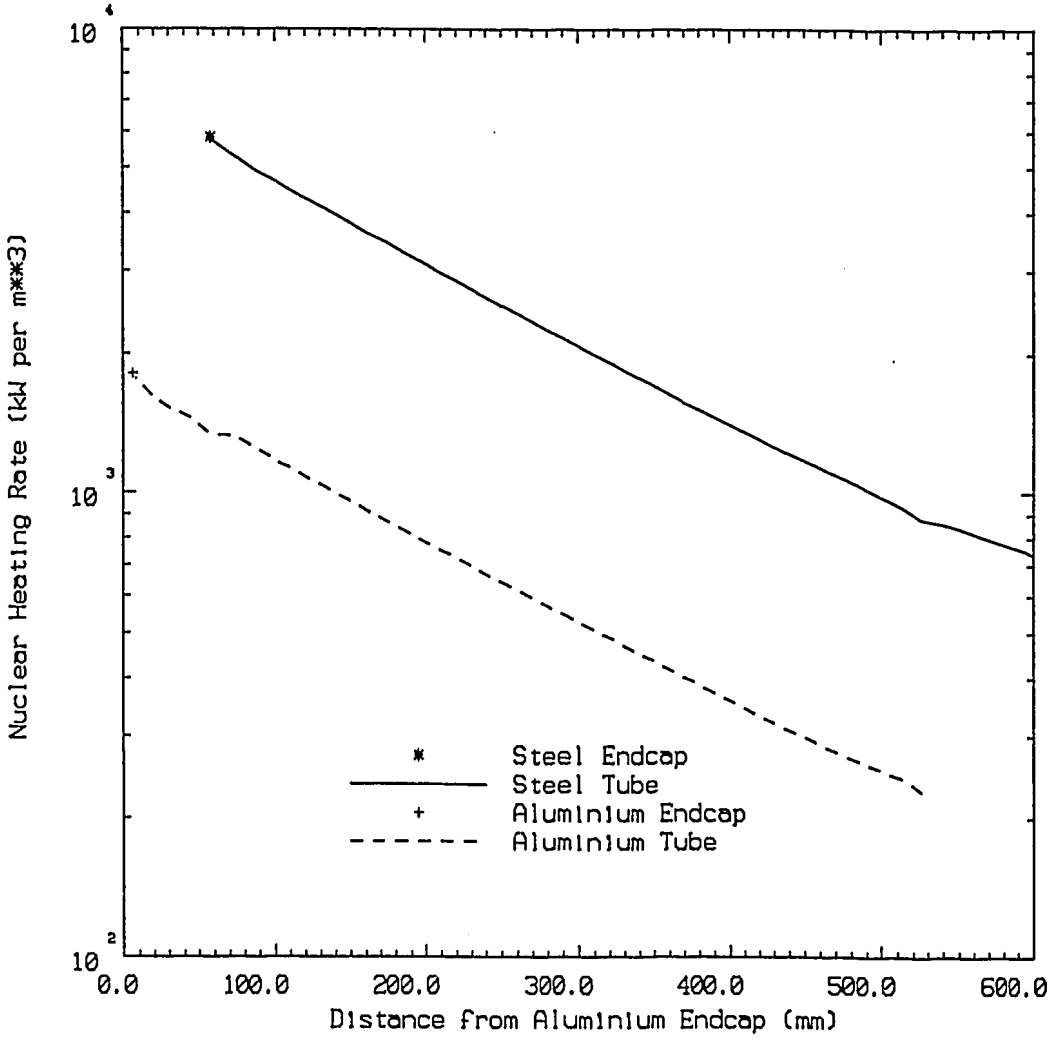

8.3. Appendix A-3

AUSTRALIAN NUCLEAR SCIENCE & TECHNOLOGY ORGANISATION

MINUTE PAPER

7 April 1992

REACTIVITY WORTH OF HIFAR SAFETY RODS

File:LH84/209
Dr B. E. Clancy
Leader, Nuclear Analysis Section

1. Introduction

The reactivity worth of the HIFAR safety rods has never been put on a firm basis. The compilation of measured worths [HIFAR Safety Manual, Section 4.4] shows both an extreme dependence on CCA angle and a large scatter of results. The curve due to Culley [1970] was simply derived from a crude inclusion of the CCA arms in an RZ model and normalized to the measurements. The scatter of results has been attributed to variation of the absorber loading in the vicinity of the safety rods but no quantitative estimate of the effect of such variations has been available.

The current calculations of the worth of the safety rods have been made using the 3D diffusion model of HIFAR including the CCA arms [Robinson 1991a]. This note details the method of including the safety rods in this model, provides a comparison with the most extensive set of measurements of the safety rods [Connolly & McKenzie 1960] and gives results for safety rod worths in operational cores.

2. Inclusion of Safety Rods in the Standard 3D HIFAR Model

The standard 3D HIFAR model uses the POW3D edge-mesh diffusion code with two neutron groups and a coarse spatial mesh. Most of the detail is included in the conventional manner by including each facility in one or more mesh boxes. However, localized absorbers such as the CCA blades and the in-core rigs are represented by a number of point absorbers at the mesh points. Since the safety rods are on the same pitch as the fuel elements, they have also been represented by point absorbers. The method of obtaining neutron cross sections to represent the rods is now considered.

The basic idea was to derive cross sections for a diffusion model using the same representation of a safety rod as the 3D model, which matched the reactivity worth calculated from a detailed S_N calculation. This cross section matching was done for a rod at the centre of the core with a 304.8 mm square replaced by D_2O. In the radial S_n model, the safety rod was represented as a 2 mm thick cadmium tube of OD 41.529 mm and a 1.4 mm thick steel tube of ID 41.529 mm. The remainder of the fixed aluminium tube of OD 54 mm and thickness 3.81 mm was voided. The diffusion model used the same groups and mesh as the 3D model so the cross section which reproduced the S_N rod worth could be used in the 3D model.

Two corrections were applied. First, since the thermal absorber worth at the centre of the 2-group XY diffusion model was 4% less than the radial S_N model, the S_N result was reduced by 4%. Secondly, an estimate of the error in the absorber worth in the 3D model at the location of the safety rod was made by comparing the worth in a 2-group XY model with a standard 5-group XY model, and the smeared fuel element model with a discrete fuel element model. These

comparisons showed there was a 6% underestimate due to the use of a 2-group model with smeared fuel elements. This method of estimating the error in the 2-group model in the reflector is an extension of that previously used to estimate errors in the thermal reflector flux [Robinson 1991b]. This error was compensated by increasing the S_N result for the safety rod worth to be matched.

3. Comparison with Measured Worths

In order to validate the calculated results, they have been compared with the measurements of safety rod worth performed during HIFAR commissioning [Connolly & McKenzie 1960]. These measurements on clean cores of Mark II fuel elements with either 100 or 115 g of ^{235}U provide the most extensive set of results. The safety rod worths were measured on cores with CCA angles varying from 5° to 32°. At low angles, there were no vertical facilities in the reflector at all. At high angles, the reflector was heavily poisoned in the 2V and 6V facilities which were voided and had long steel rods or "black" absorber rods included. This method of poisoning was also used during the CCA calibration. In order to make comparisons with these measurements, it is necessary to use a fairly accurate representation of the reflector poisoning.

The calculations were performed with fuel cross sections derived for 100g Mark II elements. Voiding of the 6V and 2V facilities was included simply by reducing the volume fraction of D_2O in the appropriate mesh boxes. The resulting reactivity worth of all the voided facilities was in reasonable agreement with the measured value. This is somewhat fortuitous given the importance of neutron streaming. The absorber rods were included by including a volume fraction of thermal absorber which matched the measured worth of the absorber. This was done with some care to ensure that the worth was matched for the same CCA angle and loading of other absorbers as the measurement. It was generally assumed that it was only necessary to match a particular rod once for any facility represented by a particular mesh and that the same thermal absorber could then be used in equivalent facilities.

The safety rod worths as a function of angle were calculated for three core states. The first was with no vertical facilities loaded at all, which is appropriate to low angles of about 5° to 8°. The second was with steel rods in all 2V and 6V facilities (No. 3 & 5 rods), which is appropriate to angles of about 16°. The third was with "black" rods in all 2V and 6V facilities (No. 6 & 7 rods), which is appropriate to angles above about 24°. The results for individual safety rods and for the safety rod pair are compared with the measurements in the attached figures. All the results have been adjusted to worths in a 2.75 kg core using a $M^{-0.7}$ mass dependence. The measured values have also been scaled by a factor of 0.92 from that reported to allow for the latest assessment of the reactivity scale [Connolly et al 1988]. An average of the two rods has been used for the calculated values for individual rod worths because the difference is small. The three sections of the calculated curve correspond to the three core states. The increase in reflector poisoning results in a large reduction in the safety rod worth. The main features of the measured results are well represented. Connolly & McKenzie comment on the difference between values of 0.85% and 0.50% for SR1 and SR2 at 18.5 degrees and ascribe it to the presence of a No. 6 absorber in 2V6 compared to a No. 1 absorber in 2V1. Calculations using No. 3 in all 2V except No. 6 in 2V6 and No. 5 in all 6V gave 0.77% and 0.64% for SR1 and SR2. This implies that the effect of the No. 6 rod is significantly underestimated. However, this is not apparent in the remaining results.

It is concluded that the calculated values for safety rod worth have been validated. Large variations in measured safety rod worth with angle are a function of the corresponding change in reflector poisoning rather than CCA angle. Safety rod worth is essentially independent of CCA angle for angles greater than about 15°.

4. Calculated Safety Rod Worths for Operational Cores

The calculated safety rod worths as a function of angle for operational cores have also been included in the attached figures. The core state actually used in these calculations was that for the CCA calibrations in operating program 332. To assess possible variations from this result, a number of changes to this core state have been made and the safety rod worths calculated for a CCA angle of 23°. The results are given in the following table for the cases:

A) Standard as for CCA calibration, rigs in 2V1 to 2V7, 2V9, 6V1, 6V3, 6V4
B) No reflector rigs
C) With 2V rigs but not 6V
D) With 1992 2V rigs (OP412) i.e. in 2V3, 2V5 and 2V6 only
E) As D with rig in 6V2 worth 0.35% (3.2 kg)
F) X163 in E1 worth 0.53% (3.2 kg)
G) Fuel with ~80g ^{235}U in A4 and B6 rather than ~130g, mass 2.61 kg
H) Mark 4/23 fuel (170g) and 99.7% D_2O

Case	Reactivity Worth (% in 2.75 kg core)		
	SR1 only	SR2 only	Both SR
A	0.954	0.954	1.991
B	1.099	1.030	2.240
C	1.049	0.996	2.147
D	1.087	1.014	2.211
E	1.111	1.000	2.221
F	0.767	0.981	1.820
G	1.039	0.771	1.880
H	1.027	1.029	2.153

It can be seen that the maximum variation from the standard case is about 20 per cent for an individual rod and 10 per cent for the pair for this range of cases. The cases were chosen to show the maximum variation likely to occur due to an individual change or related group of changes. The X163 rig is the in-core rig having maximum reactivity worth. The current reflector loading (Case E) and D_2O purity (Case H) should result in the worth of the rod pair remaining above 2% in a 2.75 kg core except under unusual core loadings.

5. References

Connolly J.P. & McKenzie C.D. [1960] - Reactor physics studies on the HIFAR twenty-five element cores. AAEC/TM 64.

Connolly, J.W., Robinson, G.S. & Storr, G.J. [1988] - Re-evaluation of some HIFAR physics data. NT/TN116

Culley, D [1970] - Investigation of flux distributions and reactivity effects in HIFAR using 2D models. AAEC/TM533.

Robinson G.S. [1991a] - 3D diffusion calculations of HIFAR including the coarse control arms and their burnup. ANSTO/E703.

Robinson G.S. [1991b] - Calculation of neutron damage fluences for the HIFAR reactor aluminium tank. NTP/TN 172.

G. S. Robinson,
Nuclear Analysis Section,

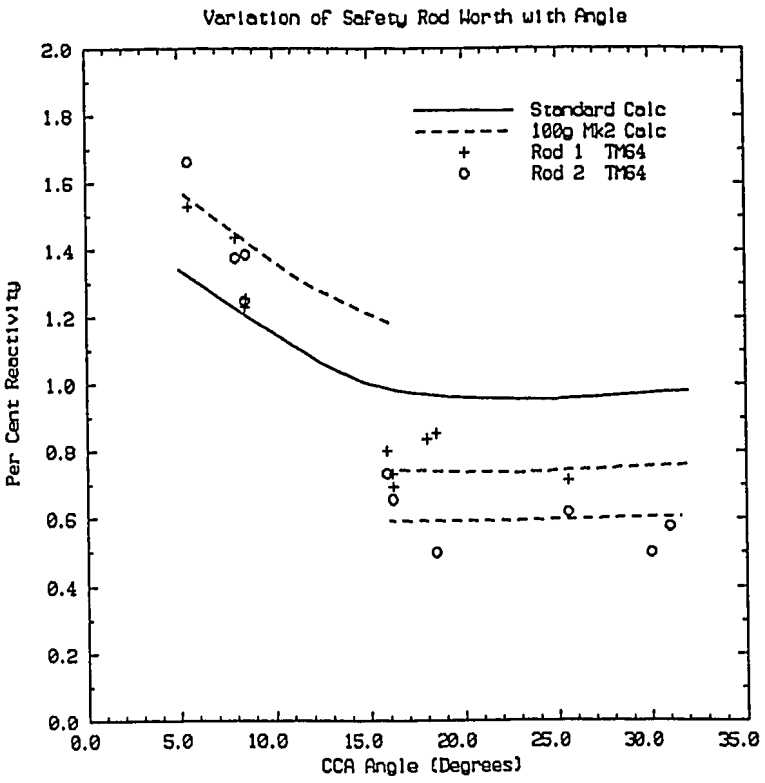
Variation of Safety Rod Worth with Angle
Standard Calc
100g Mk2 Calc
Rod 1 TM64
Rod 2 TM64
Per Cent Reactivity
CCA Angle (Degrees)
0.0
0.2
0.4
0.6
0.8
1.0
1.2
1.4
1.6
1.8
2.0
5.0
10.0
15.0
20.0
25.0
30.0
35.0

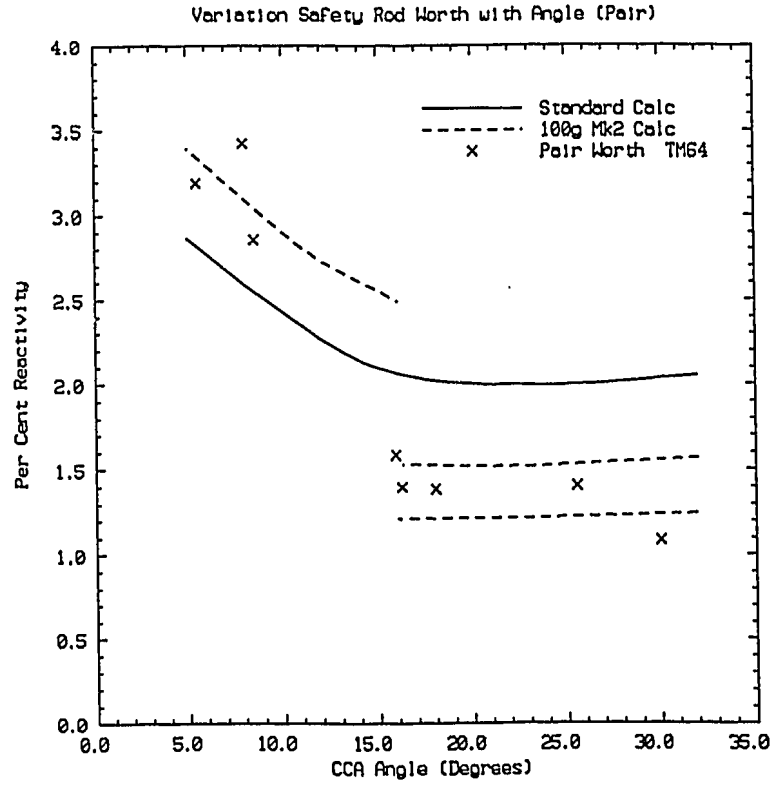
Variation Safety Rod Worth with Angle (Pair)
Standard Calc
100g Mk2 Calc
Pair Worth TM64
Per Cent Reactivity
CCA Angle (Degrees)
0.0
0.5
1.0
1.5
2.0
2.5
3.0
3.5
4.0
5.0
10.0
15.0
20.0
25.0
30.0
35.0

8.4. Appendix A-4

AUSTRALIAN NUCLEAR SCIENCE & TECHNOLOGY ORGANISATION

MINUTE PAPER

16 July 1992

HIFAR DECAY HEAT AND FISSION PRODUCT GAMMA SPECTRA

File: 84/209

Mr J. W. Connolly
Consultant HIFAR Physicist

1. Introduction

This minute sets out the current basis for the calculation of decay heat and fission product gamma spectrum for HIFAR and gives results for

- decay heat and gamma fraction for an element for short decay periods,
- fission product gamma spectrum while at power and that typical of short decay periods,
- fraction of gamma energy deposited in a central element, which had been operating at peak power, under loss of coolant conditions.

2. Basis of Calculations

In recent years, decay heat for HIFAR has been calculated simply from the 'American National Standard for Decay Heat Power in Light Water Reactors' - ANSI/ANS-5.1-1979. The justification for this and maximum decay heat of a fuel element for decay periods up to 4 days are given in my minute to K Lawther 'Calculated Decay Heat for a HIFAR Fuel Element' - File:84/209 [1989]. The AUS code system has now been extended so that the full set of 744 radioactive fission products included on ENDF/B V is available. Previously AUS inventory calculations were restricted to those fission products with half-lives greater than 10 seconds. As well as the average beta and gamma energy per decay for each nuclide, the gamma spectrum is available for 265 nuclides. These data have been processed into the AUS 37 group gamma structure and are available on the AUS directory as the file "endf.fisprodsp". It may be accessed using the XSLIB directive in the CHAR module.

3. Fuel Element Decay Power

For short decay periods, the decay power cannot be read accurately from the figure in the 1979 minute. The following table gives results for decay periods up to an hour for a peak fuel element power of 830 kW. This is the same case as that in used in 1979, but for short decay periods a single cycle of 25 days gives the peak decay power. In the table, the power is the ANS standard result. The ratio of AUS to ANS standard for the decay power shows good agreement except at short times. It is recommended that the ANS value be used. The gamma fraction column gives the ratio of gamma power to total (beta plus gamma) decay power. The spectrum factor is the ratio of total gamma power to gamma power of those fission products with known gamma spectra. This factor has been used to multiply the calculated gamma spectra and indicates the accuracy of the spectrum as a function of time. The accuracy of the spectrum can be considered to be good for times greater than a minute.

DECAY POWER AFTER 1 CYCLE AT 830 kW				
Time (min)	Power (kW)	AUS/ANS Ratio	Gamma Fraction	Spectrum Factor
0.167	37.61	0.949	0.497	1.154
0.333	33.30	0.952	0.511	1.108
0.500	30.87	0.954	0.519	1.085
0.667	29.17	0.958	0.524	1.071
0.833	27.86	0.961	0.528	1.062
1.0	26.80	0.964	0.531	1.055
2.0	22.97	0.975	0.542	1.035
4.0	19.68	0.985	0.550	1.024
6.0	18.00	0.989	0.555	1.020
8.0	16.86	0.993	0.559	1.018
10.0	15.99	0.995	0.562	1.016
20.0	13.24	1.003	0.570	1.010
30.0	11.64	1.007	0.573	1.007
40.0	10.53	1.009	0.575	1.005
50.0	9.72	1.010	0.575	1.003
60.0	9.08	1.010	0.574	1.002

To complete the picture, a similar table is also given for decay times up to 96 hours. For these periods, results after three cycles are presented as these tend to give the maximum decay powers. There is good agreement with the value of 0.59 for the gamma fraction quoted in the HIFAR safety document for 10 to 24 hours after shutdown. To be conservative in fuel element cooling requirements, a low value of gamma fraction appropriate to the times being considered should be used.

DECAY POWER AFTER 3 CYCLES AT 830, 789, 749 kW				
Time (hr)	Power (kW)	AUS/ANS Ratio	Gamma Fraction	Spectrum Factor
1.	8.70	1.011	0.574	1.002
4.	5.28	1.000	0.551	1.000
12.	3.50	1.002	0.568	1.000
24.	2.67	1.009	0.591	1.000
48.	2.07	1.015	0.606	1.000
72.	1.79	1.017	0.610	1.000
96.	1.62	1.018	0.610	1.000

4. Fission Product Gamma Spectra at Power

For most HIFAR calculations requiring the fission product gamma spectrum while at power, the data from 'PWR Shielding Benchmark' - NEACRP-L-264 [1964] has been used in recent years. Calculations of the fission product gamma spectrum at power for HIFAR and for a PWR have now been made and compared with NEACRP-L-264. In the following tables, HIFAR results are for 25 days at power while PWR results are at 16000 MWd/te burnup. Peak PWR results of 7.05 photons and 5.70 MeV per fission were calculated at about 2000 MWd/te. The basis of the NEACRP-L-264 data is unknown. In view of the large factor by which the spectrum had to be multiplied, the obvious lack of higher energy photons in the AUS calculations, and the fact that

the AUS calculations of HIFAR and PWR are similar; it is recommended that the NEACRP-L-264 data be retained for use on HIFAR.

	HIFAR	PWR	NEACRP-L-264
Photons/fission	6.802	6.919	6.69
MeV/fission	5.608	5.395	6.33
Spectrum Factor	1.326	1.362	

DATA ON PHOTON SPECTRA

Group	Lower Energy (MeV)	Photon Spectra (Photons/Fission) HIFAR	PWR	NEACRP-L-264	Spectrum (2 min) (Photons/Photon) HIFAR
1	12.0	0.0	0.0	0.0	0.0
2	10.0	0.0	0.0	0.00048	0.0
3	8.0	0.0	0.0	0.00084	0.0
4	6.5	0.00008	0.00005	0.00389	0.0
5	5.0	0.00578	0.00428	0.01996	0.00025
6	4.0	0.02379	0.01758	0.04894	0.00166
7	3.0	0.09158	0.07623	0.14557	0.00784
8	2.5	0.11792	0.10161	0.15891	0.01434
9	2.0	0.21036	0.18607	0.27406	0.03230
10	1.66	0.23559	0.21561	0.29261	0.02777
11	1.33	0.52185	0.48770	0.42412	0.07687
12	1.0	0.71105	0.65118	0.74470	0.09275
13	0.8	0.84180	0.81675	0.71513	0.13961
14	0.6	0.97398	1.11588	1.02080	0.15576
15	0.4	1.01788	1.06110	1.14760	0.15059
16	0.3	0.46805	0.52576	0.57358	0.06348
17	0.2	0.45634	0.46382	0.57358	0.06432
18	0.1	0.50845	0.53110	0.54778	0.07370
19	0.045	0.15320	0.15257	0.0	0.02334
20	0.02	0.32138	0.36713	0.0	0.05371
21	0.01	0.14311	0.14492	0.0	0.02172

5. Deposition of Gamma Power

The fractional gamma spectrum is also included in the above table for a decay time of two minutes. The spectrum as a function of decay period varies slowly for the calculated periods. The spectrum at two minutes has been used to calculate the fraction of gamma power which is released in a fuel element. This has been calculated for the condition of loss of coolant. It was done for a new 170g fuel element at the centre of the reactor using a 1D radial S_{16} P_3 ANAUSN calculation with the full set of photon groups. The central element was represented explicitly but other elements which were burnt to 110g of ^{235}U had to be smeared over the fuel element cell. The axial direction was simply represented by a buckling of 7 m^{-2}. The single fuel element, without the surrounding reactor, was calculated to absorb 0.124 of the gamma power generated by the element. This fraction increased to 0.134 when reflection by the surroundings was included. When a flat power distribution was used to provide a source in the other elements, the fraction

increased to 0.274. Using a more reasonable power distribution, that for a uniformly fueled core, the fraction decreased slightly to 0.259. The axial buckling does not greatly affect the result; using no buckling gave 0.287 rather than 0.259. These results are not sensitive to the decay time used to define the spectrum. Using the spectrum at 60 minutes gave an increase from 0.259 to 0.270 only. A central 170g element gives the worst possible case when considering a loss of coolant accident. Using a power distribution for a uniformly fueled core in conjunction with this, implies that all elements are generating power at the peak rate of new fuel elements. Thus the final result of 0.26 for the fraction is quite conservative.

G. S. Robinson,
Nuclear Analysis Section,
Nuclear Technology Program

cc B. E. Clancy
D. R. Beattie
B. J. McGregor
B. V. Harrington
G. J. Malosh
R. M. Godfrey

8.5. Appendix A-5
Tabulation of Thermal Data.

Fuel alloy properties

T	k(T)	C(T)	1/V dV/dT	$\int_{T}^{913} C(T')\,dT'$
Temp	Thermal Conductivity	Volumetric Specific Heat	Expansion Coeff	Volumetric Heat Capacity to melting
(K)	W $m^{-1}K^{-1}$	MJ $m^{-3}K^{-1}$	K^{-1}	MJ m^{-3}
293.0	172.6	2.260	0.0000655	1621.5
313.0	171.8	2.288	0.0000659	1576.1
333.0	171.0	2.315	0.0000663	1530.0
353.0	170.1	2.341	0.0000666	1483.5
373.0	169.3	2.368	0.0000669	1436.4
393.0	168.5	2.393	0.0000672	1388.8
413.0	167.6	2.418	0.0000675	1340.7
433.0	166.8	2.443	0.0000677	1292.0
453.0	165.9	2.467	0.0000679	1242.9
473.0	165.1	2.491	0.0000680	1193.3
493.0	164.3	2.515	0.0000681	1143.3
513.0	163.4	2.537	0.0000682	1092.8
533.0	162.6	2.560	0.0000683	1041.8
553.0	161.8	2.582	0.0000683	990.4
573.0	160.9	2.603	0.0000683	938.5
593.0	160.1	2.624	0.0000683	886.2
613.0	159.3	2.645	0.0000682	833.6
633.0	158.4	2.665	0.0000681	780.5
653.0	157.6	2.685	0.0000680	727.0
673.0	156.8	2.704	0.0000678	673.1
693.0	155.9	2.722	0.0000677	618.8
713.0	155.1	2.740	0.0000674	564.2
733.0	154.2	2.758	0.0000672	509.2
753.0	153.4	2.775	0.0000669	453.9
773.0	152.6	2.792	0.0000666	398.2
793.0	151.7	2.809	0.0000663	342.2
813.0	150.9	2.824	0.0000659	285.9
833.0	150.1	2.840	0.0000655	229.2
853.0	149.2	2.855	0.0000650	172.3
873.0	148.4	2.869	0.0000646	115.0
893.0	147.6	2.883	0.0000641	57.5
912.9	146.7	2.897	0.0000636	0.0
913.1	56.4	2.537	0.0000636	0.0
923.0	56.4	2.537	0.0000633	0.0

Clad properties

T	k(T)	C(T)	1/V dV/dT	$\int_{T}^{922} C(T')\,dT'$
Temp	Thermal Conductivity	Volumetric Specific Heat	Expansion Coeff	Volumetric Heat Capacity to melting
(K)	$W\,m^{-1}K^{-1}$	$MJ\,m^{-3}K^{-1}$	K^{-1}	$MJ\,m^{-3}$
293.0	164.8	2.426	0.0000702	1752.8
313.0	166.5	2.449	0.0000702	1704.0
333.0	168.0	2.472	0.0000702	1654.8
353.0	169.5	2.495	0.0000702	1605.1
373.0	170.8	2.518	0.0000702	1555.0
393.0	172.1	2.541	0.0000702	1504.4
413.0	173.2	2.564	0.0000702	1453.4
433.0	174.3	2.587	0.0000702	1401.9
453.0	175.2	2.610	0.0000702	1349.9
473.0	176.1	2.633	0.0000702	1297.5
493.0	176.9	2.655	0.0000702	1244.6
513.0	177.6	2.678	0.0000702	1191.2
533.0	178.3	2.701	0.0000702	1137.5
553.0	178.9	2.724	0.0000702	1083.2
573.0	179.4	2.747	0.0000702	1028.5
593.0	179.9	2.770	0.0000702	973.3
613.0	180.4	2.793	0.0000702	917.7
633.0	180.8	2.816	0.0000702	861.6
653.0	181.1	2.839	0.0000702	805.1
673.0	181.5	2.862	0.0000702	748.0
693.0	181.8	2.885	0.0000702	690.6
713.0	182.0	2.907	0.0000702	632.7
733.0	182.3	2.930	0.0000702	574.3
753.0	182.5	2.953	0.0000702	515.5
773.0	182.8	2.976	0.0000702	456.2
793.0	183.0	2.999	0.0000702	396.4
813.0	183.2	3.022	0.0000702	336.2
833.0	183.5	3.045	0.0000702	275.5
853.0	183.7	3.068	0.0000702	214.4
873.0	184.0	3.091	0.0000702	152.8
893.0	184.2	3.114	0.0000702	90.8
913.0	184.6	3.137	0.0000702	28.3
922.0	184.7	3.147	0.0000702	0.0
933.0	71.1	2.604	0.0000702	0.0
953.0	71.1	2.604	0.0000702	0.0

Liquid D_2O properties

T	k(T)	C(T)	1/V dV/dT	$\int_T^{373} C(T')\,dT'$	Density
Temp	Thermal Conductivity	Volumetric Specific Heat	Expansion Coeff	Volumetric Heat Capacity to saturation	
K	$W\,m^{-1}K^{-1}$	$MJ\,m^{-3}K^{-1}$	K^{-1}	$MJ\,m^{-3}$	$kg\,l^{-1}$
293.0	0.5902	4.689	0.0001304	366.2	1.1053
303.0	0.6003	4.676	0.0002416	319.4	1.1032
313.0	0.6090	4.654	0.0003422	272.7	1.1000
323.0	0.6165	4.625	0.0004321	226.4	1.0957
333.0	0.6228	4.589	0.0005113	180.3	1.0906
343.0	0.6278	4.549	0.0005798	134.6	1.0847
353.0	0.6316	4.507	0.0006377	89.3	1.0781
363.0	0.6343	4.465	0.0006848	44.4	1.0710
373.0	0.6359	4.424	0.0007213	0.0	1.0635
393.0	0.6357	4.353	0.0007621	0.0	
413.0	0.6312	4.309	0.0007602	0.0	

8.6. Appendix A-6

From gsr Fri Dec 4 11:12 EST 1992
Date: Fri, 4 Dec 92 11:12:17 EST
From: gsr (Graham Robinson)
To: bec
Content-Type: text
Content-Length: 2268
Status: R

Effect of D2O Upgrade from 98.6% to 99.7% on integral CCA worth
October 1992

The results below were calculated for a uniform core of 170 g fuel elements burnt to 110 g to give a 2.75 Kg core mass. The raw Keff results are included as well as the integral CCA worths as a function of angle. The final column gives the ratio of the integral worths. To apply these results to the measured CCA calibration, I suggest that this ratio be scaled to the required D2O change, used to multiply the measured integral worths and then the fitting of integral worths be repeated.

Note that the data can also be used to give the effect on reactivity of the D2O upgrade at any CCA angle. At typical startup and shutdown angles of 15 and 25 degrees, this gives 0.46% and 0.64%. Unless this can be reconciled with the observed reactivity changes at the time of the upgrade, the justification for modifying the CCA calibration must be weak.

G. S. Robinson,
Nuclear Analysis Section

Angle	Keff		CCA Rho %		Ratio
	98.6	99.7	98.6	99.7	99.7/98.6
56.	0.99283	1.00313	0.00	0.00	0.0000
35.	0.98901	0.99774	0.39	0.54	1.3843
31.	0.98562	0.99348	0.74	0.97	1.3142
29.	0.98299	0.99032	1.01	1.29	1.2789
28.	0.98137	0.98842	1.18	1.48	1.2614
27.	0.97944	0.98619	1.38	1.71	1.2436
26.	0.97729	0.98374	1.60	1.96	1.2268
25.	0.97472	0.98086	1.87	2.26	1.2095
24.	0.97185	0.97767	2.17	2.60	1.1939
23.	0.96869	0.97424	2.51	2.96	1.1777
22.	0.96501	0.97028	2.90	3.38	1.1623
21.	0.96052	0.96548	3.39	3.89	1.1474
20.	0.95592	0.96065	3.89	4.41	1.1335
19.	0.95010	0.95459	4.53	5.07	1.1190
18.	0.94471	0.94901	5.13	5.69	1.1081

17.	0.93814	0.94229	5.87	6.44	1.0962
16.	0.93203	0.93608	6.57	7.14	1.0868
15.	0.92381	0.92778	7.53	8.10	1.0759
14.	0.91707	0.92101	8.32	8.89	1.0682
13.	0.90933	0.91333	9.25	9.80	1.0597
12.	0.90149	0.90549	10.21	10.75	1.0533
11.	0.89296	0.89702	11.26	11.79	1.0468
10.	0.88501	0.88914	12.27	12.78	1.0415
7.	0.86156	0.86593	15.35	15.79	1.0292
0.	0.80803	0.81232	23.04	23.42	1.0165

This page of Section 8 intentionally left blank